TU WIEN
DEPARTMENT OF
GEODESY AND
GEOINFORMATION

DISSERTATION

# Parameter estimation based on global multi-GNSS network data

Ausgeführt zum Zwecke der Erlangung des akademischen Grades eines/r Doktors/in
der technischen Wissenschaften unter Leitung von

Ao. Univ. Prof. Dipl.-Ing. Dr.techn. Robert Weber
E120-4
Department für Geodäsie und Geoinformation
Forschungsbereich Höhere Geodäsie

eingereicht an der Technischen Universität Wien
Fakultät für Mathematik und Geoinformation

von

**Dipl.-Ing. Dzana Halilovic**
Matrikelnummer: 01634335

Wien, September 2024

Unterschrift (Verfasser/in) Unterschrift (Betreuer/in)

# Eidesstattliche Erklärung

Ich erkläre an Eides statt, dass die vorliegende Arbeit nach den anerkannten Grundsätzen für wissenschaftliche Abhandlungen von mir selbstständig erstellt wurde. Alle verwendeten Hilfsmittel, insbesondere die zugrunde gelegte Literatur, sind in dieser Arbeit genannt und aufgelistet. Die aus den Quellen wörtlich entnommenen Stellen, sind als solche kenntlich gemacht.

Das Thema dieser Arbeit wurde von mir bisher weder im In- noch Ausland einer Beurteilerin/einem Beurteiler zur Begutachtung in irgendeiner Form als Prüfungsarbeit vorgelegt. Diese Arbeit stimmt mit der von den Begutachterinnen/Begutachtern beurteilten Arbeit überein.

Wien, September 2024 ________________________

## Acknowledgements

As I sat one day in front of my computer, surrounded by research papers and theses of my fellow colleagues, my daughter Safija approached me asking: "Mom, what are you doing?". To keep things simple for a 2-year-old, I replied: "I am writing a book, honey." "For me?", she asked. "No, unfortunately. It's about my work at the university, and I need to finish it." After a few more questions and answers about the book I was writing, we agreed that I would write a book for her as soon as I had completed this one. Two years later, the book is finally done.

First and foremost, I sincerely thank God, the Most Gracious, the Most Merciful, for His endless guidance and blessings, which enabled me to complete this work.

I am profoundly grateful to my supervisor, Prof. Dr. Robert Weber, who believed in my abilities and guided me throughout this journey. No matter how busy you were, you always made time to discuss my research, offering valuable ideas on how to proceed or solve problems. And of course, there was always room for a quick chat. My heartfelt thanks also go to Prof. Dr. Medžida Mulić, who played a pivotal role in helping me pursue my PhD. Without the efforts of both of you, this thesis would not have been possible. Your support, comments, and advice have been invaluable, easing many challenges along the way.

To Prof. Dr. Johannes Böhm, thank you for always being available and for your excellent leadership of our research unit of Higher Geodesy. I cannot recall a single moment when you didn't greet me with a smile whenever I came to your office with a question.

To my colleagues and friends at the university, thank you for the wonderful years we spent together, especially to my officemates. I truly appreciated your company and the stimulating discussions that shaped my thinking and approach.

I am deeply thankful to my family. To my parents and sister, thank you for your unconditional support throughout the years. Through all my ups and downs, knowing you were by my side gave me the strength and motivation to keep going. To my husband, thank you for your love, patience, and constant support throughout this journey. I know it was not easy for you. To my daughters, Safija and Sara, thank you for being my source of joy and inspiration, even when you didn't fully understand what I was doing, and my work took time away from our moments together. To my mother-in-law, thank you for sharing your kind words, thoughtful concerns, and wise advice with me.

Each of you played a unique role in giving me the strength and motivation to continue my work, and I will be forever grateful for that.

Now, as I finish this book, I look forward to fulfilling my promise to Safija and starting the new one for her. I suppose she'll have to share it with Sara too.

# Kurzfassung

Die Geodäsie hat mit dem Aufkommen moderner Weltraumgeodätischer Techniken eine tiefgreifende Veränderung durchlaufen. Diese Methoden ermöglichen präzise Messungen der Form, der Rotation und der Orientierung der Erde im Raum. Zudem spielen sie eine entscheidende Rolle bei der Überwachung der Erdatmosphäre und der Beobachtung geophysikalischer Phänomene. Sie dienen sowohl der wissenschaftlichen Forschung als auch praktischen Anwendungen.

Im Rahmen dieser Arbeit wurden GNSS-basierte Anwendungen genutzt. Diese nehmen eine herausragende Stellung unter den Weltraumgeodätischen Techniken ein. Sie ermöglichen präzise Schätzungen der Polkoordinaten (x, y) und der Tageslänge (LoD), die gemeinsam als Erdrotationsparameter (ERPs) bezeichnet werden. Hochgenaue ERP-Zeitreihen sind unerlässlich, um komplexe Dynamiken der Erde zu verstehen und genaue Referenzsysteme zu etablieren. Davon profitieren die meisten Anwendungen in der Navigation und Positionierung. Dank eines umfangreichen Netzwerks weltweit aktiver GNSS-Stationen ist eine globale Abdeckung gewährleistet, welche eine beispiellos genaue Bestimmung der ERPs ermöglicht.

Allerdings sind mehrere Fehlerquellen, welche die GNSS-Signallaufzeit zwischen Satellit und Empfänger beeinflussen, zu beachten. Eine Hauptfehlerquelle ist die Ionosphäre, ein für Mikrowellen dispersives Medium das Signalverzögerungen verursacht, wenn die Signale durch die Erdatmosphäre zu bodengebundenen Empfängern gelangen. Durch die Nutzung von Beobachtungen auf 2 Frequenzen ist es allerdings möglich, mit der sogenannten ionosphärenfreien Linearkombination einen erheblichen Teil dieser Verzögerung zu eliminieren. Andererseits ermöglicht die geometriefreie Linearkombination von Mehrfrequenzbeobachtungen die Erstellung von Ionosphärenmodellen und damit die Beschreibung von ionosphärischen Zustandsgrößen. Diese Modelle können anschließend verwendet werden um Laufzeitkorrekturen für Beobachtungen von Massenmarkt- Einfrequenz-Empfängern zu berechnen.

Das Ziel dieser Arbeit war es, die bereits erwähnten Erdrotationsparameter (ERPs) als auch ionosphärische Informationen in Form von VTEC-(Vertical Total Electron Content)-Karten zu schätzen und zu analysieren. Hierfür wird insbesondere eine Kombination aus GPS- und Galileo-Beobachtungen prozessiert, um zu beurteilen, inwieweit diese Lösungen durch die Verwendung von Multi-GNSS-Kombinationen im Gegensatz zu einzig auf GPS Daten basierenden Beobachtungen verbessert wurden.

Besondere Aufmerksamkeit gilt dem europäischen Galileo-System. Seit dem Start seines ersten Testsatelliten im Dezember 2005 hat Galileo eine entscheidende Rolle als Ergänzung zu etablierten GNSS-Systemen wie dem US-amerikanischen GPS und dem russischen GLONASS gespielt. Es kann gezeigt werden, dass die Kombination von Galileo- mit GPS-Beobachtungen eine deutlich verbesserte Genauigkeit bei der präzisen Parameterabschätzung liefert, sofern für Galileo hochpräzise Bahndaten basierend auf neuen Strahlungsdruckmodellen zur Verfügung stehen.

Die Methodik dieser Forschung umfasste die Verarbeitung von Beobachtungsdaten in der Bernese GNSS Software Version 5.2 (BSW). Beobachtungen von einem weltweit verteilten Netzwerk von GNSS IGS-Stationen wurden verwendet, um ERP-Zeitreihen (Erdrotationsparameter) zu schätzen. Je nach Kombination der Beobachtungen (nur GPS oder kombiniertes GPS+Galileo) und dem verwendeten Strahlungsdruckmodell wurden sechs Lösungen über 1-Tages- und 3-Tages-Bögen berechnet. Zusätzlich wurde ein detailliertes regionales Ionosphärenmodell für die mittleren Breiten Europas mithilfe von Daten von GNSS IGS- und EPOSA-Permanentstationen (Echtzeit Positionierung Austria) erstellt, wobei die modifizierte Single-Layer-Mapping-Funktion (MSLM) und die geometriefreie lineare Kombination verwendet wurden. Die Ergebnisse wurden anhand einer Gegenüberstellung mit etablierten Modellen validiert. Dabei konnten erhebliche Verbesserungen bei der Integration von Multi-GNSS-Daten hervorgehoben werden.

Der Beitrag dieser Studie spiegelt sich in der Demonstration einer verbesserten Genauigkeit wider, die durch die Integration von Multi-GNSS erreicht werden kann, in diesem Fall bei ERP- und Ionosphärenmodellierung. Die Ergebnisse dieser Studie bestätigen die Bedeutung der Verwendung mehrerer GNSS-Systeme für präzise geodätische Anwendungen. Es wird daher empfohlen, auf kombinierte Beobachtungsdaten zurückzugreifen, um künftige Verbesserungen gewährleisten zu können.

Die Genauigkeitssteigerung für ERPs liegt bei ungefähr 25%, während die VTEC Schätzungen im Sommer um etwa 60% und im Winter bis zu 80% im Vergleich zu externen Referenzmodellen verbessert werden konnten.

# Abstract

With the advent of modern space geodetic techniques Geodesy has undergone a profound transformation. These methods enable precise measurements of the Earth's shape, rotation, and orientation in space. Moreover, they play a crucial role in monitoring the Earth's atmosphere and observing geophysical phenomena. They serve both scientific research and practical applications.

This study leverages GNSS-based applications, which hold a prominent position among space geodetic techniques. They enable precise estimations of the pole coordinates (x, y) and the length of day (LoD), collectively referred to as Earth Rotation Parameters (ERPs). Highly accurate ERP time series are essential for understanding the complex dynamics of the Earth and establishing precise reference systems. Most navigation and positioning applications benefit from this. Thanks to a comprehensive network of globally active GNSS stations, global coverage is ensured, allowing for an unprecedentedly accurate determination of ERPs.

However, several error sources that affect the GNSS signal travel time between the satellite and the receiver must be considered. A major error source is the ionosphere, a medium dispersive for microwaves, causing signal delays as the signals pass through the Earth's atmosphere to ground-based receivers. By using observations on two frequencies, it is possible to eliminate a significant portion of this delay with the so-called ionosphere-free linear combination. On the other hand, the geometry-free linear combination of multi-frequency observations enables the creation of ionospheric models and thus the description of ionospheric state variables. These models can then be used to calculate travel time corrections for observations from mass-market single-frequency receivers.

The aim of this work was to estimate and analyze the aforementioned Earth Rotation Parameters (ERPs) as well as ionospheric information in the form of VTEC (Vertical Total Electron Content) maps. For this purpose, a combination of GPS and Galileo observations was processed to assess the extent to which these solutions are improved by using multi-GNSS combinations versus GPS-only data.

Special attention is given to the European Galileo system. Since the launch of its first test satellite in December 2005, Galileo has played a crucial role as a complement to established GNSS systems such as the American GPS and the Russian GLONASS. The study shows that combining Galileo with GPS observations significantly improves accuracy in precise parameter estimation, provided that high-precision orbit data based on new radiation pressure models are available for Galileo.

The methodology for this research involved processing observation data in the Bernese GNSS Software version 5.2 (BSW). Observations from a globally distributed network of GNSS IGS stations were used to estimate ERP (Earth rotation parameters) time series. Six solutions across 1-day and 3-day arcs were calculated, depending on the combination of observations (GPS-only or GPS+Galileo combined) and the radiation pressure model used. Additionally, a detailed regional ionosphere model covering mid-latitude Europe was generated using data from GNSS IGS and EPOSA (Echtzeit Positionierung Austria) permanent stations, employing the modified single-layer mapping function (MSLM) and the geometry-free linear combination. Results were validated against established models, highlighting significant improvements when integrating multi-GNSS data.

The contribution of this study is reflected in the demonstration of improved accuracy, which can be achieved through multi-GNSS integration, in this case in ERP and ionospheric modeling. The findings verify the importance of utilizing multiple GNSS systems for precise geodetic applications. Thus, it is recommended that combined observation data be relied on for future improvements.

The accuracy improvement for ERPs is approximately 25%, while the VTEC estimates could be improved within the range of 60% during summer months up to 80% in winter, with respect to external reference models.

# Contents

# List of Figures

# List of Tables

# List of Acronyms

**AC** Analysis Center

**AGW** Atmospheric Gravity Waves

**AIUB** Astronomical Institute at the University of Bern

**AR** Ambiguity Resolution

**ARPL** Aeronomy and Radiopropagation Laboratory

**AS** Authorized Service

**BeiDou** Chinese Navigation Satellite System

**BIH** Bureau International de l'Heure

**BSW** Bernese GNSS Software

**CDDIS** Crustal Dynamics Data Information System

**CDMA** Code Division Multiple Access

**CIO** Celestial Intermediate Origin

**CIP** Celestial Intermediate Pole

**CIRS** Celestial Intermediate Reference System

**CME** Coronal Mass Ejection

**CODE** Center for Orbit Determination in Europe

**CODG** Code Global

**COSPAR** Committee on Space Research

**CRF** Celestial Reference Frame

**DCB** Differential Code Bias

**DD** Double Difference

**DoD** Department of Defense

**DORIS** Doppler Orbitography Radiopositioning Integrated by Satellite

**EC** European Commission

**ECOM** Empirical Code Orbit Model

**EIA** Equatorial Ionization Anomaly

**EOP** Earth Orientation Parameters

**EOP-PC** Earth Orientation Parameters Product Center

**EPOSA** Echtzeit Positionierung Austria

**ERA** Earth Rotation Angle

**ERP** Earth Rotation Parameter

**ESA** European Space Agency

**ESM** Extended Slab Model

**ESOC** European Space Operations Centre

**EUSPA** European Union Agency for the Space Programme

**EUV** Extreme Ultraviolet

**EWS** Early Warning Service

**FCN** Free Core Nutation

**FOC** Full-Operational-Capability

**GAL** Galileo

**Galileo** Europe's Global Satellite Navigation System

**GAS** GPS Augmentation Service

**GCRS** Geocentric Celestial Reference System

**GCS** GPS Complementary Service

**GCS** Ground Control Segment

**GEO** Geosynchronous Equatorial Orbit (Geostationary Orbit)

**GFZ** German Research Centre for Geosciences

**GGOS** Global Geodetic Observing System

**GIM** Global Ionospheric Map

**GIOVE** Galileo In-Orbit Validation Element

**GLONASS** Globalnaja Nawigacionnaja Sputnikowaja Sistiema

**GMS** Ground Mission Segment

**GMST** Greenwich Mean Sidereal Time

**GNSS** Global Navigation Satellite Systems

**GPS** Global Positioning System

**GRC-MS** Galileo Reference Center – Member States

**GSA** European GNSS Agency

**GSS** Galileo Sensor Station

**HAS** High Accuracy Service

**HF** High Frequency

**IAAC** Ionosphere Associate Analysis Center

**IAU** International Astronomical Union

**ICRF** International Celestial Reference Frame

**ICRS** International Celestial Reference System

**IDS** International DORIS Service

**IERS** International Earth Rotation and Reference Systems Service

**IGS** International GNSS Service

**IGSG** IGS Global

**IGSO** Inclined Geosynchronous Orbit

**IIWG** IGS Ionosphere Working Group

**ILRS** International Laser Ranging Service

**ILS** International Latitude Service

**IMF** Interplanetary Magnetic Field

**InSAR** Interferometric Synthetic Aperture Radar

**IONEX** Ionosphere Map Exchange Format

**IOV** In-Orbit Validation

**IPP** Ionospheric Pierce Point

**IPY** International Polar Year

**IRI** International Reference Ionosphere

**IRNSS/NavIC** Indian Regional Navigation Satellite System (IRNSS)/Navigation Indian Constellation

**ITRF** International Terrestrial Reference Frame

**ITRS** International Terrestrial Reference System

**ITU-R** International Telecommunication Union, Radiocommunication

**IUGG** International Union of Geodesy and Geophysics

**IVS** International VLBI Service

**JPL** Jet Propulsion Laboratory

**KLOG** Klobuchar Global

**LC** Linear Combination

**LLR** Lunar Laser Ranging

**LOD** Length of Day

**LS** Large-scale

**LSA** Least Squares Adjustment

**MCS** Message Communications Service

**MEO** Medium Earth Orbit

**MGNSS** Multi Global Navigation Satellite System

**MODIP** Modified Dip Latitude

**MS** Medium-scale

**MSISE** Mass Spectrometer - Incoherent Scatter Empirical

**MSL** Mean Sea Level

**MSLM** Modified Single-Layer Mapping

**MW** Melbourne-Wübbena

**NaN** Not a Number

**NEQ** Normal Equation System

**NEQG** NeQuick G

**NNR** No Net Rotation

**NOAA** National Oceanic and Atmospheric Administration

**OS** Open Service

**PCA** Polar Cap Absorption

**PCO** Phase Center Offset

**PCV** Phase Center Variation

**PPP** Precise Point Positioning

**PPS** Precise Positioning Service

**PRS** Public Regulated Service

**PS** Precision Service

**QIF** Quasi-Ionosphere Free

**QZSS** Quasi-Zenith Satellite System

**RAAN** Right Ascension of the Ascending Node

**RINEX** Receiver Independent Exchange Format

**RMS** Root Mean Square

**RNSS** Regional Navigation Satellite Systems

**RS** Restricted Service

**SA** Selective Availability

**SAR** Search and Rescue Service

**SD** Single Difference

**SID** Sudden Ionospheric Disturbance

**SIDC** Sunspot Index Data Centre

**SINEX** Solution Independent Exchange Format

**SLM** Single Layer Model

**SLR** Satellite Laser Ranging

**SPP** Single Point Positioning

**SPS** Standard Positioning Service

**SRP** Solar Radiation Pressure

**STEC** Slant Total Electron Content

**SWF** Short Wave Fadeout

**TD** Triple Difference

**TEC** Total Electron Content

**TECU** TEC Units

**TGP** Tide Generating Body

**TID** Traveling Ionospheric Disturbance

**TIO** Terrestrial Intermediate Origin

**TIRS** Terrestrial Intermediate Reference System

**TRF** Terrestrial Reference Frame

**TT** Terrestrial Time

**TUW** Technische Universität Wien

**TUWR** TUW Regional

**UAW** Unified Analysis Workshop

**ULS** Up-link Station

**UPC** Universitat Politécnica de Catalunya

**URSI** International Union of Radioscience

**UT** Universal Time

**UT1** Universal Time 1

**UTC** Universal Time Coordinated

**UV** Ultraviolet

**VLBI** Very Long Baseline Interferometry

**VMF** Vienna Mapping Functions

**VTEC** Vertical Total Electron Content

**WADS** Wide Area Differential Service

**SMS** Short Message Service

**WG** Working Group

**WL/NL** Wide-lane/Narrow-lane

**ZD** Zero Difference

# 1. Introduction

## 1.1. Motivation

Since the launch of the first Galileo satellite in December 2005, the individual global navigation satellite systems, GPS and GLONASS, have not only gained a new competitor but also found an essential complement for GNSS applications, both in everyday use and research. Thanks to Galileo's interoperability with these GNSS systems, it is possible to enhance the accuracy of precise parameter determinations by complementing the existing observations with Galileo data.

In today's rapidly evolving world, where the need for precision and accuracy is in constant growth, geodesy plays a pivotal role in providing the essential framework for a multitude of applications, from navigation and cartography to environmental monitoring, as well as disaster management. Various geodetic parameters, including station coordinates, Earth rotation parameters (pole coordinates and Length of Day (LoD)), atmospheric parameters (troposphere and ionosphere), or horizontal and vertical displacement components, form the foundation upon which these applications rely.

This investigation is motivated by the recognition that the dynamic Earth requires continuous refinement and improvement of geodetic methods and models. Earth's ever-changing conditions, influenced by factors such as tectonic movements and ionospheric fluctuations, demand a careful reevaluation of existing techniques and the exploration of possible new approaches. The following questions have been set to be addressed within this thesis:

- How can the precision and reliability of global geodetic parameters, in this case, Earth rotation parameters (ERPs), be enhanced by incorporating multi-GNSS systems, with a specific focus on the Galileo system?
- What impact does the integration of Galileo alongside GPS have on the estimation of ERPs, and how does it compare to conventional solutions?
- Can a regional ionosphere model, based on multi-GNSS observations, provide accurate and dependable results, and potentially benefit single-frequency receivers?

By addressing these questions, this study strives to contribute to the ongoing development of geodetic science, enabling more accurate satellite navigation, Earth observation, and a deeper understanding of the dynamic nature of planet Earth.

## 1.2. Outline

**Chapter 2 - The Earth rotation** provides information about the dynamic nature of the system Earth. It explores the inconsistent rotational behavior of the Earth, leading to changes in the direction of the Earth's axis and the position of the Earth's body. The definition and establishment of sufficient reference frames are crucial to accurately monitor these effects. Therefore, we will discuss the terms "celestial reference frame" (CRF) and "terrestrial reference frame" (TRF), as well as the transformation from one reference frame to the other. The link between them, the Earth orientation parameters (EOPs), will be described in more detail. The EOPs consist of five transformation angles, namely precession and nutation, polar motion, and the Earth rotation angle. Additionally, dynamic ocean tides, as a predominant influence in the Earth's rotation, are described and associated high-frequency EOP models (ocean tide-based and empirical models), recommended to the IERS by the High frequency EOP Working Group (HF EOP WG) on Diurnal and Semi-diurnal EOP Variations, are introduced. This chapter is wrapped up by an overview of the techniques, used nowadays, to determine EOPs, pointing out their advantages, as well as their deficiencies.

**Chapter 3 - The Ionosphere** guides us through the main features of the Ionosphere, starting with the term "Ionization" itself, moving on to its structure, describing the key characteristics of each region separately. The chapter continues with the basics of wave propagation in the Ionosphere, describing the Ionospheric refraction in more detail. Furthermore, variabilities due to the Sun and solar activity, as well as different types of ionospheric disturbances and irregularities of the Ionosphere are described. The geomagnetic field, together with the magnetosphere, is described and illustrated within this chapter, given its significant impact on the Ionosphere, by altering the movement of charged particles within this region. Some established existing ionospheric models are presented at the end of this chapter. They will provide the reference values needed for the evaluation of the ionospheric model presented in this work.

**Chapter 4 - Global Navigation Satellite Systems** starts with an overview of the development of GNSS as a satellite-based technique. It offers a summary on currently operational GNSS (GPS, GLONASS, Galileo, BeiDou) and RNSS (QZSS, IRNSS/NavIC), by pointing out their main characteristics, in terms of frequency band coverage, satellite orbit features, altitude, services offered, and so on. Afterward, this chapter concentrates mainly on describing the two GNSS used in this work, namely GPS and Galileo. Therefore, in the following lines, these two GNSS are elaborated in more detail. The chapter continues with the description of GNSS observation equations for code- and phase-based measurements. Finally, the most common linear combinations used for the elimination or mitigation of possible error sources, as well as for ambiguity resolution, are presented at the end of this chapter.

**Chapter 5 - Parameter estimation** leads us to the processing strategy itself. It is divided into two parts. The first one, Earth rotation parameters, describes the processing scheme for the determination of ERPs, which is based on observation data of a globally distributed network of permanent GNSS IGS stations. Three solutions are calculated in total, each covering a 1- and 3-day solution, making in total 6 different solution types. A GPS-only, a combined GPS/Galileo + old ECOM model, and a combined GPS/Galileo + ECOM2 model solution are performed. ECOM, short for Empirical CODE Orbit Model, is a solar radiation pressure model that has two versions available for use: the older ECOM and the newer ECOM2 model. Both ECOM versions are described, in terms of how the radiation pressure is modeled. Later on, the whole processing chain is detailed, from the required input, over data preparation and residual screening up to the first ambiguity fixed solution. In this regard, corresponding equations for residuals estimation are shown. Furthermore, a description of the least-squares adjustment is presented, along with the procedure of blocking retrograde terms in polar motion. The second part of this chapter deals with regional ionosphere modeling. It comprises a detailed description of the processing steps for the regional ionosphere model generation, which is, contrary to the previous parameter estimation, based on observation data of a regionally distributed set of GNSS IGS and EPOSA permanent stations. This model covers mainly the mid-latitudes in Europe and it is based on the modified single-layer mapping function (MSLM), which is, together with its theoretical background, discussed within this chapter. The following lines give a thorough description of the geometry-free linear combination, which is used to extract the signal delay caused by ionospheric refraction. Later on, the main processing steps are explained as in the previous part, starting with the input required for the processing, over data preparation and pre-processing, and up to the actual processing where the IONEX file is generated.

**Chapter 6 - Results** pays attention to the improvement gained when processing combined GNSS observations, in this case, adding Galileo data to GPS. Different ways of comparisons were carried out in order to investigate the benefits of using combined GNSS data. ERP time series were estimated based on GPS-only and combined GPS and Galileo observations and plotted against each other while comparing their respective 1-day and 3-day arc solutions. The corresponding tidal wave coefficients were estimated as well and presented w.r.t. chosen reference models. Another aspect was achieved through regional ionosphere modeling, where the generated GPS/GAL combined regional model was compared against established ionosphere models.

**Chapter 7 - Summary and Outlook** concludes this work, by wrapping up all findings obtained through this study. Conclusions gained from the results shown in the previous chapter are here discussed thoroughly. Furthermore, some recommendations regarding the current processing setup and future improvements are given at the end of this chapter.

The list of **Acronyms** used within this thesis is given at the beginning of the document. The **Bibliography** is located at the end of this document.

# 2. The Earth rotation

The closest approximation of the Earth's figure is known to be the geoid, which is, according to Gauss, the mathematical figure of the Earth (Gauss, 1828). Its figure can further be simplified as an oblate rotational ellipsoid (Arora, 2020; Fowler, 2005), being flattened at the poles, and bulged at the equator. Nowadays, life on this planet would be almost inconceivable, without the understanding of Earth's shape, structure, as well as its dynamics, considering the number of applications that are based on this knowledge and the corresponding data (Fowler, 2005). When talking about the masses within the Earth, it is important to note that its body is not rigid, nor is the distribution of the masses homogenous (Arora, 2020). This deformable Earth affects its rotational behavior tremendously causing consequences in the direction of the Earth's axis w.r.t. the space and the position of the Earth's body w.r.t. the Earth's axis (Arora, 2020; Halilović et al., 2023).

## 2.1. Reference frames

The proper monitoring of the previously mentioned phenomena depends on the definition and establishment of sufficient reference frames. Reference frames are the realization of reference systems (Arora, 2020). They are described by a set of physical and mathematical parameters (Altamimi et al., 2011), which include origin, scale, orientation, and temporal resolution (Arora, 2020). One of the primary objectives of the International Earth Rotation and Reference System Service (IERS), the International Astronomical Union (IAU), and the International Union of Geodesy and Geophysics (IUGG) is to take care of the structure and maintenance of reference frames (Arora, 2020).

### 2.1.1. Celestial reference frame

According to the IAU recommendations, the celestial reference frame is an equatorial system, with its origin placed in the barycentre of the Solar system and its pole being aligned with the direction of the J2000.0 standard epoch. This direction is obtained from VLBI (Very Long Baseline Interferometry) corrections w.r.t. former IAU standard precession and nutation models (Arias et al., 1995). The latest realization of the International Celestial Reference

Frame (ICRF), ICRF3, was adopted at the 30th IAU General Assembly, held in August 2018, comprising the positions of 4536 extragalactic sources in total (Charlot et al., 2020). With this decision, the previous realization, ICRF2, was replaced by its successor on January 1$^{st}$, 2019. For further details on the ICRF3, refer to the article of Charlot et al. (2020).

### 2.1.2. Terrestrial reference frame

The terrestrial reference system can be defined as a geocentric cartesian coordinate system, having its origin in the Earth's centre of mass (oceans and atmosphere included) and its orientation agreeing with the orientation of the BIH (Bureau International de l'Heure) at epoch 1984.0. To ensure the elimination of the datum defect of the ITRS, as well as to represent velocities without referring to a particular plate, a no-net-rotation condition is imposed on the horizontal lithospheric motions on the whole Earth. This further ensures the time evolution of the ITRS (Petit and Luzum, 2010). The pole of the ITRS roughly agrees with the mean rotation pole at the beginning of the 20$^{th}$ century, while the origin of the longitudes almost matches the Greenwich meridian (S. Böhm, 2012). The ITRS is shaped as a reference trihedron that is fixed in position relative to the Earth and rotates along with it. (Petit and Luzum, 2010).

The realization of the ITRS is called the ITRF (International Terrestrial Reference Frame) and as of setting up this thesis, its latest realization was the ITRF2014. Compared to previous releases, this was the first time in ITRF history, that the realization was calculated including enhanced modeling of both nonlinear station motions, covering annual and semi-annual station position signals, and post-seismic deformation sites, which were affected by large-scale earthquakes (Altamimi et al., 2016). The ITRF coordinates were derived by combining several individual TRF solutions, all being calculated by IERS analysis centers. These calculations are based on observation data from different space geodetic techniques: GNSS (Global Navigation Satellite Systems), VLBI, SLR (Satellite Laser Ranging), LLR (Lunar Laser Ranging), and DORIS (Doppler Orbitography Radiopositioning Integrated by Satellite) (Petit and Luzum, 2010). The positions of the ITRF2014 are referring to the epoch 2010.0. For more information about the ITRF2014, refer to the literature of Altamimi et al. (2016) and Mulić (2018). In 2021, the most recent updated ITRF version, the ITRF2020, was released. The new ITRF is based on the reprocessing results of four space geodetic techniques: VLBI, SLR, GNSS, and DORIS. The input data of the computation consisted of time series of station positions and EOPs, which were provided by the corresponding centers of the four space geodetic solutions. The time span of input data, from the analysis centers of each space geodesy technique, is listed below (Altamimi et al., 2023):

- International VLBI Service (IVS): **1980.0 - 2021.0**,
- International Laser Ranging Service (ILRS): **1983.0 - 2021.0**,
- International GNSS Service (IGS): **1994.0 - 2021.0**,
- International DORIS Service (IDS): **1993.0 - 2021.0**.

### 2.1.3. Transformation between ICRF and ITRF

The Earth orientation parameters (EOP) can be defined as components describing the transformation between the ICRF and ITRF. They enable the transformation between space-fixed, geocentric, and Earth-fixed reference frames (S. Böhm, 2012), hence the EOPs can be considered as the link between these two frames. EOPs comprise 5 transformation angles, which can be divided into three categories, namely:

- **Celestial Pole Offsets - CPO (given by Precession, Nutation models):** two angles describing long-periodic motions of a previously allocated reference direction (usually the rotation axis) w.r.t. the CRF (S. Böhm, 2012; Schindelegger, 2014). The corrections w.r.t. the celestial pole coordinates are given by the IAU 2006 precession and IAU 2000A nutation models (GGOS, 2023),
- **Pole Coordinates (Polar Motion):** two angles providing the movement of this reference direction w.r.t. the TRF, and the
- **Earth rotation angle (ERA):** an angle representing the actual phase of the TRF rotation w.r.t. the CRF (S. Böhm, 2012; Schindelegger, 2014). Earth rotation is experiencing changes in speed, which can be described as deviations of the Universal Time 1 (UT1) w.r.t. the uniform atomic time (Universal Time Coordinated – UTC). Those changes in Earth's rotation speed can be expressed as:

$$dUT1 = UT1 - UTC \tag{2.1}$$

  or, in other words, as variations in length of day (LoD) (Schuh and S. Böhm, 2020).

Given that the choice of the reference direction/axis is entirely conventional, it was agreed to be the Celestial Intermediate Pole (CIP) according to the resolution B1.7 adopted by the IAU in 2000. The currently most precise precession-nutation model, adopted by the IAU Resolutions (2000, 2006) is the IAU 2006/2000A. This model is used by all space geodetic techniques, meaning that the corresponding observations refer also to the CIP (Schindelegger, 2014).

According to the IAU 2000 and 2006 Resolutions, the relation between the International Terrestrial Reference System (ITRS) and the Geocentric Celestial Reference System (GCRS) at epoch $t$ can be expressed by the following transformation equation (Petit and Luzum, 2010):

$$GCRS(t) = Q(t)\,R(t)\,W(t) \cdot ITRS(t) \tag{2.2}$$

The GCRS has been moved from the barycentre to the geocentre. Due to the ICRS not being a geocentric system (origin located in the barycenter of the solar system), relativistic effects as aberration and parallaxes, have to be considered when transferring from a barycentric to a geocentric system (Schuh and S. Böhm, 2020). Nevertheless, the orientation of the ICRS matches the orientation of the GCRS (Figure 2.1).

By convention, the behavior of the Earth's rotation is divided into the movement of the rotation axis in the solid Earth and its respective motion in space. For this purpose, intermediate reference systems are introduced, namely the Terrestrial Intermediate Reference System (TIRS) having its origin at the Terrestrial Intermediate Origin (TIO), and the Celestial Intermediate Reference System (CIRS) having its origin at the Celestial Intermediate Origin (CIO). The previously mentioned CIP is the link between those two intermediate systems, representing the common reference pole (Zajdel, 2021).

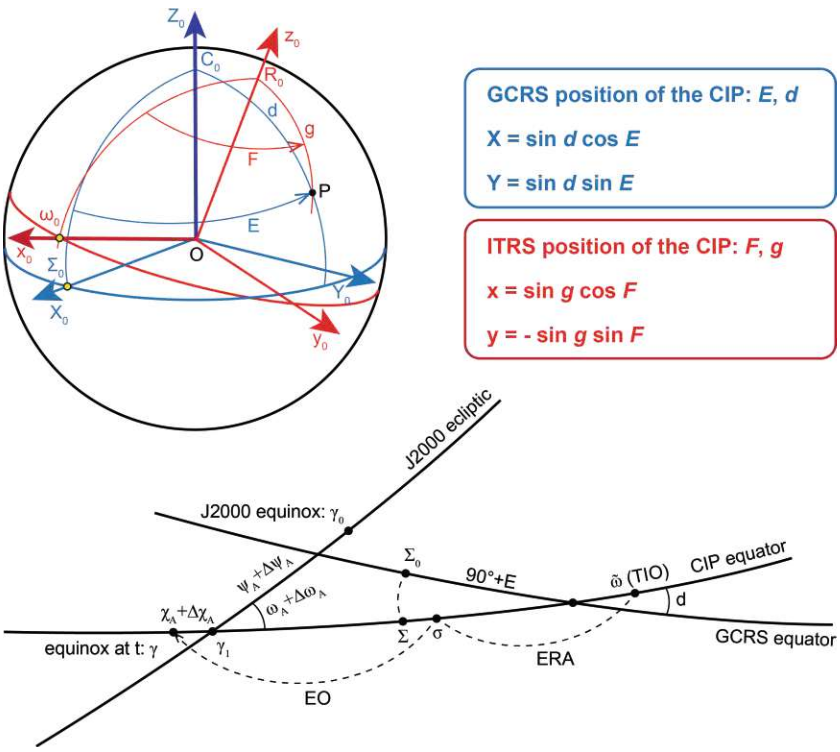


Figure 2.1: The celestial and terrestrial motions of the CIP and the ERA according to the IAU 2000 Resolution B1.8.

- W(t) is the polar motion matrix[1]. It compounds of rotations around the polar motion coordinates $x_p$ and $y_p$ of the CIP in the Earth-fixed system. Furthermore, it contains a rotation around the angle *s'*, which represents the position of the TIO on the equator of the CIP (Schuh and S. Böhm, 2020). The polar motion matrix can be expressed as follows:

$$W(t) = R_3(-s'(t)) \cdot R_2(x_p(t)) \cdot R_1(y_p(t)) \tag{2.3}$$

where:

[1]"W" for Wobble

$R_i$ is the rotation matrix about the axis i,

$x_p(t), y_p(t)$ are the pole coordinates, or the coordinates of the CIP in the Earth--fixed system, and

$s'(t)$ is the position of the TIO on the equator. -s' = -47 $t_{J2000}$ $\mu as$. $t_{J2000}$ is the time measured from the reference epoch J2000.0 to the epoch of computation. It is measured in Terrestrial Time (TT) and expressed in Julian centuries (Zajdel, 2021).

- R(t) is the rotation between the CIO and TIO. It is expressed by the Earth Rotation Angle (ERA) measured on the equator of the CIP at epoch $t$. The Earth rotation matrix can be written as (Zajdel, 2021):

$$R(t) = R_3(-ERA) \tag{2.4}$$

with:

$$\begin{aligned} ERA\,(T_u) = 2\pi\,(&UT1\ Julian\ day\ fraction\ +\ 0.7790572732640 + \\ &0.00273781191135448\ T_u) \end{aligned} \tag{2.5}$$

where:

$$\begin{aligned} T_u &= Julian\ UT1\ date - 2451545.0 \\ UT1 &= UTC\ +\ (UT1 - UTC) \end{aligned} \tag{2.6}$$

- Q(t) represents the precession and nutation matrix. It comprises of rotations around the angles X and Y and around the angle s. X and Y are the coordinates of the CIP in the celestial system, whereas s describes the location of the CIO on the equator of the CIP (Schuh and S. Böhm, 2020). The precession and nutation matrix has the following form (Zajdel, 2021):

$$Q(t) = \begin{pmatrix} 1-a(X+dX)^2 & -a(X+dX)(Y+dY) & (X+dX) \\ -a(X+dX)(Y+dY) & 1-a(Y+dY)^2 & (Y+dY) \\ -(X+dX) & -(Y+dY) & 1-a[(X+dX)^2+(Y+dY)^2] \end{pmatrix} \cdot R_3(s) \tag{2.7}$$

where:
$a = \frac{1}{2} + \frac{1}{8}[(X+dX)^2\ +\ (Y+dY)^2]$,
$dX, dY$ are celestial pole offsets.

For transformation purposes, according to the IAU resolutions 2000, EOPs are represented by the set of parameters $\{x_p,\ y_p,\ dUT1,\ X,\ Y\}$. In order to use the older transformation approach, based on the ecliptic and the equator, it is required to replace the parameters X and Y with $d\varepsilon$ and $d\psi$ (nutation in obliquity and longitude) (Schuh and S. Böhm, 2020).

This means that the complete set of EOPs comprises a total of five parameters. On the other hand, the subset containing the pole coordinates $\{x_p$ and $y_p\}$ and $UT1-UTC$, or $LoD$, is referred to as Earth rotation parameters (ERPs) (S. Böhm, 2012).

## 2.2. The variability of Earth's dynamics

It takes 23h 56m 04s (a full cycle) for the Earth to rotate around its axis and 365.2422 days to revolve around the Sun. Earth's dynamic motion contains different types of variations including both, periodic, as well as secular types of motions (Sidorenkov, 2009). These variations can be distinguished depending on their cause and frequency of occurrence. They can be divided into those triggered by the direct action of external gravitational torques exerted by other celestial bodies on the Earth's figure, and those caused by fluctuations previously generated by geophysical processes. The second group can further be divided into tidal and non-tidal variations.

Variations with tidal features can be described as high-frequency, or short-periodic variations if their period repeats a minimum of once a day and low-frequency, or as long-periodic variations if their periods amount several days to years. Non-tidal variations include secular, decadal, interannual, seasonal, intraseasonal and episodic events. Besides gravitationally and geophysically generated changes in Earth's rotation, there is another type of variation which can be identified, and this one is related to Earth's free oscillations. These oscillations are mainly consisting of the Chandler wobble and the free core nutation (S. Böhm, 2012).

### 2.2.1. Earth Orientation Parameters

Section 2.1.3 has introduced the reader to the term CIP, which, as previously described, defines an intermediate pole. By definiton, according to the IAU 2000 Resolution B1.7, the CIP divides the polar motion of the ITRS in the GCRS into two parts, namely the celestial and the terrestrial part[2]. Precession and nutation $\{X,\ Y\}$ belong to the celestial part. It contains all motions with periods > 2 days, as seen from space. This period length corresponds to the frequency span between -0.5 and +0.5 cycles per sidereal day (cpsd) (Petit and Luzum, 2010). Frequencies outside this range in the Earth-fixed system belong to the terrestrial part, or the polar motion $\{x_p,\ y_p\}$. This means frequencies below -1.5 and above -0.5 cpsd refer to the terrestrial part (Figure 2.2).

The plus sign contained in the frequency values denotes prograde motions, or motions in the direction of the Earth rotation, whereas the minus sign refers to retrograde motions, or motions opposite to the direction of the Earth rotation (Schindelegger, 2014; Schuh and S. Böhm, 2020).

As it can be seen from Figure 2.2, by definition no retrograde diurnal polar motion terms can be found, nor do prograde diurnal nutation terms exist.

[2]IAU Commission C.A3 Fundamental Standards: https://www.iaufs.org/res.html

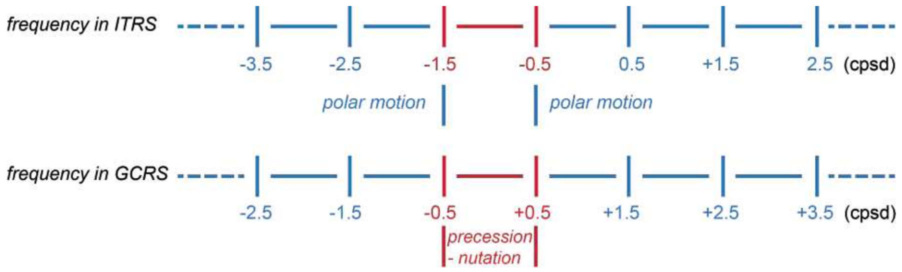


Figure 2.2: Precession-nutation and the corresponding polar motion of the CIP, conventionally divided by frequency, viewed in the ITRS (top), or the GCRS (bottom), with a 1 cpsd shift as a result of the rotation of the ITRS with respect to the GCRS (after Petit and Luzum (2010)).

### 2.2.2. Precession and nutation

Long-term and periodic variations of the Earth's axis direction w.r.t. a space-fixed reference system are referred to as precession and nutation. Earth's axis does not align with the axis of the ecliptic north pole (Figure 2.3 and 2.4), but is rather inclined closing an angle of about 23.5° with the ecliptic normal.

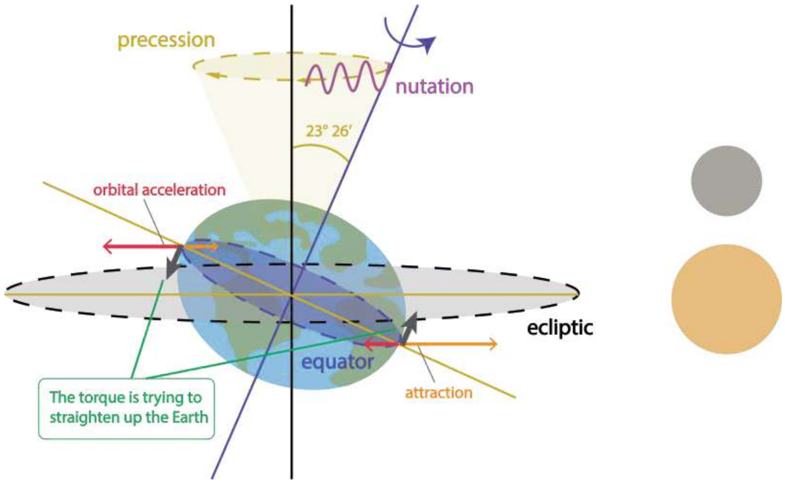


Figure 2.3: Precession and nutation of the Earth (1).

The movement of the Earth's polar axis w.r.t. the space fixed system is called precession and results in first place in a cone-shaped orbit. Precession is induced by tidal forces of the Moon and the Sun. One precession cycle or revolution period of the precession lasts 25 800 years or 50"/yr at aperture 2·23.5°. This period is known as the Platonic year. Projected onto the Earth surface, this period corresponds to a velocity of around 600 m/yr (Figure 2.4) (Schindelegger, 2014). However, given its shape and the inclination of its rotation axis, the Earth is continuously being dragged by gravitational torques, which are trying to enforce the Earth's equatorial plane onto the ecliptic. The rotation of the Earth, combined with this forced motion are causing the rotation axis to move on the precession cone, thus making the Earth behave like a gyroscope. This resulting movement is called nutation. It can be defined as short-periodic oscillations, that are superimposing the precession. Gravitational impacts of the Sun, Moon, and the planets when revolving around the Earth are responsible for the existence of nutation waves.

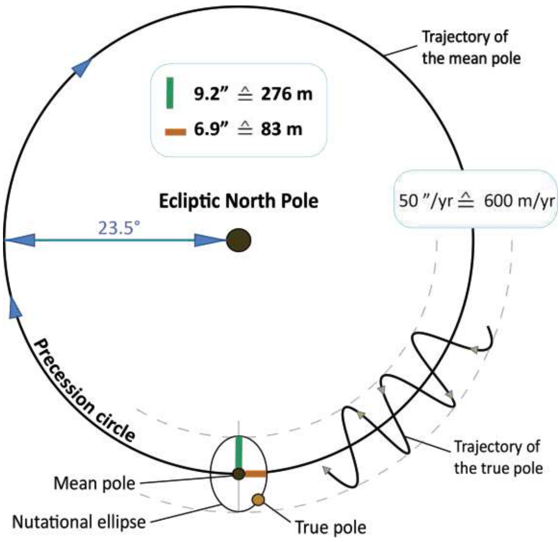


Figure 2.4: Precession and nutation of the Earth (2).

Several motions of the Earth's rotation axis w.r.t. the space-fixed system with different periods are included in the nutation, whereas 18.6 years is the longest period. It is also known as the lunar nodal cycle (Schuh and S. Böhm, 2020). The amplitudes of the 18.6 year period (in obliquity and ecliptic) projected onto the Earth's surface of a nutational ellipse, as illustrated in Figure 2.4, are approximately 274 m and 83 m (Cerveira, 2009).

### 2.2.3. Polar motion

Polar motion can be described as the direction change of Earth's axis or the CIP axis w.r.t. a terrestrial reference frame. It is defined by the pole coordinates in a two-dimensional coordinate system ($x_p$, $y_p$) (see Figure 2.5, 2.6 and 2.7).

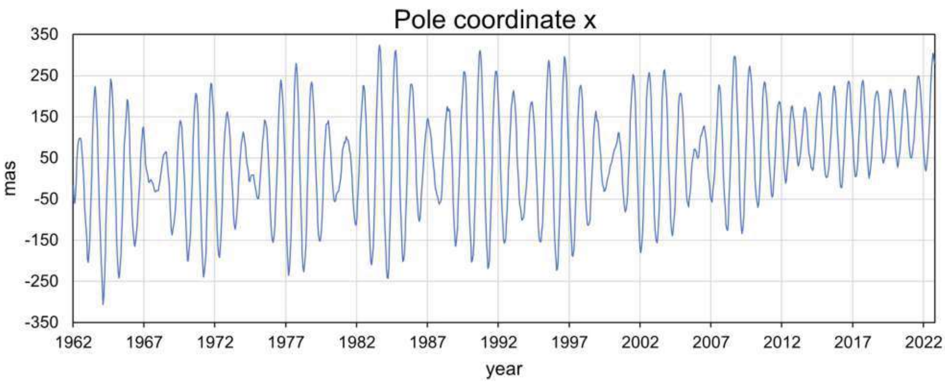


Figure 2.5: x coordinate from 1962 to 2022. The data for this plot were obtained from the EOP (IERS) C01 parameter time series.[3]

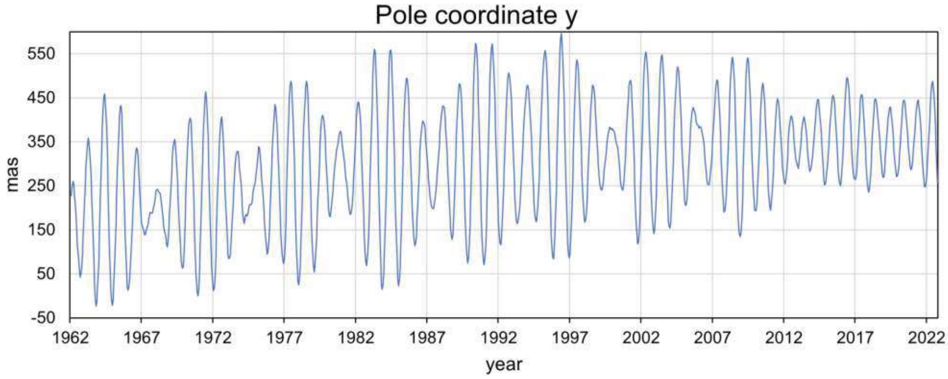


Figure 2.6: y coordinate from 1962 to 2022. The data for this plot were obtained from the EOP (IERS) C01 parameter time series.[4]

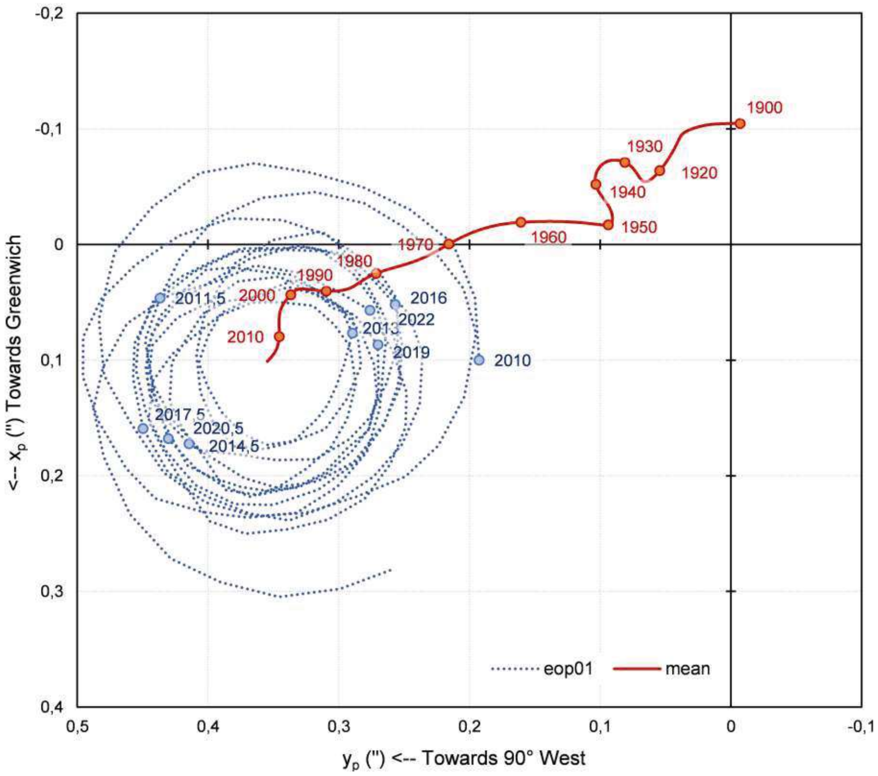


Figure 2.7: Polar motion from 2020 to 2022 (in blue) and mean pole from 1900 to 2016 (in red). The figure is based on data downloaded from the IERS/EOP website.[5]

[3]IERS Earth Orientation Parameters Product Center (EOP-PC):
https://hpiers.obspm.fr/eoppc/eop/eopc01/eopc01.iau2000.1900-now.dat. The parameters are given at a 0.05 year interval. For more information, refer to The EOP (IERS) C01 Guide (EOP-PC) and The EOP (IERS) C01 Readme (EOP-PC) websites.

[4]IERS Earth Orientation Parameters Product Center (EOP-PC):
https://hpiers.obspm.fr/eoppc/eop/eopc01/eopc01.iau2000.1900-now.dat.

[5]The data describing the polar motion were acquired from the following links:
EOP01 (EOP-PC): https://hpiers.obspm.fr/eoppc/eop/eopc01/eopc01.1900-now.dat,
Mean (EOP-PC): https://hpiers.obspm.fr/eoppc/eop/eopc01/mean-pole.tab).
For more information refer to The Mean Pole Readme (EOP-PC) file for the mean pole position calculation.

According to the IERS conventions, the x-axis aligns with the orientation of the Greenwich meridian, while the y-axis is positively aligned towards 90° W longitude (Schuh and S. Böhm, 2020). Polar motion superimposes a large number of periodic terms. A forced annual variation and the free Chandler wobble (free Chandler oscillation) can be mentioned as the most prominent ones. The annual variation is showing almost constant amplitudes of approximately 100 mas, while the free Chandler oscillation shows irregular amplitudes within the range 100 – 200 mas (Gross, 2000). The latter was named after Seth Carlo Chandler, who was investigating latitude observations at the end of the 19th century. The results of his work were published in 1891, where he demonstrated that the analysed series were superimposed by terms with a period of approximately 428 days, which is roughly equivalent to 14 months. S. Newcomb later supported this finding, stating that it was correct, considering the Earth's non-rigid nature. Taking into account the deformations of the Earth and the ocean, this 14-month period can range from 10 to 14 months.

These discoveries were soon followed by the establishment of the International Latitude Service (ILS) in 1899. The main objective behind the founding of the ILS was the monitoring of the movement of the North pole (Sidorenkov, 2009).

The annual oscillation of the polar motion interferes with the free Chandler wobble yielding to a beat-shaped pole curve (Schindelegger, 2014). The period of the beat is about 6.3 years, having a maximum amplitude of 9 m on Earth's surface. Polar motion can be split into short-periodic and long-periodic variations. The first ones are showing diurnal and semidiurnal periods and they are usually a result of ocean tides caused by Sun and Moon, whereas the latter are mostly associated to processes inside of the Earth, although a relation to the solar cycle cannot be excluded (Schuh and S. Böhm, 2020).

Polar motion *p(t)* can be expressed as (Petit and Luzum, 2010):

$$\begin{aligned} p(t) &= x_p(t) - i y_p(t) \\ &= A_{pro} e^{i\Phi_{pro}} e^{i\alpha(t)} + A_{retro} e^{i\Phi_{retro}} e^{-i\alpha(t)}. \end{aligned} \tag{2.8}$$

where:

| | |
|---|---|
| $p(t)$ | denotes the polar motion, |
| $x_p(t)$ and $y_p(t)$ | are the polar motion coordinates, |
| $A_{pro}$ and $A_{retro}$ | are the amplitudes of the prograde and retrograde polar motion components, |
| $\Phi_{pro}$ and $\Phi_{retro}$ | are the phases of the prograde and retrograde polar motion components, |
| $\alpha(t)$ | is the tidal argument. More on tides and tidal terms can be found in Section 2.3. |

The pole coordinate $y_p(t)$ is set to be negative due to the coordinate system being left-handed. The functions of polar motion time series can be expressed as Fourier series (Zajdel et al., 2021):

$$
\begin{aligned}
x_p(t) &= \sum_{k=0}^{\infty} S_{k,x} \sin(\phi_{k(t)}) + C_{k,x} \cos(\phi_{k(t)}), \\
y_p(t) &= \sum_{k=0}^{\infty} S_{k,y} \sin(\phi_{k(t)}) + C_{k,y} \cos(\phi_{k(t)})
\end{aligned}
\tag{2.9}
$$

where:

| | |
|---|---|
| $C_{k,x}$ and $S_{k,x}$ | are the amplitudes for the cosine and sine terms of the element $k$ of the $x_p(t)$ coordinate, |
| $C_{k,y}$ and $S_{k,y}$ | are the amplitudes for the cosine and sine terms of the element $k$ of the $y_p(t)$ coordinate and |
| $\phi_{k(t)}$ | is the astronomical fundamental argument for the $k$ tide at the epoch $t$ (Petit and Luzum, 2010). |

The amplitudes ($A_{pro}$,$A_{retro}$) and phases ($\Phi_{pro}$,$\Phi_{retro}$) of polar motion from Eq. 2.8 can be derived in prograde an retrograde directions, by combining Eq. 2.8 and Eq. 2.9 (Zajdel et al., 2021):

$$A_{k,retro} = \sqrt{(0.5\,(C_{k,x} + S_{k,y}))^2 + (0.5\,(S_{k,x} - C_{k,y}))^2}, \tag{2.10}$$

$$\Phi_{k,retro} = \arctan\left(\frac{(S_{k,x} - C_{k,y})}{(C_{k,x} + S_{k,y})}\right). \tag{2.11}$$

$$A_{k,pro} = \sqrt{(0.5\,(C_{k,x} - S_{k,y}))^2 + (0.5\,(C_{k,y} + S_{k,x}))^2}, \tag{2.12}$$

$$\Phi_{k,pro} = \arctan\left(-\frac{(S_{k,x} + C_{k,y})}{(C_{k,x} - S_{k,y})}\right). \tag{2.13}$$

The decomposition of the polar coordinates time series into prograde and retrograde motions is especially significant for the analysis of polar motion variations caused by geophysical processes (ocean tides).

### 2.2.4. Length of Day (LoD)

LoD can be described as the difference between the measured length of day, obtained by using space geodetic techniques, and the nominal length of day[6] (Equation 2.14) (Modiri et al., 2020). It can be used to represent the Earth rotation velocity, additionally to UT1 – UTC (Schuh and S. Böhm, 2020).

$$LoD = \frac{-d(UT1 - UTC)}{dt} \tag{2.14}$$

[6]The duration of the nominal length of day is 86 400 s.

LoD variations can be distinguished depending on their origin and time scale. Table 2.1 shows a list of different kinds of LoD variations ordered by frequency of occurrence from short-periodic to long-periodic ones. The most dominant influences staying behind each of those fluctuations, are listed in this table as well.

In addition to the entries in Table 2.1, there is evidence of existing LoD variations on a century timescale, as well as an oscillation of 1500 years (Schuh and S. Böhm, 2020).

High-temporal resolution short-periodic ΔLOD time series (derivative of UT1-UTC) can be estimated using GNSS observations, whereas mid- and long-periodic ΔLOD time series, as well as UT1-UTC time series, can be provided directly only by VLBI. In fact, all GNSS-based techniques face the same limitation when determining UT1-UTC (Seitz and Schuh, 2010).

This is because a nearly one-to-one correlation exists between changes in UT1-UTC and variations in the orbital elements, which makes a parallel estimation of satellite orbital elements and dUT offsets impossible (Rothacher et al., 1999). On the other hand, highly accurate LoD estimates can be obtained from satellite observations.

Table 2.1: Types of LoD variations divided by temporal resolution and the main origin of occurrence, listed in order from short-periodic to long-periodic ones. (after Schuh and S. Böhm (2020))

| **LoD variation** | **Main driving force (largest impact)** |
|---|---|
| 0.5 - 1 day (short-period range) | ocean tides caused by the Moon and the Sun |
| ∼14 and ∼28 days (few weeks to months) | solid Earth tides |
| 40 – 90 days | zonal winds |
| annual and semi-annual (seasonal variations) | angular momentum changes of the atmosphere |
| ∼1-year period | annually changing wind patterns |
| every 4 - 6 years | large-scale climate signals (can be brought into relation with the El Niño oscillation) |
| decadal fluctuations | internal coupling between the Earth's core and mantle |
| secular trend in LoD variations[7] | tidal friction and long-term mass variations |

## 2.3. Tidal effects on Earth Rotation

As stated before, the complex rotation behaviour and orientation in space of the Earth can be described through polar motion, LoD, precession and nutation, or in other words, by the Earth Orientation Parameters (EOPs). Within the diurnal and semi-diurnal band, Earth rotation is predominantly influenced by dynamic ocean tides (Girdiuk et al., 2017).

[7] This trend causes a prolongation of the day by ∼1.8 ms in 100 years.

Tides can be defined as periodic variations in the solid or fluid component of a celestial body (e.g., the Earth), resulting in dilation and contraction. These fluctuations occur due to gravitational forces exerted by the Moon and the Sun, as well as centrifugal forces resulting from the Earth's rotation around the Sun and the rotation of the Earth and Moon around their common center of mass. The interaction of these forces causes the periodic rise and fall of sea levels and affects other aspects of the body's environment. (S. Böhm, 2012).

The periodic effects of the Moon's gravitational attraction on the Earth's oceans have been known for centuries, causing increasing and decreasing water levels. However, the explanation for the twice-per-day occurring tides eluded scientists until the establishment of Newton's law of gravitation. According to that law, the force of attraction between two bodies is proportional to the masses of the bodies and inversely proportional to the square of the distance between them. When applying this law to the Earth, the attracting force exerted by the Moon decreases with the Earth's distance from the Moon by the inverse square law. Similar relationships can be established for other celestial two-body systems, such as Earth-Sun or Earth-Planet (Torge, 2001). Figure 2.8 shows the Earth-Moon system. The Earth and the Moon are traveling around a common central point, the mass center of the system, which is located within the Earth, but not in its center. The attraction force of the Moon does not have the same impact on every point on the Earth. It is actually weaker on the far side of the Earth compared to the Earth's center, resulting in the rising of water away from the Moon.

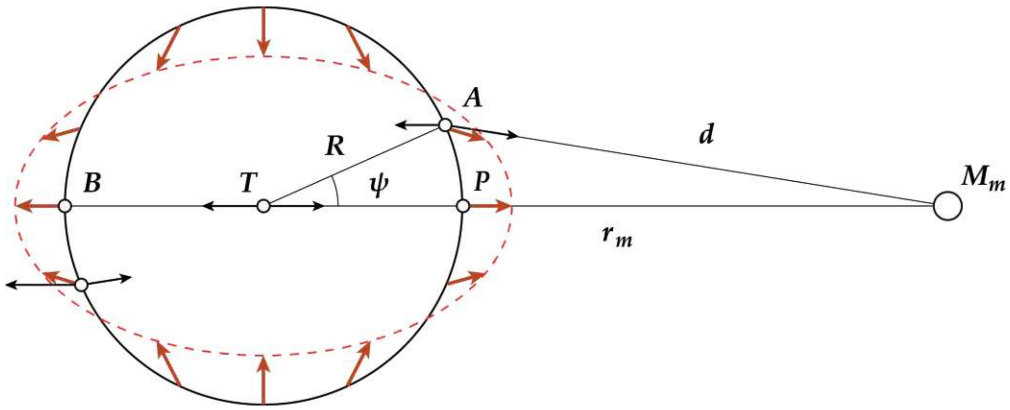


Figure 2.8: The tidal force in the Earth-Moon system when neglecting Earth rotation and bulge advance (tidal force vectors depicted as red arrows).

On the other hand, the Moon's attraction is stronger on the near side of the Earth than in the Earth's center, causing the water to move in the opposite direction, towards the Moon, but again, away from the Earth. This results in two tidal bulges (red dotted ellipse with two diametrically opposite points P and B in Figure 2.8) (Feynman et al., 1963). In reality, the bulge is advanced by about 3 degrees relative to the vector between the Moon and the geocenter due to Earth's rotation causing long-term tidal friction. Considering that point P on the Earth's surface is maximally attracted to the Moon, while the attractive force has minimal effect on the Earth's surface around point B, one can conclude that the corresponding accelerations $\overrightarrow{a}_P$ and $\overrightarrow{a}_B$ behave as follows:

$$\overrightarrow{a}_B < \overrightarrow{a}_T < \overrightarrow{a}_P \tag{2.15}$$

where $\overrightarrow{a}_T$ is the acceleration of the Earth's center (Girdiuk et al., 2017).

The resulting tidal force $\boldsymbol{f}_t$, perceived by an arbitrary mass point $A$ on Earth can be calculated as (S. Böhm, 2012):

$$\boldsymbol{f}_t = m \cdot \boldsymbol{a}_t \tag{2.16}$$

where:

$m$ is the mass point and

$\boldsymbol{a}_t$ is the tidal acceleration in surface point $A$

It is the differential force between the gravitation $\boldsymbol{f}$, which depends on the position of the surface point $A$, and the constant part $\boldsymbol{f}_0$, which equals the centrifugal force in the Earth's center (Torge, 2001):

$$\boldsymbol{f}_t = \boldsymbol{f} - \boldsymbol{f}_0 \tag{2.17}$$

When applying the law of gravitation to Eq. 2.17, it transforms into:

$$\boldsymbol{f}_t = \frac{GM_m}{d^2}\frac{\boldsymbol{d}}{d} - \frac{GM_m}{r_m^2}\frac{\boldsymbol{r_m}}{r_m} \tag{2.18}$$

where:

$G$ is the gravitational constant ($= 6.674 \cdot 10^{-11} m^3 kg^{-1} s^{-2}$),

$M_m$ is the mass of the Moon,

$d$ is the distance from an arbitrary point $A$ on Earth to the Moon and

$r_m$ is the distance from the Earth's center of mass T to the Moon.

The Earth's gravity field is subject to tidal forces, which give rise to a tidal acceleration field. This field exhibits diurnal and semidiurnal variations due to Earth's rotation around its axis. (Torge, 2001).

### 2.3.1. Expansion of tidal potential

The tidal force field can be expressed by the tidal potential $V_t$. It can be defined through the following relation (Torge, 2001):

$$\boldsymbol{f}_t = grad\, V_t \; = grad(V - V_0) \tag{2.19}$$

describing the effect of tidal forces on a unit mass. In the geocentric system, the potential of the tide-generating body at the surface point $A$ (spherical Earth assumed) yields:

$$V = \frac{GM_m}{d} \tag{2.20}$$

with

$$d = (R^2 + r_m^2 - 2Rr_m \cos\psi)^{\frac{1}{2}} \tag{2.21}$$

with $R$ being the Earth radius and $\psi$ the angle at Earth center $T$ (Figure 2.8).

The potential of the homogeneous $f_0$-field can be obtained when multiplying $f_0$ from Eq. 2.17 with $R\cos\psi$:

$$V_0 = \frac{GM_m}{r_m^2} R\cos\psi. \tag{2.22}$$

After inserting equations 2.20, 2.21 and 2.22 into Eq. 2.19 and by applying the condition $V_t$=0 for $R$=0 (i.e. $V_t$ at the geocenter) and $d = r_m$, the tidal potential yields (Torge, 2001):

$$V_t = GM_m \left( \frac{1}{d} - \frac{1}{r_m} - \frac{R\cos\psi}{r_m^2} \right) \tag{2.23}$$

The reciprocal distance $1/d$ is developed into a series of spherical harmonics. $P_n(\cos\psi)$ are the Legendre polynomials of degree $n$ in $\cos\psi$.

$V_t$ essentially represents a centered quantity with respect to the geocenter and thus eliminates the zero-order term of the series expansion. If the coordinate center also coincides with the geocenter, the first-order term in Eq. 2.24 also disappears, resulting in the tidal expansion starting at degree two:

$$V_t = \frac{GM_m}{r_m} \sum_{n=2}^{\infty} \left( \frac{R}{r_m} \right)^n P_n(\cos\psi) \tag{2.24}$$

Around 98% of the overall tidal potential arises from the degree two term, which means that equation 2.24 can be narrowed down to the degree $n$=2. After doing so, the main term of the tidal potential series is equal to:

$$V_{t2} = \frac{GM_m}{r_m} \left( \frac{R}{r_m} \right)^2 P_2(\cos\psi) = GM_m \frac{R^2}{r_m^3} P_2(\cos\psi) \tag{2.25}$$

where $\psi$ is the spherical distance between the spherical points $A$ (given with $\theta, \lambda$) and $P$ (given with $\theta', \lambda'$). The spherical distance $\psi$ is illustrated in Figure 2.9 and can be expressed as follows (Hofmann-Wellenhof and Moritz, 2005):

$$\cos\psi = \cos\theta \cos\theta' + \sin\theta \sin\theta' \cos(\lambda' - \lambda) \tag{2.26}$$

Equation 2.26 can be introduced to describe the Legendre polynomials $P_n(\cos\psi)$ with the corresponding spherical coordinates $\theta, \lambda$ and $\theta', \lambda'$ (Hofmann-Wellenhof and Moritz, 2005). This enables the decomposition of $P_n(\cos\psi)$ into Legendre polynomials $P_n$ and Legendre functions $P_{nm}$, which are the functions of the spherical coordinates of the points $A$ and $P$ (S. Böhm, 2012).

For this purpose, the spherical cosine law (Equation 2.26) and the addition theorem of spherical functions (Equation 2.25) will be utilized to express the spherical distance $\psi$ in terms of the spherical coordinates of point $A$ $(\theta, \lambda)$ and the sub-surface point $P$ $(\theta', \lambda')$ of the tide generating body:

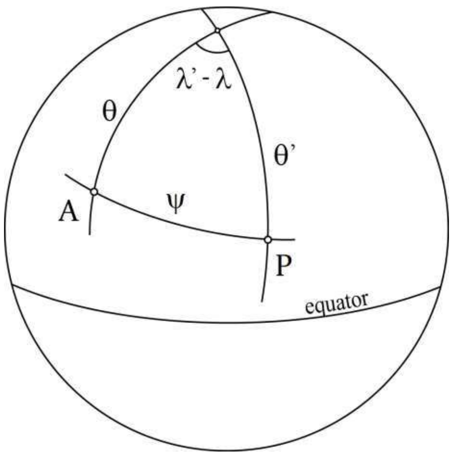


Figure 2.9: Spherical distance $\psi$.

$$
\begin{aligned}
P_2(\cos\psi) = & P_{20}(\cos\theta)P_{20}(\cos\theta')+ \\
& \frac{1}{3}\left[P_{21}(\cos\theta)P_{21}(\cos\theta')\cos(\lambda'-\lambda)\right]+ \\
& \frac{1}{12}\left[P_{22}(\cos\theta P_{22}(\cos\theta')\cos 2(\lambda'-\lambda))\right]
\end{aligned}
\tag{2.27}
$$

This substitution formally breaks down the tidal potential into three parts (Equation 2.28, Figure 2.10) (S. Böhm, 2012; Hofmann-Wellenhof and Moritz, 2005):

- Zonal part (zonal harmonics)[8]: includes only latitude-dependent terms, thus describing only those components of the tidal spectrum, belonging to the low-frequency range. The periods are on a scale from a few days to years (Eq. 2.29).
- Tesseral part[9] (tesseral harmonics): additionally depends on the longitude of the tide-raising body (e.g. the Moon). Therefore, it represents varying tidal forcing on a diurnal scale (Eq. 2.30).
- Sectorial part (sectorial harmonics): given that it depends on $2\lambda'$, its periods are almost semidiurnal (Eq. 2.31)

[8] Since the sphere is divided into zones
[9] "Tessera" means square or rectangle, but can also refer to a tile

$$V_{t2} = V_{t20} + V_{t21} + V_{t22} \tag{2.28}$$

$$V_{t20} = GM_m \frac{R^2}{r_m^3} P_{20}(\cos\theta) P_{20}(\cos\theta') \tag{2.29}$$

$$V_{t21} = \frac{1}{3} GM_m \frac{R^2}{r_m^3} P_{21}(\cos\theta) P_{21}(\cos\theta') \cos(\lambda' - \lambda) \tag{2.30}$$

$$V_{t22} = \frac{1}{12} GM_m \frac{R^2}{r_m^3} P_{22}(\cos\theta) P_{22}(\cos\theta') \cos 2(\lambda' - \lambda). \tag{2.31}$$

The corresponding Legendre functions of degree two can be written as follows:

$$P_{20}(\cos\theta) = \frac{3}{2}\cos^2\theta - \frac{1}{2}, \quad P_{21}(\cos\theta) = 3\sin\theta\cos\theta, \quad P_{22}(\cos\theta) = 3\sin^2\theta \tag{2.32}$$

The total tidal potential can be expressed as a sum of elements, each composed of a location function and an angular function, which are commonly referred to as 'tides'. These tides encompass various periodicities, including semidiurnal ($V_{t22}$), diurnal ($V_{t21}$), and significantly longer periods ($V_{t20}$). They represent deviations from a uniform mean circular orbit of a celestial body in the equatorial plane (Declination = 0). Tidal elements that are solely dependent on the celestial body's declination generate tidal waves with a monthly or 14-day period in the case of the Moon and with an annual or semi-annual period in the case of the Sun. The diurnal terms (m=1) contribute to precession, nutation, and, to some extent, polar motion. On the other hand, the semidiurnal terms play a role in the secular decrease in Earth's rotation speed and can be detected in the polar motion.

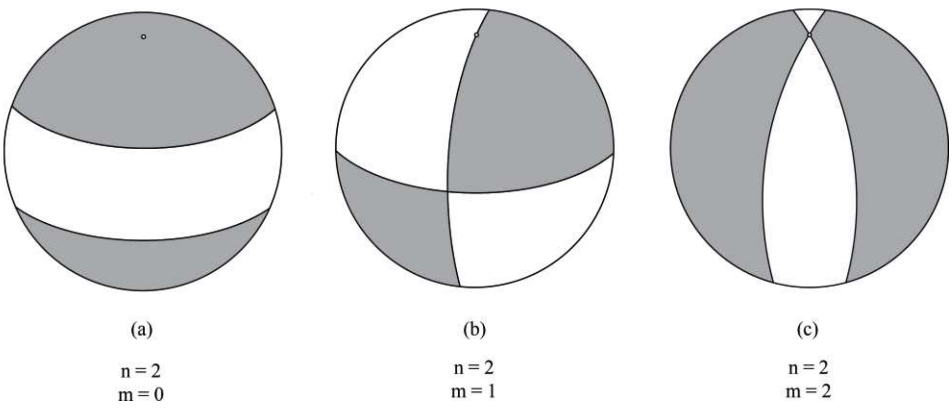


Figure 2.10: Types of spherical harmonics: (a): zonal, (b): tesseral and (c): sectorial.

Equations 2.29, 2.30 and 2.31 express the tidal potential caused by the Moon. In general, those equations can apply to any celestial body revolving around the Earth. The overall tidal potential at the Earth's surface is furthermore the sum of the individual potential fields of each tide-raising body. Usually, only the influence of the Moon and the Sun are taken into account, considering that the tidal effects of the planets nearest to the Earth (e.g. Venus, Mars) are four orders of magnitudes smaller (S. Böhm, 2012).

There are two ways to estimate the tidal potential. Either one can calculate it from the ephemerides of the celestial bodies, or one can get it by using a spherical harmonics expansion. Usually, tidal potential catalogues contain coefficients of the spherical harmonics expansion, while ephemerides-based results serve as a control for the catalogues. The first one to carry out a harmonical expansion for the Sun and the Moon was Doodson (1921) (Torge, 2001). Moreover, he defined the six variables, which are used to describe the lunar and solar ephemeris. These variables are still in use today (S. Böhm, 2012). Later, in the 1970s, two more harmonical expansion developments were performed, namely by Cartwright and Tayler (1971) and Cartwright and Edden (1973). They cover 505 partial tides with an accuracy less than 1 $nms^{-2}$. Hartmann and Wenzel (1995) have published a tidal catalogue, which is based on a spherical harmonics expansion up to degree 6 for the Moon and up to degree 3 for the Sun. Effects of Venus, Mars and Jupiter are taken into account (despite their considerably smaller tidal effects compared to the ones of the Sun and Moon), as well as the flattening of the Earth. This catalogue provides 12 935 partial derivatives with an accuracy of $\pm$ 0.001 $nms^{-2}$ (Torge, 2001).

Since the Earth is not a rigid body, it does behave differently in reaction to the tidal force. The reaction of the solid part has predominantly the characteristics of an elastic body (Earth's body tides). In the oceans, the situation is more complicated because the tidal oscillations have a strong dependence on the ocean-bottom topography. Depending on that, huge differences appear in the ocean reaction when comparing shelf areas and coastlines (ocean tides) (Torge, 2001). Given that ocean tide amplitudes are estimated within this work and compared to established recommended models (more on these models in section 2.4), ocean tides will be discussed in more detail in the following section.

### 2.3.2. Ocean tides

The ocean responds to the gravitational forces of other celestial, tide-generating, bodies in the form of tidal oscillations (Rahman et al., 2017). The first one to theoretically interpret the influence of tide-generating forces on oceans was Isaac Newton, who explained it through the equilibrium tide theory in his work *Principia*. According to this theory, ocean tides are always assumed to be static (Ng, 2015), i.e. the surface of the ocean is assumed to be fixed in space and, thus, changes w.r.t. the rotating surface of the Earth (Brosche and Schuh, 1998). Furthermore, it idealizes the shape of the Earth, portraying it as a perfect sphere, while ignoring the existence of landmasses and assuming the Earth is uniformly covered by a global ocean of frictionless water (until the arrival of tides). The equilibrium theory enjoys wide popularity, especially among students, due to its relatively simple concept describing the tidal bulges (Ng, 2015). Tidal bulges would build up until the moment an equilibrium condition has been met between pressure gradients and tidal force. After this point, the tidal deformation stays unaltered, being stationary towards the tide-generating body. Newton's equilibrium theory is well-fitted for the approximation of long periods. On the other hand, it does not apply for diurnal and semidiurnal periods (S. Böhm, 2012).

Even though the true astronomic nature of tides was discovered by Newton, the first hydrodynamic equations of ocean tides were first derived by Pierre-Simon Laplace (Rahman et al., 2017). He described the ocean tides as forced oscillations, defining their corresponding periods based on the main periods of the tide-generating bodies, namely the Moon and the Sun (Brosche and Schuh, 1998). Compared to equilibrium tides, considerable flood and ebb currents accompany dynamic tides. The height and time of arrival strongly depend on the ocean topography, as well as on the ocean basin morphology and free oscillations, thus resulting in a rather complex height and arrival time. The development of the ocean tidal deformation field into a spherical harmonics expansion includes zonal, tesseral, and sectorial terms covering a variety of periods. LoD variations and polar motion, induced by ocean tides, indicate long, diurnal, and subdiurnal periods. Several ocean tide models are used to estimate and predict variations in Earth rotation caused by ocean tides (S. Böhm, 2012).

### 2.3.3. Major ocean tide constituents

Concerning the Earth, ocean tides are manifested as periodic motions of the waters in the sea, induced by gravitational forces of the Moon and the Sun, as the positions of these two tide-generating bodies change with respect to the rotating Earth. The tidal movement of the waters can further be broken down into two components: a vertical movement (rise and fall) of the water, which is known as the "tide", and a horizontal movement known as the "tidal current". How the tidal height changes over time is simply illustrated in Figure 2.11. The line indicating the tidal height change resembles a sine wave. It reaches its maximum height at the water level called "high water".

The minimum height reached by the sine curve is placed at the water level labeled as "low water". In this figure, the mean sea level (MSL) is the central line around which the tidal height changes occur. It is the average of water level measurements over some period of time. The sine curve representing tidal height changes oscillates at open sea above and below the MSL.

The "tidal period" from Figure 2.11 is the time between two consecutive high waters or, analogously, between two low waters. Aside from the position of the Moon (which has the primary influence) and the Sun, the coastline, distance between continents, as well as the depth and shape of the ocean itself, are significant factors determining the onset of tides. The length of a tidal period is usually about 12 hours (semi-diurnal) or 24 hours (diurnal) (Parker, 2007), or in some cases longer than one day.

Long-period tides are known as gravitational tides. The long-period tidal components with notable powerful forcing include the lunar fortnightly ($M_f$, 14 days period) and lunar monthly ($M_s$, ≈28 days period) constituents, as well as the solar semiannual ($S_{sa}$, 1/2 year period) and solar annual ($S_a$, 1 year period) constituents (Wunsch et al., 1997). These constituents will not be mentioned any further in this work, given that the subject of interest and analysis are high-frequency tidal terms, i.e. diurnal and semidiurnal tidal constituents with periods < 27h (Table 2.2).

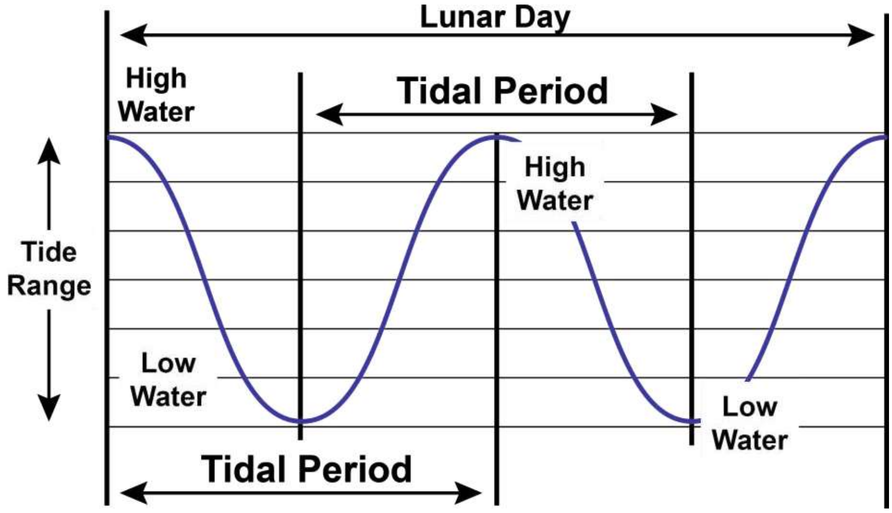

Figure 2.11: Example of a simple tide curve.

Important to note is that water level variations are not only induced by ocean tides, but also by changes in wind speed and direction, atmospheric pressure, river discharge, and water density. Unlike astronomical tides, these non-tidal changes are less predictable due to their dependence on changing weather conditions. There are nonetheless cases with short-periodic currents and annual variations in water level and currents, which are driven by non-tidal meteorological or seasonal effects. For more information on non-tidal effects on water level variations, please refer to Sections 2.3.6 and 3.7 in Parker (2007).

Tides oscillate with the same frequency as the tide-generating forces, which are influenced by the relative periodic motions of the Earth, Moon, and the Sun. As a result, tidal energy contributes to the tide. This contribution at a particular frequency is usually represented by a tidal harmonic constituent, which consists of an amplitude and a phase lag (epoch) (Parker, 2007). The 8 major tidal constituents (Table 2.2), typically manifesting the greatest effects on diurnal and semi-diurnal tides, are:

Table 2.2: Periods of principal tidal constituents (after DiMarco and Reid (1998)).

| Symbol | Name | Period (solar hours) |
|---|---|---|
| | **Diurnal waves** | |
| **Q1** | larger lunar elliptic | 26.87 |
| **O1** | principal lunar diurnal | 25.82 |
| **P1** | principal solar diurnal | 24.07 |
| **K1** | luni-solar diurnal | 23.93 |
| | **Semidiurnal waves** | |
| **N2** | larger lunar elliptic | 12.66 |
| **M2** | principal lunar | 12.42 |
| **S2** | principal solar | 12.00 |
| **K2** | luni-solar semidiurnal | 11.97 |

As seen in this table, the tidal harmonic constituents' names consist of a capital letter (for some cases this letter refers to the background of the tide-generating force) followed by a number indicating the approximate number of cycles per day of the constituents (in this case, 1 means 1 cycle per day and 2 means 2 cycles per day). Besides this nomenclature form, there are a few tidal constituents whose names contain Greek letters, more than one letter, or lower case letters in their names (used for compound tides or long-period tides). A discussion on the background behind the naming convention can be found in Parker (2007).

The largest amplitude belongs to the semidiurnal lunar tidal harmonic constituent M2, followed by the semidiurnal solar constituent S2. Their symbols indicate that the tide-generating forces responsible for these constituents are the Moon and the Sun respectively. The period of the semidiurnal M2 constituent is half a lunar day (12.42 hours)[10] (Parker, 2007). It is the largest lunar constituent, responsible for 2 peaks every 24 hours and 50 minutes (NOAA, 2023). The solar S2 tidal constituents have a period of 12 hours, or half a solar day[11]. As the Sun's distance from the Earth is much larger than the Moon's distance from the Earth, this results in the S2 constituent being considerably smaller in size compared to the M2 constituent. During new and full moons, the Moon and Sun are aligned. When this happens, their joint tidal forces generate larger tide ranges together, the so-called spring tides. On the other hand, during the first and third quarters, an opposite scenario is taking place. The tidal forces of the Moon and Sun counteract each other, leading to the production of smaller tide ranges, the so-called neap tides. The M2 tidal constituent experiences a modulation in lunar tidal force. This is due to the Earth-Moon orbit being elliptical, therefore

[10] One lunar day (24.84 hours) is the time the Earth needs to complete one rotation with respect to the Moon

[11] A solar day (24 hours) is the time the Earth needs to complete a rotation with respect to the Sun. The Moon follows a similar direction of rotation around the Earth as the Earth's rotation itself. As a result, a lunar day, or one full rotation of the Earth relative to the Moon, takes longer than the standard 24-hour solar day. This is because the Moon orbits the Earth, completing a small portion of its orbit by the time the Earth has completed a full rotation.

the distance between them varying from perigee[12] to apogee[13] and back to perigee within a 27.55-day period. The modulation of lunar tidal force (or the increase and decrease in tidal force) over this period can be represented by combining M2 with the semidiurnal lunar elliptic constituent N2 (with the period of 12.66 hours)(Parker, 2007). Another semidiurnal constituent, quite large in range, is the luni-solar K2 (with a period of 11.97 hours). As the name already reveals, K2 is affected by both, the Moon and the Sun. However, it is primarily influenced by the Moon's gravitational pull.

Throughout the lunar cycle, the Moon moves north and south of the equator, as well as directly over it. When the Moon is at zero declination (directly over the equator), its gravitational forces on Earth are stronger. However, as the Moon moves toward maximum declination over the poles, these tidal forces weaken. The diurnal lunar tidal forces, represented by the tidal constituents O1 (with a period of 25.82 hours) and K1 (with a period of 23.93 hours), result from the lunar declination. Similar to the lunar cycle, there is also a solar movement relative to the Earth, resulting in diurnal tidal constituents. It is this movement, which leads to the December solstice[14] (when the Sun is furthest south of the equator) and June solstice[15] (when the Sun is furthest north of the equator), as well as to the vernal[16] and autumnal[17] equinox (when the Sun is over the equator). The diurnal tidal constituents arising from this movement are P1 (with a period of 24.07 hours) and another K1, which means that also K1 has both lunar and solar components. The two tidal constituents P1 and the solar component of K1 experience a minimum combined effect at vernal and autumnal equinoxes and a maximum combined effect at winter and summer solstices. Moreover, the period of the K1 tide (23.93 h), which is responsible for the precession in the space-fixed system, coincides with the Earth's rotational period, leading to a full resonance with the Earth's rotation. The previously mentioned modulation of lunar tidal force on Earth (adding N2 to M2 in the semidiurnal band), due to the Moon's elliptic orbit is present in the diurnal band as well and contributes to the Q1 tide (with a period of 26.87 hours) (Parker, 2007). In the Earth-fixed system, diurnal and semi-diurnal tides occur simultaneously, causing the two tidal bulges associated with these tides to interact and superimpose on each other. This interaction results in complex combined tidal patterns, that exhibit diurnal as well as semi-diurnal features. As a result, multiple low and high tides occur over a 24-hour period, with different amplitudes and phases, which depend on the particular place and time.

The first version of a model for sub-daily tidal effects on ERPs covering these 8 major tidal constituents has been published within the IERS Conventions (1996) (McCarthy, 1996).

[12] Perigee is the point where the Moon is closest to the Earth

[13] Apogee is the spot where the Moon is the furthest from the Earth

[14] The December solstice, around December 21$^{st}$, marks the beginning of winter in the Northern Hemisphere and the beginning of summer in the Southern Hemisphere

[15] The June solstice, around June 21$^{st}$, implies the beginning of summer in the Northern Hemisphere and the beginning of winter in the Southern Hemisphere, contrary to the December solstice

[16] The vernal equinox takes place around March 21$^{st}$

[17] The autumnal equinox occurs around September 21$^{st}$

They were calculated as time-dependent sine and cosine amplitudes for polar motion, UT1, LoD, and rotation speed (S. Böhm, 2012). Currently, the conventional high-frequency ERP model for ocean tidal variations covers 71 harmonic terms (Petit and Luzum, 2010)[18]. More on high-frequency ocean tide models can be found in the following section.

## 2.4. High-frequency EOP models for the diurnal and semi-diurnal frequency bands

The IERS working group on diurnal and semi-diurnal Earth orientation variation (HF - EOP) has been established as a result of the GGOS/UAW (Global Geodetic Observing System/Unified Analysis Workshop) in Paris, July 2017. The responsibilities of this WG comprise the evaluation of existing high-frequency EOP models and, based on the evaluation results, giving recommendations to the IERS (Gipson, 2018). The list of current models considered for test purposes is available with their corresponding coefficient tables on the IVS website (International VLBI Service) and summarized in Table 2.3. The first six sub-daily ERP models are based on different ocean tide models, whereas the last three models are empirical models based on VLBI and combined VLBI and GPS data.

Table 2.3: High-frequency EOP models tested by the HF EOP WG (after Gipson (2018) and Nilsson (2018)).

| **Model** | **Based on** | **Reference** |
|---|---|---|
| | **Ocean Tide Models** | |
| **IERS** | TPXO4 | Petit and Luzum (2010) |
| **Desai-Sibois** | TPXO8 | Desai and Sibois (2016) |
| EOT11a | EOT11a | Karbon et al. (2018) |
| FES2012 | FES2012 | Karbon et al. (2018) |
| HAMTIDE | HAMTIDE | Karbon et al. (2018) |
| Madzak | EOT11 | Madzak et al. (2016) |
| | **Empirical Models** | |
| **Gipson** | VLBI data | Gipson and Hesslow (2015) |
| ABN VLBI | VLBI data | Artz et al. (2011) |
| ABN Comb. | VLBI and GPS | Artz et al. (2012) |

In this work, three models are used for the evaluation of the multi GNSS (GPS and GPS/Galileo) sub-daily tidal coefficients, namely the IERS, Desai-Sibois, and Gipson models. The model, which was recommended in the IERS 2010 Conventions[19], was derived from an ocean tide forward model combined with TOPEX/Poseidon satellite altimetry data (TPXO.2, Egbert et al. (1994)). Since this current Earth rotation model was issued by the IERS, more than

[18] The corresponding coefficients tables can be found in the IERS Conventions 2010, Ch. 8

[19] IERS2010 Model: https://ivscc.gsfc.nasa.gov/hfeop_wg/models/iers2010_xyu.txt

20 years have passed. According to Girdiuk et al. (2017) and Zajdel (2021), deficiencies in the conventional model, as well as the increasing precision of space geodetic techniques caused the scientific community to require the development of an up-to-date conventional high-frequency ERP model.

This led to the establishment of the aforementioned IERS HF-EOP WG and to their activities in recent years, as well as their efforts to find a potential replacement for the current conventional model. The Desai-Sibois model[20] is technique-independent and based on an updated altimetry-constrained ocean tide atlas TPXO.8 (Egbert et al., 1994), while libration effects where handled by the model from Mathews and Bretagnon (2003). The Desai-Sibois model is a solely geophysical model based on the ocean tide atlas, meaning that it describes only the Earth rotation variations that are induced by the oceans (Zajdel, 2021). According to the study of Desai and Sibois (2016), GPS-based tidal coefficients achieve the best consistency with the predictions from this TPXO.8-based model for ocean tide effects together with the model for libration effects. Their comparison showed a closure at the level of less than 10, 2, and 5 µas in prograde diurnal, prograde semidiurnal, and retrograde semidiurnal tidal variations in polar motion, respectively. As stated in Table 2.3, the Gipson model is an empirical model. It is estimated based on all available VLBI data until November 2017. Two high-frequency EOP models are provided by Gipson within the IERS HF-EOP WG. Their only difference is whether libration was included in the apriori model or not. Therefore, the two models available on the IERS HF-EOP WG webpage are:

- 2017a_astro_lib_xyu.txt[21] (libration was included in the apriori model) and
- 2017a_astro_xyu.txt[22] (libration was not included in the apriori model).

Within this work, the first model from Gipson (libration included), was chosen for the analysis, in order to follow the same approach as in the Desai-Sibois model, and therefore, keep consistency among the used models. Corresponding coefficients tables of sine and cosine arguments of sub-diurnal variations in pole coordinates ($x_p$, $y_p$) and LoD caused by the 8 major ocean tides for the three used HF-EOP models (IERS, Desai-Sibois, and Gipson (with libration included) can be found in Appendix A.2.3. The Analysis Centers (ACs) of the IGS began the third reprocessing campaign in October 2019 in order to reanalyze all GPS data collected by the IGS global network since 1994. The purpose of this campaign is to provide input for the ITRF2020 in a consistent way and using the latest models and methodology. According to the recommendations of the HF-EOP WG, the Desai-Sibois model for diurnal and sub-diurnal EOP variations has been chosen to be used within this campaign.[23]

[20] Desai and Sibois Model: https://ivscc.gsfc.nasa.gov/hfeop_wg/models/desai_model_jgrb51665-sup-0002-ds01.txt
[21] Gipson tidal model (libration included): https://ivscc.gsfc.nasa.gov/hfeop_wg/models/2017a_astro_lib_xyu.txt
[22] Gipson tidal model (libration not included): https://ivscc.gsfc.nasa.gov/hfeop_wg/models/2017a_astro_xyu.txt
[23] 3rd IGS Data Reprocessing Campaign

## 2.5. Techniques for the determination of EOPs

For about five decades Earth orientation parameters (EOPs) have been determined predominantly by modern space geodetic techniques (Figure 2.12).

Depending on which space geodetic techniques are used, they may estimate one or more EOP parameters, as shown in Table 2.4, and play varying roles in parameter estimation—serving as either primary or supplementary methods for determining EOPs (Schindelegger, 2014). As visible from Table 2.4, VLBI is actually the only technique able to directly observe precession, mutation, and UT1-UTC. Apart from VLBI, nutation and UT1-UTC can also be solved by using LLR. The advantage of VLBI and LLR in determining Earth Orientation Parameters (EOPs) lies in their ability to reach beyond the Earth system, making them independent of satellite systems, unlike GNSS.

On the other hand, VLBI typically provides data with lower temporal resolution as its products are typically obtained on a session-wise basis. This is where satellite-based techniques like GNSS and SLR offer an advantage. These techniques have the potential to densify the UT1-UTC series by deriving its first derivative, known as the excess length of day (Zajdel, 2021). In fact, satellite techniques are only able to measure the time derivation of the nutation and UT1-UTC, or in other words, the nutation rates and LoD.

This limitation, as mentioned in section 2.2.4, is the result of the correlation between nutation and UT1-UTC with the orbital elements of the satellites (Schuh and S. Böhm, 2020), or to rephrase it, with the right ascension of the ascending node and the argument of latitude. This relation can be expressed by the following equation (Rothacher et al., 1999; Zajdel, 2021):

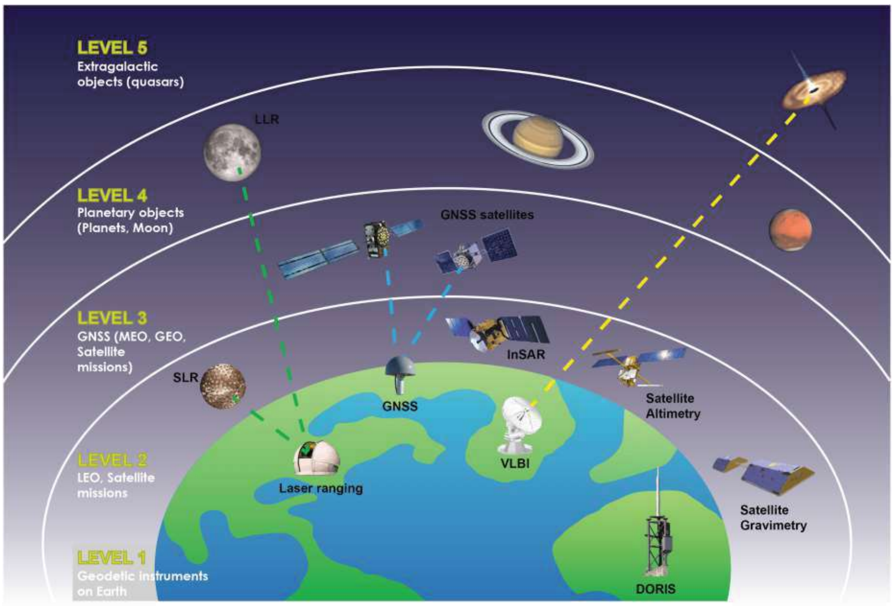


Figure 2.12: Space geodetic techniques.

Table 2.4: Earth rotation parameters and space geodetic techniques used for deriving particular parameters. III – a major technique, II – a supporting technique, I – a capability for a parameter determination. After Zajdel (2021) and Sośnica et al. (2015).

| Parameter type | VLBI | GNSS | DORIS | SLR | LLR | Altimetry, InSAR | Gravity missions |
|---|---|---|---|---|---|---|---|
| **Nutation** | III | I | | I | II | | |
| **Polar motion ($x_p$, $y_p$)** | II | III | I | II | I | I | |
| **UT1-UTC (dUT1)** | III | | | | II | | |
| **Length-of-Day (ΔLOD)** | II | III | I | II | I | | |
| **Sub-daily ERPs** | III | III | I | I | I | III | I |

$$\Delta(UT1-UTC) = -\frac{\Delta\Omega + \cos(i)\Delta u_0}{k} \tag{2.33}$$

where:

$u_0$ is the argument of latitude

$\Omega$ is the right ascension of the ascending node

$i$ is the inclination angle and

$k$ is the ratio of the universal time to sidereal time.

However, GNSS is the most precise technique used for the determination of pole coordinates, due to the dense station network and uninterrupted tracking of the satellites (Zajdel, 2021).

# 3. The Ionosphere

The Earth's atmosphere can be divided into two regions, the upper and lower part, where the ionosphere belongs to the upper atmosphere. The ionosphere refers to the atmosphere's ionized component, containing a considerable number of free electrons and positive ions (Hargreaves, 1992). Such an environment is affecting the propagation direction and speed of electromagnetic waves (Todorova, 2008), thus disturbing GNSS signals being broadcasted from satellites in space to receivers on Earth. This effect is called ionospheric refraction. It must be considered when measuring the signal propagation speed by all space geodetic techniques that utilize electromagnetic waves (Todorova, 2008). Ionospheric refraction varies with time and geographical location (i.e., latitude) and depends on the number of free electrons along the ray path, as well as the magnetic and solar activity (Magnet, 2019; Todorova, 2008).

The ionosphere is a dispersive medium causing a group delay of GNSS pseudorandom noise codes (PRN) and a phase advance of GNSS carrier frequencies (Horozović et al., 2015; V. Zhang and Zhiqi Li, 2015). Additionally, the signal path is bending while propagating through this layer, making it slightly longer compared to the direct path between satellite and receiver (V. Zhang and Zhiqi Li, 2015). In terms of dealing with the ionospheric propagation delay, GNSS offers different solutions. Multi-frequency GNSS measurements can be used to form specific linear combinations to either eliminate the ionospheric refraction and so to correct, for example, single-frequency range-measurements. On the other hand, the state of the ionosphere regarding its structure can be described in the form of, so-called, ionospheric maps (Magnet, 2019). For a more detailed description on GNSS-based linear combinations for the mitigation of ionospheric refraction and representation of the ionospheric state, refer to Sections 4.3.1 and 5.2.1.

## 3.1. Ionization

The ionosphere is generated through the ionization process, where solar radiation plays a key role. Directed towards the Earth's atmosphere, radiation arriving from the Sun ionizes the molecules of atmospheric gases such as O, O2, and N2, resulting in the production of free electrons and ionized particles (Figure 3.1) (Horozović, 2014). The solar radiation responsible for these processes is emitted in the extreme ultraviolet and X-ray parts of the electromagnetic spectrum for middle and low latitudes (Hargreaves, 1992). On the other hand, corpuscular ionization is, to a lesser extent, present over high latitudes (Zolesi and Cander, 2014).

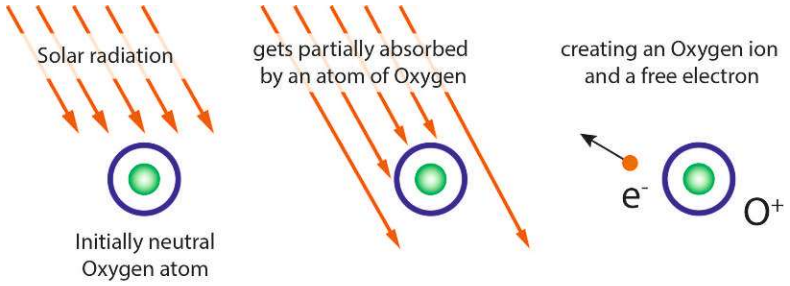


Figure 3.1: Ionization process: The strong ultraviolet radiation from the Sun causes the electron to detach from its neutral atom, producing an ionized atom and a free electron.

## 3.2. Structure of the ionosphere

The ionosphere is located above the stratosphere raising from an altitude of about 50 km above the Earth's surface during the daytime and at about 90 km during night-time. It contains the atmospheric layers known as the mesosphere, thermosphere, and exosphere (Zolesi and Cander, 2014). The upper boundary of the ionosphere is considered to be at a height of approximately 1000 km, even though it cannot be defined absolutely. This is because the intensity of ionization decreases progressively with increasing height, after reaching a maximum electron density at about 350 km (F2-peak) above the Earth's surface.

Below the ionosphere, solar radiation is almost totally absorbed by the Earth's atmosphere (neutral atmosphere), while the medium above its upper limit has a decreased density and gets completely ionized (plasmasphere) (Magnet, 2019; Todorova, 2008). Figure 3.2 shows an illustration of the atmospheric layers and the electron density distribution along the ionosphere for up to 600 km height. The main regions of the ionosphere, known as the D, E, F1, and F2 (see Figure 3.2), are characterized by specific ionization processes. The ionospheric layers were named in increasing order of altitude, with D as the lowest and F2 as the highest region (Hobiger and Jakowski, 2017). Different chemical elements exist in the upper neutral atmosphere and each of them interacts differently with ultraviolet (UV) radiation.

Because of that, several electron density maxima can be found in the ionosphere and these maxima can be used to determine the ionospheric layers (Zolesi and Cander, 2014). At night, regions D and F1 vanish, while regions E and F2 remain with weakened intensity. All layers are existing during daytime (Hargreaves, 1992). Table 3.1 contains a list of the ionospheric layers with their main characteristics during daytime.

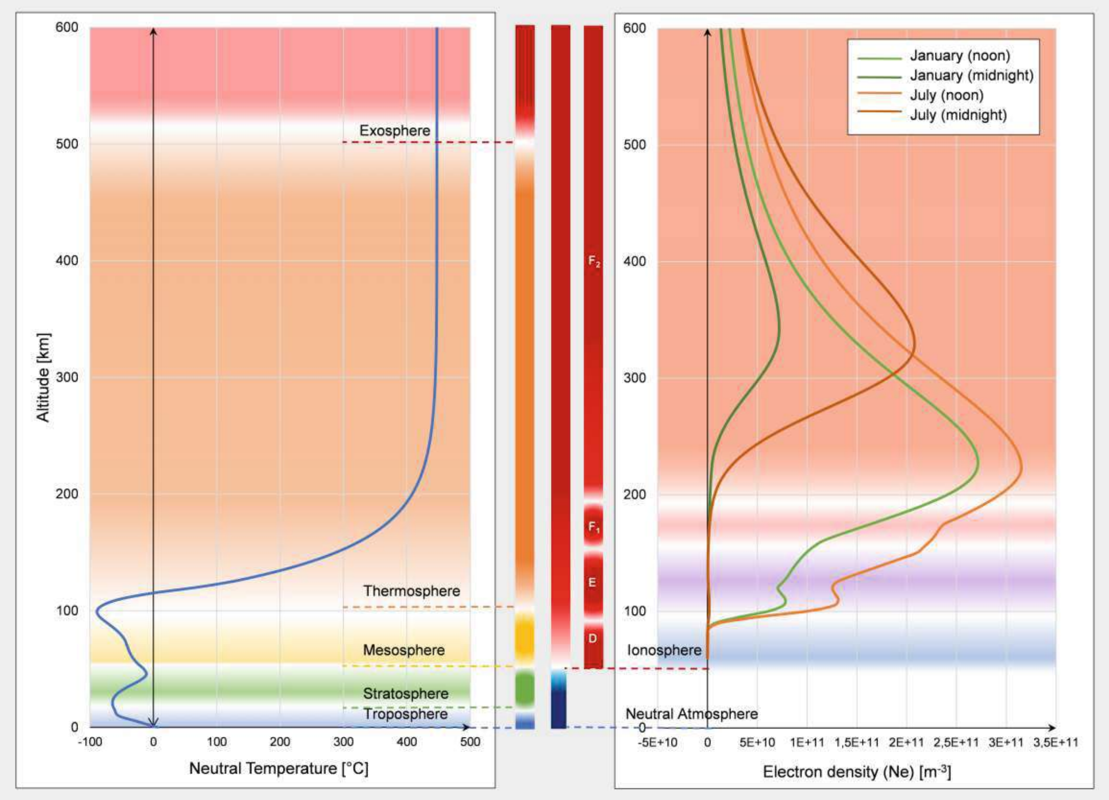


Figure 3.2: Vertical structure of the atmospheric layers containing the neutral atmospheric temperature for January 1st, 2020 (left) and electron density distribution in the ionosphere for January 1st, 2020, and July 1st, 2020, at noon and midnight respectively (right). The diagrams are produced using data from the MSISE-90 (Mass Spectrometer - Incoherent Scatter Empirical) and IRI (International Reference Ionosphere) 2016 model for Vienna.

Photochemical processes are having the biggest impact on the lower atmosphere in terms of composition and balance of ionization (up to 100 km), whereas the upper region is dominated by the transfer of charged particles in plasma, thermospheric winds, as well as interactions between the ionosphere and magnetosphere (Zolesi and Cander, 2014).

Table 3.1: Ionospheric layers (after Hargreaves (1992)).

| **Region** | **Altitude [km]** | **Electron density [m$^{-3}$]** |
|---|---|---|
| D | 60 - 90 | $10^8$ - $10^{10}$ |
| E | 105 - 160 | several $10^{11}$ |
| F1 | 160 – 180 | several $10^{11}$ - $10^{12}$ |
| F2 | 180 - 1000 | up to several $10^{12}$ |

### 3.2.1. D layer

The ionospheric D layer is located at an approximate altitude of 50 – 90 km. The electron density ranges from around $10^8$ to $10^{10}$ m$^{-3}$ depending on the height (Zolesi and Cander, 2014). This region is mostly influenced by solar radiation and partially by cosmic rays.

During the daytime, the level of ionization is high, especially at noon when it reaches its maximum. On the other hand, there is almost no ionization during the night. That means that the layer exists only during daytime, while it vanishes during night-time, due to the absence of solar radiation (Magnet, 2019). Different variations affect its state, for example diurnal, seasonal, and solar cycle variations (Zolesi and Cander, 2014).

### 3.2.2. E layer

Between an altitude of about 90 – 150 km above the Earth's surface extends the E layer of the ionosphere, also known as the Kennelly-Heaviside layer. This region is primarily influenced by X-rays and ultraviolet (UV) radiation. The main components are positive ions and electrons, with a mean electron density of $10^{11}$ $m^{-3}$. This layer is just weakly ionized during night-time.

Additionally, an E2 and a sporadic Es layer can be found in this area. The E2 layer appears near the upper limit of the E layer, right beneath the F1 layer, at an altitude of approximately 150 km (Zolesi and Cander, 2014). It takes place during the summer months at mid-latitudes and during daytime, typically lasting only a few minutes to a few hours. According to its name, the electron density of the Es layer increases sporadically, up to the 25-fold (Magnet, 2019).

### 3.2.3. Sporadic Ionospheric Es layer

Although this layer appears at altitudes, that overlap with the E region (90 – 140 km), the sporadic Es layer is acting independently from it. The Es layer experiences extremely different variations at all latitudes (high, mid, and low), generated by different physical mechanisms. For instance, in terms of spatial distribution, it can either be expanded over a large area or limited to a smaller one. Moreover, it shows diverse diurnal and seasonal patterns, meaning that it, for example, can appear at any time during the day or night. For low and mid-latitude regions, the Es is most likely to appear during the day, predominantly during summer months. The opposite happens for the high latitudes, where the Es usually occurs at night and is oftentimes related to the aurora. This sporadic layer can have an electron density similar to the F region. Nevertheless, its unpredictable nature, in terms of time and place of occurrence, makes it challenging to predict its behavior (Zolesi and Cander, 2014).

Among all the theories that try to explain the sporadic Es layer, the wind-shear theory seems to be the most widely accepted one. For further details on this theory, please refer to Hargreaves (1992) and Zolesi and Cander (2014).

### 3.2.4. F layer

The uppermost layer of the ionosphere, the F layer, extends from approximately 150 km above the Earth's surface. It is the largest and also the most significant layer of the ionosphere when it comes to radio communication, as well as satellite navigation. It is also known as the Appleton layer. The solar radiation causes this layer to split into the F1 and F2 layers during the day. In doing so, F1 disappears during night-time, while forming together with the F2 layer the F region again during the day.

The ionization level of the F1 layer is mostly affected by extreme ultraviolet (EUV) solar radiation. The maximum electron density is reached at noon, being more intense during summer compared to wintertime. Sometimes, this layer even disappears in the daytime during winter.

The F2 layer has a high variability, reaching timescales from a few seconds up to the 11-year-long solar cycle or longer, which depends on the solar-terrestrial environment. The Sun has a strong impact on the electron density, causing it to increase immediately after sunrise. After that, the electron density maximum can appear at any moment during the day (Zolesi and Cander, 2014).

## 3.3. Wave propagation in the Ionosphere

A propagating electromagnetic wave in space is defined by its frequency $f$ and wavelength $\lambda$. When propagating through a dispersive medium, such as the ionosphere, the propagation velocity depends on the frequency of the electromagnetic wave (Alizadeh, 2013). In vacuum, the phase $v_{ph}$ and group $v_{gr}$ velocities are the same and approximately equal to the speed of light in vacuum ($c = 2.997\,924\,58 \cdot 10^8$ ms$^{-1}$). However, in a dispersive medium, they are different.

The phase velocity $v_{ph}$ of electromagnetic waves propagating with the frequency $f$ and the wavelength $\lambda$ can be expressed as follows:

$$v_{ph} = \lambda f \tag{3.1}$$

The group velocity $v_{gr}$ is given by the following equation:

$$v_{gr} = -\frac{df}{d\lambda}\lambda^2 \tag{3.2}$$

The carrier waves propagate with the phase velocity, while code measurements propagate with the group velocity (Alizadeh, 2013). To find out the relation between equations 3.1 and 3.2, it is needed to differentiate equation 3.1 first:

$$dv_{ph} = f d\lambda + \lambda df \tag{3.3}$$

This equation can further be written as:

$$\frac{df}{d\lambda} = \frac{dv_{ph}}{\lambda d\lambda} - \frac{f}{\lambda} \tag{3.4}$$

The term $df/d\lambda$ from 3.4 can be substituted into 3.2 leading to:

$$v_{gr} = -\lambda \frac{dv_{ph}}{d\lambda} + f\lambda \tag{3.5}$$

The term $f\lambda$ from Eq. 3.5 can further be substituted by the phase velocity $v_{ph}$ according to Eq. 3.1, giving finally the relation between the phase and group velocities, known as the Rayleigh Equation (Magnet, 2019):

$$v_{gr} = v_{ph} - \lambda \frac{dv_{ph}}{d\lambda} \tag{3.6}$$

As previously mentioned, the propagation speed of waves is not the same in a vacuum and a given medium. The relation between the velocity of a wave in vacuum $c$ and its velocity in a medium $v$ is given by the refractive index $n$:

$$n = \frac{c}{v} \tag{3.7}$$

According to Equation 3.7, the refractive index for phase $n_{ph}$ and group $n_{gr}$ velocities can be written as follows:

$$n_{ph} = \frac{c}{v_{ph}} \tag{3.8}$$

$$n_{gr} = \frac{c}{v_{gr}} \tag{3.9}$$

The differentiation of Equation 3.8 with respect to $\lambda$ leads to the following:

$$\frac{dv_{ph}}{d\lambda} = -\frac{c}{n_{ph}^2} \frac{dn_{ph}}{d\lambda} \tag{3.10}$$

The substitution of 3.10, 3.9 and 3.8 into 3.6 yields:

$$\frac{c}{n_{gr}} = \frac{c}{n_{ph}} + \lambda \frac{c}{n_{ph}^2} \frac{dn_{ph}}{d\lambda} \tag{3.11}$$

The previous equation can be divided by $c$, leading to the following:

$$\frac{1}{n_{gr}} = \frac{1}{n_{ph}} \left(1 + \lambda \frac{1}{n_{ph}} \frac{dn_{ph}}{d\lambda}\right) \tag{3.12}$$

Equation 3.12 can be rewritten by using the approximation $(1+\varepsilon)^{-1} \doteq 1 - \varepsilon$, which is valid for small quantities of $\varepsilon$:

$$n_{gr} = n_{ph} \left(1 - \lambda \frac{1}{n_{ph}} \frac{dn_{ph}}{d\lambda}\right) \tag{3.13}$$

or

$$n_{gr} = n_{ph} - \lambda \frac{dn_{ph}}{d\lambda}, \tag{3.14}$$

which is the modified Rayleigh equation (Hofmann-Wellenhof et al., 1993). Another form can be obtained by taking the derivative of $c = \lambda f$, with respect to both $\lambda$ and $f$:

$$\frac{d\lambda}{\lambda} = -\frac{df}{f}, \tag{3.15}$$

and substituting it into Equation 3.14, resulting in a slightly different expression (Equation 3.16):

$$n_{gr} = n_{ph} + f \frac{dn_{ph}}{df}. \tag{3.16}$$

### 3.3.1. Ionospheric refraction

In order to quantify the effects of ionospheric refraction on the propagation of electromagnetic waves, the refractive index of the ionosphere has to be defined. According to Seeber (2003), the phase refractive index $n_{ph}$ can be approximated with the series:

$$n_{ph} = 1 + \frac{c_2}{f^2} + \frac{c_3}{f^3} + \frac{c_4}{f^4} + \cdots \tag{3.17}$$

Coefficients $c_i$ are not frequency dependent, but they do depend on the ionospheric state (Seeber, 2003). The quantity describing the state of the ionosphere is known as the electron density $N_e$. It is the number of electrons per cubic meter (Dach et al., 2015). By cutting off the series expansion after the second term in Equation 3.17, one can get a simplified equation for the phase refraction index:

$$n_{ph} = 1 + \frac{c_2}{f^2} \tag{3.18}$$

To get the equation for the group refraction index, 3.18 has to be differentiated first:

$$dn_{ph} = -\frac{2c_2}{f^3} df \tag{3.19}$$

Substituting the values for $n_{ph}$ (see Eq. 3.18) and $dn_{ph}$ (see Eq. 3.19) into Equation 3.16 leads to the expression for the group refractive index:

$$\begin{aligned} n_{gr} &= 1 + \frac{c_2}{f^2} - f \frac{2c_2}{f^3} \frac{df}{df} \\ &= 1 + \frac{c_2}{f^2} - f \frac{2c_2}{f^3} \end{aligned} \tag{3.20}$$

or

$$n_{gr} = 1 - \frac{c_2}{f^2} \tag{3.21}$$

It can be noticed that equations 3.18 and 3.21 differ only by the sign in front of the second term. According to Magnet (2019), the coefficient $c_2$ has the value:

$$c_2 = -\frac{e^2}{8\pi\varepsilon_0 m_e} N_e = -40.3\, N_e\, [Hz^2] \tag{3.22}$$

where:

$e$ is the electron charge,

$\varepsilon_0$ is the permittivity of free space, and

$m_e$ is the electron mass.

Since the electron density $N_e$ is always a positive value, the group refractive index is larger than the phase refractive index. Therefore, the group velocity is smaller than the phase velocity. This is resulting in a group delay and a phase advance, meaning that GNSS ranging codes are being delayed, while carrier phases are being advanced. As a result, compared to the geometric range between satellite and receiver, code pseudoranges are longer and carrier phase pseudoranges are shorter. The difference of these pseudoranges with respect to the geometric range is the same, when higher-order series expansion terms beyond second order are ignored (see Eq. 3.17), only with opposite sign (Hofmann-Wellenhof et al., 2007).

The measured range $s$ between satellite and receiver can be obtained by integrating along the signal path:

$$s = \int n ds \tag{3.23}$$

The geometric range $s_0$, a straight line connecting satellite and receiver can be computed using equation 3.23 and by defining $n$=*1*:

$$s_0 = \int n ds_0 \tag{3.24}$$

The ionospheric refraction $\Delta^{Iono}$ is the difference between the measured and the geometric range. It is given by the following equation:

$$\Delta^{Iono} = \int n ds - \int n ds_0 \tag{3.25}$$

Considering the two refractive indices $n_{ph}$ and $n_{gr}$, equation 3.25 can be rewritten as follows:

$$\Delta^{Iono}_{ph} = \int \left(1 + \frac{c_2}{f^2}\right) ds - \int ds_0 \tag{3.26}$$

for the phase refractive index $n_{ph}$ (see 3.18), and

$$\Delta_{gr}^{Iono} = \int \left(1 - \frac{c_2}{f^2}\right) ds - \int ds_0 \tag{3.27}$$

for the group refractive index $n_{gr}$ (see 3.21). Equations 3.26 and 3.27 can be simplified if the first term is approximated by the integration along the geometric range, which means that $ds$ has to be replaced by $ds_0$. In this case, equations 3.26 and 3.25 take the following form:

$$\Delta_{ph}^{\text{Iono}} = \int \frac{c_2}{f^2} ds_0, \quad \Delta_{gr}^{Iono} = -\int \frac{c_2}{f^2} ds_0 \tag{3.28}$$

or, when substituting 3.22 into 3.28, these equations can be written as:

$$\Delta_{ph}^{\text{Iono}} = -\frac{40.3}{f^2} \int N_e ds_0, \quad \Delta_{gr}^{Iono} = \frac{40.3}{f^2} \int N_e ds_0 \tag{3.29}$$

Further, the total electron content (TEC) can be defined by:

$$TEC = \int N_e ds_0 \tag{3.30}$$

By introducing the TEC in equations 3.29, one can obtain the phase and group ionospheric delay in meters:

$$\Delta_{ph}^{\text{Iono}} = -\frac{40.3}{f^2} TEC, \quad \Delta_{gr}^{Iono} = \frac{40.3}{f^2} TEC \tag{3.31}$$

The TEC is defined as the number of free electrons integrated between receiver and satellite along a cylinder with a cross-section of 1 $\text{m}^2$. The TEC is usually given in TEC units (TECU), where:

$$1 \quad TECU = 10^{16}\ electrons/m^2 \tag{3.32}$$

The Slant Total Electron Content (STEC) for an arbitrary ray path between satellite and receiver can be calculated by using equation 3.30. To obtain the Vertical Total Electron Content (VTEC), a Mapping Function $M$ (see chapter 5.3) has to be introduced in order to project the STEC to the VTEC. The VTEC depends on the zenith angle of the satellite, so it has to be taken into account (Magnet, 2019).

$$VTEC = \frac{1}{M} STEC \tag{3.33}$$

## 3.4. The Chapman profile

According to the Chapman profile, the electron density in the ionosphere changes depending on the height above the Earth's surface ($h$) and the solar radiation angle ($\chi$). The Chapman function, formulated in 1931 by S. Chapman (Davies, 1990), gives the production rate of ion pairs in the ionosphere (Equation 3.34). It describes the correlation between the free electron density and the height, as well as the movement of the Sun, assuming the following statements (Todorova, 2008):

- only the solar radiation is being considered. The impact of cosmic rays is being ignored, even though their contribution to ionization is the second strongest after solar radiation;
- the atmosphere is composed of a single-component isothermal gas, which is distributed in horizontally layered shells with constant scale height;
- solar radiation is monochromatic, and it is absorbed proportionally to the gas-particle concentration.

This function is defined as follows (Schaer, 1999):

$$q(h,\chi) = q_0 e^{1-z-\sec\chi\, e^{-z}} \quad \text{with} \quad z = \frac{h-h_0}{\Delta h} \tag{3.34}$$

where:

| | |
|---|---|
| $q(h,\chi)$ | is the ion production rate, |
| $h$ | is the height above Earth surface, |
| $\chi$ | is the solar zenith angle[24], |
| $q_0$ | is the ion production rate at $z$=0, |
| $z$ | is the scaled altitude, |
| $h_0$ | is the reference height of maximum ion production at $\chi = 0$ (when the Sun is in zenith direction), |
| $\Delta h$ | is the scale height. |

The ion production rate can be calculated as:

$$q_0 = \frac{\phi(\infty)\eta}{\Delta h\, e} \tag{3.35}$$

where:

| | |
|---|---|
| $\phi(\infty)$ | is the solar flux density outside the atmosphere (measured in photons/area), |
| $\eta$ | is the number of produced ion pairs per photon. |

The height, at which the ion production rate reaches its maximum can be calculated by differentiating equation 3.34:

$$h_{\max} = h_0 + \Delta h\, z_{\max} \quad \text{with} \quad z_{\max} = \ln\sec\chi \tag{3.36}$$

[24]It is the angle between the incident solar radiation and the perpendicular to the observer's position on the Earth's surface. The angle varies depending on the observer's location, changing throughout the day, as well as throughout the year due to Earth's rotation and revolution. For further information on how to calculate the solar zenith angle, please refer to the work of Zolesi and Cander (2014), specifically Section 2.3.2.3.

The maximum amount of the ion production rate can be obtained by using the following equation:

$$q_{\max} = q_0 \cos\chi \tag{3.37}$$

The electron density $N_e$ is proportional to the recombination rate of ions and electrons in the ionosphere. Their relation, when neglecting the electron transportation processes, can be expressed with the following equation:

$$\frac{dN_e}{dt} = q - \mathrm{a}\, N_e^{\frac{1}{\alpha}} \tag{3.38}$$

where:

| | |
|---|---|
| a | is the mean recombination coefficient for molecular ions, |
| $\alpha$ | is the constant depending on the ionospheric altitude. |

At higher latitudes, the recombination rate depends linearly on $N_e$. The simple Chapman profile implies that the distribution of electron density is reached at photochemical equilibrium, i.e., when $dN_e/dt=0$ (Rishbeth and Garriott, 1969):

$$N_e(z,\chi) = N_{e,0}\, e^{\alpha(1-z-\sec\chi\, e^{-z})} \quad with \quad N_{e,0} = \left(\frac{q_0}{\mathrm{a}}\right)^{\alpha} \tag{3.39}$$

where:

| | |
|---|---|
| $N_{e,0}$ | is the electron density at scaled altitude z=0. |

The maximum electron density is reached at the altitude $h_{max}$ (Equation 3.36). Therefore, it can be calculated as follows (Schaer, 1999):

$$N_{e,max}(\chi) = N_{e,0} \cos^{\alpha}\chi \tag{3.40}$$

The Sun's zenith angle $\chi$ affects the maximum electron density $N_{e,max}$ and its corresponding height $h_{max}$. Around noon, When the Sun is in zenith ($\chi = 0$), the electron density reaches its maximum value. Conversely, during sunrise and sunset, when the Sun's zenith angle is at its lowest, the maximum value for $h$ is reached and $N_e$ is at its minimum (Magnet, 2019). The simple Chapman profile for solar zenith angles from 0° to 80° is illustrated in Figure 3.3.

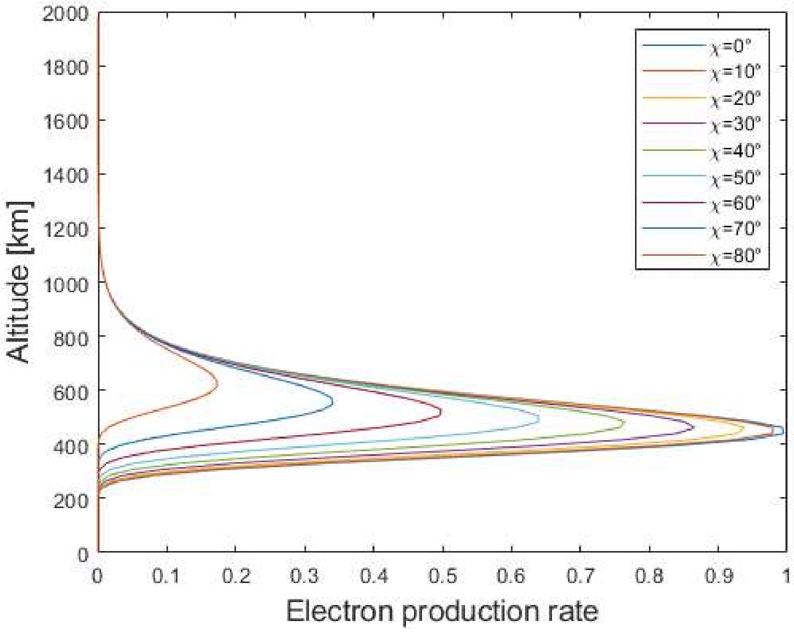


Figure 3.3: Electron production rate according to the Chapman profile for different solar zenith angles.

Considering that the altitude of maximum ion production is found at heights between 200 and 700 km, the reference height $h_0$, at which the ion production rate reaches its maximum was set to 450 km. This is due to the fact that at lower latitudes, despite there being a large number of ionizable molecules, the ion production decreases because of the reduction of photons and ionization of higher layers in the atmosphere. On the other hand, given the low molecule density at higher latitudes, the probability of an increased quantity of photons is rather low (Alizadeh, 2013; Todorova, 2008).

Even though the Chapman theory is based on quite simplified assumptions to describe the electron density distribution in the ionosphere, it is considered a fundamental reference in the theory of ionosphere modeling, as it reliably represents the main characteristics of the ionosphere. As seen from Figure 3.3, the highest electron production rate, is achieved at noon, i.e., when $\chi$=*0*. This rate applies to only a thin layer in the ionosphere, as it can be noticed here. This means that the maximum electron density is concentrated in an approximately thin layer, at a height usually between 300 and 500 km above the Earth's surface (Todorova, 2008). Since the maximum electron density height falls into the height range of the F2 layer, the maximum concentration of electrons is also known as the F2-peak. The F2-peak can be described by the following three parameters (Magnet, 2019):

- $N_mF_2$ (maximum electron density of the F2 layer)
- $h_mF_2$ (altitude of the F2-peak)
- $HF_2$ (scale height of the F2-peak).

A time series of the first two parameters, $N_mF_2$ and $h_mF_2$, is shown in Figure 3.4.

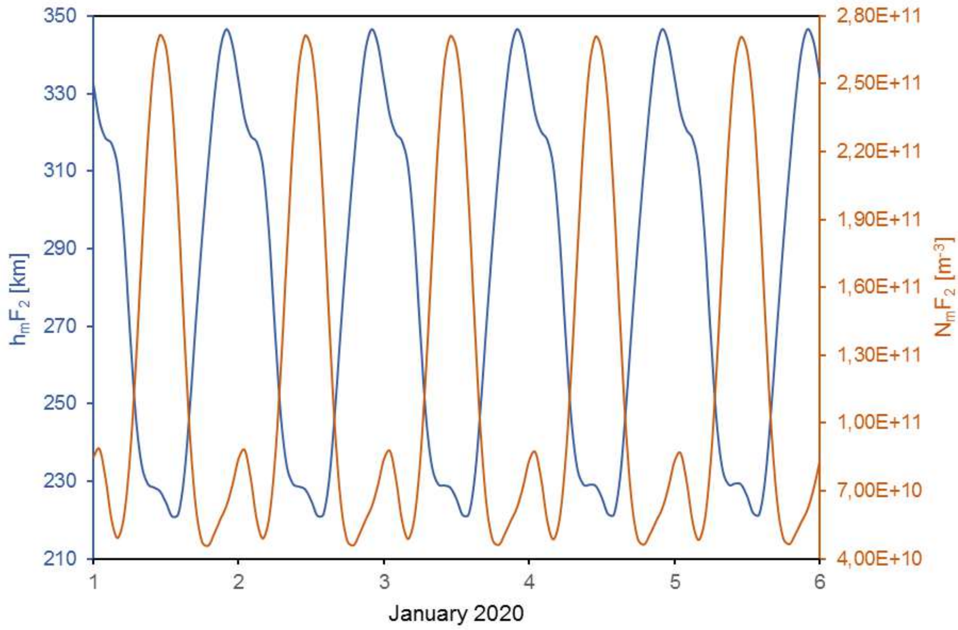


Figure 3.4: Evolution of the height of the F2 peak ($h_mF_2$) and the peak of electron density of the F2 layer ($N_mF_2$) from January 1st to January 6st, 2020. The diagram is produced using data from the IRI (International Reference Ionosphere) 2016 model for a location near Vienna.

The corresponding values are calculated using the IRI 2016 model (Bilitza et al., 2017) for five days in January 2020. These values are computed for the location φ=48°N, λ=16°E, which is close to Vienna, Austria. $N_mF_2$ and $h_mF_2$ are showing opposite trends over time. The maximum electron density $N_mF_2$ reaches its maximum value at daytime due to the high ionization caused by solar radiation, whereby it experiences two minima around midnight. The values range from approximately 0.4 to 3x$10^{11}$ m$^{-3}$. On the other hand, the altitude of the F2-peak, $h_mF_2$, has its maximum value during night-time, being around 350 km, and its minimum at noon, being approximately 220 km.

An ionosphere model widely accepted and used for the calculation of Global Ionospheric Maps (GIM) by various analysis centers is the Single Layer Model (SLM). It is based on the Chapman theory and it assumes that all free electrons are concentrated in an infinitesimally thin layer at a given height. This approach is applied in the current work (for further information, refer to section 5.2).

## 3.5. The variability of the Ionosphere

The Earth's ionosphere is driven by several effects that determine its structure and behavior on a global scale at any moment. The most prominent influence acting on the electron density, and thus, the ionospheric state comes from the Sun. Solar radiation causes variations at different time scales, ranging from diurnal and seasonal changes, up to the 11-year solar cycle. Such an effect attributed to the Sun is the day-night change, causing the electron density to vary daily, reaching its maximum during daytime and minimum at night. As stated before, there are also seasonal variations. Such changes happen because the Earth's two hemispheres are not exposed to the same amount of sunlight during summer and winter months, i.e., more sunlight in summer and less in winter. Furthermore, the behavior of the ionosphere is strongly influenced by the geomagnetic field (Forbes et al., 2000; Magnet, 2019).

### 3.5.1. Sun and Solar Activity

**3.5.1.1. Sunspots** The key indicator of solar activity is the sunspot number. The reason behind it lies in the length of the available record (Hathaway, 2015). Sunspots are probably the most important phenomenon in the photosphere. They appear as dark areas or spots on the Sun's surface, located usually between the solar latitudes 5° and 30° (Hargreaves, 1992; Todorova, 2008), and are characterized by a lower temperature compared to the rest of its surface. The lower temperature can be explained by the activity of strong magnetic fields, which are hindering hot gases from relocating from lower layers to the photosphere. Their lifespan varies from a few days up to several months (Zolesi and Cander, 2014).

The quantity of sunspots is usually expressed by the Wolf sunspot number $R$:

$$R = k(f + 10g) \tag{3.41}$$

where:

| | |
|---|---|
| $f$ | is the total amount of observed individual spots, |
| $g$ | is the number of disturbed areas, which can be sunspot groups or single sunspots, |
| $k$ | is the correction constant, different for each observatory and dependent of the sensitivity of the equipment, with a value close to 1 (Hargreaves, 1992; Todorova, 2008; Zolesi and Cander, 2014). |

Figure 3.5 shows the progression of the monthly mean sunspot number over the years, starting from 1749 up to the end of 2021. The 11-year solar cycle is strongly noticeable in the time series. This is the average duration of a solar cycle or sunspot cycle, whereas it can vary from 9 to 14 years (Magnet, 2019). Furthermore, the 27-day period is well pronounced, which is related to the solar rotation. The latest solar maximum occurred in 2014.

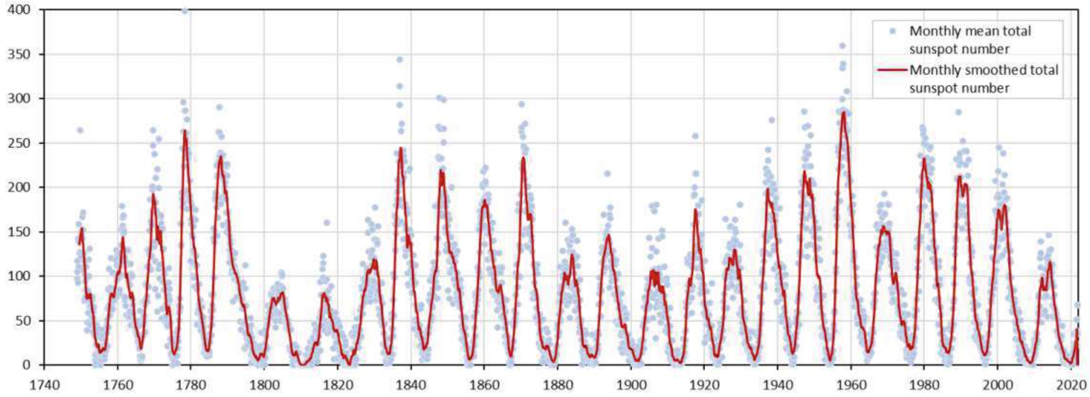


Figure 3.5: Monthly mean total sunspot number (light blue dots) and monthly smoothed total sunspot number (dark red line) from January 1749 to December 2021. Sunspot data from the World Data Center SILSO, Royal Observatory of Belgium, Brussels.

The electron density is higher during a solar maximum period. This is because of the more frequent occurrence of magnetic storms, which are causing the emission of charged particles, as well as solar ultraviolet and X-ray radiation to increase, thus affecting the number of electrons (Todorova, 2008).

**3.5.1.2. The Solar wind** Research conducted by Chapman and E. N. Parker has demonstrated that, unlike the Earth's atmosphere, the solar corona is not in hydrostatic equilibrium and is constantly shedding matter and radiation into space. This steady outflow of material, known as the solar wind, is an integral aspect of the solar system. The interplanetary magnetic field (IMF), which is carried with the solar wind toward Earth, plays a critical role in determining the extent to which the solar wind interacts with the Earth's atmosphere, especially in relation to the weak magnetic field. Even though the solar wind does not penetrate all the way to the ground of the Earth, it is still a vital component of the geospace environment, as some of the most extraordinary phenomena can be directly attributed to fluctuations in the solar wind and its magnetic field (Hargreaves, 1992).

### 3.5.2. Geomagnetic field and the Magnetosphere

The Earth itself is acting like a magnet (Hargreaves, 1992). The most appropriate approximation of its geomagnetic field is a field generated by a dipole (Figure 3.6). The corresponding axis is inclined by around 11° compared to the rotation axis of the Earth (Magnet, 2019; Zolesi and Cander, 2014) and intersects the Earth at two points, namely the geomagnetic north and south poles. The geomagnetic equator (or dip) is the intersection between the surface of the Earth and the plane passing through the Earth's center perpendicular to the dipole axis (Schaer, 1999). This dipole field expands beyond the terrestrial surface. It passes through the troposphere all the way to the ionosphere and past it. Whilst it has no influence on the neutral atmosphere, the effect of the geomagnetic field on the ionosphere has proven to be significant. The geomagnetic field is directly affecting the movement of charged particles in the ionosphere, therefore altering its electric currents, as well as the bulk movement of the plasma. Moreover, the higher the altitude of the atmosphere, the bigger becomes the impact of the geomagnetic field. The reason for this lies behind the fact that with increasing altitude the atmosphere becomes sparser, but has an increased level of ionization (Hargreaves, 1992).

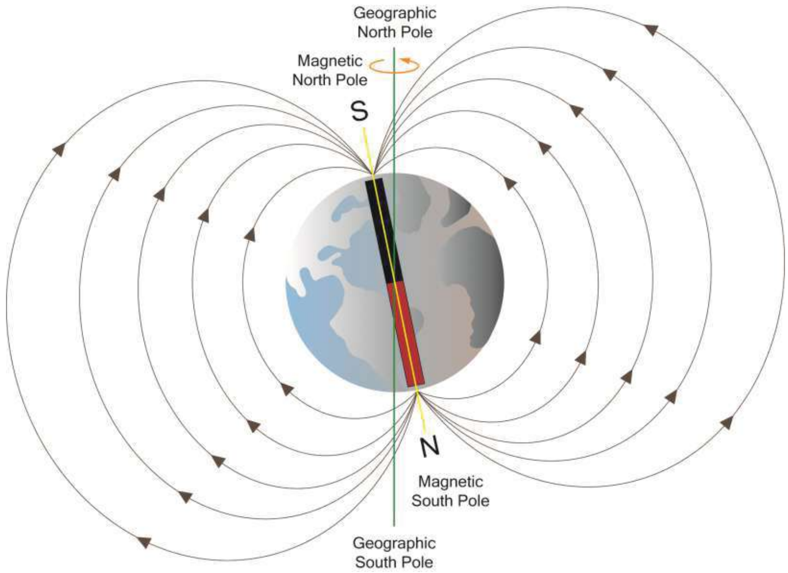


Figure 3.6: Earth's magnetic field.

At heights of more than some thousands of kilometers above the Earth's surface, the geomagnetic field dominates all other behavior, causing this region to be called the magnetosphere (Figure 3.7). Whereas there is no clear boundary between the ionosphere and the magnetosphere (Hargreaves, 1992), the boundary between the magnetosphere and space is defined by the magnetopause (Magnet, 2019). The magnetopause is of high relevance considering that at this boundary most of the magnetosphere's and ionospheric behavior at high latitudes is determined. This is caused by energy being coupled at this boundary from the solar wind into the magnetosphere (Hargreaves, 1992). The shape of the geomagnetic field is changing due to the interaction between charged particles of the solar wind, released by the Sun, and lines of the geomagnetic field. This interaction results in a deformation of the geomagnetic lines, compressing them on the Sun-facing side of the Earth and extending to a tail on the opposite side (Zolesi and Cander, 2014).

The region located below the lower part of the magnetosphere is called the plasmasphere and it is formed like a torus around the Earth. It is considered the utmost layer of the ionosphere, starting from an altitude of 1000 km above the Earth's surface (Zolesi and Cander, 2014). The plasmapause lies at an altitude of approximately 26 000 km around the plasmasphere, being its outer boundary (Magnet, 2019).

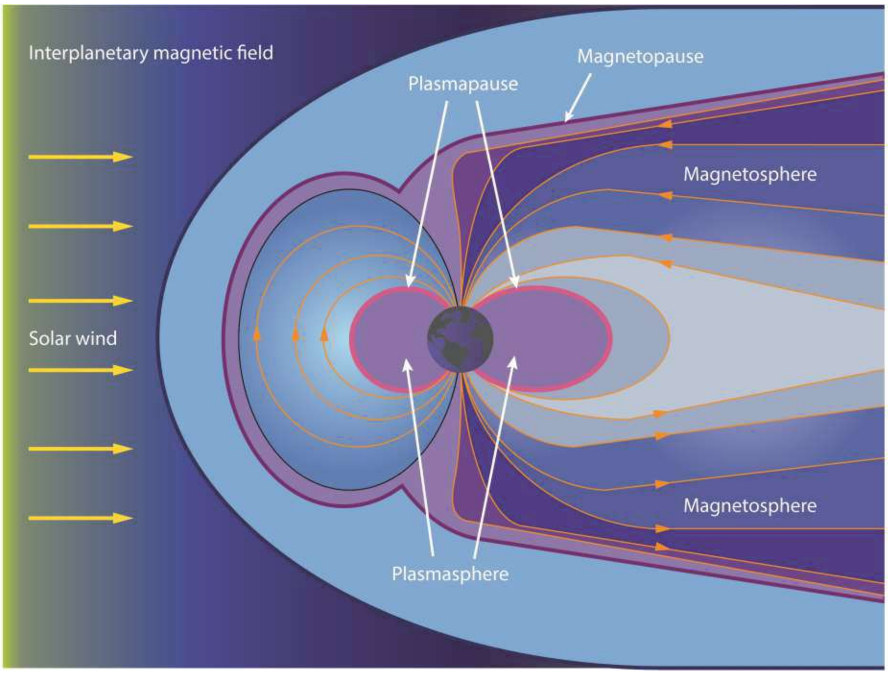


Figure 3.7: Illustration of Earth's magnetosphere.

**3.5.2.1. Latitude dependent regions of the ionosphere** Due to the behavior of the terrestrial magnetic field, three main geographic regions of the ionosphere can be identified (Figure 3.8):

- **Low latitude (equatorial) region** is located within 20° on both sides of the magnetic equator. This area is characterized by the highest electron density and scintillation effects. At the F2 layer, the peak electron density distribution exhibits a minimum at the geomagnetic equator, with two maximum peaks located at magnetic latitudes of 15° - 20° north and south on each side of the magnetic equator. This occurrence is known as the Appleton anomaly, or the Equatorial Ionization Anomaly (EIA) (Alizadeh, 2013; Zolesi and Cander, 2014).
- **Mid-latitudes**, which extend from 60° to 20° on either side of the magnetic equator in terms of geomagnetic latitude, are characterized by relatively stable ionospheric conditions. As a result, this region is easier to model than others. Typically, ionospheric conditions in this region are "normal" or "quiet" approximately 98% of the time. However, during the remaining 2%, geomagnetic storms can cause disturbances in the ionosphere. Due to its predictable nature and relatively stable conditions, the mid-latitudes have been extensively studied and are often used as a basis for ionospheric modeling and prediction (Zolesi and Cander, 2014).
- **High latitude (polar) region**, covering the geomagnetic latitudes 90°- 60° on each side of the magnetic equator. A further division into sub-regions can be done for the high latitudes into the auroral and polar cap regions. Studies, especially the ones performed during the International Polar Year (IPY 2007-2009), have confirmed that this region undergoes the

highest variability out of all the ionospheric regions. This is due to its connection to the magnetosphere and the interplanetary medium, via the terrestrial magnetic field. The free electron density is, on the other hand, relatively low. The main source of ionization is energetic charged particles. Unlike in other regions, solar radiation-driven ionization (i.e., by solar EUV radiation and X-rays) at high latitudes is rather weak due to the low elevation angle of the Sun. In the polar ionosphere, at geomagnetic latitudes higher than approximately 75°, the total energy budget of the upper atmosphere is dominated by the dissipated energy of solar winds. Extremely dynamic processes of energy redistribution by heating and cooling, as well as winds and waves, are taking place in this region. Their impact on a global scale maximizes even more during geomagnetic storms (Zolesi and Cander, 2014).

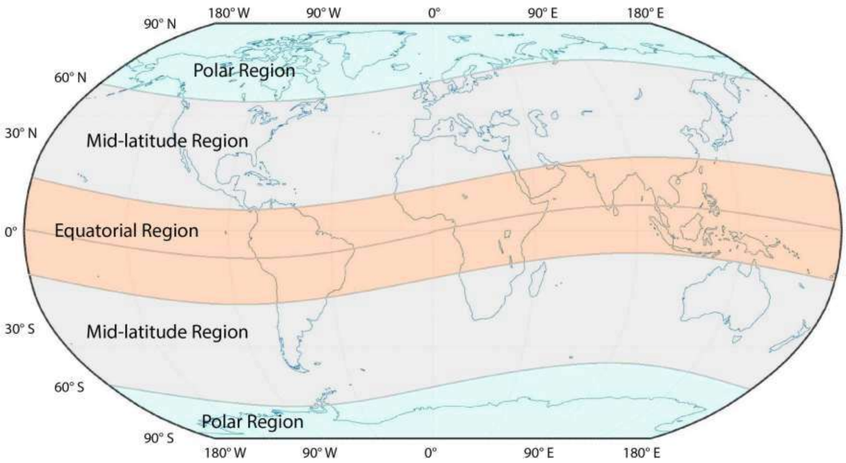

Figure 3.8: Main geographic regions of the ionosphere.

### 3.5.3. Ionospheric disturbances

The term "ionospheric disturbance" is used to cover a wide range of conditions in the ionosphere that are characterized by a deviation from its usual state (Davies, 1965). The near-Earth plasmas are experiencing various changes originating from the effects of solar radiation, as well as from geomagnetic, magnetospheric, and ionospheric activity. These effects differ in timescale, significance, predictability, and aftereffect (Table 3.2). They can be divided into:

- direct effects (caused by sudden changes in solar UV radiation and X-ray emission during solar flare events)
- indirect effects (caused by interactions between the solar wind and the magnetosphere-ionosphere-atmosphere system (Zolesi and Cander, 2014).

Table 3.2: Types of ionospheric disturbances and their practical consequences (taken after Hargreaves (1992)).

| Event | Effect | Users |
|---|---|---|
| Solar flare (X-rays) | Sudden Ionospheric disturbance (SID) | Radio communicators<br>Ship and airlines |
| Polar cap absorption (protons) | Damaging radiation | Space Agencies<br>Airlines |
| Ionospheric storm | Ionospheric changes | Radio communicators<br>Ship and airlines |
| Geomagnetic storm | Induced Earth currents<br>Field perturbations<br>Enhanced particle fluxes in space | Electric power companies<br>Magnetic surveyors<br>Satellite operators |

**3.5.3.1. Solar flares and Sudden Ionospheric disturbances (SID)** Solar flares are sudden bursts of light, which occur near a sunspot in solar active regions (Davies, 1965; L. Liu et al., 2011). Solar flares are more frequent and intense near times of maximum sunspot number, i.e., during the solar maximum. They last from approximately 10 minutes to several hours. During a solar flare event, enormous energy is released from the Sun, leading to differently intensified amplitudes of radio, visible light, and EUV wavelengths. It takes approximately 8 minutes after a solar flare occurs, for the extremely severe radiation to hit the Earth, after traveling towards it at light speed. This incident modifies immediately the structure and state of the ionosphere and thermosphere on the sunlit side of the Earth, causing, so-called, sudden ionospheric disturbances (L. Liu et al., 2011). These events are primarily affecting the D ionospheric layer, leading to an increase in electron density, which may be as high as an order of magnitude as a response to severe solar flares (Zolesi and Cander, 2014). It occurs within a few seconds, causing a strong absorption of radio waves, which can be enhanced to such an extent as to interrupt radio communication signals. This interruption is referred to as "radio fadeout", or "short wave fadeout" (SWF) (Budden, 1988; Davies, 1965). The increases in electron density by approximately 20 - 30 % in response to strong solar flares can be noticed for the E layer as well. The F region is experiencing a minor impact, given the ionization from EUV radiation (Zolesi and Cander, 2014).

**3.5.3.2. Geomagnetic storm** Geomagnetic storms are disturbances of the Earth's magnetic field (Davies, 1965), caused by intensified solar winds due to coronal mass ejections (CME) (Magnet, 2019). They usually last from a few hours to several days. During geomagnetic storms, components of the geomagnetic field experience fluctuations of significantly larger amplitudes (several percent of the total field in middle latitudes) compared to their fluctuations under normal or quiet conditions (a few tenths of one percent). Magnetic disturbances are most pronounced near auroral regions (Davies, 1965). The graph below shows the number of days with a geomagnetic storm per year and how strong those storms were.

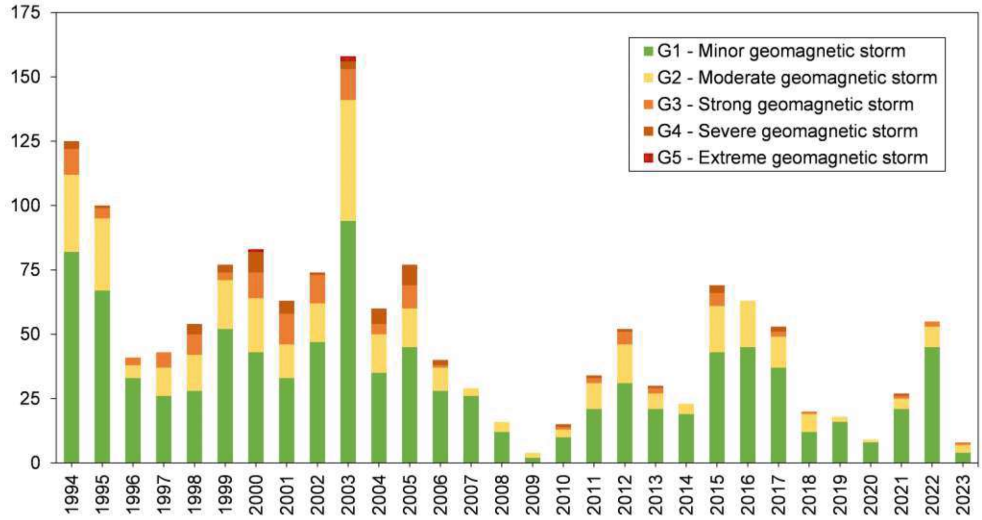


Figure 3.9: Number of days with a geomagnetic storm per year (as of 23.03.2023) (Data from Space Weather Live[25]).

**3.5.3.3. Ionospheric storm** Ionospheric storms are large-scale disturbances causing fluctuations in total electron content, density distribution, and the ionospheric structure itself. They are acting as a kind of response to geomagnetic storms, being one of the most dramatic outcomes of magnetosphere-ionosphere-thermosphere coupling (Zolesi and Cander, 2014). During ionospheric storms, extremely strong solar winds cause immense perturbations in high latitudes of the ionosphere and thermosphere. These further result in fluctuations of the plasma density, which in general travels towards the lower latitudes. Furthermore, ionospheric storms are responsible for the increase of the total electron content (TEC) by more than 10 Total Electron Content Units (TECU) (Alizadeh, 2013).

**3.5.3.4. Polar Cap absorption (PCA)** This phenomenon is characterized by an enhanced ionization of the D region in the high-latitude ionosphere (polar caps). The additional amount of ionization comes from a flux of energetic protons released from the Sun during a solar flare event (Hargreaves, 1992). It often results in a collapse of medium and high frequency (MF/HF) communications on polar paths and is more prominent during times near the solar maximum, similar to solar flares. Polar Cap absorption events can appear during both daytime and night-time (Zolesi and Cander, 2014), with an average duration time of

[25] Space Weather Live: https://www.spaceweatherlive.com/en/solar-activity/solar-cycle.html.

3 days (Davies, 1965). They are presumably the most significant disturbance of the high latitude lower ionosphere since they affect both ground-based and space-based systems (Zolesi and Cander, 2014).

### 3.5.4. Irregularities of the Ionosphere

Ionospheric irregularities comprise states and conditions in the ionosphere that cannot be accurately represented by conventional ionospheric models, as well as occurrences that are not behaving according to patterns, determined based on their physical causes (Zolesi and Cander, 2014). The F region is highly variable manifesting several irregularities. Some of them will be described in more detail in further sections.

**3.5.4.1. Traveling ionospheric disturbances (TIDs)** Traveling ionospheric disturbances are irregularities of the F region and can be described as wave-shaped oscillations in the plasma density (Alizadeh, 2013; Zolesi and Cander, 2014). They are spreading through the ionosphere at different velocities and frequencies (Alizadeh, 2013). TIDs can cause the TEC value to change by up to several percent (Schaer, 1999). Considerable diurnal, seasonal, and sunspot cycle variations can be noticed during a TID phenomenon (Zolesi and Cander, 2014). TIDs are usually seen in mid-latitudes and they are more prominent near the solar maximum (Alizadeh, 2013; Hernández-Pajares et al., 2006). TIDs are classified into two types:

- ***Large-scale TIDs (LS TIDs)***: they have a period of 1-3 h and a horizontal wavelength of 1000-4000 km. They reach a velocity of more than 300 m/s. LS TIDs are related to geomagnetic activities (Alizadeh, 2013). Surges in the auroral electrojet produce large-scale TIDs, which are traveling towards the equator, causing the ionospheric height to increase significantly (Zolesi and Cander, 2014).
- ***Medium-scale TIDs (MS TIDs)***: they have shorter periods ranging from 10 minutes to 1 hour and horizontal wavelengths of up to 300 km. They move slower compared to LS TIDs, at velocities 50-300 m/s. MS TIDs arise primarily from meteorological phenomena, such as neutral winds or the solar terminators, which produce atmospheric gravity waves (AGW) that manifest TIDs at various ionospheric altitudes (Alizadeh, 2013; Zolesi and Cander, 2014).

**3.5.4.2. Scintillation** Ionospheric scintillations refer to rapid changes in the amplitude and phase of a signal caused by short-term variations ($<$ 15 seconds) in the number of electrons along a signal path from a satellite to a receiver. When the carrier experiences a sudden change in phase due to these variations, it can cause problems in the receiver's carrier tracking loop, leading to disruptions in GNSS observations (Langley, 2000). Ionospheric scintillation is one of the factors that can lead to cycle slips in GNSS. This phenomenon introduces noise into GNSS observations, causing the receiver to lose phase lock with the satellite signal (Seeber, 2003). The effect of scintillation on GNSS receivers depends on their hardware and software. Moreover, receivers that make carrier-phase measurements are more susceptible to scintillations than those that only use code measurements (Langley, 2000).

The equatorial regions (extending up to 20° on both sides of the geomagnetic equator), as well as polar and auroral regions, are areas where the most severe scintillation effects are observed. Additionally, a correlation between strong scintillations and the sunspot number can be noticed. Strong scintillation effects on GNSS in the equatorial and lower latitude regions are observed during the years of maximum solar activity. On the other hand, at higher latitudes (auroral and polar cap latitudes), any pronounced magnetic storm activity can generate scintillation effects (Alizadeh, 2013).

**3.5.4.3. Spread-F** Spread-F is an irregularity of the ionosphere that occurs when the F region becomes diffused causing radio waves to scatter. The irregularities appear in stain-like shapes, with their sizes ranging from 20 km up to more than 100 km. The spread-F occurrence depends on the solar cycle and seasonal variations, as well as the local time and latitude. The commonness of occurrence of the spread-F, as well as its characteristics, changes with the latitude (Zolesi and Cander, 2014).

At the equator, geomagnetic activity has no impact on the spread-F, while, on the other hand, it influences the spread-F at high latitudes. At low- and mid-latitudes, spread-F appears primarily during night-time. In contrast to that, at high latitudes, near the magnetic poles, spread-F can be found both, during day and night-time. Regarding the time of occurrence, it is most likely to be observed around the equinoxes at low latitudes and during winter at mid-latitudes (Zolesi and Cander, 2014).

### 3.5.5. Indices of Solar and Geomagnetic activity

The ionospheric condition and behavior strongly depend on both solar and geomagnetic activity. Therefore, it is important to measure quantities of the solar and geomagnetic field which can provide an insight into the ionospheric state. Moreover, such measures play a significant role in predicting and modeling conditions of the ionosphere.

Solar indices can be described as a measure of the Sun's activity. Some of them are $R_i$, $R_k$, $R_{12}$, $\Phi$ and $\Phi_{12}$. $R_i$ is the International Sunspot Number. In January 1981 it replaced the most widely quoted average sunspot number at that time, the Zürich number ($R_z$). The mean of the daily sunspot numbers for a single month is known as $R_k$, while the corresponding smoothed monthly index is denoted by $R_{12}$. The solar radio noise flux $\Phi$ of 10.7 cm wavelength (frequency 2.8 GHz) is another helpful indicator of solar activity, by describing the level of radiation received from the Sun at the wavelength of 10.7 cm. The relation between the $R_{12}$ and $\Phi_{12}$ can be expressed as:

$$\Phi_{12} = 63.7 + 0.728\,R_{12} + 8.9x10^{-4}\,R_{12}^2 \tag{3.42}$$

Different organizations are publishing the measured and predicted values for $R$ and $\Phi$, as well as for their 12-month running mean values. One such organization is the Sunspot Index Data Centre (SIDC) of the Royal Observatory of Belgium in Brussels, Belgium[26](Zolesi and Cander, 2014).

The geomagnetic activity can be described by several indices that are regularly derived from magnetic records and published. The most widely used are the $K_p$, $A_p$ and $AE$ index (Hargreaves, 1992). The $K_p$ index is derived from 3-hourly measurements collected by ground-based magnetometers distributed all over the world. At each magnetometer station the $K$ index is obtained, which is a 3-hour-long quasi-logarithmic local index, representing the geomagnetic activity of its location and time in comparison to conditions of a quiet day. Those values are further collected by an algorithm that calculates the global $K_p$ index. $K_p$ is usually expressed with numbers 0-9, where 0 indicates that there is little geomagnetic activity and 9 indicates extreme geomagnetic activity. The integer values are subdivided into thirds by adding the signs -, 0, +, which results in a 28-step scale ranging from 00 to 90 (Hargreaves, 1992; Zolesi and Cander, 2014).

The $A_p$ index is a daily index, which is based on the same input data as $K_p$, but converted to a linear scale, the 3-hour $a_p$ (Hargreaves, 1992). The value of $a_p$ can range from 0 to 400. Eight 3-hour $a_p$ indices are further averaged over one day to get the daily planetary $A_p$ for one day UT. $K_p$ and $A_p$ values are published on a regular basis by the GFZ Helmholtz Centre[27], Potsdam.

The $AE$ index represents variations in the geomagnetic field driven by currents in the auroral region of the ionosphere (Zolesi and Cander, 2014). While stations engaged in the calculation of the $K_p$ and $A_p$ indices are located at different latitudes and longitudes, but predominantly in the higher mid-latitudes, the stations contributing to the calculation of the $AE$ index are located at different longitudes around the auroral zone. The $AE$ values are published by the Data Analysis Center for Geomagnetic and Space Magnetism Faculty of Science[28], Kyoto (Zolesi and Cander, 2014).

### 3.5.6. Existing ionospheric models

**3.5.6.1. Klobuchar model** The Klobuchar model was developed in 1986 for GPS single-frequency users. It is based on a simple algorithm, able to correct approximately 50% of the range error caused by ionospheric refraction. It is actually approximating the vertical ionospheric refraction by estimating the vertical time delay for code measurements. The algorithm utilizes eight ionospheric coefficients that are broadcast within the GPS navigation

[26]SIDC website: http://www.sidc.be/
[27]Geomagnetic Kp index from GFZ available at: https://www.gfz-potsdam.de/kp-index
[28]World Data Center for Geomagnetism, Kyoto: https://wdc.kugi.kyoto-u.ac.jp

message to model the global diurnal variation of the vertical ionospheric delay (Hofmann-Wellenhof et al., 2007). This is achieved by implementing a half-cosine function, where the amplitude and period of the function are centered at 14:00 local time. During night time, the vertical ionospheric delay is fixed at a constant value of 5 ns, which is equivalent to 1.5 m at the GPS L1 frequency (Hobiger and Jakowski, 2017). Therefore, the time delay $\Delta T_v^{ion}$ in *nanoseconds*, modeled with the Klobuchar model, can be expressed using the following equation:

$$\Delta T_v^{ion} = A_1 + A_2 \cos\left(\frac{2\pi(t - A_3)}{A_4}\right) \tag{3.43}$$

where:
$A_1 = 5 \cdot 10^{-9} s = 5\ ns$,
$A_2 = \alpha_1 + \alpha_2 \varphi_{IPP}^m + \alpha_3 {\varphi_{IPP}^m}^2 + \alpha_4 {\varphi_{IPP}^m}^3$,
$A_3 = 14^h$ local time,
$A_4 = \beta_1 + \beta_2 \varphi_{IPP}^m + \beta_3 {\varphi_{IPP}^m}^2 + \beta_4 {\varphi_{IPP}^m}^3$.

$A_1$ is the constant night-time value, $A_3$ is the constant phase shift fixed at 14:00 local time, whereas $A_2$ and $A_4$ depend on the satellite-transmitted ionospheric coefficients $\alpha_i, \beta_i$ (i = 1,…,4) (Hobiger and Jakowski, 2017) given in *s/(semicircle)*$^i$ (U.S. Air Force GPS Directorate, 2021). $t$ is the local time of the ionospheric pierce point (IPP) and is calculated as follows (Hofmann-Wellenhof et al., 2007):

$$t = \frac{\lambda_{IPP}}{15} + t_{UT} \tag{3.44}$$

where:

| | |
|---|---|
| $\lambda_{IPP}$ | is the geographic longitude of the IPP in degrees, |
| $t_{UT}$ | is the observation epoch in Universal Time (UT), |
| $\varphi_{IPP}^m$ | from Equation (3.43) is the spherical distance between the geomagnetic pole and the IPP in semicircles. It is derived from: |

$$\cos \varphi_{IPP}^m = \sin \varphi_{IPP} \sin \varphi_0 + \cos \varphi_{IPP} \cos \varphi_0 \cos(\lambda_{IPP} - \lambda_0) \tag{3.45}$$

where:

| | |
|---|---|
| $\varphi_{IPP}, \lambda_{IPP}$ | are the geographic coordinates of the IPP and |
| $\varphi_0, \lambda_0$ | are the geographic coordinates of the geomagnetic pole. |

**3.5.6.2. NeQuick and NeQuick G Model** NeQuick is a three-dimensional and time-dependent ionospheric electron density model. It was developed by the Aeronomy and Radio propagation Laboratory (ARPL) of the Abdus Salam International Centre for Theoretical Physics in Trieste (Italy) and the Institute for Geophysics, Astrophysics and Meteorology of the University of Graz (Austria) (Hofmann-Wellenhof et al., 2007). NeQuick is based on an empirical climatological characterization of the ionosphere, which is forecasting the monthly mean electron density from analytical profiles (European Commission, 2016). Since this model is three-dimensional and time-dependent, the TEC can be obtained at any given location and time. The required input parameters are position, time, and solar flux. The latter can be expressed by the 12-month running mean sunspot number $R_{12}$ or by the average 10.7 cm solar radio flux $F_{10.7}$[29] (Hofmann-Wellenhof et al., 2007). The relation between $R_{12}$ and $F_{10.7}$ is given with:

$$R_{12} = \frac{F_{10.7} - 57}{0.93} \tag{3.46}$$

The International Telecommunication Union, Radiocommunication (ITU-R) sector has adapted the first version of the NeQuick model (NeQuick 1) for TEC estimation applied in radio wave propagation predictions. A newer version, NeQuick 2, based on updated formulations is recommended according to ITU-R Recommendation P.531 (Annex A [3], European Commission (2016)).

Finally, the ***NeQuick G*** model, adapted for real-time Galileo single-frequency ionospheric corrections, has been developed. The solar flux as an input parameter has been replaced by the Effective Ionization Level ($Az$). This single parameter is needed to derive real-time ionospheric predictions. $Az$ is calculated by using three ionospheric coefficients, broadcast in the navigation message. Therefore, NeQuick G is recommended for the implementation in user equipment considering its consistency with the transmitted coefficients (European Commission, 2016). The Effective Ionization Level, $Az$, is determined as follows:

$$Az = a_0 + a_1\mu + a_2\mu^2 \tag{3.47}$$

where $a_0, a_1$ and $a_2$ are coefficients contained in the Galileo navigation message and broadcasted to the users. $\mu$ is the Modified Dip Latitude at the receiver location (also referred to as MODIP). It is expressed in degrees and can be obtained by the following equation:

$$\tan\mu = \frac{I}{\sqrt{\cos\varphi}} \tag{3.48}$$

$I$ is the magnetic dip or magnetic inclination. Its value is 0° at the magnetic equator and 90° at each magnetic pole (Hofmann-Wellenhof et al., 2007). A table grid of $\mu$ values as

[29]A 10.7 cm solar flux measurement is an assessment of the intensity of solar radio waves within a 100 MHz-wide band centered at 2800 MHz (equivalent to a wavelength of 10.7 cm), averaged over a duration of one hour. The measurement is typically reported in solar flux units (*sfu*), where 1 *sfu* equals $10^{-22}$ W $m^{-2}$ $Hz^{-1}$ (Tapping, 2013).

a function of geographical location is provided with the NeQuick G model for the receiver (European Commission, 2016), which then calculates the TEC by integrating the electron density $N$ along a signal path (Magnet, 2019):

$$TEC = \int_{h_1}^{h_2} N(h)\,dh \tag{3.49}$$

The further calculation leans on the definition of three profile anchor points, or in other words, the heights of maximum electron density in three ionospheric layers, namely the E layer peak (fixed height of 120 km), F1 peak, and F2 peak (European Commission, 2016). The ionospheric layers were previously explained in Chapter 3.2.

Based on the corresponding ionospheric parameters $N_mF_2$, $h_mF_2$, $h_mF_1$ and $h_mE$, the model can define the bottom side and topside electron density (Magnet, 2019):

$$N(h) = \begin{cases} bottomside\, N, & if\, h \leq h_mF_2 \\ topside\, N, & if\, h > h_mF_2 \end{cases} \tag{3.50}$$

**3.5.6.3. IRI Model** The work on the International Reference Ionosphere (IRI) has begun out of the goal of developing a reference ionospheric model, which can serve as an international standard, offering the most important plasma parameters in the Earth's ionosphere. It is a joint project between the Committee on Space Research (COSPAR) and the International Union of Radioscience (URSI) that started in 1969. IRI provides monthly averages of electron density, electron temperature, ion temperature, and ion composition for altitudes 50 – 2000 km all around the globe.

It is an empirical model based entirely on observation data, including data from ionosondes, incoherent scatter radars, topside sounders, rockets, GNSS, in situ measurements, and radio occultation. Being a data-based model means that its reliability and accuracy depend on the spatial and temporal coverage of the mentioned data sources. In other words, dense data coverage (as in the northern hemisphere) delivers a good accuracy, whereas the performance in the case of sparsely distributed data (as in auroral polar and equatorial regions) is not as good (Bilitza, 2018).

The latest version of the IRI model, IRI2016 was introduced by Bilitza et al., 2017. It can be accessed online via the IRI2016 webpage[30]. For more information on the IRI model, please refer to Bilitza et al. (2017) or to the official IRI model description[31], where a link to the corresponding Fortran source code and supporting documents can be obtained.

**3.5.6.4. CODE Model** The Center for Orbit Determination in Europe CODE is one of the Analysis Centres of the International GNSS Service (IGS) (Schaer et al., 1996). The

[30]International Reference Ionosphere - IRI (2016): https://ccmc.gsfc.nasa.gov/modelweb/models/iri2016_vitmo.php
[31]International Reference Ionosphere Description: webpage http://irimodel.org

Global Ionospheric Maps (GIMs) provided by CODE are routinely generated on a daily basis since January 1st, 1996, using TEC data from approximately 300 GNSS sites of the IGS and other institutions. The vertical TEC is modeled in a solar-geomagnetic reference frame, by applying a spherical harmonics expansion up to degree and order 15. For the representation in the time domain, piece-wise linear functions are used, where the interval of their vertices is set to 1 hour. This means that one daily GIM file contains 25 1-hourly VTEC maps.

The modified single-layer model mapping function (MSLM), explained in Chapter 5.2, was adopted to convert the line-of-sight TEC into the corresponding VTEC value. Since March 2002, CODE has carried out a 3-day combination analysis (Jee et al., 2010). In other words, the final solution corresponds to the middle day of this analysis, which enables discontinuities at day boundaries to be minimized.

The spatial resolution of the GIMs is 2.5° x 5° in latitude and longitude, thus solving 73 times 256, or 18 688 VTEC parameters. Furthermore, 3 daily sets of GNSS code bias parameters are estimated for each day as constant values. It has to be noted that only GPS bias values are included in the same file, whereas the whole set of GNSS bias results can be found in an additional Bias SINEX file (ftp.aiub.unibe.ch/CODE/).

**3.5.6.5. IGS Model** The IGS Ionosphere Working Group (IIWG) was established in 1998 with the aim to produce and provide reliable global ionospheric maps (GIMs), calculated from GNSS-based TEC measurements. Currently, there are seven Ionosphere Associate Analysis Centers (IAACs) that are regularly providing GIMs of total vertical electron content values within the IGS frame (J. Chen et al., 2020).

Different mapping techniques have been developed by each center, especially regarding slant-to-vertical mapping, each using a different mapping technique of ground-based observations. The IGS-generated GIM (IGSG), is the result of the combination of GIMs provided by the Center for Orbit Determination in Europe (CODE), Universitat Politècnica de Catalunya/IonSAT (UPC), the European Space Operations Center of the European Space Agency (ESA), and the Jet Propulsion Laboratory (JPL) by using a weighted mean method. This method is determined by a self-consistency test (Hernández-Pajares et al., 2017; Roma-Dollase et al., 2018).

The spatial and temporal resolution of the resulting GIMs is 2.5° x 5° in latitude and longitude and 2 h, respectively. Such a combination offers exceptionally high accuracy, as well as high reliability, or in other words availability and continuity. This is due to the fair assessment of the accuracy and consistency of the individual GIMs used for the final IGS GIM (Hernández-Pajares et al., 2017).

# 4. Global Navigation Satellite Systems

Observations of distant objects have been used for hundreds of years to determine the positions of points on the Earth's surface. However, high-accuracy positioning and navigation were only possible at the beginning of the space age. The space age was introduced in the late 1950s and 1960s with the development of space-based systems (Langley et al., 2017). Global navigation satellite systems (GNSS) are a common term for all currently existing global navigation satellite systems (Magnet, 2019). They refer to constellations of satellites, which provide signals, that are transmitted from space to receivers on the Earth. The signals contain data on position and time. This data is further used by receivers to determine the location (Euspa, 2021c). Even though initially developed for military purposes, these systems serve nowadays as one of the precise satellite geodetic techniques that significantly contribute to the development of Earth's science (Zajdel, 2021).

Satellite navigation methods can be classified into active and passive. Active methods require the signals to be broadcast by the user. In the case of passive methods, satellites emit modulated signals containing the transmission time (to compute ranges) and modeling parameters (to derive satellite positions), while the user receives the transmitted signals. Another classification of satellite navigation methods is into one-way and two-way ranging systems. One-way systems can further be distinguished into uplink (earth-to-space) and downlink (space-to-earth) systems. GNSS are passive one-way downlink ranging systems (Hofmann-Wellenhof et al., 2007).

Today, GNSS is used in a wide range of applications, for example, location-based services, civil applications (personal, road, aviation, rail applications, and more), land surveying, mapping, precise orbit determination, satellite real-time navigation, earth science, etc. (Barradas Pereira and GMV, 2011). This broad usage became possible thanks to the high accessibility of precise GNSS receivers, which are quite affordable and, therefore, available to the public. Furthermore, it should be noted that over the years, the processing methods for transmitted signals have significantly improved in terms of accuracy and precision, and are constantly under development. (Zajdel, 2021). The extensive utilization of GNSS has resulted in the establishment of a dense worldwide network of receivers that continuously gather satellite observations.

There are currently six GNSS/RNSS (Regional Navigation Satellite Systems) in operation (Figure 4.1). The first GNSS to be fully operational was the American Global Positioning System (GPS), followed by the Russian Globalnaja Nawigacionnaja Sputnikowaja Sistema (GLONASS). They were complemented by the global systems Galileo from Europe and BeiDou from China. The two RNSS are the Japanese Quasi-Zenith Satellite System (QZSS) and the Indian Regional Navigation Satellite System (IRNSS)/Navigation Indian Constellation (NavIC) (Langley et al., 2017).

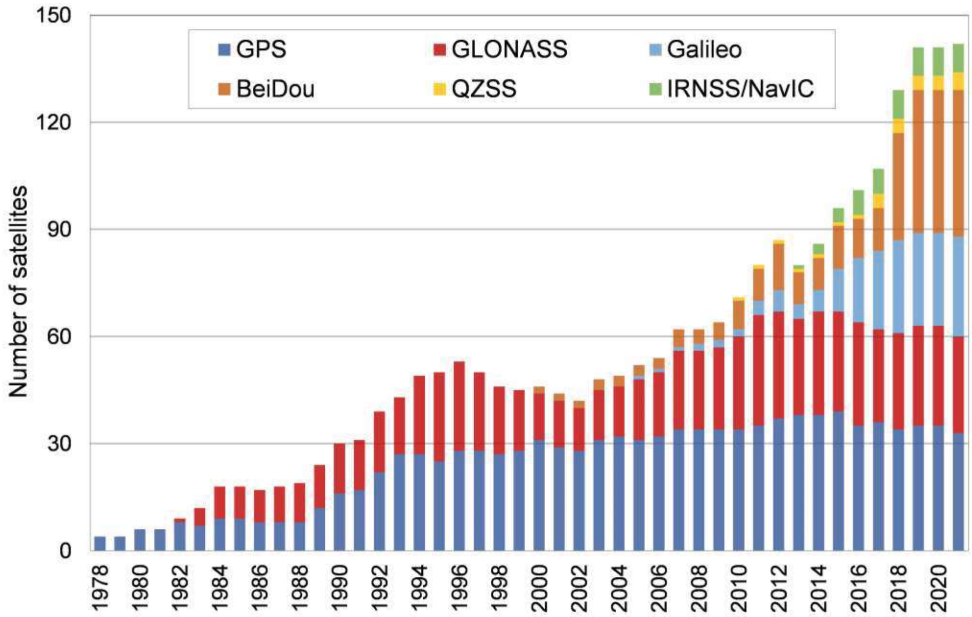


Figure 4.1: Number of operational GNSS and RNSS per year since 1978.

Each system is constructed on three main pillars, the space segment, the ground segment, and the control segment. An overview of their constellation parameters is given in Table 4.1. The corresponding frequency bands of the four GNSS are illustrated in Figure 4.2:

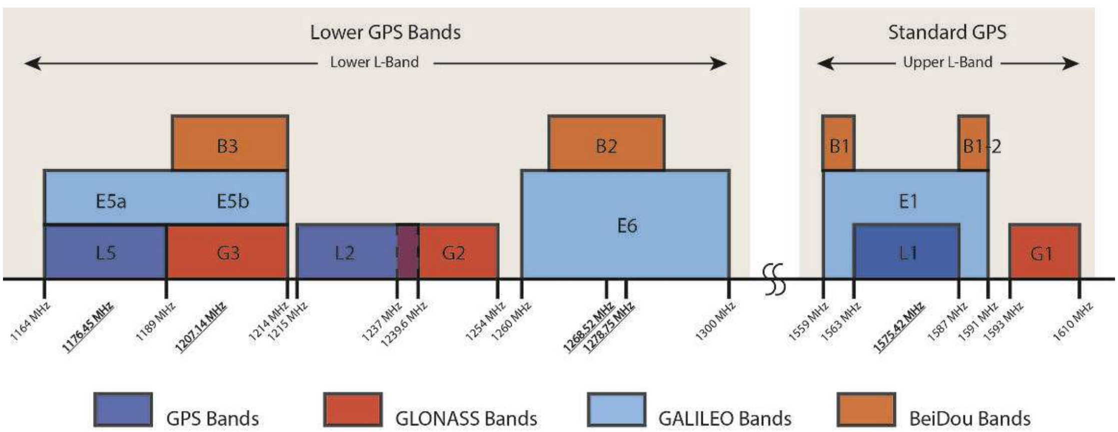


Figure 4.2: GNSS navigation radio frequency bands.

Table 4.1: Main characteristics of the current GNSS/RNSS constellations. This table was adapted based on Langley et al. (2017), Zajdel (2021), Parkinson et al. (2020), and Euspa (2022).

| System | GPS | GLONASS | Galileo: Nominal constellation | Galileo: Satellites on eccentric orbits | BeiDou | QZSS | IRNSS/NavIC |
|---|---|---|---|---|---|---|---|
| **Type** | GNSS | | | | RNSS | | |
| **Provider** | United States | Russian Federation | European Union | | China | Japan | India |
| **Orbit** | MEO | MEO | MEO | | MEO, IGSO, GEO | IGSO, GEO | IGSO, GEO |
| **Nominal number of satellites** | 24 | 24 | 30 | | 27, 3, 5 | 3, 1 | 4, 3 |
| **Constellation type** | 6 planes | 3 planes Walker (24/3/1) | 3 planes Walker (24/3/1) + 6 in-orbit-spares + 1 plane for satellites in eccentric orbits | | 3, 3, 1 Walker (24/3/1) | 1, 3 IGSOs | 1, 1 IGSOs |
| **Inclination [°]** | 55 | 64.8 | 56 | 50 | 55 | 43 | 29 |
| **Altitude [km]** | 20 200 | 19 132 | 23 225 | 16 819 – 25 395 | 21 528 35 786 | 32 000 – 40 000 | 35 786 |
| **Rev. period** | 11h 58m | 11h 16m | 14h 05m | 12h 56m | 12h53m 23h56m | 23h56m (IGSO) | 23h56m (IGSO) |
| **Services** | SPS, PPS | SPS, PPS | OS, OSNMA, HAS, PRS, SAR, CAS | | OS, AS, WADS, SMS | GCS, GAS, PRS, EWS, MCS | SPS, RS |
| **Initial service** | Dec 1993 | Sep 1993 | 2016/2017 | | Dec 2012 | 2018 | 2016 |
| **Fully operational** | 1995 | 2011 | 2020 | | 2020 | 2018 | 2018 |
| **Coverage** | Global | Global | Global | | Global | East Asia Oceania region | -30° < φ < 50° 30° < λ < 130° |
| **Frequency (MHz)** | L1 1575.42<br>L2 1227.60<br>L5 1176.45 | L1 1602.00<br>L2 1246.00<br>L3 1202.025 | E1 1575.42<br>E5a 1176.45<br>E5b 1207.14<br>E6 1278.75 | | B1 1561.098<br>B2 1207.14<br>B3 1268.52 | L1 1575.42<br>L2 1227.60<br>L5 1176.45<br>E6 1278.75 | L5 1176.45<br>S 2492.028 |

SPS: Standard Positioning Service
PPS: Precise Positioning Service
OS: Open Service
OSNMA: Open Service Navigation Message Authentication
HAS: High Accuracy Service
PRS: Public Regulated Service
SAR: Search and Rescue Service
CAS: Commercial Authentication Service
AS: Authorized Service
WADS: Wide Area Differential Service
SMS: Short Message Service
GCS: GPS Complementary Service
GAS: GPS Augmentation Service
EWS: Early Warning Service
MCS: Message Communications Service
PS: Precision Service
RS: Restricted Service

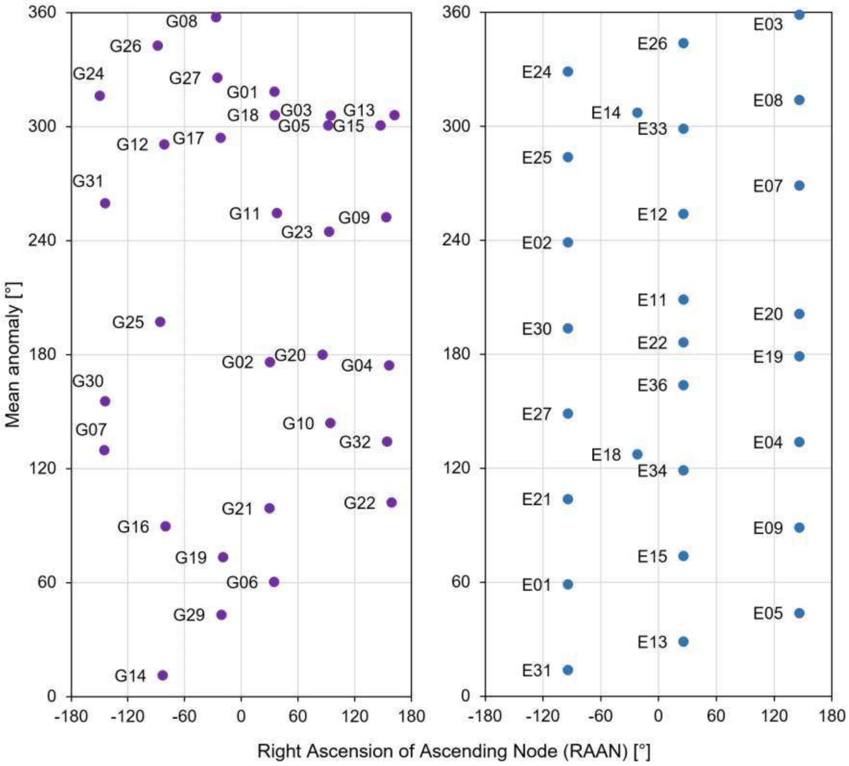


Figure 4.3: Distribution of GPS (violet) and Galileo (blue) satellites as a function of the RAAN (right ascension of the ascending node) and argument of latitude (as of 01.01.2022).

Since observations from GPS and Galileo were used in this work, these two systems will be described in more detail in the following sections (Figure 4.3, Figure 4.4). For further details on these GNSS, as well as other GNSS and RNSS, please refer to Langley et al. (2017) and Hofmann-Wellenhof et al. (2007).

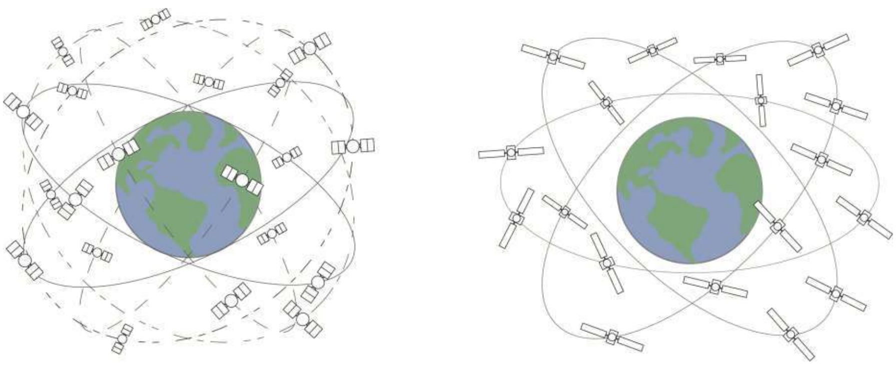

Figure 4.4: The GPS satellite constellation (left) and the Galileo satellite constellation (right).

## 4.1. Global Positioning System (GPS)

A comprehensive definition of GPS is given in 1985 by W. Wooden: "The NAVSTAR Global Positioning System (GPS) is an all-weather, space-based navigation system under development by the Department of Defense (DoD) to satisfy the requirements for the military forces to accurately determine their position, velocity, and time in a common reference system, anywhere on or near the earth on a continuous basis." (Hofmann-Wellenhof et al., 2007). Some features of past, current, and future GPS blocks are summarized in Table 4.2.

Table 4.2: GPS space segment evolution (after Parkinson et al. (2020) and Shi and Wei (2020)).

| | **LEGACY SATELLITES** | | | **MODERNIZED SATELLITES** | | |
|---|---|---|---|---|---|---|
| **Generation** | **BLOCK I** | **BLOCK II/IIA "2$^{nd}$ generation", "Advanced"** | **BLOCK IIR "Replenishment"** | **BLOCK IIR-M "Modernized"** | **BLOCK IIF "Follow-on"** | **GPS III/IIIF "Follow-on"** |
| **No. of operational satellites** | 0 | 0 | 7 | 7 | 12 | 4 |
| **Civil code** | C/A on L1 | C/A on L1 | C/A on L1 | 2$^{nd}$ civil signal L2C added | 3$^{rd}$ civil signal L5 added | 4$^{th}$ civil signal L1C added |
| **Military code** | P(Y) on L1L2 | P(Y) on L1L2 | P(Y) on L1L2 | M code for enhanced jam resistance added | | |
| **Designed lifetime (years)** | 4.5 | 7.5 | 7.5 | 7.5 | 12 | 15 |
| **Launch time** | 1978-1985 | 1990-1997 | 1997-2004 | 2005-2009 | 2010-2016 | 2016-present |
| **Selective availability (SA)** | No SA ability | | | | | No SA ability |
| **Improvement** | | | | | Advanced atomic clocks; Increased accuracy, signal strength and quality | Improved signal reliability, accuracy, and integrity; IIIF: laser prism reflectors |
| | | Last one decommis-sioned in 2019 | | | | |

GPS was established in 1973, and according to the previous definition, it was first intended for military purposes. Free civilian access was offered by the US President to civilian users in 1983, after the incident of the Korean Airlines Flight 007. The first operational satellite was launched in 1989 and, six years later, in 1995, GPS became fully operational. The intentional degradation of GPS signals available to civilian users called Selective Availability (SA), was turned off in 2000 (Hofmann-Wellenhof et al., 2007). The first GPS satellite was successfully launched into orbit in 1978. As of November 21, 2021, a total of 75 GPS satellites were successfully launched, 31 of them being currently operational. The evolution of the GPS constellation resulted over time in characteristic changes among the blocks. Size, weight, transmitted signals and frequencies, cost, and installed satellite clock type are only a few of the improved characteristics (Hegarty, 2017).

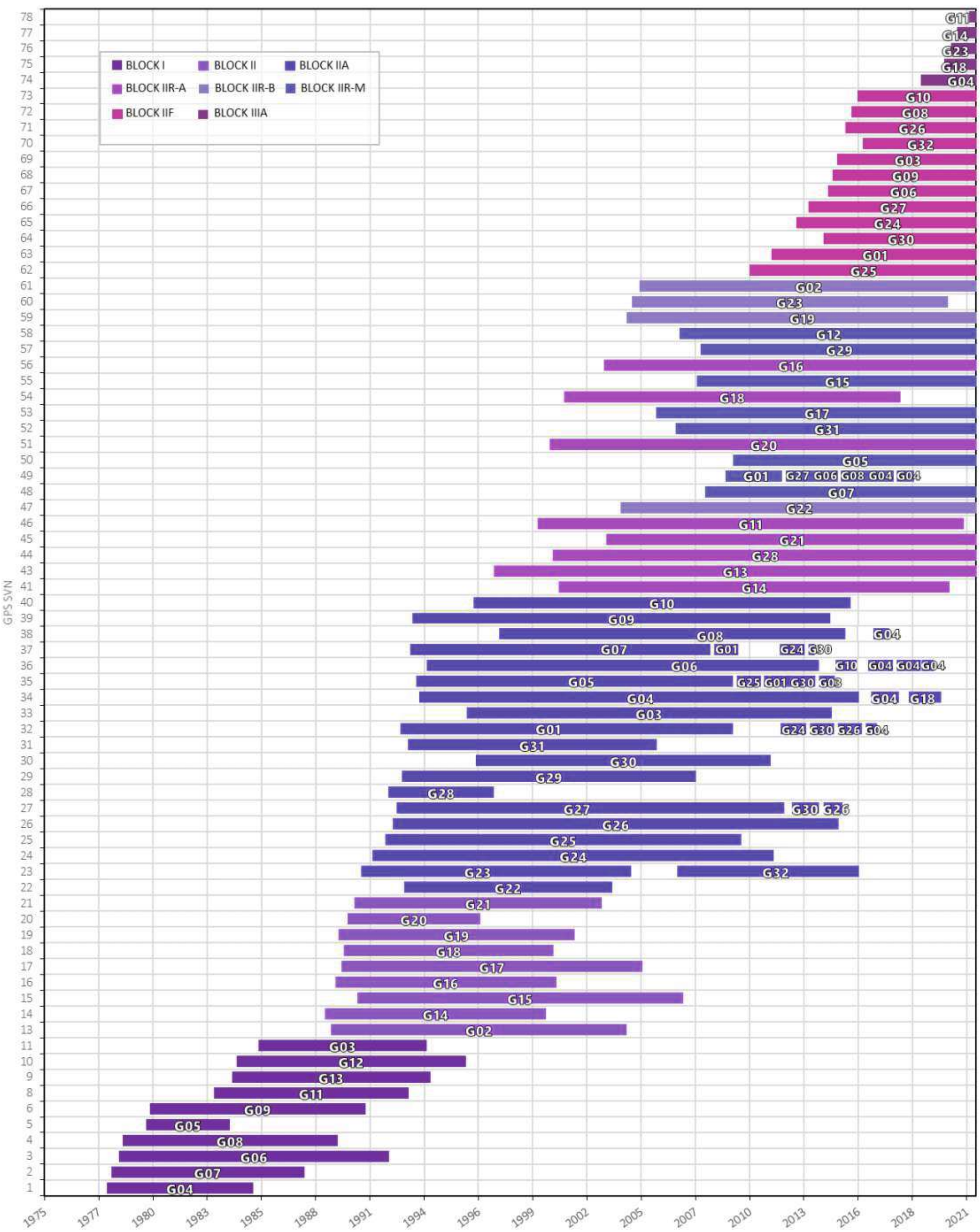


Figure 4.5: The development of the GPS constellation from 1978 to 2021.

As of November 20, 2021, there were a total of 30 operational satellites in the GPS constellation, not considering the decommissioned, on-orbit spares. The evolution of the GPS constellation, including the development of its individual blocks, is illustrated in Figure 4.5.

The nominal GPS constellation contains 24 satellites, distributed on six circular orbits, four satellites per orbital plane, whereas the satellite orbits' inclination is 55° with respect to the Earth's equatorial plane. The satellite orbits have a nominal altitude of about 20 200 km, which provides an orbital period of approximately 11h 58m. This equals a period of one-half a sidereal day, causing the satellite ground track to repeat daily. Due to Earth's non-uniform gravitational field, those repeating ground tracks, despite being convenient for GPS applications, result in resonant forces on each GPS satellite (Hegarty, 2017). The current GPS constellation consists of old and new satellites from different generations.

## 4.2. Galileo

The global navigation satellite system Galileo was developed in collaboration with the European Commission (EC) and the European Space Agency (ESA). Galileo was designed to provide full compatibility and interoperability with the existing GNSS while being independent from them. It is a global system, open for civilian users, offering a high level of service reliability (Hofmann-Wellenhof et al., 2007).

The launch of two test satellites, called GIOVE-A (Galileo In-Orbit Validation Element) and GIOVE-B in 2005 and 2008, respectively, marked the beginning of the development of the Galileo constellation. Both satellites were operational until summer 2012 (Figure 4.6). Today, the space segment of the European GNSS consists of IOV (in-orbit validation) and FOC (full-operational-capability) satellites, nominally 24 (Sośnica et al., 2018). In the following phase, four Galileo IOV satellites, have been launched in 2011 and 2012 (Langley et al., 2017), which is the minimum number of satellites to enable independent positioning and timing solutions (Falcone et al., 2017). One year later, the first successful determination of a ground location using only Galileo observations led to the start of the broadcast of Galileo navigation messages solutions (Falcone et al., 2017).

The success of the IOV campaign was followed by the launch of the next satellite generation, namely the FOC. The first pair of FOC satellites to be launched in 2014 (E14 and E18), unfortunately ended up being placed in the wrong orbits (non-nominal elliptic orbits) due to a malfunction in the carrier rocket (Falcone et al., 2017; Langley et al., 2017). Initially, these satellites were considered not fully operational for the needs of Galileo users. However, in 2015, efforts were made to correct their orbits using onboard sensors. Subsequently, their navigation payloads were activated and tested to validate their technology and performance. As a result, these satellites began broadcasting navigation signals and are now also utilized for clock technology validation (Falcone et al., 2017). The distinctive orbital characteristics of these satellites have also provided advantages for scientific research, such as testing relativistic theories (Rodríguez et al., 2020). Nevertheless, as stated in the General Notice by Euspa (European Union Agency for the Space Programme), satellites E14 and E18 have been declared unavailable starting with February, 18$^{th}$, 2021 (Euspa, 2021b).

Until December 2021, 22 more FOC satellites have been successfully launched into orbit (Figure 4.6). Therefore, a total of 28 satellites (4 IOV/24 FOC) have been launched so far.

As of now (April 2023), the last pair of satellites was brought into orbit on December 5, 2021.

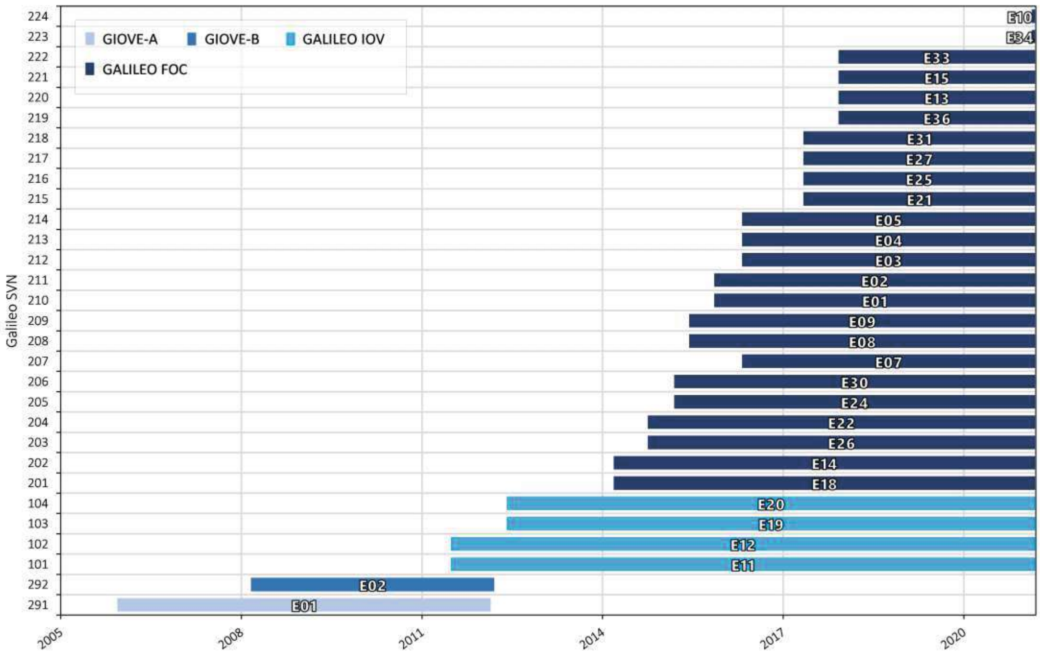


Figure 4.6: The development of the Galileo constellation from 2005 to 2021.

As mentioned previously, the nominal constellation of Galileo consists of 24 satellites. They are distributed among three orbital planes at an altitude of 23 220 km and with an inclination of 56° with respect to the Earth's equatorial plane (similar to the inclination of GPS, which equals 55°). Their revolution period is 14h 04m 42s (Table 4.1). Therefore, the satellites' ground track is repeated after 10 sidereal days or 17 orbital revolutions, which results in a weak resonance with the Earth rotation (Sośnica et al., 2018).

Galileo satellites use the CDMA (Code Division Multiple Access) systems to broadcast carrier signals on the following frequency bands: E1, E5a, E5b, and E6. Six types of services are currently provided via these signals: the Open Service (OS), the Open Service Navigation Message Authentication (OSNMA), the High Accuracy Service (HAS), the Public Regulated Service (PRS), the Search and Rescue Service (SAR), and the Commercial Authentication Service (CAS). The OS is free of charge and provides positioning and timing services. The OSNMA is also a free access service, offering authenticated data about the OS to users. With this complementing information, users can be sure about the authenticity of the navigation message transmitted by the Galileo satellite system. HAS provides high-accuracy PPP corrections, computed for Galileo E1/E5a/E5b/E6; E5 AltBOC and GPS L1/L5; L2C. Free-of-charge corrections are accessible through the Galileo E6b signal and via the internet (Euspa, 2023). PRS is an encrypted navigation service intended for governmental authorized users only. It is utilized exclusively for sensitive applications, where high continuity is required (Euspa, 2021a). SAR is Europe's contribution to COSPAS-SARSAT (Search and Rescue Satellite-Aided Tracking). The OS is further complemented by the CAS, which provides a controlled access and authentication function for users (Shi and Wei, 2020; Langley et al., 2017; Euspa, 2022).

The Galileo E1 and E5a are coordinated with the GPS L1 and L5 signals. Given that both systems are based on equivalent modulation foundations, it is expected to achieve an improved positioning performance when using a combination of these two independent radio navigation systems (Falcone et al., 2017).

The Galileo ground segment consists of two main parts, the GCS (Ground Control Segment) and the GMS (Ground Mission Segment). The GCS provides global coverage thanks to a worldwide network of S-band telemetry, tracking, and command (TT&C) stations hosted on Galileo remote sites. It is in charge of all activities encompassing the command and control of the satellite constellation. The GMS produces the navigation message by using previously measured and monitored Galileo navigation signals, which is done by L-band Galileo sensor stations (GSS). The navigation message is then sent to the satellites via C-band up-link stations (ULS) to be broadcast later to the users via L-band signals. Additional external interfaces of the Galileo ground segment are installed in order to connect to providers of Galileo services. These interfaces are managed by the European GNSS Agency (GSA) (Falcone et al., 2017; Rodríguez et al., 2020). For more information on the Galileo ground segment, as well as its corresponding centers and external interfaces, refer to Falcone et al., 2017 and Rodríguez et al., 2020.

## 4.3. Observation equations for GNSS processing

Among the basic GNSS observations, code and carrier phase measurements between satellites and receivers are the fundamental observables when it comes to GNSS data processing. GNSS satellites are broadcasting radio wave signals on several wavelengths. These signals contain the navigation code (comprising information relevant to the satellite status as satellite clock, orbit, health status, etc.), and the broadcast message, modulated on a carrier wave (Zajdel, 2021).

GNSS receivers measure the travel time of a signal emitted from a navigation satellite to a ground station by searching for the maximum correlation between the incoming code sequence and the code sequence generated by the receiver. This measured time shift multiplied by the speed of light $c$ gives the pseudorange from code measurements (Magnet, 2019; Seeber, 2003; Zajdel, 2021):

$$p_r^s = c\left(t_r(r) - t^s(s)\right) \tag{4.1}$$

where:

$p_r^s$ is the pseudorange (code observable) between satellite $s$ and receiver $r$ in [m],

$c$ is the speed of light in vacuum in [m/s],
$t_r(r)$ is the time at which the receiver registered the signal, given in the receiver's time frame in [s],
$t^s(s)$ is the time at which the signal was transmitted by the satellite, given in the satellite's time frame in [s].

For the sake of bringing both clock readings under the umbrella of one common time frame, Equation 4.1 can be written as follows (Seeber, 2003):

$$p_r^s = c[(t_r + dt_r) - (t^s + dt^s)] = c(\Delta t + \Delta dt) \tag{4.2}$$

where:
$dt_r$ is the time-dependent receiver clock bias, w.r.t. the respective GNSS time,
$dt^s$ is the time-dependent satellite clock bias, w.r.t. the respective GNSS time,
$c\Delta t$ is the product of the speed of light and code travel time referring to the distance between satellite at moment $t^s$ and receiver at moment $t_r$.
$t_r, t^s$ and $\Delta t = t_r - t^s$ refer to the same time frame.

The product $c\Delta t$ does not exactly equal the geometric distance between satellite and receiver. It is loaded with errors of different types and origins, ranging from atmospheric effects, over instrumental sources, up to relativistic and multipath effects. For precise geodetic applications, these effects and error sources must be considered in the observation equation of GNSS measurements. Therefore, when taking into account the most prominent error sources in the propagation of GNSS signals, the observation equation of code measurements can be expressed as follows (Glaner, 2022; Hauschild, 2017a):

$$p_r^s(t) = \rho_r^s(t) + c\,(dt_r(t) - dt^s(t)) + T_r^s(t) + I_r^s(t) + B_r - B^s + \epsilon_r^s(t) \tag{4.3}$$

where:
$\rho_r^s(t)$ is the geometric distance between satellite $s$ and receiver $r (= c\Delta t)$,
$dt_r(t), dt^s(t)$ are the receiver and satellite clock error w.r.t. the GNSS time system,
$T_r^s(t)$ is the tropospheric signal delay,
$I_r^s(t)$ is the frequency-dependent ionospheric signal delay,
$B_r, B^s$ are the receiver and the satellite's code hardware delay converted to range,
$\epsilon_r^s(t)$ are the remaining unmodeled errors, observation noise, and multipath.

In the case of carrier phase measurements, the GNSS receiver measures the difference between the received Doppler-shifted carrier wave and the reference frequency generated by the receiver. The resulting difference comprises a fractional part and an integrated integer number of phase cycles. The initial number of integer phase cycles between satellite and receiver carriers is unknown. It is defined as phase ambiguity $N$ (Meindl, 2011). According to this statement, the simplified observation equation for carrier phase measurements can be written as follows (Hofmann-Wellenhof et al., 2007):

$$L_r^s(t) = L_r(t) - L^s(t) \tag{4.4}$$

with:

$$L_r(t) = f_r t - L_{0r} \tag{4.5}$$

$$L^s(t) = f^s t - f^s \frac{\rho}{c} - L_0^s \tag{4.6}$$

where:

$L_r(t)$ is the phase of the receiver-generated signal with frequency $f_r$ [cycles],
$L^s(t)$ is the phase of the received signal with frequency $f^s$ [cycles],
$\rho$ is the range between satellite and receiver,
$c$ is the speed of light,
$t$ is the time passed since the initial epoch $t_0$.

The initial phases $L_{0r}$ and $L_0^s$ at epoch $t_0$ can be written as:

$$\begin{aligned} L_{0r} &= -f_r dt_r \\ L_0^s &= -f^s dt^s \end{aligned} \tag{4.7}$$

where:

$dt_r$ is the clock bias of the receiver,
$dt^s$ clock bias of the satellite.

Under the assumption that the phase ambiguity at epoch $t_0$ equals $N$, the pseudorange from phase measurements can be given by the following equation (Glaner, 2022; Hauschild, 2017a):

$$L_r^s(t) = \rho_r^s(t) + c\,(dt_r(t) - dt^s(t)) + T_r^s(t) - I_r^s(t) + \lambda(N_r^s + b_r - b^s) + \epsilon_r^s(t) \tag{4.8}$$

where:

$L_r^s(t)$ is the carrier phase observable [m],
$\zeta_r^s(t)$ are the phase center offsets of the receiver and satellite antennas (another symbol was used compared to the code pseudorange observation to highlight the difference of the correction terms for both observables),
$\lambda$ is the wavelength [m],
$N_r^s$ is the unknown integer number of cycles,
$b_r, b^s$ are the phase biases originating from hardware delays from receiver and satellite,

$\epsilon_r^s(t)$ is the residual error term containing the combined effect of the receiver carrier--phase tracking noise and multipath.

The impact of the atmosphere on GNSS signals, as demonstrated in Equations 4.3 and 4.8, can be divided into two components: the tropospheric signal delay, $T_r^s(t)$, and the frequency-dependent ionospheric signal delay, $I_r^s(t)$. The tropospheric signal delay, $T_r^s(t)$, affects both GNSS observation equations with the same sign. On the other hand, the ionospheric delay, $I_r^s(t)$, appears in the GNSS equations for code and phase observations with opposite signs. Consequently, the code observations experience a delay as they traverse the ionosphere from the satellite to the receiver. In contrast, the phase observations encounter an advancement or acceleration as they pass through the ionosphere (Glaner, 2022).

The basic observation Equations 4.3 and 4.8 are known as zero-differences (ZD). In GNSS analyses, however, it is a common practice to form differences between observation equations in order to eliminate common observation errors (for example clock errors and biases). There are three types of observation differences used in GNSS analysis (Zajdel, 2021):

- single differences (SDs),
- double differences (DDs),
- triple differences (TDs).

Single differences, SDs, can be formed between two receivers $(r_1, r_2)$, two satellites $(s_1, s_2)$, or two observation epochs $(t_1, t_2)$. The difference between two SDs is referred to as double difference, DD, and is usually formed at one observation epoch. Finally, the difference between two DDs at different observation epochs is called triple difference, TD (Zajdel, 2021). For a more detailed explanation of observation differences, please refer to Seeber (2003).

### 4.3.1. Linear combinations

Within Chapter 4, the reader was introduced to the principles of GNSS including the most important characteristics of each global/regional navigation satellite system. As shown in Table 4.1, all satellite systems are operating on more than one frequency. In other words, the navigation satellites transmit radio waves on different wavelengths to receivers on Earth. This means that there are as many observation equations ((4.3) and (4.8)) as the number of wavelengths on which the observations are broadcast for each pair satellite-receiver. Multiple observation equations for each satellite-receiver pair are allowing us to form linear combinations. This is beneficial in various aspects of GNSS applications. Linear combinations of frequencies are widely used to either eliminate or reduce the effect of different error sources or to extract these errors for modeling and research purposes (Seeber, 2003). However, it should be noted that a certain increase in noise level must be expected (Magnet, 2019).

When considering GNSS solutions on a global scale, the most commonly used linear combinations are the L3 ionosphere-free linear combination and the L4 geometry-free linear combination (Zajdel, 2021). The basic concept of a linear combination for two carrier-phase observations is given by:

$$L_i = \alpha_{i1}L_1 + \alpha_{i2}L_2 = \alpha_{i1}f_1t + \alpha_{i2}f_2t = f\,t \tag{4.9}$$

where:

$\alpha_{i1}, \alpha_{i2}$ are coefficients,
$f_1, f_2$ are carrier wave frequencies,
$f$ is the frequency of the combined carrier wave signal $(= \kappa_1 f_1 + \kappa_2 f_2)$.

For the wavelength of the combined signal applies:

$$\lambda = \frac{c}{f} = \frac{c}{\kappa_1\lambda_1 + \kappa_2\lambda_2} \tag{4.10}$$

where $\lambda_1, \lambda_2$ are the wavelengths of the carrier waves *L1* and *L2*. An overview of commonly used linear combinations applying GPS and Galileo observations is shown in Table 4.3.

**4.3.1.1. Ionosphere-free linear combination** The $L_{IF}$, often referred to as $L_3$, is a well-known and widely used linear combination. It eliminates the first-order ionospheric refraction term in the Equations (4.3) and (4.8). The corresponding equation is formed as follows (Todorova, 2008):

$$L_3 = \alpha_{31}L_1 + \alpha_{32}L_2 \tag{4.11}$$

The coefficients $\alpha_{3j}$ $(j = 1, 2)$ are:

$$\begin{aligned} \alpha_{31} &= \frac{f_1^2}{f_1^2 - f_2^2} \\ \alpha_{32} &= -\frac{f_2^2}{f_1^2 - f_2^2} \end{aligned} \tag{4.12}$$

When introducing the coefficients $\alpha_{31}, \alpha_{32}$ in Equation (4.11), the ionosphere-free linear combination takes the following form:

$$L_3 = \frac{f_1^2}{f_1^2 - f_2^2} L1 - \frac{f_2^2}{f_1^2 - f_2^2} L_2 \tag{4.13}$$

By multiplying the carrier waves with the coefficients $\alpha_{31}, \alpha_{32}$ the first-order ionospheric term vanishes. The downside of this linear combination is that the integer nature of ambiguities gets lost and the observation noise increases considerably compared to the basic observables *L1* and *L2*. In Chapter 5.1, the ionosphere-free linear combination was used for the estimation of ERP time series.

Table 4.3: Frequently used linear combinations of GNSS observations (GPS and Galileo) (after Teunissen and Montenbruck (2017), Glaner (2017), and Sanz Subirana et al. (2011)). GPS specific in grey; Galileo specific in blue.

| Name | $\lambda$ | Signals | | $\kappa_1$ | $\kappa_2$ | $\alpha_1$ | $\alpha_2$ | Purpose |
|---|---|---|---|---|---|---|---|---|
| **GPS** ($f_0 = 10.230\ MHz$) | | | | | | | | |
| $L_1$ ($f_1 = 1575.42\ MHz$) | $\approx$ 190 mm | $L_1$ | | 1 | | 1 | | GPS L1 signal |
| $L_2$ ($f_2 = 1227.60\ MHz$) | $\approx$ 244 mm | $L_2$ | | 1 | | 1 | | GPS L2 signal |
| $L_5$ ($f_5 = 1176.45\ MHz$) | $\approx$ 255 mm | $L_5$ | | 1 | | 1 | | GPS L5 signal |
| **Galileo** ($f_0 = 5.115\ MHz$) | | | | | | | | |
| $E_1$ ($f_1 = 1575.42\ MHz$) | $\approx$ 190 mm | $E_1$ | | 1 | | 1 | | Galileo E1 signal (aligned with GPS L1 C/A, L1C) (Falcone et al., 2017) |
| $E_{5b}$ ($f_{5b} = 1207.14\ MHz$) | $\approx$ 248 mm | $E_{5b}$ | | 1 | | 1 | | Galileo $E_{5b}$ signal |
| $E_{5a}$ ($f_{5a} = 1176.45\ MHz$) | $\approx$ 255 mm | $E_{5a}$ | | 1 | | 1 | | Galileo $E_{5a}$ signal (aligned with GPS L5) (Falcone et al., 2017) |
| Narrow-Lane $L_{NL}$ ($L_{53}$) | $\approx$ 107 mm | $L_1$ | $L_2$ | 1 | 1 | $\frac{f_1}{f_1+f_2}$ | $\frac{f_2}{f_1+f_2}$ | used for ambiguity resolution and parameter estimation |
| | $\approx$ 108 mm | $E_1$ | $E_{5b}$ | | | | | |
| Medium-Lane $L_{ML}$ | $\approx$ 751 mm | $L_1$ | $L_2$ | 1 | -1 | $\frac{f_1}{f_1-f_5}$ | $-\frac{f_5}{f_1-f_5}$ | used for ambiguity resolution |
| | $\approx$ 751 mm | $E_1$ | $E_{5a}$ | | | | | |
| Wide-Lane $L_{WL}$ ($L_5$) | $\approx$ 862 mm | $L_1$ | $L_2$ | 1 | -1 | $\frac{f_1}{f_1-f_2}$ | $-\frac{f_2}{f_1-f_2}$ | used for ambiguity resolution on single- or double-differences |
| | $\approx$ 814 mm | $E_1$ | $E_{5b}$ | | | | | |
| Extra Wide-Lane $L_{EWL}$ | $\approx$ 5861 mm | $L_2$ | $L_5$ | 1 | -1 | $\frac{f_2}{f_2-f_5}$ | $-\frac{f_5}{f_2-f_5}$ | used for ambiguity resolution |
| | $\approx$ 9768 mm | $E_{5b}$ | $E_{5a}$ | | | | | |
| Ionosphere-free $L_{IF}$ ($L_3$) | $\approx$ 107 mm | $L_1$ | $L_2$ | | | $\frac{f_1^2}{f_1^2-f_2^2}$ | $\frac{f_2^2}{f_1^2-f_2^2}$ | eliminates the ionospheric error, used for parameter estimation on long baselines with extended observation spans |
| | $\approx$ 108 mm | $E_1$ | $E_{5b}$ | | | | | |
| Geometry-free $L_{GF}$ ($L_4$) | $\infty$ | $L_1$ | $L_2$ | | | 1 | -1 | eliminates satellite orbit, station coordinate and clock errors; used for the estimation of global and regional ionosphere models |
| | $\infty$ | $E_1$ | $E_{5b}$ | | | | | |

**4.3.1.2. Geometry-free linear combination** The $L_{GF}$ eliminates errors related to satellite orbits, geometric distance, troposphere, as well as satellite and receiver clocks. Consequently, the geometry-free combination eliminates all geometric terms from the observation equations, isolating the frequency-dependent components. The remaining terms primarily consist of the ionospheric delay, the integer ambiguity at different wavelengths, and hardware delays specific to the satellite and receiver (Glaner, 2017). The geometry-free linear combination is particularly useful for estimating regional and global ionospheric models. For code and phase measurements, the geometry-free linear combination is formed as follows (Glaner, 2022):

$$P_4 = P_1 - P_2 \tag{4.14}$$

$$L_4 = L_1 - L_2 \tag{4.15}$$

In Chapter 5.2, the geometry-free linear combination was utilized to generate IONEX maps, which provide Vertical Total Electron Content (VTEC) values over a designated region grid. These maps were employed as part of the regional ionosphere modeling process. More on the geometry-free linear combination, used to generate the regional ionospheric model provided in this work can be found in section 5.2.1.

**4.3.1.3. Wide-lane linear combination** This linear combination is built by forming a difference between phase observations. It is beneficial for solving for ambiguities given the fact that the resulting wavelength is significantly longer compared to the initial wavelengths of the carrier waves (862 mm for GPS $L_1$, $L_2$ and 814 mm for Galileo $E_1$, $E_{5B}$). The longer wavelength narrows down the search space. Before the introduction of the third frequency, the combination of GPS $L_1$ and $L_2$ frequency was the only linear combination that offered a longer resulting wavelength compared to the initial wavelength of the two carrier waves. Therefore, this combination was named the wide-lane combination. However, more available frequencies have opened new possibilities to form linear combinations offering two new forms of wide-lane combinations. They were called according to their resulting wavelength and relative to the first possible wide-lane combination. This means that the combination with the largest wavelength is the extra-wide-lane combination ($L_{EWL}$), while the linear combination with the shortest wavelength among the wide-lane group was called medium lane combination ($L_{ML}$). More on the input frequencies and resulting wavelengths can be found in Table 4.3 (Glaner, 2017). The equation of the wide-lane linear combination reads:

$$L_5 = \frac{f_1}{f_1 - f_2} L_1 - \frac{f_2}{f_1 - f_2} L_2 \tag{4.16}$$

with the wide-lane wavelength $\lambda_5$:

$$\lambda_5 = \frac{c}{f_1 - f_2} \tag{4.17}$$

where:

$$\alpha_1 = \frac{f_1}{f_1 - f_2}, \quad \alpha_2 = -\frac{f_2}{f_1 - f_2} \tag{4.18}$$

**4.3.1.4. Narrow-lane linear combination** The $L_{NL}$ is created by summing up two frequencies, leading to a resulting wavelength shorter than the wavelengths of the two original carrier waves (Glaner, 2017). The narrow-lane has the lowest noise level of all linear combinations. Therefore, it offers the best results. On the other hand, the ambiguity resolution is quite challenging, thus this combination is usually used for shorter distances between stations (Seeber, 2003). The narrow-lane combination is formed as (Hauschild, 2017b):

$$L_{NL} = \frac{f_1}{f_1 + f_2} L1 + \frac{f_2}{f_1 + f_2} L_2 \tag{4.19}$$

with the associated narrow-lane wavelength:

$$\lambda_{NL} = \frac{c}{f_1 + f_2} \tag{4.20}$$

As noted in Hauschild (2017b), the narrow-lane linear combination ($L_{NL}$) can reduce the noise in carrier-phase measurements by a factor of $\approx 0.71$ compared to the original carrier-phase measurement. This factor was derived from the analysis of GPS frequencies L1 and L2. It is important to note that this factor is approximately the same for all current GNSS signal combinations of observations in both the lower (1100-1300 MHz) and upper L-band (near 1600 MHz). For more information see Hauschild (2017b), page 587.

**4.3.1.5. Melbourne-Wübbena linear combination** This linear combination is built by using two frequencies of code and phase observations (Glaner, 2017). It involves combining wide-lane carrier-phase observations and narrow-lane pseudorange observations. Given that the ambiguity parameter remains in this combination, the Melbourne-Wübbena linear combination allows for the detection of cycle slips and the resolution of wide-lane ambiguities (Magnet, 2019). This linear combination can be formed between observations on different frequencies. When using in particular GPS L1 and L2, it is expressed by the following equation (Glaner, 2017; Magnet, 2019):

$$L_{MW} = L_{WL} - P_{NL} = \frac{f_1 L_1 - f_2 L_2}{f_1 - f_2} - \frac{f_1 P_1 + f_2 P_2}{f_1 + f_2} \quad . \tag{4.21}$$

where $L_{WL}$ represents the wide-lane carrier-phase observation, $P_{NL}$ denotes the narrow-lane pseudorange observation, $f_1$ and $f_2$ are the frequencies associated with the observations on L1 and L2, respectively. As shown in Equation 4.21, the MW linear combination is actually the combination of the geometry-free, $L_{GF}$, and the ionosphere-free, $L_{IF}$, linear combination of code and phase measurements (Glaner, 2022).

# 5. Parameter estimation

In order to obtain the selected set of GNSS parameters, i.e. the ERP parameters and regional ionospheric maps, two different automated processes have been set up. In the following sections, processing details for both solutions are described in detail.

## 5.1. Earth rotation parameters

The processing scheme for the determination of ERPs has been designed to gather and process raw observation data from GPS and Galileo, collected from a global network of permanent multi-GNSS stations (Figure 5.1). All steps of the processing are performed using the Bernese GNSS Software version 5.2 (BSW) (Dach et al., 2015). A summary of the key characteristics of the processing is given in Table 5.1. 1-day and 3-day solutions based on a GPS-only and a combined GPS+Galileo solution were performed and analyzed for the time span 2018-2019. Given the objective of this research to assess the advantages of incorporating Galileo observations into the solution, it was reasoned that including observations predating 2017 would be impractical. The number of operational Galileo satellites before 2017 was insufficient, falling below 18 before this year. Consequently, Galileo was not fully operational during this period. The selection of stations for the global GNSS network was driven by the aim to obtain Galileo observations. This is why only multi-GNSS stations were chosen, from which some already started receiving Galileo signals before 2018 (the majority of the stations) and others incorporated this GNSS later, during 2018 or even 2019. Although the latter group may not have contributed to the observations for the entire duration (providing solely GPS observations), they were still included in the global network due to their locations, enabling the improvement of the station network geometry. Stations that belong to the IGS14 core network (Rebischung and Schmid, 2016) and are part of the ITRF2014.FIX[32] station selection file (Bernese–formatted file of reference sites prepared by the Astronomical Institute of the University of Bern - AIUB) are selected for the datum definition. The station distribution is not homogeneous, as can be seen from Figure 5.1. The reason behind that lies primarily in the fact that two main conditions had to be met in or-

[32]Data available at the: http://ftp.aiub.unibe.ch/BSWUSER52/STA/

der to include a station in the global solution. First, the station, as mentioned before, had to track multi-GNSS signals, in our case, GPS and Galileo observations, and, second, the station had to be listed in the coordinate solution file for ITRF2014 computed by CODE. When this condition is met, it means that there is input on the corresponding station velocity, as well as the station information containing data about the station receiver and antenna types[33]

The final station distribution is presented in Figure 5.1.

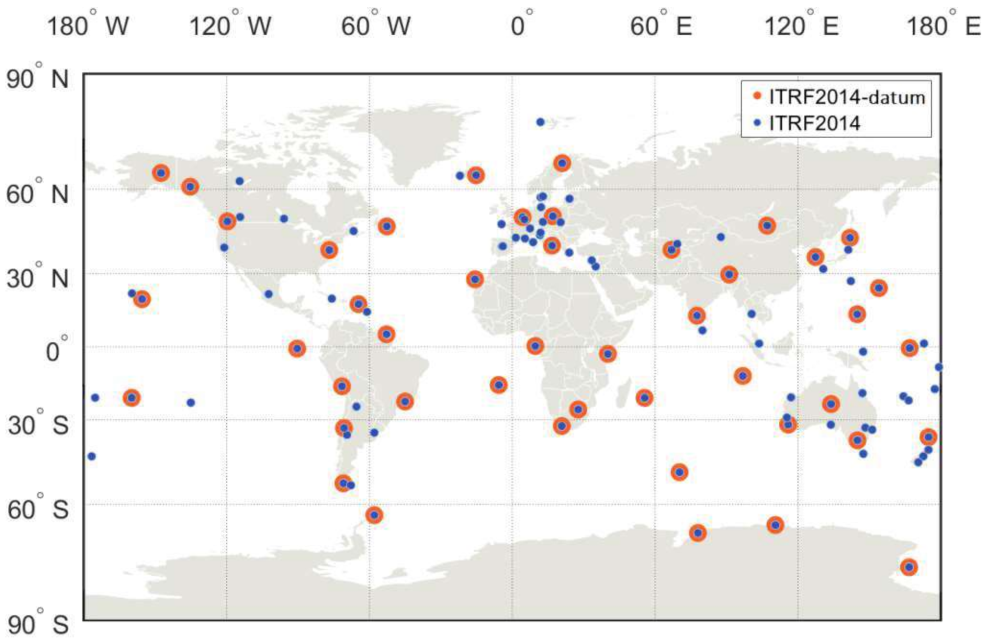


Figure 5.1: Global GNSS network distribution (blue marker denotes all chosen stations and the orange marker denotes the stations used for the datum definition).

The set of ERP parameters including offsets and rates is calculated with a 1-hour high temporal resolution, resulting in 25 estimates for each parameter per day. To estimate the required sub-daily ERP results, it is requested to ensure continuity at boundaries between each daily solution (between the end of the previous and the beginning of the next solution). This was achieved by creating overlapped 3-day arc solutions based on three 1-day solutions. In fact, 1-day normal equation files (NEQs) of three consecutive days were stacked, namely the day before, the day of interest, and the day after, making the middle day of a 3-day solution overlap with the first day of the subsequent solution, as well as with the last day of the preceding solution. In the analysis only the ERP set of the middle day of a 3-day solution is extracted. Although the set of ERP parameters being estimated in this work comprises polar motion and UT1-UTC, satellite techniques and with this GNSS, are only able to determine the absolute values for polar motion, namely the x and y pole coordinates, while UT1-UTC is generated from the integration of its first derivative (LOD).

[33]the coordinate (ITRF2014_R.CRD), velocity (ITRF2014_R.VEL) and station information file (IGS_FULL.STA) are available via the same link as the ITRF2014.FIX (reference sites) file: http://ftp.aiub.unibe.ch/BSWUSER52/STA/.

Table 5.1: Main characteristics of the processing strategy.

| Processing characteristic | Applied processing strategy |
|---|---|
| **Software** | Bernese GNSS Software version 5.2 (BSW) (Dach et al., 2015) |
| **Processing period** | Jan 2018 – Dec 2019 (DoY 02 2018 – 364 2019) |
| **Station Network** | 112 stations |
| **Processing scheme** | Double-difference network processing using phase and code observations (ionosphere-free linear combination) |
| **Constellation** | GPS and GPS+Galileo |
| **Signals** | GPS (L1+L2), Galileo (E1+E5a) |
| **Cut-off angle** | 5 degree |
| **Ambiguity resolution** | QIF ambiguity resolution for baselines < 2000 km, Melbourne-Wübbena for baselines 2000 - 6000 km |
| **Solution type** | 1-day/3-day solution (1h time resolution) |
| **Reference frame** | ITRF2014 (Altamimi et al., 2016) |
| **Stations for datum definition** | NNR applied on 45 stations chosen from the IGS14 core stations (Rebischung and Schmid, 2016) and from the ITRF2014.FIX station list (AIUB FTP Server[34]) |
| **Absolute Antenna Model** | GPS, Galileo: phase center variations (PCV) and phase center offsets (PCO) from IGS14 (Rebischung and Schmid, 2016) |
| **Troposphere** | VMF1 grid (J. Böhm et al., 2006) |
| **Troposphere gradients** | Chen-Herring model (G. Chen and Herring, 1997) |
| **Earth's Gravity** | EGM2008_SMALL (Pavlis et al., 2012) |
| **Planetary Ephemerides** | DE405 (Standish Jr, 1990) |
| **A priori solar radiation pressure** | C0601001 (Code Model COD9801, Springer et al., 1999) |
| **Sub-daily Pole model** | IERS2010XY (based on Ray et al., 1994) |
| **Nutation model** | IAU2000R06 |
| **Solid Earth Tide Model** | TIDE2000 (IERS2000) (Petit and Luzum, 2010) |
| **Apriori Earth orientation parameters** | IERS-14-C04 (Bizouard et al., 2019) |
| **Ocean Tide Model** | FES2004 (Lyard et al., 2006) |

Now, why is GNSS limited in this sense? The answer lies in the correlation between UT1-UTC and the orbital elements of the GNSS satellites (for a detailed explanation of the mathematical correlation between UT1-UTC and the orbital elements, please refer to Rothacher et al., 1999). The singularity arising from this correlation can be fixed by constraining the first UT1-UTC value of the 3-day arc to the corresponding apriori value from the reference IERS-C04-14 time series. After constraining the first value, the rate of change of UT1-UTC is freely estimated by GNSS, meaning that all results related to the variation of UT1-UTC are based only on the corresponding rates (Rothacher et al., 2001). The reference time series IERS-C04-14 is obtained from Very Long Baseline Interferometry (VLBI) (Nothnagel et al., 2017). Figure 5.4 illustrates the processing chain where the main steps of the ERP estimation are listed and briefly described. In the following section, every step will be discussed in detail.

[34]Available at: http://ftp.aiub.unibe.ch

### 5.1.1. Processing steps

Automated processing is set up for the assembled global network of 112 GNSS ground stations. The estimation is based on a double-difference solution of phase and smoothed code observations, which is tied to the reference frame ITRF2014 by means of a No-Net-Rotation (NNR) condition. This condition was applied to 45 stations.

***Input***

First, all required input data is downloaded into corresponding data directories. Satellite orbit and pole files are retrieved from the ESOC/ESA website:

http://navigation-office.esa.int/products/gnss-products/wwww/[35]

The following file naming convention is assigned to the pole and orbit files respectively:

ESA0MGNFIN_yyyyddd0000_01D_01D_ERP.ERP.gz

ESA0MGNFIN_yyyyddd0000_01D_05M_ORB.SP3.gz[36]

Ground station observation data are obtained via the CDDIS[37] server:

https://cddis.nasa.gov/archive/gnss/data/daily/yyyy/ddd/yyd[38].

All 112 ground stations building the global network for this processing are currently offering multi-GNSS observations (as of 31.10.2022) in RINEX V3 format. In this case, the term multi-GNSS is referring first and foremost to data containing Galileo aside from GPS observations. Not all stations of this network were tracking Galileo satellites throughout the whole processing period given that this GNSS was yet on the way to reaching its nominal constellation. That implies that the amount of Galileo observations increase over time in the processing as new satellites have been launched into space (Figure 4.6), and since more and more receivers are being able to track these satellites.

The file naming of RINEX V3 observation data looks like this:

XXXXMRCCC_K_YYYYDDDHHMM_01D_30S_tt.FFF.gz[39]

The clock files are produced within the processing by extracting the satellite clock information from the RINEX files. The satellite and station DCB[40] file P1C1 is downloaded from the CODE website:

http://ftp.aiub.unibe.ch/CODE/yyyy/

[35] wwww: GPS week

[36] ESA: European Space Agency; MGN: multi GNSS; FIN: final; yyyy: 4-digit year; ddd: 3-digit day of year; 01D and 05m: parameter resolution 1 day and 5 minutes respectively; ORB: orbit; SP3: standard product format 3; gz: compressed file

[37] CDDIS: Crustal Dynamics Data Information System

[38] yy: 2-digit year

[39] XXXX: 4-character IGS station name; M:monument or marker number (0-9); R: receiver number (0-9); CCC: ISO country code; K: Data source (R, S or U); YYYY: 4-digit year; DDD: 3-digit day of year; HH: 2-digit hour; MM:2-digit minute; 01D: daily file; 30s: 30 s data sampling; tt: type of data (in this case MO: Mixed Observation data; FFF: File format (in this case rnx: rinex); gz: compressed file. For more information, please visit the CDDIS site: https://cddis.nasa.gov/Data_and_Derived_Products/GNSS/daily_30second_data.html/.

[40] DCB: Differential Code Bias

As for the troposphere, VMF1[41] files from the Vienna University of Technology, Department of Geodesy and Geoinformation are downloaded:

https://vmf.geo.tuwien.ac.at/trop_products/GRID/2.5x2/VMF1/VMF1_OP/yyyy/,

while the global ionospheric maps are downloaded from CODE via the same website as for the DCB files.

***Data preparation***

After all essential input files have been stored in associate data directories, the processing continues with preparing the data files for the pre-processing steps. At first, the a priori coordinates of the station observation files are propagated from the reference epoch $t_0 =$ 2010.0 to the epoch of the observation file $t$, creating a corresponding a priori file of station coordinates. In this case, the epochs cover the timespan Jan 2018 – Dec 2019. The following formula describes the epoch propagation process in a simple way:

$$X_t = X_0 + v_x \cdot (t - t_0) \tag{5.1}$$

where:

| | |
|---|---|
| $X_t$ | is the geocentric station coordinate of the processed epoch (or epoch of observation file) in the respective terrestrial frame (in this case the ITRF2014) |
| $X_0$ | is the geocentric station coordinate of the reference epoch in the same reference frame (i.e. ITRF2014) |
| $v_x$ | is the station velocity in m/yr |
| $t$ | is the processed epoch expressed in decimal years and |
| $t_0$ | is the reference epoch expressed in decimal years. |

The pole and orbit files are then converted into a Bernese-supported format. The nutation model IAU2000R06.NUT and the sub-daily pole model IERS2010XY.SUB are used to generate the files. Regarding the definition of the coordinate frame and the setup of dynamical orbit parameters within the orbit generation, there are two options, which have been considered (Figure 5.2):

- DYX Sun oriented (D, Y, X constant and once-per revolution accelerations): This set of parameters is known as the old Empirical CODE Orbit Model (old ECOM), which was in use by CODE until December 2014. This model is used in this work for the GPS only and for the combined GPS+Galileo solution.
- D2X Sun oriented (constant in all directions, once-per-revolution in X, twice per revolution in D, and four times per revolution in D accelerations): This set of parameters is called the new Empirical CODE Orbit Model (new ECOM or ECOM2) and it is in use since January 2015 (Dach et al., 2015). This model is applied for another run of the combined GPS+Galileo solution making in total 3 different solutions.

[41]Vienna Mapping Functions 1

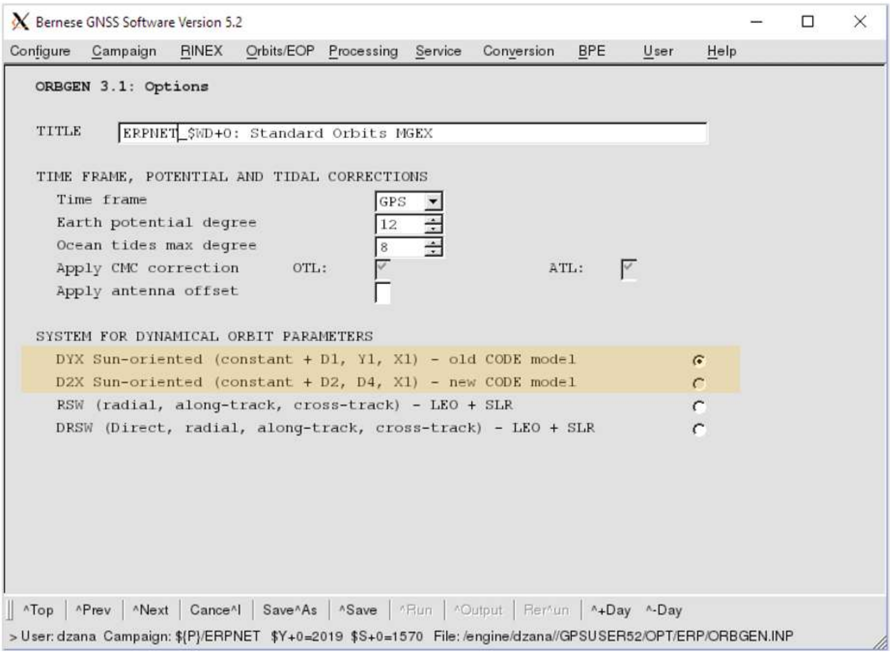


Figure 5.2: Panel of the Bernese program ORBGEN used for orbit generation. It shows the possible options for the dynamical orbit parameters systems with the two models used in this work being highlighted.

Depending on which system for dynamical orbit parameters was marked, corresponding radiation pressure parameters have to be chosen in the following panel. The chosen parameters are then estimated to fit the precise ephemerides (Figure 5.3):

According to the old ECOM model, the radiation pressure is defined with the following equations (Dach et al., 2015):

$$\begin{aligned} D(u) &= D_0 + D_C \cdot \cos u + D_S \cdot \sin u \\ Y(u) &= Y_0 + Y_C \cdot \cos u + Y_S \cdot \sin u \\ X(u) &= X_0 + X_C \cdot \cos u + X_S \cdot \sin u. \end{aligned} \tag{5.2}$$

where the functions $D(u), Y(u)$ and $X(u)$ are written as Fourier series truncated after the once-per-revolution terms. The parameters in Eq. 5.2 and seen in Figure 5.3 are known as the nine parameters of the old ECOM model. On the other hand, the new ECOM model defines the radiation pressure as follows (Dach et al., 2015):

$$\begin{aligned} D(u) &= D_0 + D_{2C} \cdot \cos 2u + D_{2S} \cdot \sin 2u + D_{4C} \cdot \cos 4u + D_{4S} \cdot \sin 4u \\ Y(u) &= Y_0 \\ X(u) &= X_0 + X_C \cdot \cos u + X_S \cdot \sin u. \end{aligned} \tag{5.3}$$

where:

$u$ is the satellite argument of latitude w.r.t. the argument of latitude of the Sun
$D$ is the direct solar radiation pressure (direction Sun $\rightarrow$ satellite)
$Y$ is the y-bias (direction of the satellite's solar panel axis)
$X$ is the acceleration vertical to the D and Y directions.

The extended ECOM model (ECOM2) is of significant relevance for elongated satellite bodies (which is the case with Galileo satellites) since it is superior in taking into account the differently illuminated cross-section of such satellite (Arnold et al., 2015). No stochastic pulses (changes in the satellite's velocity in radial, along-track, and out-of-plane directions) were set up in the old ECOM mode. Considering different constellation approaches, as well as different ways of SRP modeling, a brief summary of the different solution types is listed in Table 5.2.

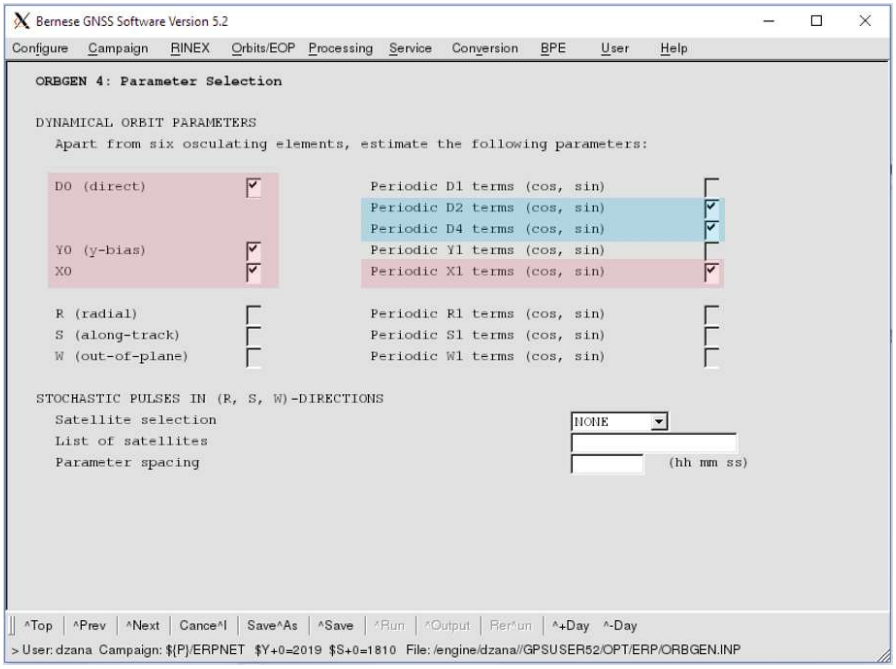

Figure 5.3: The possible dynamical orbit parameters to be selected, depending on the chosen system. Parameters in red are estimated in both, the ECOM (GPS, GPS/Galileo) and the ECOM2 (GPS/Galileo) mode. Parameters in blue are additionally estimated in the ECOM2 mode.

Table 5.2: Description of the solution types.

| Solution | Constellation | SRP modeling | Arc-length |
|---|---|---|---|
| 1 | GPS | ECOM (5 param.) | 1-day/3-day |
| 2 | GPS+Galileo | ECOM (5 param.) | 1-day/3-day |
| 3 | GPS+Galileo | ECOM2 (9 param.) | 1-day/3-day |

The next step involves cleaning and smoothing GNSS observations, which is particularly important when working with RINEX3 observation files. Unlike RINEX2, the RINEX3 format is not compatible with the Bernese GNSS software. Version 5.2 of the software is designed to process up to two frequencies for phase and code observations, totaling four observations in parallel. However, RINEX3 files can now contain observations from more than two frequencies, depending on the specific GNSS system. Importing a file with more than four observations in total would result in an error. Therefore, a preprocessing step is necessary to select the specific signals to be processed. The selected observation information is then written in an internal RINEX2-style format compatible with Bernese. Only RINEX3 files are used for this processing. The following text describes all the actions performed within this step.

At first, observations are checked for cycle slips based on the comparison of the four observations (phase L1 and L2 and pseudorange P1 and P2) per epoch to each satellite, by using different linear combinations. First, the Melbourne-Wübbena linear combination (Section 4.3.1.5) of phase and code observations is formed in order to detect cycle slips. The minimum size of detectable cycle slips is set to 1.0 L5 cycles, while the minimum size of detectable outliers is set to 5.0 L5 cycles. If there are detected cycle slips in the previous linear combination, a geometry-free linear combination of phase observations (L4) (Section 4.3.1.2) is built next in order to estimate their size. In order to do that, a linear fit is calculated for a specified amount of observations before and after the detected cycle slip (in this case, the number of L4 observations for fit is set to 10). After that, an additional screening is performed based on the ionosphere-free linear combination (L3, P3) (Section 4.3.1.1) to discover the remaining outliers in the observations. In this screening process, outliers are removed until the RMS of the observation arc is lower than the specified RMS value. The output of this step is smoothed (corrected for cycle slips) observation RINEX files, which are further (as the previous input data files) converted into Bernese formatted files.

Later on, receiver clocks from previously obtained smoothed code zero-difference observations are synchronized with GPS time. Using the same measurements, a first apriori coordinate solution is estimated via SPP (single point positioning) using the L3 linear combination. The elevation cut-off angle was set to 4°.

Afterward, single-difference observation files (or baselines) are formed based on zero-difference phase measurements. The set of baselines will be created according to the number of mutual observations for the corresponding stations. After considering all possible combinations, the algorithm chooses the set of baselines containing the maximum possible mutual observations. This step is actually performed twice. The reason for that is the choice of the GNSS to be processed. Even though it is possible to perform this step once by choosing the combination GPS/Galileo, this choice cannot guarantee that the optimum number of Galileo observations will be preserved and eventually saved in the baseline file. In order to keep as many as possible Galileo observations, it is thus recommended to perform the baseline creation twice for each GNSS. In a first run, the GNSS Galileo is chosen first in order to guarantee the maximum amount of Galileo-based observation in the baseline files. In a second run, GPS is chosen and by introducing a baseline list in the predefined baselines, generated in the first run, the same baselines are created again, adding GPS baselines to the already built Galileo single-differences. This way, no Galileo-based observations are lost and the amount of created baselines could be kept at an optimum. After those two runs, the same step is repeated for smoothed code-based zero difference measurements by, again, introducing the previously generated baseline file in order to keep a consistent set of single-differences.

***Phase-based pre-processing and residual screening***

Phase-based single-difference observation files are in the following step screened for cycle slips. As long as the size of a cycle slip can be determined, the corresponding observation will be corrected. Otherwise, if this is not possible, the corresponding observation is removed as an outlier or another ambiguity parameter gets introduced. The screening process is based on the combined frequency check of L1 and L2, or in other words, building the L3 linear combination, since the size of the station network, and thus the baseline length, requires such an approach because of the ionospheric term. Additionally, all observations below the cut-off angle of 4° are not checked by this step, but they are rather marked with a flag without any screening, which means, that they are not used in further steps of the processing. This treatment of low-elevation observations is performed based on the assumption that such observations are corrupted by the tropospheric delay and multipath. The screening consists of a non-parametric and a parametric screening part. In the first part, a double-difference screening is done by building differences between two satellites of one epoch of single-difference observations. The second part consists of creating triple differences between two consecutive epochs from the previously built satellite differences by using the L3 linear combination, leading to an epoch-difference solution. The next step is the estimation of residuals in phase-based single-difference observations. This step is performed based on the L3 linear combination for observations above the elevation cut-off angle of 5°. The used observations are further weighted by an elevation-dependent weighting function ($\cos^2 z$). The estimated residuals are also called *normalized residuals* and they are calculated by dividing the real residuals (adjusted minus actual observations) by the square root of the diagonal element of the residual cofactor matrix (Dach et al., 2015):

$$v_{norm}(i) = \frac{v(i)}{\sqrt{D_{ii}(v)}} \tag{5.4}$$

with $v(i) = \hat{y}(i) - y(i)$,

where:

| | |
|---|---|
| $v_{norm}(i)$ | is the normalized residual vector, |
| $v(i)$ | is the real residual vector, |
| $\hat{y}$ | is the adjusted observation vector and |
| $y$ | is the actual observation vector. |

*D(v)* is the residual cofactor matrix and it can be obtained by calculating the difference between the weight matrix of the actual observations $y$ and the cofactor matrix of the adjusted observations $\hat{y}$ (Dach et al., 2015):

$$D(v) = P^{-1} - D(y) \tag{5.5}$$

with

$$D(y) = A(A^T PA)^{-1}A^T \tag{5.6}$$

where:

| | |
|---|---|
| $P$ | is the weight matrix of the actual observations $y$, |
| *D(y)* | is the cofactor matrix of the adjusted observations $\hat{y}$ and |
| $A$ | is the design matrix. |

***Phase-based ambiguity resolution (AR) - QIF***

In the following step, a first ambiguity resolution, the QIF (Quasi-Ionosphere-Free) strategy is performed for phase-based baselines up to 2000 km length. The QIF-based solution, which resolves the L1 and L2 ambiguities directly by utilizing the ionosphere-free linear combination (L3) (Section 4.3.1.1), was proposed by Mervart (1995). It is basically searching for the combination of $N_{L1}$ and $N_{L2}$ integer candidates, that mostly fit the real-valued narrow-lane ambiguities (G. C. Liu, 2001).

After retrieving ambiguity estimates in an initial least-squares adjustment using both frequencies L1 and L2, the ionosphere-free bias $\tilde{B}_3$ can be computed (Dach et al., 2015):

$$\tilde{B}_3 = \frac{c}{f_1^2 - f_2^2}(f_1 b_1 - f_2 b_2) \tag{5.7}$$

where:

| | |
|---|---|
| $b_1$, $b_2$ | are the real-valued ambiguity estimates |

This bias can further be expressed in narrow-lane cycles (one cycle is equal to a wavelength of approximately 11 cm, see Section 4.3.1.4 and 4.3 for more information):

$$\begin{aligned}\tilde{b}_3 &= \frac{\tilde{B}_3}{\lambda_3} = \tilde{B}_3 \cdot \frac{f_1 + f_2}{c} \\ &= \frac{f_1}{f_1 - f_2} b_1 - \frac{f_2}{f_1 - f_2} b_2 \\ &= \beta_1 b_1 + \beta_2 b_2.\end{aligned} \tag{5.8}$$

The integer L3-bias can be written as:

$$b_{3pq} = \beta n_{1p} + \beta n_{2q} \tag{5.9}$$

where:
$n_{1p}$ and $n_{2q}$ are the correct (resolved) integer ambiguity values.

The criterion, used in this approach, to select the best fitting pair of integers $n_{1p}$, $n_{2q}$ is created by building the difference between the real-valued and integer L3-bias:

$$d_{3pq} = |\tilde{b}_3 - b_{3pq}| \tag{5.10}$$

For more information, refer to Mervart et al. (1994) and Dach et al. (2015).

***Code-based pre-processing and residual screening***

The previously formed smoothed code-based single-differences are introduced in the following step to resolve ambiguities by using the L3 linear combination. Afterward, a screening for outliers is performed in the corresponding residual file, followed by marking the identified outliers in the associate observation files. By analysing the summary of the residual screening step, misbehaving stations and/or satellites are being detected.

***Phase- and smoothed code-based ambiguity resolution (AR) - Melbourne-Wübbena***

Baselines with a length between 2000 – 6000 km are introduced next for the residual screening. This is done by using the Melbourne-Wübbena linear combination. In a first run, wide-lane L5 ambiguities are resolved from phase- and smoothed code-based single-differences. In the second run, the resolved wide-lane (L5) ambiguities are introduced to an L3 ambiguity resolution applied on phase-based single-differences only.

***Ambiguity fixed resolution***

***1-day solution***

The previously performed ambiguity resolutions have produced corresponding normal equation systems files, which are combined in the following step to produce an ambiguity-fixed solution. Essential input files here are the baseline normal equation files, the a priori coordinate file for the processed epoch, the station information, and the pole file. The main purpose of this station network processing is the estimation of Earth rotation parameters. In this step, a final 1-day solution is produced. Additional parameters, estimated within this step, are a final coordinate solution for the processed epoch and troposphere parameters. The Bernese GNSS Software applies the least square adjustment (LSA) method based on the Gauss-Markov parameterized approach for the parameter estimation process (Zajdel, 2021), which will be described in the further text.

The troposphere zenith path delays and the troposphere gradients are estimated with a temporal spacing of 4h and 24h respectively, whereas the ERPs are estimated with a time resolution of 1h. They are modeled as piece-wise linear functions. The No-Net-Rotation (NNR) condition is applied in this step on 45 stations, tying them to the ITRF2014 reference frame.

Retrograde diurnal periods (terms) are blocked in polar motion since it is not possible to separate the retrograde diurnal x-y variation from a rotation of the orbital system in inertial space. Thus, by blocking those retrograde terms, one will avoid this singularity (Dach et al., 2015). The Bernese GNSS Software v5.2 contains by default an implementation of handling retrograde diurnal terms. The procedure includes the use of pseudo-observations in the least-squares adjustment (LSA). This method is described by Hefty et al. (2000). The procedure for handling retrograde diurnal periods in polar motion is described in the following text.

Retrograde diurnal polar motion can be written as (Hefty et al., 2000; Zajdel et al., 2021):

$$\begin{aligned} x_p(t) &= A\cos(\omega t + \Phi) \\ &= A_c\cos(\omega t) - A_s\sin(\omega t), \\ y_p(t) &= A\sin(\omega t + \Phi) \\ &= A_c\sin(\omega t) + A_s\cos(\omega t). \end{aligned} \tag{5.11}$$

where:

| | |
|---|---|
| $\omega$ | is the angular velocity of the Earth rotation, |
| $A$ | is the amplitude coefficient, |
| $\Phi$ | is the phase coefficient and |
| $A_c$ and $A_s$ | are the amplitudes of the cosine and sine coefficients. |

Estimated polar motion time series $(x_p(t), y_p(t))$ won't show retrograde diurnal terms if a fit of the estimated parameters (all derivatives are treated individually) does not contain a retrograde diurnal signal. For derivatives $l = 0, 1$ the estimated parameters $x_{1l}, x_{2l}, ..., x_{nl}$ and $y_{1l}, y_{2l}, ..., y_{nl}$ are separately fitted by using the equations for retrograde diurnal polar motion (Eq. 5.11). The resulting fit has to equal zero. The corresponding equations for pseudo-observations can be written as follows:

$$\begin{aligned} A\cos(\omega t_i + \Phi) - x_i &= v_i, \\ A\sin(\omega t_i + \Phi) - y_i &= \omega_i, \quad i = 1, 2, ..., n \end{aligned} \tag{5.12}$$

where:

| | |
|---|---|
| $v_i$ and $\omega_i$ | are the residuals. |

The linearized form of observation equations 5.12 may be written as:

$$\begin{aligned} A_c\cos(\omega t_i) - A_s\sin(\omega t_i) - x_i &= v_i, \\ A_c\sin(\omega t_i) + A_s\cos(\omega t_i) - y_i &= \omega_i, \quad i = 1, 2, ..., n \end{aligned} \tag{5.13}$$

where:

$$A_c = A\cos(\Phi)$$
$$A_s = A\sin(\Phi). \tag{5.14}$$

Equations 5.13 can be noted in matrix form:

$$Ax - l = v \tag{5.15}$$

where:

$A$ is the first design matrix,

$l$ is the matrix of the estimates $x_p(t), y_p(t)$ ($l^T = (x_{10}, y_{10}, x_{20}, y_{20}, ..., x_{n0}, y_{n0})$),

$x^T = (A_c, A_s)$ and

$v$ is the residual matrix.

Finally, the solution for this parameter estimation problem has the following form:

$$x = (A^T A)^{-1} A^T l \tag{5.16}$$

If the condition $x = 0$ is met, no retrograde diurnal terms can be found in these estimates (Hefty et al., 2000).

Due to the high correlation of UT1-UTC and nutation with the rotation of the orbital planes, their first parameter sets are being constrained with high a priori weights, while a relatively looser constraint is applied for their remaining parameter estimates. The a priori sigmas set for UT1-UTC and nutation offsets are 0.00001 ms and 0.0001 mas respectively. For the subsequent parameters, the loose constraint applied to the nutation offsets is 0.1 mas, which means that the subsequent parameter sets are estimated almost freely by GNSS observations, in this case GPS and GPS/Galileo.

With this, a final daily solution of ERPs is estimated. In order to ensure continuity at boundaries between each daily solution, 3-day arc solutions have to be estimated based on three consecutive 1-day solutions.

**5.1.1.1. Theory of Least-Squares Adjustment (LSA)** As previously stated, the estimation of the ERPs based on global GNSS observations is performed by a least-squares adjustment method. The equation describing the functional model reads (Magnet, 2019; Zajdel, 2021):

$$L + v = F(X) \tag{5.17}$$

with

$$X = X_0 + x \tag{5.18}$$

where:

| | |
|---|---|
| $L$ | are the measured observations (*nx1*), |
| $v$ | are the observation corrections (*nx1*), |
| $n$ | is the number of observations, |
| $X$ | are the adjusted parameters (unknowns) (*ux1*), |
| $X_0$ | are the approximate values of the unknowns (*ux1*), |
| $x$ | are the differences of the unknowns to the approximate values (*ux1*) and |
| $F(X)$ | is the functional model (*nx1*). |

A first-order linearization is applied to the functional model (Eq. 5.17). After leaving only the correction vector $v$ on the left side of the linearized system, Equation 5.17 can be formulated as:

$$v = Ax - (L - F(X_0)) \tag{5.19}$$

with

$$l = L - F(X_0). \tag{5.20}$$

Furthermore, Equation 5.19 can be simplified by inserting Equation 5.20:

$$v = Ax - l \tag{5.21}$$

where:

| | |
|---|---|
| $A$ | is the first-design matrix (*nxu*) and |
| $l$ | is the difference between the observations and approximated observations derived from the functional model by using $X_0$ $(= L - F(X_0))$. |

The first design-matrix $A$ (*nxu*) is created by performing a partial derivation of the observation equations (*nx1*) with respect to the unknown parameters $X$ (*ux1*) which are approximated by the values $X_0$:

$$A = \left. \frac{\partial F(X)}{\partial X} \right|_{X=X_0}. \tag{5.22}$$

The general concept of the least squares adjustment method can be defined with the following condition:

$$v^T P v \rightarrow min \tag{5.23}$$

where:

$P$ is the matrix of weights for each observation (*nxn*).

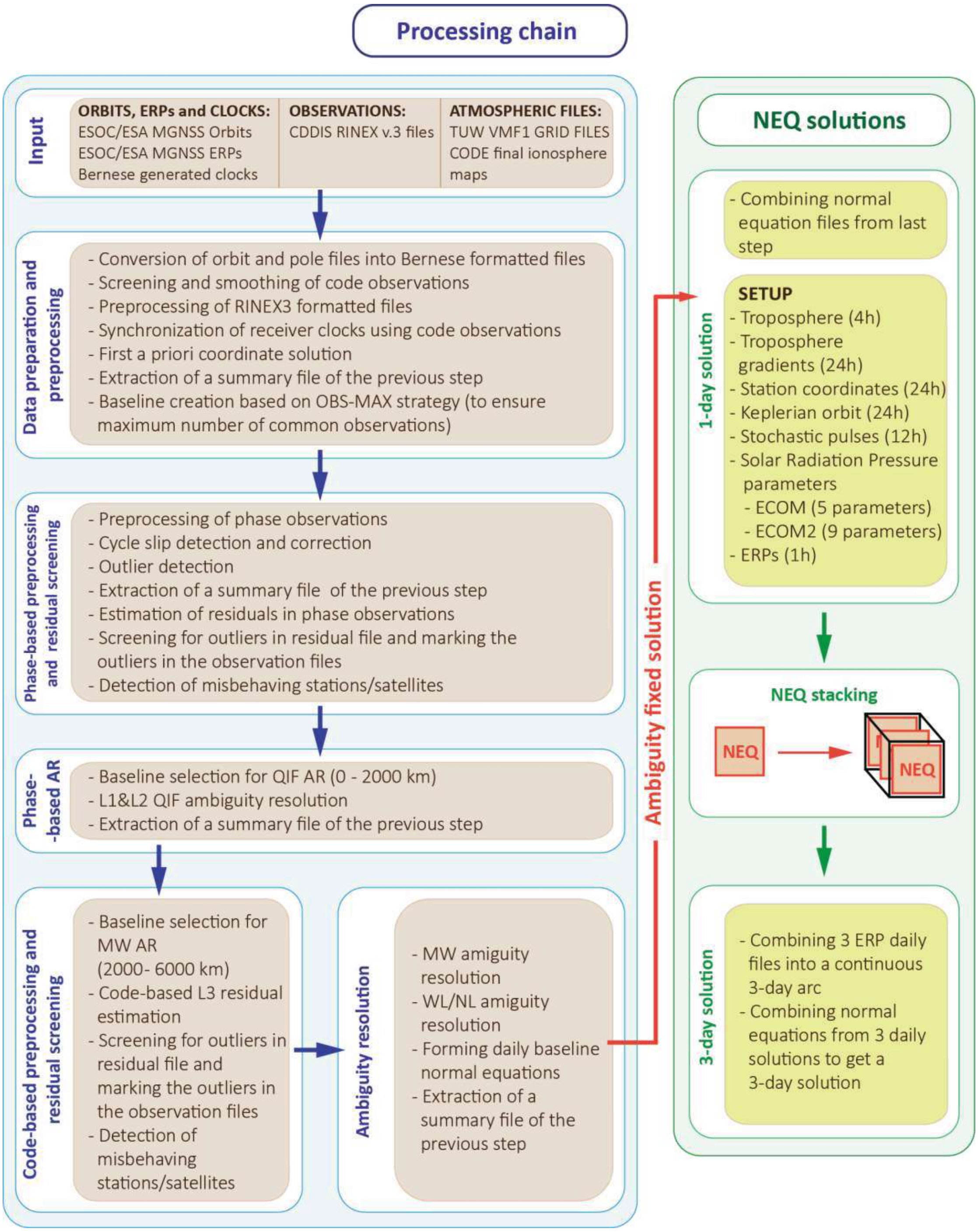


Figure 5.4: Processing chain for ERP solution. ESOC: European Space Operation Centre. ESA: European Space Agency. MGNSS: Multi Global Navigation Satellite System. ERPs: Earth Rotation Parameters. CDDIS: Crustal Dynamics Data Information System. RINEX: Receiver Independent Exchange Format. TUW: Technische Universität Wien. VMF1: Vienna Mapping Functions 1. CODE: Center for Orbit Determination in Europe. QIF: Quasi Ionosphere Free. AR: Ambiguity Resolution. MW: Melbourne-Wübbena. WL/NL: Widelane/Narrow-lane. NEQ: Normal Equation System. ECOM: Empirical CODE Orbit Model.

According to Equation 5.23, the system of observation equations is solved by minimizing the weighted sum of square observation corrections $v$ (residuals). Introducing (5.21) into (5.23) leads to the following equation (Magnet, 2019; Todorova, 2008):

$$\begin{aligned} v^T P v &= (x^T A^T - l^T) P (Ax - l) \\ &= x^T A^T PAx - x^T A^T lAx - l^T PAx + l^T Pl \end{aligned} \tag{5.24}$$

The minimum condition is met when setting the first partial derivative of Equation 5.23 with respect to parameters $x$ to zero:

$$\frac{\partial v^T v}{\partial x} = 2A^T PAx - 2A^T Pl = 0 \tag{5.25}$$

leading further to:

$$\underbrace{A^T PA}_{\mathrm{N}}\, x = \underbrace{A^T Pl}_{\mathrm{b}} \Longrightarrow Nx = b \tag{5.26}$$

where:

$N$ is the normal equation matrix *(uxu)* and

$b$ is the right-hand side of the normal equation system *(ux1)*

Finally, the vector of unknowns can be calculated from Equation 5.26 as follows:

$$x = (A^T PA)^{-1} A^T Pl = N^{-1} b. \tag{5.27}$$

The variance-covariance matrix gives insight into the accuracy of the estimated parameters. Its main diagonal contains the variances of the estimated parameters. The matrix is basically the inverse form of the normal equation matrix:

$$Q_{xx} = N^{-1}. \tag{5.28}$$

The a posteriori adjustment accuracy is then calculated by multiplying the a posteriori variance factor $\sigma_0^2$ of unit weight with the variance-covariance matrix, leading to the covariance matrix of estimated parameters $C_{xx}$ (Zajdel, 2021):

$$C_{xx} = \sigma_0^2 Q_{xx} = \sigma_0^2 N^{-1} \tag{5.29}$$

with:

$$\sigma_0^2 = \frac{v^T P v}{n - u} \tag{5.30}$$

where:

$n$ is the number of observations and

$u$ is the number of estimated parameters (unknowns).

The formal errors of estimated parameters are the square roots of the diagonal elements in matrix $C_{xx}$, or in other words, standard deviations of estimated parameters. Non-diagonal elements refer to the correlation between the estimated parameters, whereas the correlation coefficient can be calculated as:

$$\rho_{ij} = \frac{C_{xx,ij}}{C_{xx,ii} C_{xx,jj}} \tag{5.31}$$

where:

$C_{xx,ii}$ is the variance of the parameter $i$,
$C_{xx,jj}$ is the variance of the parameter $j$ and
$C_{xx,ij}$ is the covariance between the parameters $i$ and $j$.

***3-day solution***
To calculate a 3-day arc solution, first, a corresponding a priori 3-day pole file is produced based on a priori pole files for three consecutive days (one day before, the processed day, and one day after). Further, 1-day normal equation files of three consecutive days are stacked into one 3-day normal equation file. Then, the same step, as for the 1-day solution, is performed again, with the difference that a 3-day ERP set is produced. One difference to point out is that the a priori sigmas for the remaining nutation offsets are here set to 0.05 mas. By stacking solutions and creating 3-day estimates, one can achieve that the middle day of such solution overlaps with the first day of the subsequent solution, as well as with the last day of the previous solution, making the estimated times series as a whole smoother, and thus, improving continuity between the individual sets.

## 5.2. Regional ionosphere modeling

The regional ionospheric model presented in this work provides so-called ionospheric maps, which contain grids of VTEC values over a chosen region (in this case the European mid-latitudes). This model has been set up in the framework of the GRC-MS (Galileo Reference Center – Member States) project, established by the European GNSS Agency. This project officially started in the last quarter of 2018 and has been successfully wrapped up with the end of the second quarter of 2022 (Ngayap et al., 2023).

Within this period, the responsibilities related to the Department of Geodesy and Geoinformation of TUW (Vienna University of Technology) included the study and analysis of the NeQuick G ionospheric model (described in section 3.5.6) in different latitudinal regions. In particular, TUW was in charge of the Central European latitudes, meaning latitudes within the range 30°N - 60°N.

Driven by the idea of this project, a regional model, covering the tested area, has been developed in order to study and validate it in the same way it is done with the NeQuick G model. Same as in the ERP determination, the concept is to have a model based on multi-GNSS observation data, or, in other words, combined GPS and Galileo observation data.

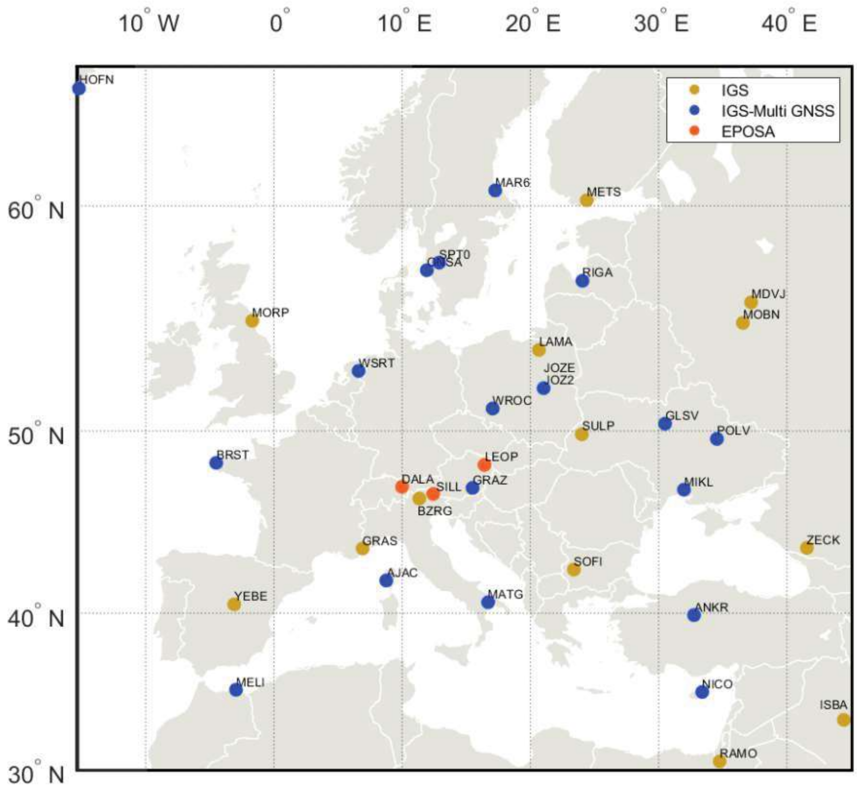


Figure 5.5: Regional GNSS network distribution (yellow markers denotes IGS stations, blue markers are showing IGS-Multi GNSS stations and orange markers denote EPOSA stations).

The regional model, called TUWR in the following text, is based on observation data from 35 ground stations (Figure 5.5), covering the range 30°N - 65°N and 15°W - 45°E in latitude and longitude respectively. Most of the stations belong to the IGS (or IGS-Multi GNSS) network, while three stations belong to the EPOSA (Echtzeit Positionierung Austria) network, an Austrian GNSS network, although these stations are currently able to track only GPS data.

The model has been calculated regularly since October 1st 2018, maintaining the same station network and setup. Table 5.3 shows its main characteristics.

The deterministic component of the ionosphere in this model is described by the modified single-layer (MSLM) mapping function. The Single-Layer Model (SLM) assumes that all free electrons are concentrated within an infinitesimal thin shell (Dach et al., 2015) at constant height, $h$, above the Earth's surface (Magnet, 2019). For simplification purposes, GNSS-derived models are usually based on the SLM. Figure 5.6 shows an outline of the Single-Layer Model. As seen from this figure, the signal path between receiver and satellite passes through the ionospheric single-layer.

Table 5.3: Main characteristics of the TUWR regional ionospheric model.

| Model characteristic | Applied strategy |
|---|---|
| **Software** | Bernese GNSS Software version 5.2 (BSW) |
| | (Dach et al., 2015) |
| **Network** | 35 permanent ground stations |
| | (IGS + IGS multi-GNSS + EPOSA) |
| **Start DoY** | 274 (2018) |
| **Grid size** | 0.5° x 0.5° |
| **Coverage** | 30°N – 65°N lat |
| | 15° W – 45° E lon |
| **Temporal resolution** | 1h → 25 VTEC maps per file |
| **Observation type** | geometry-free zero-difference code and carrier phase |
| **Satellite system** | GPS + Galileo |
| **Mapping function** | MSLM (modified single-layer model) |
| **Integrated electron density** | spherical harmonics expansion (up to degree 6) |
| **A priori single layer height** | 450 km |
| **Geomagnetic pole** | 79°N lat |
| | 71°E lon |
| **Absolute sigma** | 10 TECU |
| **Processing** | Post-processing mode |

This intersection point is known as the IPP or Ionospheric Pierce Point. The SLM mapping function can be written using the following equation (Magnet, 2019):

$$\sin z' = \frac{R_e}{R_e + h} \sin z \tag{5.32}$$

where:

$z', z$ are the zenith angles at the IPP and at the observing site, respectively,

$R_e$ is the mean radius of the Earth (= 6371 km),

$h$ is the height of the single layer of the ionosphere, usually chosen to be between 350 km and 550 km, i.e. the expected height of the electron density maximum.

As already mentioned, GNSS-based ionosphere products, like ionospheric maps, usually deliver grids of VTEC values. However, signal paths provide only STEC values. The relation between STEC and VTEC can be expressed by using a zenith angle-dependent mapping function, $M$, known as the Single-Layer Mapping Function (SLM MF):

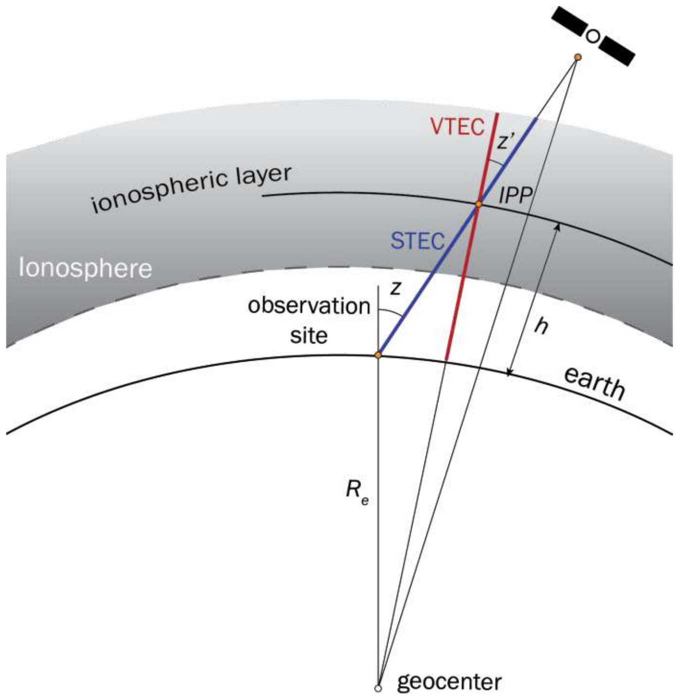


Figure 5.6: Single-layer model for the ionosphere and relation between VTEC (red line) and STEC (blue line).

$$M(z) = \frac{STEC}{VTEC} \cong \frac{1}{\cos z'} = \frac{1}{\sqrt{1-\sin^2 z'}} \tag{5.33}$$

After introducing Equation (5.32) into (5.33), the mapping function takes the following form:

$$M(z) = \frac{1}{\sqrt{1-\left(\frac{R_e}{R_e+h}\sin z\right)^2}} \tag{5.34}$$

The relation between the VTEC and STEC can be seen in Figure 5.6 (Magnet, 2019).

The Center of Orbit Determination in Europe (CODE) uses a “modified” version of the SLM mapping function, the so-called Modified Single-Layer Model Mapping Function (MSLM) (Dach et al., 2015). It includes an additional constant, $\alpha$ (Schaer, 1999):

$$M(z) = \frac{1}{\sqrt{1-\left(\frac{R_e}{R_e+h}\sin \alpha z\right)^2}} \tag{5.35}$$

This mapping function achieves the best fit with respect to the JPL Extended Slab Model (ESM) mapping function at height $h = 506.7$ km, for $\alpha = 0.9782$, and assuming that the maximum zenith angle is 80° (when using R = 6371 km).

There are three types of ionosphere models, describing the deterministic component of the ionosphere, that are supported by the Bernese GNSS Software version 5.2., namely:

- Local models, which are calculated using two-dimensional Taylor series expansions,
- Global (or regional) models based on spherical harmonics expansions, and
- Station-specific models, which can be obtained in the same manner as global and regional ionospheric models (Dach et al., 2015).

Given the range that the TUWR model is covering (regional scale), consequently, the global model approach was applied.

Both, local and global/regional models will be described, whereas station-specific models will not be discussed any further, considering that they are estimated the same way as global models.

***Local TEC Model***

The local TEC model can be expressed by the following equation (Schaer, 1999):

$$E(\beta, s) = \sum_{n=0}^{n_{max}} \sum_{m=0}^{m_{max}} E_{nm}(\beta - \beta_0)^n (s - s_0)^m \tag{5.36}$$

where:

| | |
|---|---|
| $\beta, s$ | are the solar-geographic coordinates of the IPP, |
| $n_{max}, m_{max}$ | are the maximum orders in latitude $\beta$ and longitude s of the two-dimensional Taylor series, |
| $E_{nm}$ | are the estimated local ionosphere model parameters (unknown TEC coefficients), |
| $\beta_0, s_0$ | are the origin of Taylor series development. |

The relation between $s$ and the local solar time ($LT$) can be written as (Dach et al., 2015):

$$s = LT - \pi \approx UT + \lambda - \pi \tag{5.37}$$

where:

| | |
|---|---|
| $UT$ | is the Universal Time and |
| $\lambda$ | is the geographical longitude of the IPP. |

More details on local TEC representation can be found in (Wild, 1994).

***Global/Regional TEC Model***

Considering the limitations in the $(\beta, s)$ space, Equation (5.36) used for the local TEC modeling is not suitable to parameterize the TEC on a global or regional scale. According to (Schaer et al., 1996), global and regional TEC representation may be written as a spherical harmonics expansion:

$$E(\beta, s) = \sum_{n=0}^{n_{max}} \sum_{m=0}^{n} \tilde{P}_{nm}(\sin\beta)(a_{nm}\cos(m \cdot s) + b_{nm}\sin(m \cdot s)) \tag{5.38}$$

where:

| | |
|---|---|
| $n_{max}$ | is the maximum degree of the spherical harmonics expansion, |
| $\tilde{P}_{nm} = \Lambda(n,m)P_{nm}$ | is the normalized associated Legendre functions of degree $n$ and order $m$, based on normalization function $\Lambda(n,m)$ and Legendre functions $P_{nm}$ |
| $a_{nm}, b_{nm}$ | are the unknown spherical harmonics coefficients (global ionosphere model parameters). |

The number of global ionospheric map parameters ($a_{nm}, b_{nm}$) in the spherical harmonics expansion can be expressed as follows (Schaer, 1999):

$$u_E = (n_{max} + 1)^2 \tag{5.39}$$

In the case that Equation (5.38) is truncated at the maximum order $m_{max} \leq n_{max}$, the number of ($a_{nm}, b_{nm}$) parameters can be calculated as:

$$u_E = (n_{max} + 1)^2 - (n_{max} - m_{max})(n_{max} - m_{max} + 1) \tag{5.40}$$

The corresponding spatial resolution can also be obtained from $m_{max}$ and $n_{max}$:

$$\Delta\beta = \frac{2\pi}{n_{max}}, \qquad \Delta s = \frac{2\pi}{m_{max}} \tag{5.41}$$

where:

$\Delta\beta, \Delta s$ are the resolution in latitude and sun-fixed longitude and local time, respectively.

### 5.2.1. Geometry-free Linear Combination (L4)

The geometry-free linear combination contains the ionospheric information. In other words, it contains the extracted signal delay, which is caused by the ionospheric refraction. According to (Magnet, 2019), observation equations for carrier-phases at frequencies $L_1$ and $L_2$ can be written as follows:

$$\begin{aligned} L_1 &= \rho + c(\delta t_r - \delta t^s) - I^s_{r,L1} + T^s_r + \varepsilon^s_{r,L1} + \lambda_{L1}B_{L1} \\ L_2 &= \rho + c(\delta t_r - \delta t^s) - I^s_{r,L2} + T^s_r + \varepsilon^s_{r,L2} + \lambda_{L2}B_{L2} \end{aligned} \tag{5.42}$$

where:

| | |
|---|---|
| $B_{Li}$ | consists of the integer carrier-phase ambiguity N and the frequency-dependent hardware delays of the satellite and the receiver. |

The geometry-free linear combination based on carrier-phase observations reads:

$$L_4 = \alpha_{1,4} L_1 + \alpha_{2,4} L_2 \tag{5.43}$$

With $\alpha_{1,4} = 1$ and $\alpha_{2,4} = -1$, this LC contains only the ionospheric refraction and hardware delays, meaning that the geometric term and all frequency-independent effects get eliminated, leading to the following equation (Magnet, 2019; Schaer, 1999):

$$L_4 = L_1 - L_2 = -\xi_4 I + B_4 + \varepsilon_{L_4} \tag{5.44}$$

where:

$\xi_4 = 1 - \xi = 1 - \frac{f_{L1}^2}{f_{L2}^2} \approx -0.647$ is the factor that converts the ionospheric delay in $L_4$ to that of $L_1$ (the value 0.647 is based on GPS central frequencies $L_1$, $L_2$)

$B_4 = \lambda_{L1} B_{L1} - \lambda_{L2} B_{L2}$ is the bias parameter with undefined wavelength.

The corresponding observation equations for pseudorange observations P1 and P2 on two frequencies read as follows (Magnet, 2019):

$$\begin{aligned} P_1 &= \rho + c(\delta t_r - \delta t^s) + I_{r,P1}^s + T_r^s + c(d_r - d^s)_{P1} + \varepsilon_{r,P1}^s \\ P_2 &= \rho + c(\delta t_r - \delta t^s) + I_{r,P2}^s + T_r^s + c(d_r - d^s)_{P2} + \varepsilon_{r,P2}^s \end{aligned} \tag{5.45}$$

where:

$d_r, d^s$ are frequency-dependent hardware delays of the satellite and receiver.

The geometry-free linear combination for pseudorange measurements is built as follows (Magnet, 2019; Schaer, 1999):

$$P_4 = \alpha_{1,4} P_1 + \alpha_{2,4} P_2 \tag{5.46}$$

Again, with $\alpha_{1,4} = 1$ and $\alpha_{2,4} = -1$, the undifferenced observation equation reads:

$$P_4 = P_1 - P_2 = \xi_4 I + c(\delta d_r - \delta d^s) + \varepsilon_{P_4} \tag{5.47}$$

where:

$\delta d_r = d_{r,P1} - d_{r,P2}$ is the differential inter-frequency hardware delay, also known as differential code bias (DCB), of the receiver,

$\delta d^s = d_{P1}^s - d_{P2}^s$ is the differential inter-frequency hardware delay (DCB) of the satellite.

### 5.2.2. Processing steps

The generation of the TUWR model is based on a zero-difference approach by using phase and smoothed pseudorange GNSS observations. Unlike in the previous parameter estimation (ERP), double-difference was not implemented nor is it recommended if the processed station network is not of larger size. Figure 5.7 shows the workflow of the regional ionospheric model estimation.

***Input***

The necessary input files are first downloaded into their associate data directories. Satellite orbit and pole files are retrieved from the ESOC/ESA website, as in the ERP processing.

Ground station observation data are obtained via the CDDIS server, as well as from the server of the Austrian regional network EPOSA[42]. In this case, depending on the availability of RINEX V3 observations, both format version 2 and version 3 were used.

Satellite DCB files P1C1 and P1P2 are downloaded from the CODE website. Station DCBs were estimated in parallel alongside the ionospheric model parameters.

***Data preparation***

After retrieving the necessary input data, the processing chain continues with the conversion of orbit, clock, and pole files into formats, which are compatible with the Bernese GNSS software. Observations for the three EPOSA ground stations DALA, LEOP, and SILL are available only as high-rate hourly files. Given that in this work, the processing is running on a daily-based routine, all hourly files are, after being downloaded, concatenated into daily observation files. Once the RINEX files are prepared for use, the subsequent task involves the cleaning and smoothing of GNSS observation files. The approach is the same as in the ERP processing, therefore, please refer to Section 5.1.1 part "Data preparation".

***Pre-processing***

The obtained smoothed zero-difference code observations are used in the following step to perform synchronization of receiver clocks with GPS time. Additional input files used for this step are orbit, clock, pole, a priori coordinate, and P1C1 DCB files. At the same time, an approximation of station coordinates (first a priori solution) based on single point positioning (SPP) using code observations is executed at this stage as well.

Further, phase observations of all files are screened for cycle-slips on a zero-difference level. The non-parametric screening part is based on observation differences formed between two satellites of each epoch.

[42]Three stations are used from this network: DALA, LEOP, and SILL

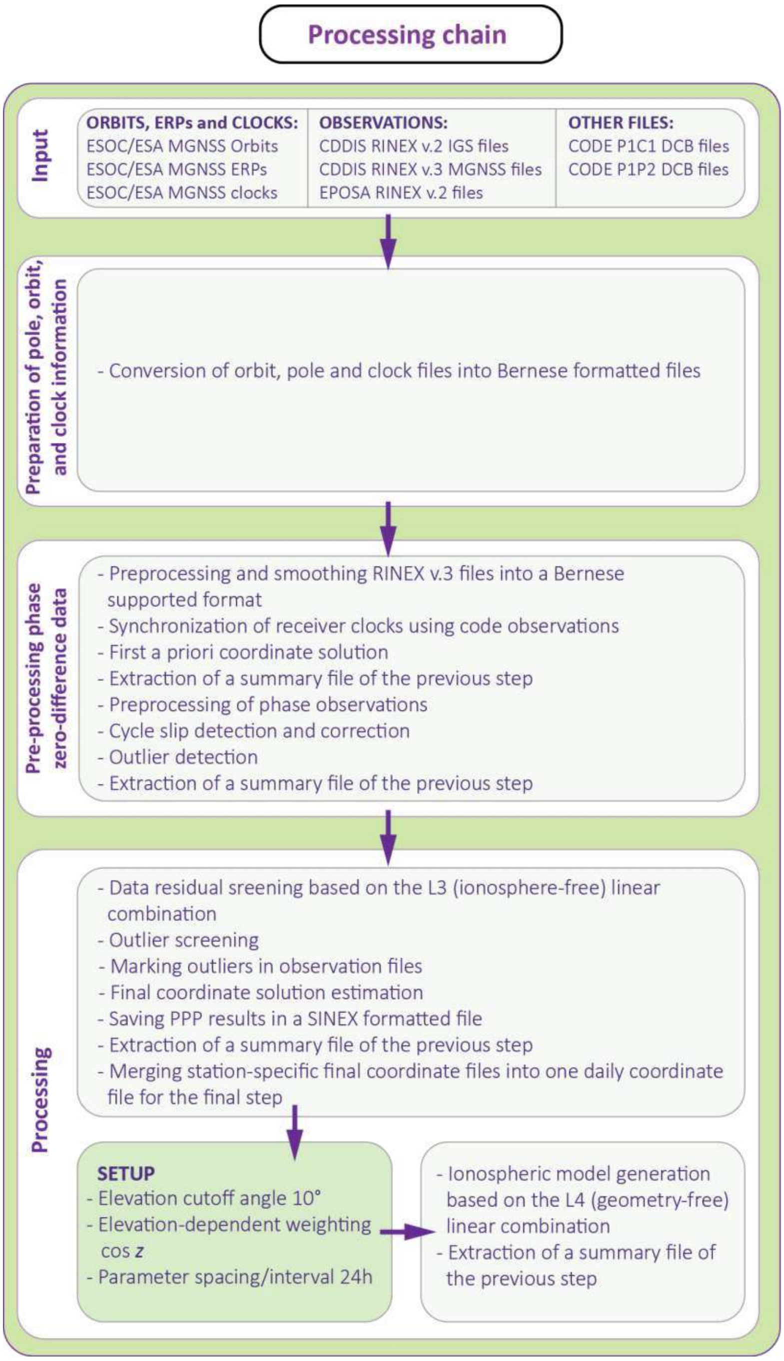


Figure 5.7: Processing chain for regional ionospheric modeling. ESOC: European Space Operation Centre. ESA: European Space Agency. MGNSS: Multi Global Navigation Satellite System. ERPs: Earth Rotation Parameters. CDDIS: Crustal Dynamics Data Information System. RINEX: Receiver Independent Exchange Format. EPOSA: Echtzeit Positionierung Austria. CODE: Center for Orbit Determination in Europe. DCB: Differential Code Biases. PPP: Precise Point Positioning. SINEX: Solution Independent Exchange Format.

Given that observations at zero-difference level are processed, the resulting screening step is called single-difference screening. It is followed by an epoch-difference solution, meaning that additional differences between two epochs are built from previously formed satellite differences. The epoch-difference solution is performed using the L3 linear combination.

***Processing***

The actual estimation starts in this section. It begins with the generation of a residual file, which is based on the L3 linear combination. The resulting file contains normalized residuals. They are calculated using an elevation-dependent weighting approach ($\cos z$), with an elevation cut-off angle of 3°. Later on, this file is used for residual screening. Outliers detected through this data screening are marked in the corresponding observation files in the following step. By introducing the observation residual file, i.e. by using the cleaned observation files, an additional L3 linear combination was built in order to perform a PPP solution (precise point positioning).

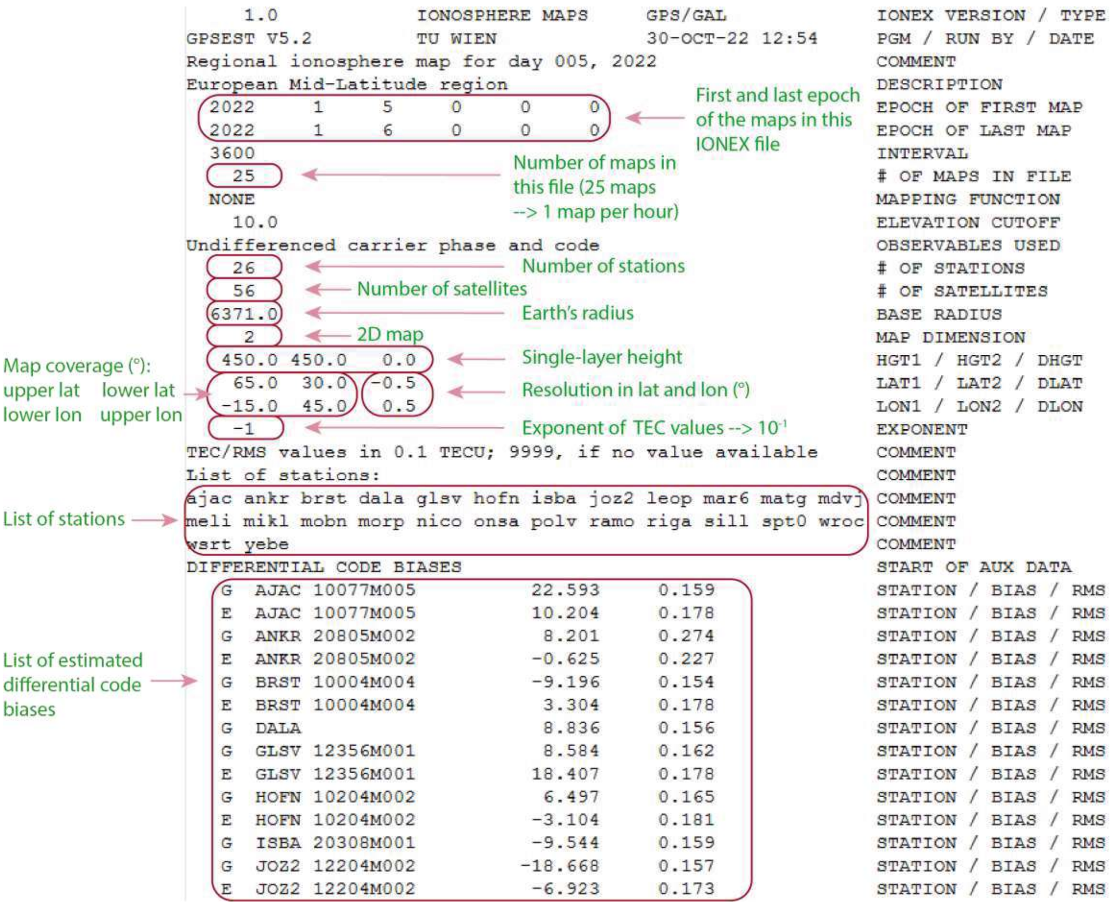

```
     1.0            IONOSPHERE MAPS     GPS/GAL             IONEX VERSION / TYPE
GPSEST V5.2         TU WIEN             30-OCT-22 12:54     PGM / RUN BY / DATE
Regional ionosphere map for day 005, 2022                   COMMENT
European Mid-Latitude region                                DESCRIPTION
  2022     1     5     0     0     0                        EPOCH OF FIRST MAP
  2022     1     6     0     0     0                        EPOCH OF LAST MAP
  3600                                                      INTERVAL
    25                                                      # OF MAPS IN FILE
  NONE                                                      MAPPING FUNCTION
    10.0                                                    ELEVATION CUTOFF
Undifferenced carrier phase and code                        OBSERVABLES USED
    26                                                      # OF STATIONS
    56                                                      # OF SATELLITES
  6371.0                                                    BASE RADIUS
     2                                                      MAP DIMENSION
   450.0 450.0   0.0                                        HGT1 / HGT2 / DHGT
    65.0  30.0  -0.5                                        LAT1 / LAT2 / DLAT
   -15.0  45.0   0.5                                        LON1 / LON2 / DLON
    -1                                                      EXPONENT
TEC/RMS values in 0.1 TECU; 9999, if no value available     COMMENT
List of stations:                                           COMMENT
ajac ankr brst dala glsv hofn isba joz2 leop mar6 matg mdvj COMMENT
meli mikl mobn morp nico onsa polv ramo riga sill spt0 wroc COMMENT
wsrt yebe                                                   COMMENT
DIFFERENTIAL CODE BIASES                                    START OF AUX DATA
   G   AJAC 10077M005          22.593      0.159            STATION / BIAS / RMS
   E   AJAC 10077M005          10.204      0.178            STATION / BIAS / RMS
   G   ANKR 20805M002           8.201      0.274            STATION / BIAS / RMS
   E   ANKR 20805M002          -0.625      0.227            STATION / BIAS / RMS
   G   BRST 10004M004          -9.196      0.154            STATION / BIAS / RMS
   E   BRST 10004M004           3.304      0.178            STATION / BIAS / RMS
   G   DALA                     8.836      0.156            STATION / BIAS / RMS
   G   GLSV 12356M001           8.584      0.162            STATION / BIAS / RMS
   E   GLSV 12356M001          18.407      0.178            STATION / BIAS / RMS
   G   HOFN 10204M002           6.497      0.165            STATION / BIAS / RMS
   E   HOFN 10204M002          -3.104      0.181            STATION / BIAS / RMS
   G   ISBA 20308M001          -9.544      0.159            STATION / BIAS / RMS
   G   JOZ2 12204M002         -18.668      0.157            STATION / BIAS / RMS
   E   JOZ2 12204M002          -6.923      0.173            STATION / BIAS / RMS
```



Figure 5.8: Header from the IONEX file TUWR22005.INX (DOY 005, year 2022).

Finally, by introducing the precisely estimated station coordinates as a priori values, along with P1P2 DCB files, cleaned phase and smoothed code observations are used to build the geometry-free linear combination L4 to extract the ionospheric information and to output corresponding IONEX files, i.e. regional ionospheric maps. The elevation-dependent weighting function is the same as in the data screening step ($\cos z$), with an elevation cut-off angle of 10°. The maximum degree, as well as the maximum order, of spherical harmonics, is set to 6. The a priori height of the single layer is chosen as 450 km, and the latitude and longitude of the geomagnetic pole are 79° and -71° respectively, whereas the absolute sigma for coefficients is 10 TECU. Figures 5.8 and 5.9 show the example of an ionospheric map generated through this processing chain. Figure 5.8 explains the file header, while Figure 5.9 describes the content in the data section.

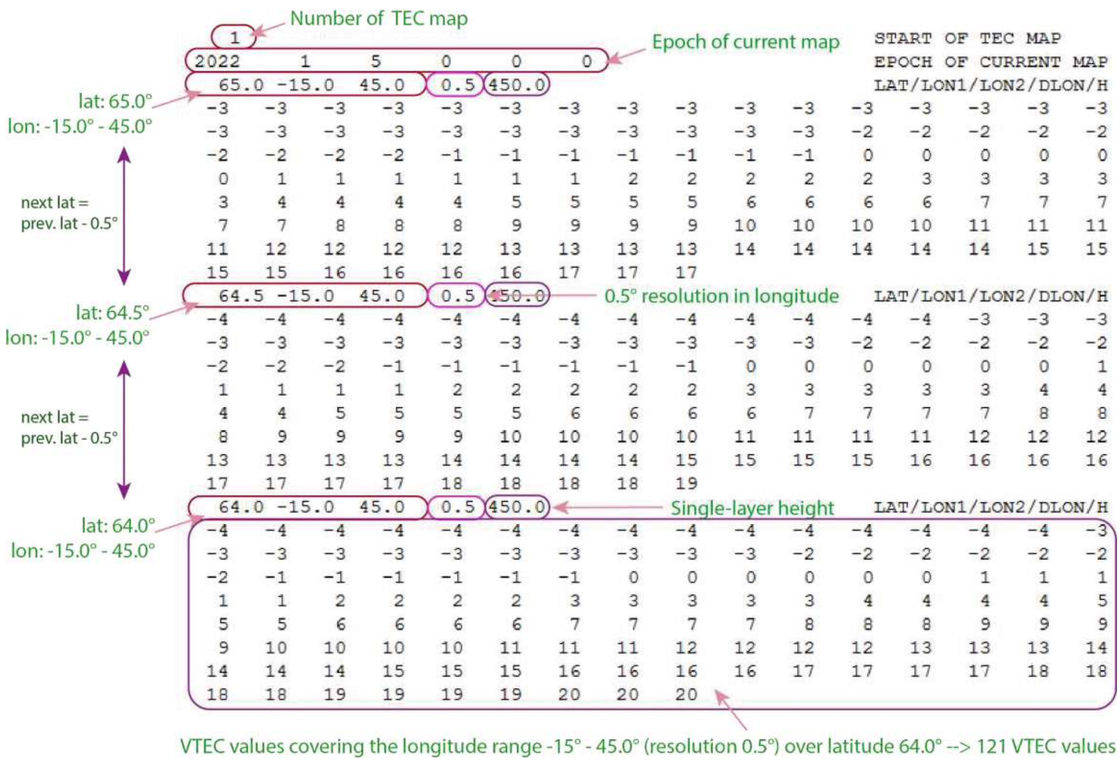


Figure 5.9: Data section from the IONEX file TUWR22005.INX (DOY 005, year 2022).

The parameter sets processed according to the procedures described in Chapter 5 are now presented and analyzed in Chapter 6.

# 6. Results

In this section, the impact of including Galileo observations will be examined and discussed. As described in the previous chapter (Chapter 5), ERP time series were estimated over a two-year period (2018-2019) using a global GNSS station network. Two implementations were conducted: one based on a GPS-only solution and the other using combined GNSS data (GPS+Galileo). The second implementation, as explained previously, was performed twice, first by applying the old ECOM model and then by introducing the new ECOM2 model (suited for the shape of Galileo satellites).

Furthermore, the regional ionosphere model, TUWR, was generated using the combined GNSS (GPS+Galileo) solution, employing a regional station network. To validate the significance of incorporating Galileo observations in these solutions, both the ERP time series and the ionosphere model were compared against well-established reference models.

The availability of RINEX3 files for both selected networks of stations was approximately 90%. All stations included in the ERP time series analysis were capable of tracking both GPS and Galileo satellites. On average, around 50 satellites were available per day: approximately 31 GPS and 16-24 Galileo satellites. Up until the end of July 2018, when 4 FOC Galileo satellites were launched into space, the average number of available Galileo satellites was 16. Following the launch, the number of available Galileo satellites has increased, ranging from 20 to 24. This significant increase in availability has led to an enhanced contribution of Galileo satellites, accounting for up to 44% of the overall satellite count. This represents a notable increase compared to the initial contribution of 34% observed during the first half of 2018.

The regional ionosphere model, as depicted in Figure 5.5 (see Section 5.2), is based on a network of 35 GNSS stations. Out of these stations, 19 are multi-GNSS stations (capable of tracking both GPS and Galileo satellites), whereas the remaining 16 stations are tracking GPS satellites only. With the availability of Galileo satellites, the multi-GNSS stations contribute up to 24% of the overall satellite count in the regional ionosphere modeling processing.

The extent to which the solutions have benefited from the inclusion of Galileo observations will be delved into in the following sections.

## 6.1. Earth rotation parameters (ERP)

### 6.1.1. Orbit fitting

Before starting the extensive calculation for the ERP time series, the daily orbital fit of Galileo satellites was tested by using a different setup and input for 6 days in January 2018. Figure 6.1 displays the resulting RMS values of 3 orbital fit scenarios depending on the used apriori orbit file and the applied solar radiation pressure model (SRP). The latter was introduced as a changing variable due to the impact of the solar radiation pressure on the orbit modeling itself, thus directly impacting the accuracy of GNSS orbits. Solar radiation pressure is the largest non-gravitational force impacting GNSS orbits, which has to be handled properly in terms of orbit modeling (Tseng and Moore, 2018).

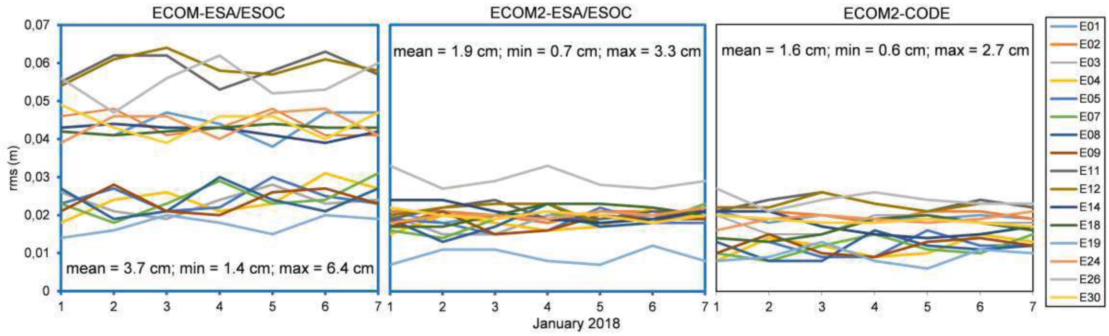


Figure 6.1: RMS values of orbital fit for Galileo satellites, showing three cases, left: ECOM SRP model + ESOC/ESA orbits, middle: ECOM2 SRP model + ESOC/ESA orbits and right: ECOM2 SRP model + CODE orbits.

The fit on the left plot was the outcome of using the precise multi-GNSS orbit files from ESOC/ESA[43] and applying the ECOM for the SRP modeling. The middle plot was generated based on the same precise multi-GNSS orbit files as in the left plot (ESOC/ESA), however, ECOM2 was utilized for the SRP modeling. In the right plot, again ECOM2 was used along with different orbit files. This time, using the final precise orbit files from CODE[44] (Dach et al., 2016).

It is clearly visible that the combination with the old ECOM model delivers the worst orbital fit for the Galileo satellites. This was expected, given that, at the time the ECOM was developed, it was adapted to suit the cubic-like shape of GPS satellites, thus, corresponding to GPS rather than to Galileo (Tseng and Moore, 2018). The mean coordinate RMS for this plot is 3.7 cm, which is approximately 2 times larger compared to the RMS values of the ECOM2 combinations, where the RMS of the middle plot amounts to 1.9 cm and for the right plot 1.6 cm. Satellite E26 (grey) in the ECOM2-ESA/ESOC (middle plot) combination is an exception, with showing an RMS in an orbital fit of 3.3 cm. The modified ECOM2 model contains one significant change for the Galileo constellation in particular. It was optimized

[43]Files are available at: http://navigation-office.esa.int/products/gnss-products
[44]Files are available at: http://www.aiub.unibe.ch/download/CODE

for elongated satellites, which are the shape of the Galileo satellites. Moreover, with the new ECOM2, even-order periodical perturbations in the direction satellite-sun were introduced (Tseng and Moore, 2018). The improvement in solar radiation pressure modeling is, without any doubt, reflected in the middle and right plots of Figure 6.1. The applied model allows fitting the orbits at the ± 3 cm level in both cases. One interesting observation regarding the ECOM case is the population of RMS orbital fits for the Galileo satellites. They are distributed according to their distribution within the orbital planes. There are three orbital planes within the Galileo constellation (Section 4.2) and in this plot, three more or less separated RMS groups can be distinguished.

The first two combinations, referring to the plots marked with blue borders in Figure 6.1, were chosen for the determination of the ERP time series (ECOM-ESA/ESOC and ECOM2-ESA/ESOC). The reason behind this selection lies actually in the objective of this work itself, to investigate the potential of adding Galileo to GPS observations. By using the old ECOM model and on the other hand the new ECOM2 model, the true potential of implementing Galileo can be revealed. First, it can be seen to which extent the observations themselves have an impact on improving the estimation, and second, going one step forward by applying a model more suited for the shape of Galileo satellites, it will be revealed how much the final results can be affected by this adaptation. The following results are therefore based on two approaches (GPS only and GPS/Galileo combined), where the combined approach is calculated twice: once by applying the old ECOM and in the second run by applying the new ECOM2 model. Since the improved SRP model won't show significant, if any, improvement when processing GPS-only observations, the first approach based on GPS observations was calculated only once, namely using the ECOM model.

### 6.1.2. Time series of pole coordinates and LoD

Figures 6.2 - 6.4 show the estimated polar motion time series in X coordinate w.r.t. the conventional IERS C04 14 reference model (Petit and Luzum, 2010) for the period January 2018 - December 2019. The temporal resolution of the estimated time series is 1 hour. On the other hand, the reference model consists of daily values. To ensure comparability, the reference time series was interpolated to increase its density and obtain compatible sets of parameters. Three solutions are shown, the 3-day arc solutions GPS+ECOM, GPS/Galileo+ECOM, and GPS/Galileo+ECOM2. They are plotted against each other in pairs.

The presented time series are the result of a previously performed outlier detection and removal, thus they can be considered as "clean" time series. The corresponding statistics are extracted and listed in Table 6.1 for both, 1-day and 3-day arc solutions. It is evident that the GPS-only solution exhibits a noticeably higher noise floor compared to the combined GPS/Galileo time series (depicted in Figures 6.2 and 6.3). In contrast to that, the comparison of the combined solutions illustrated in Figure 6.4 reveals minor discrepancies between the two solutions.

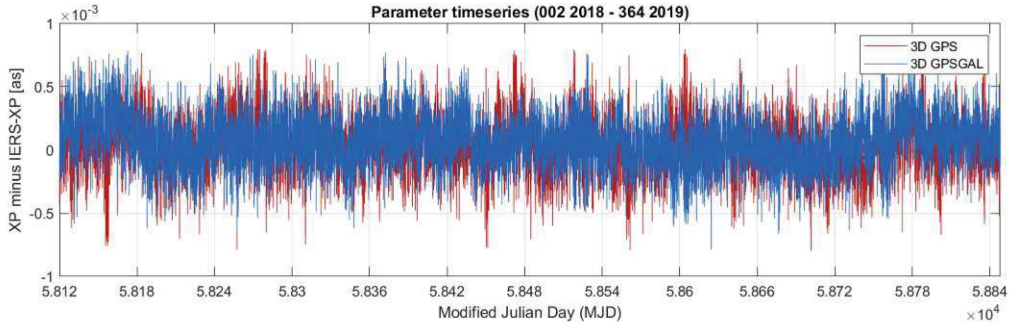


Figure 6.2: Polar motion time series (X coordinate) w.r.t. the IERS C04 14 reference model showing the 3-day arc GPS+ECOM (red) and GPS/Galileo+ECOM (blue) combined solutions (Jan 2018 - Dec 2019).

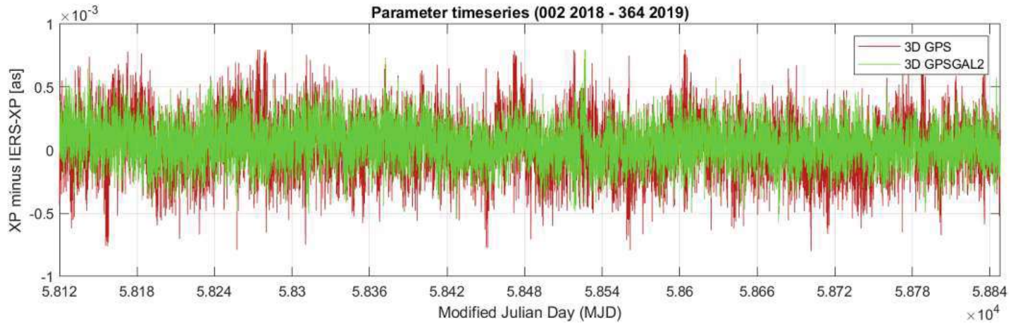


Figure 6.3: Polar motion time series (X coordinate) w.r.t. the IERS C04 14 reference model showing the 3-day arc GPS+ECOM (red) and GPS/Galileo+ECOM2 (green) combined solutions (Jan 2018 - Dec 2019).

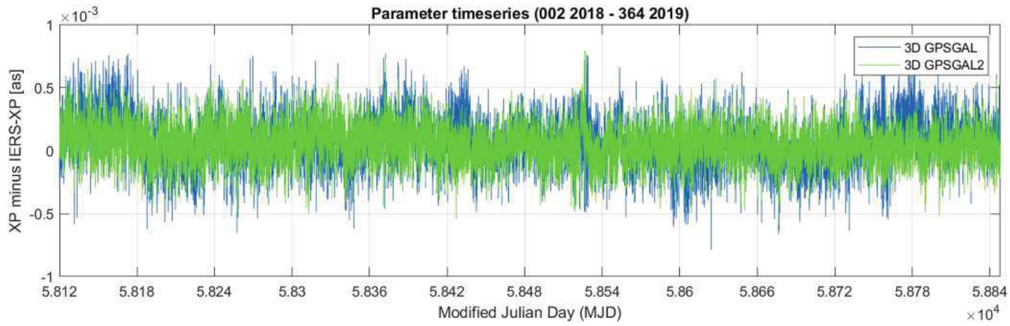


Figure 6.4: Polar motion time series (X coordinate) w.r.t. the IERS C04 14 reference model showing the 3-day arc GPS/Galileo+ECOM (blue) and GPS/Galileo+ECOM2 (green) combined solutions (Jan 2018 - Dec 2019).

This has been expected and makes sense considering the amount and nature of observations used in the combined solutions. This is further reflected in Table 6.1. In the case of the ECOM solutions, both 3-day arc time series show a slightly better performance compared to their respective 1-day arc solutions, in terms of mean, median, maximum value, as well as standard deviation.

Table 6.1: Statistics for all solutions w.r.t. the IERS C04 14 reference model extracted from the X pole coordinate time series. Numbers are given in mas.

| X pole | ECOM | | | | ECOM2 | |
|---|---|---|---|---|---|---|
| | 3D GPSGAL | 3D GPS | 1D GPSGAL | 1D GPS | 3D GPSGAL | 1D GPSGAL |
| Mean (abs.) | 0.17 | 0.17 | 0.18 | 0.18 | 0.13 | 0.13 |
| Median (abs.) | 0.14 | 0.14 | 0.15 | 0.15 | 0.11 | 0.11 |
| Max (abs.) | 0.79 | 0.80 | 0.80 | 0.80 | 0.80 | 0.74 |
| STD (+/-) | 0.20 | 0.22 | 0.22 | 0.22 | 0.15 | 0.16 |

The two ECOM2 solutions (1-day and 3-day arc) show almost the same outcome, with the differences that the 1-day arc solution has a smaller maximum value (0.74 mas) and the 3-day arc solution has a smaller standard deviation (± 0.15 mas). Overall, the ECOM2 time series shows a significant improvement in the X polar motion coordinate time series w.r.t. the reference model, when compared to the ECOM solutions, which can be seen in the mean value of all discrepancies w.r.t. the reference model. The discrepancies are 0.13 mas for both, the 1-day arc and 3-day arc GPS/Galileo+ECOM2 and its corresponding standard deviations ± 0.15 mas for the 3-day arc GPS/Galileo+ECOM2 and ± 0.16 mas for the 1-day arc GPS/Galileo+ECOM2. The largest standard deviation can be observed in the case of the 3-day arc GPS solution, being ± 0.22 mas (same as in the case of the two ECOM 1-day arc solutions). The time series of the X polar motion coordinate from all performed solutions (1-day and 3-day arcs) can be found in Figure A.1 (Appendix A.1).

Figures 6.5 - 6.7 show the estimated polar motion time series in Y coordinate w.r.t. the conventional IERS C04 14 reference model (Petit and Luzum, 2010) for the period January 2018 - December 2019. Again, three solutions are presented (a comparison of two different 3-day arc solutions in each plot). Their extracted statistics can be found in Table 6.2.

The statistics for the Y time series indicate that, again, the smallest disagreements compared to the reference model are achieved with the GPS/Galileo combined ECOM2 solution.

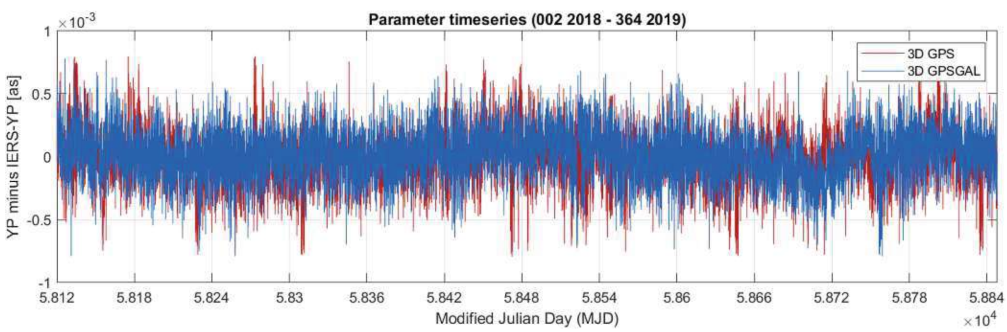


Figure 6.5: Polar motion time series (Y coordinate) w.r.t. the IERS C04 14 reference model showing the 3-day arc GPS+ECOM (red) and GPS/Galileo+ECOM (blue) combined solutions (Jan 2018 - Dec 2019).

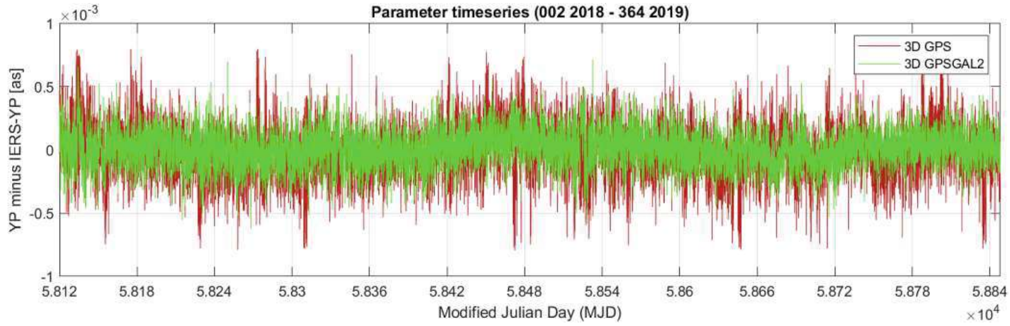


Figure 6.6: Polar motion time series (Y coordinate) w.r.t. the IERS C04 14 reference model showing the 3-day arc GPS+ECOM (red) and GPS/Galileo+ECOM2 (green) combined solutions (Jan 2018 - Dec 2019).

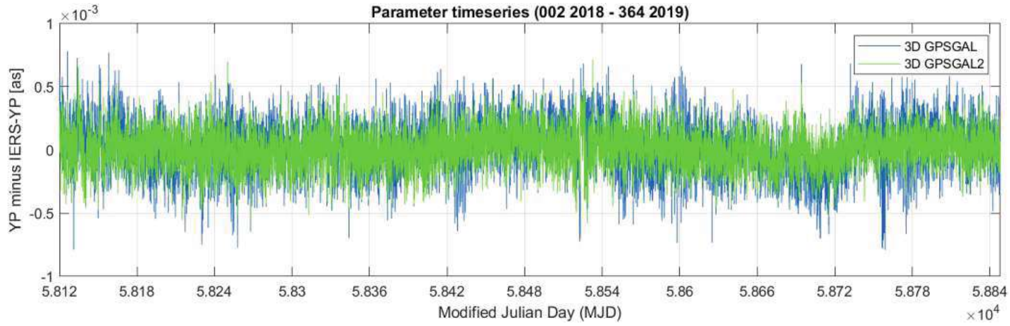


Figure 6.7: Polar motion time series (Y coordinate) w.r.t. the IERS C04 14 reference model showing the 3-day arc GPS/Galileo+ECOM (blue) and GPS/Galileo+ECOM2 (green) combined solutions (Jan 2018 - Dec 2019).

In this case, the 3-day arc shows slightly smaller coordinate RMS values compared to its 1-day arc time series. The mean of absolute differences is 0.12 mas, with a standard deviation of ± 0.15 mas and a maximum absolute difference of 0.71 mas for the 3-day GPS/Galileo+ECOM2 solution. It is interesting to note that in terms of the remaining ECOM 1-day arc solutions, the GPS-only series came closer to the values of the reference model, even though insignificantly closer than the GPS/Galileo combined solution. This is reflected in the median of absolute differences (1D GPS/GAL: 0.16 mas, 1D GPS: 0.14 mas) and in the standard deviation (1D GPS/GAL: ± 0.23 mas, 1D GPS: ± 0.22 mas).

Table 6.2: Statistics for all solutions w.r.t. the IERS C04 14 reference model extracted from the Y pole coordinate time series. Numbers are given in mas.

| Y pole | ECOM | | | | ECOM2 | |
|---|---|---|---|---|---|---|
| | 3D GPSGAL | 3D GPS | 1D GPSGAL | 1D GPS | 3D GPSGAL | 1D GPSGAL |
| Mean (abs.) | 0.15 | 0.16 | 0.18 | 0.18 | 0.12 | 0.13 |
| Median (abs.) | 0.13 | 0.13 | 0.16 | 0.14 | 0.10 | 0.10 |
| Max (abs.) | 0.79 | 0.80 | 0.80 | 0.80 | 0.71 | 0.79 |
| STD (+/-) | 0.19 | 0.21 | 0.23 | 0.22 | 0.15 | 0.16 |

The time series of the Y polar motion coordinate from all performed solutions (1-day and 3-day arcs) can be found in Figure A.2 (Appendix A.1). The amplitude spectrum of polar motion for the different solutions is demonstrated in Figures 6.8 - 6.10.

The spectrum reveals remaining signals in the diurnal and semi-diurnal prograde band. The 3D GPS+ECOM time series (red) shows the highest noise floor, as probably expected considering the previously shown results. The two combined solutions (Figure 6.10) are quite comparable, having similar amplitudes for $n$ cycle/day, when $n$>4. For the remaining cycles/day, as well as for the diurnal band, the 3D GPS/Galileo+ECOM2 time series (green) shows smaller amplitudes compared to the 3D GPS/Galileo+ECOM time series (blue).

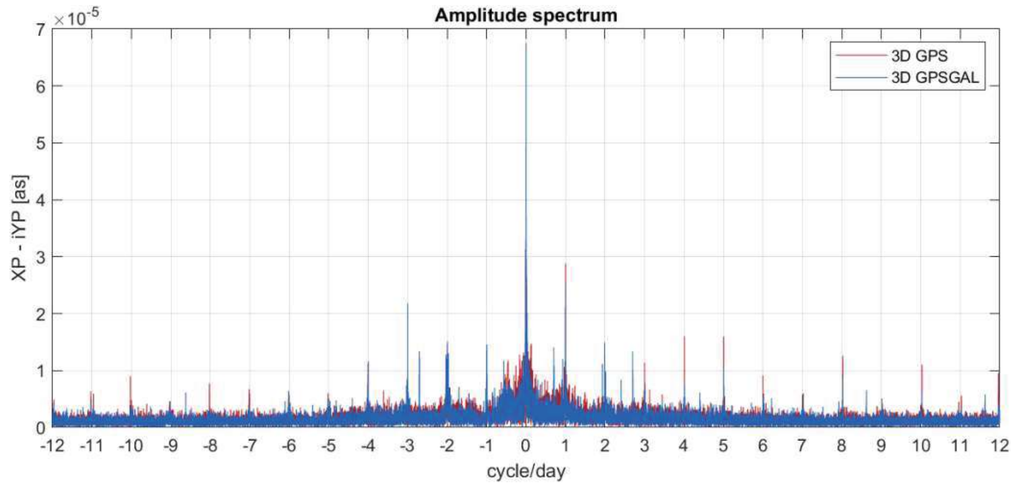


Figure 6.8: XY amplitude spectrum showing the 3-day arc combined solutions GPS+ECOM (red) and GPS/Galileo+ECOM (blue) (Jan 2018 - Dec 2019).

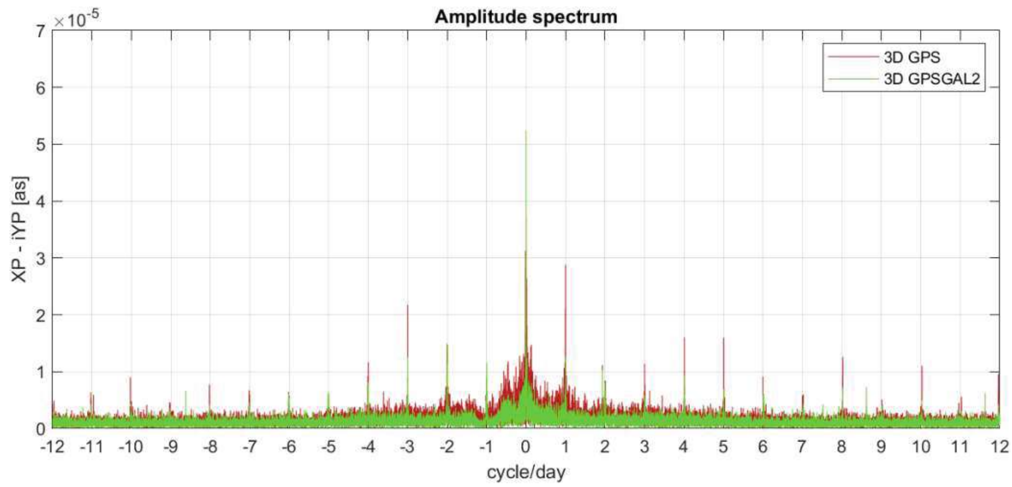


Figure 6.9: XY amplitude spectrum showing the 3-day arc combined solutions GPS+ECOM (red) and GPS/Galileo+ECOM2 (green) (Jan 2018 - Dec 2019).

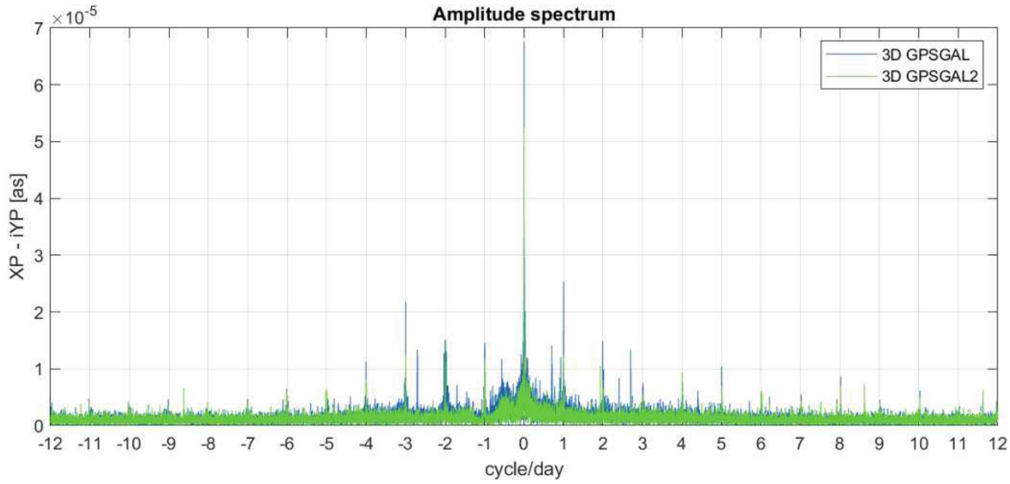


Figure 6.10: XY amplitude spectrum showing the 3-day arc combined solutions GPS/Galileo+ECOM (blue) and GPS/Galileo+ECOM2 (green) (Jan 2018 - Dec 2019).

The highest recorded peaks in the prograde band of the amplitude spectrum are 0.029 mas (3D GPS+ECOM (red)), 0.25 mas (3D GPS/Galileo+ECOM (blue)), and 0.013 mas (3D GPS/Galileo+ECOM2 (green)). The improvement in noise level is clearly visible when comparing the 3-day arc GPS/Galileo+ECOM2 solution to the remaining solution types.

However, artifacts still remain in the prograde diurnal and semi-diurnal bands. These peaks, or higher harmonics in the spectra at $n$ cycle/day can be attributed to the 1h data sampling. Plots of the XY amplitude spectrum of all performed solutions (1-day and 3-day arcs) can be found in Figure A.5 (Appendix A.1).

Figures 6.11 - 6.13 show the estimated polar motion time series in LoD w.r.t. the conventional IERS C04 14 reference model (Petit and Luzum, 2010) for the period January 2018 - December 2019. As in the previous time series plots, the three 3-day arc solutions are shown pairwise in a direct comparison against each other. Their corresponding statistics with values for all performed solutions are displayed in Table 6.3.

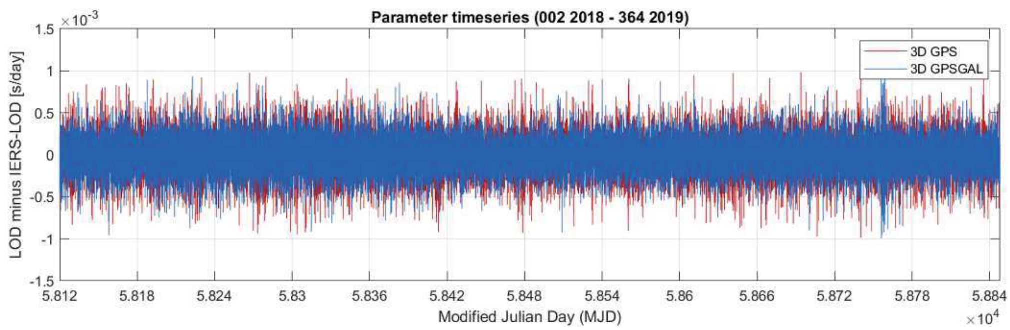


Figure 6.11: Polar motion time series (LoD) w.r.t. the IERS C04 14 reference model showing the 3-day arc GPS+ECOM (red) and GPS/Galileo+ECOM (blue) combined solutions (Jan 2018 - Dec 2019).

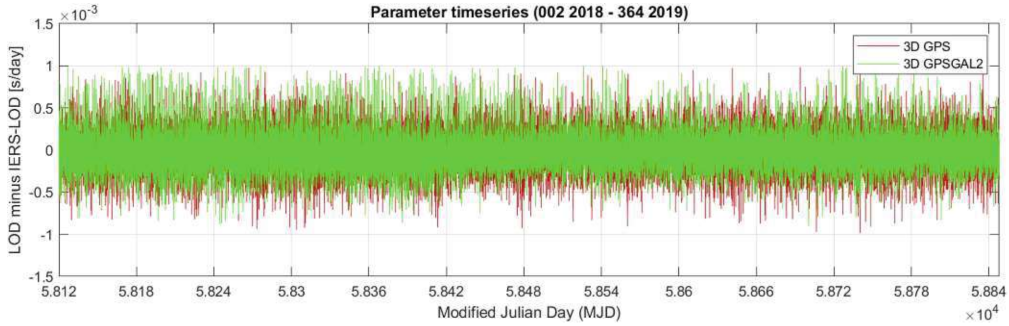


Figure 6.12: Polar motion time series (LOD) w.r.t. the IERS C04 14 reference model showing the 3-day arc GPS+ECOM (red) and GPS/Galileo+ECOM2 (green) combined solutions (Jan 2018 - Dec 2019).

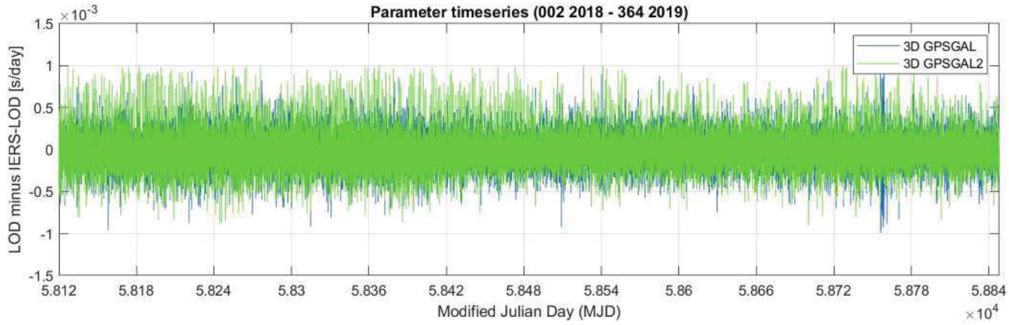


Figure 6.13: Polar motion time series (LOD) w.r.t. the IERS C04 14 reference model showing the 3-day arc combined solutions GPS/Galileo+ECOM (blue) and GPS/Galileo+ECOM2 (green) (Jan 2018 - Dec 2019).

In this case, the agreement of the 3-day arc solutions with the reference model is quite similar, with the GPS-only solution (red) showing again the highest noise floor. Unlike before, the best agreement w.r.t. reference model among the 3-day arc solutions was achieved with the 3D GPS/Galileo+ECOM solution (blue). On the other hand, the 1-day arc GPS/Galileo+ECOM2 (see Table 6.3) shows the best agreement w.r.t. reference model statistic-wise (mean: 0.17 ms/day, max: 0.98 ms/day, std: ± 0.21 ms/day). This means that in LoD, longer arc time series did not improve the solutions when assuming that the used reference value represents the true value.

Still, by comparing the GPS-only solution against the GPS/GAL combined solutions, both combined solutions reveal either the same or smaller differences w.r.t. the reference model (3D GPS/GAL+ECOM mean: 0.18 ms/day, 3D GPS+ECOM mean: 0.21 ms/day, 3D GPS/GAL +ECOM2 mean: 0.19 ms/day; 3D GPS/GAL+ECOM std: ± 0.23 ms/day, 3D GPS+ECOM std: ± 0.26 ms/day, 3D GPS/GAL+ECOM2 std: ± 0.26 ms/day). The LoD time series of all performed solutions (1-day and 3-day arc) can be found in Figure A.3 (Appendix A.1).

Comparisons of the raw LOD time series to the conventional IERS C04 14 reference model (Petit and Luzum, 2010) for the period January 2018 - December 2019 are shown in Figures 6.14 - 6.16. Please note, unlike in Figures 6.11 - 6.13, the raw LoD time series are not differences w.r.t. the reference model, but provide an insight into the actual LoD values calculated by the different solutions, plotted against the reference model.

Table 6.3: Statistics for all solutions w.r.t. the IERS C04 14 reference model extracted from the LoD pole coordinate time series. Numbers are given in ms/day.

| LOD | ECOM | | | | ECOM2 | |
|---|---|---|---|---|---|---|
| | 3D GPSGAL | 3D GPS | 1D GPSGAL | 1D GPS | 3D GPSGAL | 1D GPSGAL |
| Mean (abs.) | 0.18 | 0.21 | 0.18 | 0.21 | 0.19 | 0.17 |
| Median (abs.) | 0.15 | 0.17 | 0.15 | 0.17 | 0.16 | 0.14 |
| Max (abs.) | 0.99 | 0.98 | 0.98 | 1.00 | 1.00 | 0.98 |
| STD (+/-) | 0.23 | 0.26 | 0.23 | 0.26 | 0.26 | 0.21 |

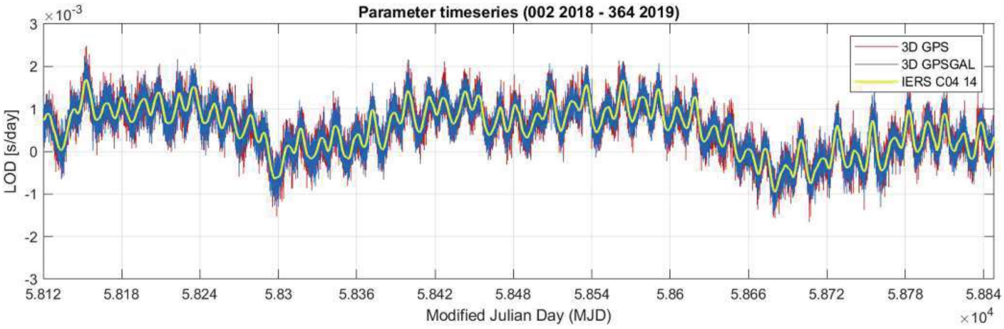


Figure 6.14: Polar motion time series (raw LoD) showing the 3-day arc GPS+ECOM (red) and GPS/Galileo+ECOM (blue) combined solutions along with the IERS C04 14 reference model (Jan 2018 - Dec 2019).

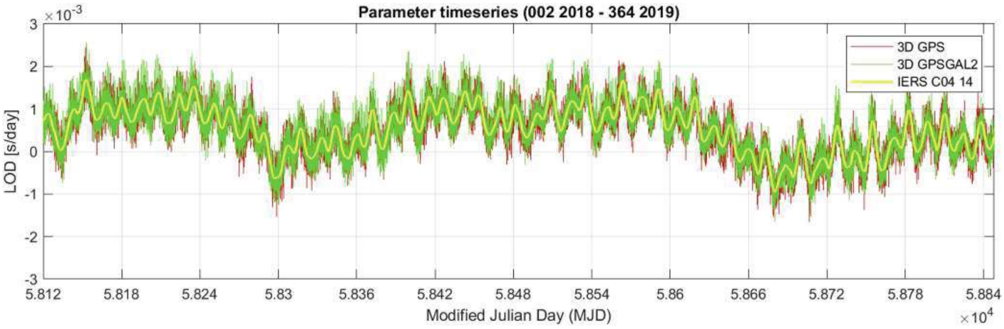


Figure 6.15: Polar motion time series (raw LoD) showing the 3-day arc GPS+ECOM (red) and GPS/Galileo+ECOM2 (green) combined solutions along with the IERS C04 14 reference model (Jan 2018 - Dec 2019).

The three solutions are again presented pairwise, together with the IERS C04 14 time series. The signal noise appears to be the least pronounced for the 3D GPS/Galileo+ECOM solution (blue), even though all time series appear to have a comparable noise floor. This only confirms the previously shown results in Figures 6.11 and 6.13, as well as in Table 6.3. The raw LoD time series of all performed solutions (1-day and 3-day arcs) can be found in Figure A.4 (Appendix A.1).

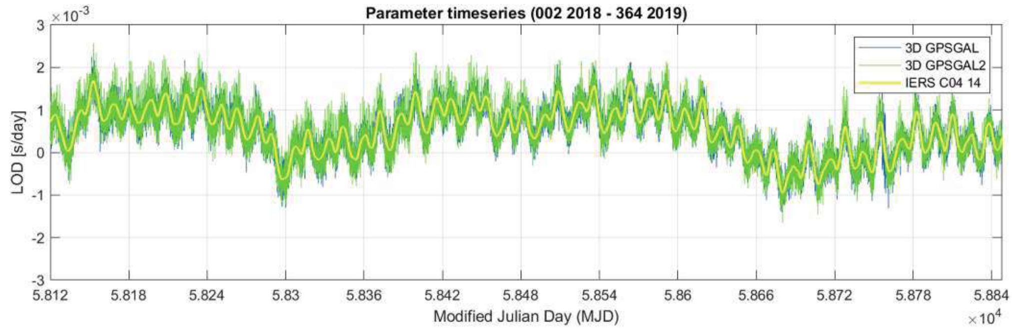


Figure 6.16: Polar motion time series (raw LoD) showing the 3-day arc GPS/Galileo+ECOM (blue) and GPS/Galileo+ECOM2 (green) combined solutions along with the IERS C04 14 reference model (Jan 2018 - Dec 2019).

The LoD amplitude spectrum of polar motion for the different solutions is demonstrated in figures 6.17 - 6.19. The spectrum reveals remaining signals in the diurnal and semi-diurnal bands, reaching up to 0.024 ms/day for the 3D GPS/Galileo+ECOM solution, 0.038 ms/day for the 3D GPS+ECOM solution, and 0.070 ms/day for the 3D GPS/Galileo+ECOM2 solution. It is important to note that these prominent peaks occur exactly at $n$ cycles/day in all solutions, revealing the presence of remaining artifacts caused by the 1-hour data sampling, as observed in the amplitude spectra of polar motions in Figures 6.8-6.10.

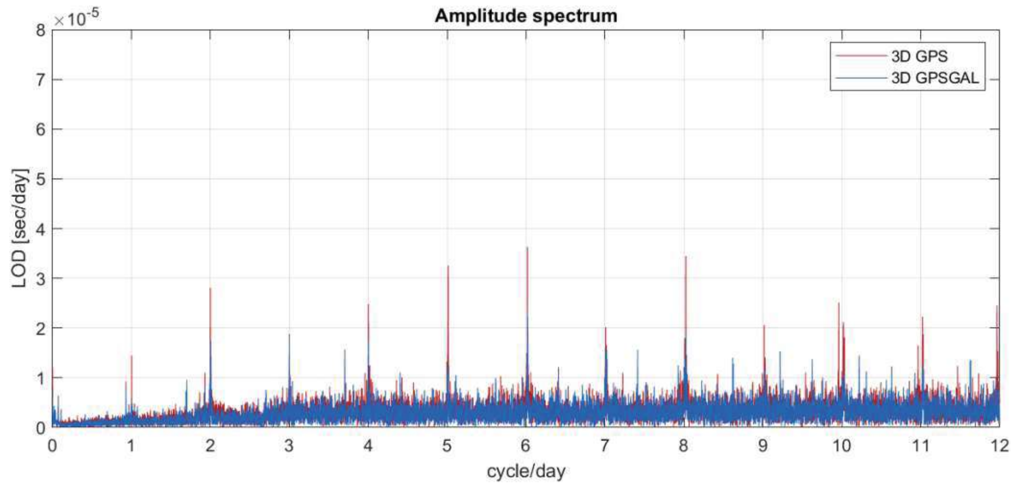


Figure 6.17: LoD amplitude spectrum showing the 3-day arc combined solutions GPS+ECOM (red) and GPS/Galileo+ECOM (blue) (Jan 2018 - Dec 2019).

The noise floor is the lowest in the case of the 3D GPS/Galileo+ECOM2 time series compared to the remaining two datasets, as seen from Figures 6.18 and 6.19. Plots of the LoD amplitude spectrum from all performed solutions (1-day and 3-day arcs) can be found in Figure A.6 (Appendix A.1).

Corresponding ocean tide coefficients can be retrieved from all time series (1-day arc and 3-day arc), at the diurnal, as well as the semi-diurnal frequencies, which has been carried out in the following step. Moreover, ocean tide coefficients for the 8 major ocean tides and their comparison to chosen reference models will be shown in the following section (Section 6.1.3).

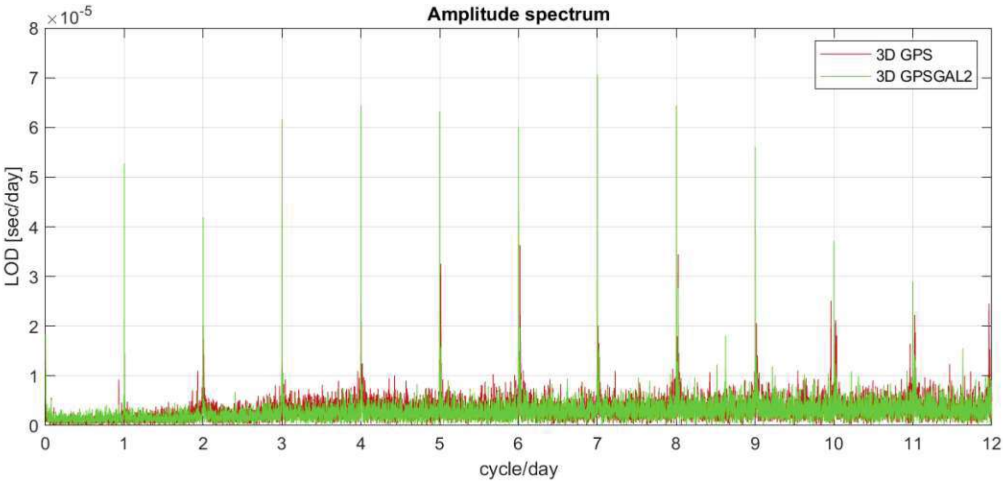


Figure 6.18: LoD amplitude spectrum showing the 3-day arc combined solutions GPS+ECOM (red) and GPS/Galileo+ECOM2 (green) (Jan 2018 - Dec 2019).

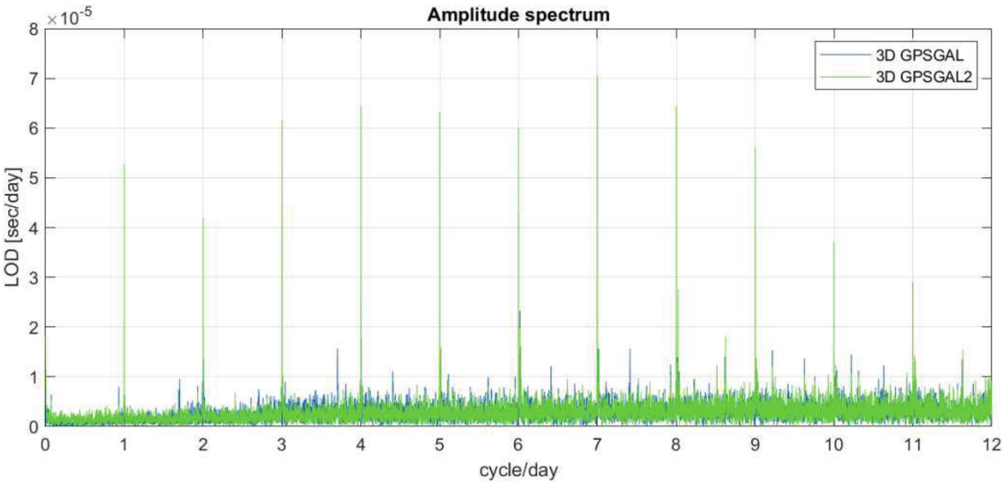


Figure 6.19: LoD amplitude spectrum showing the 3-day arc combined solutions GPS/Galileo+ECOM (blue) and GPS/Galileo+ECOM2 (green) (Jan 2018 - Dec 2019).

The mean of formal errors of estimated ERP parameters for the applied combinations of ECOM with GPS and GPS/Galileo, as well as ECOM2 with GPS/Galileo are presented in Table 6.4. As expected, based on the results shown up to now, within the ECOM group of solutions, the 3D GPS/Galileo reveals the smallest mean formal errors for all four estimated ERP time series. The formal errors are 0.055 mas and 0.080 mas for the X and Y pole coordinates respectively, while the LoD formal error is 0.007 ms/day. This solution is closely followed by the 1-day arc version of the combined GPS/Galileo solution. Significantly larger formal errors appear in the GPS-only solutions, with the X and Y formal errors being approximately twice the size of the errors in the combined solutions. Formal errors in LoD are slightly higher by 0.002 ms/day in both, the 1-day arc and 3-day arc solutions. The combination of GPS and Galileo data in the processing has improved the formal errors of the estimated ERPs, especially in terms of pole coordinates.

Further significant improvement in formal errors was achieved with the change from ECOM to ECOM2, which can be seen in Table 6.4 for both, 1-day arc and 3-day arc GPS/Galileo combined solutions. Compared to the ECOM combined solution, their formal errors are approximately half the size, with the 1-day arc time series having even smaller numbers. The mean formal errors derived from the 3D GPS/Galileo+ECOM2 time series in X and Y pole coordinates are 0.033 mas and 0.041 mas respectively, while the associate 1-day arc dataset delivers mean formal errors of 0.020 mas and 0.024 mas in X and Y pole coordinate respectively. On the other hand, no significant improvement was achieved in terms of LoD formal errors. The two ECOM2 datasets provide the same mean formal error as the 3D GPS/Galileo+ECOM time series (0.007 ms/day). However, this also means that no deterioration in the LoD formal errors was found.

Table 6.4: Mean of formal errors of estimated ERP parameters for all performed solutions (numbers for the pole coordinates are given in mas, numbers for LoD are given in ms/day).

| | ECOM | | | | ECOM2 | |
|---|---|---|---|---|---|---|
| | 3D GPS/GAL | 3D GPS | 1D GPS/GAL | 1D GPS | 3D GPS/GAL | 1D GPS/GAL |
| Xp | 0.055 | 0.166 | 0.066 | 0.175 | 0.033 | 0.020 |
| Yp | 0.080 | 0.164 | 0.108 | 0.166 | 0.041 | 0.024 |
| LoD | 0.007 | 0.010 | 0.008 | 0.010 | 0.007 | 0.007 |

In general, integrating a combined GNSS solution along with the inclusion of the ECOM2 model for solar radiation pressure, particularly when utilizing Galileo observation data, promises to enhance both the final results as well as their corresponding errors. Table 6.4 presents a progressive upgrade in formal errors, first by comparing 3-day arc to 1-day arc solutions in the ECOM time series, then further by adding Galileo observations to the GPS solution, and finally, by using an SRP model more fitted for the shape and differently illuminated surface of the Galileo satellites. However, it should be noted that the 1-day arc ECOM2 solution is comparable, if not superior, to its 3-day arc counterpart in terms of quality and accuracy.

### 6.1.3. Tidal coefficients for 8 major tidal waves

Finally, amplitude corrections for the 8 main tidal waves (described in Section 2.3.3) were derived from the 1-day and 3-day arc time series of all solution types (GPS+ECOM, GPS/Galileo +ECOM, and GPS/Galileo+ECOM2). Tidal coefficient corrections were calculated w.r.t. three different reference models, two of them being based on ocean tide models, namely Desai-Sibois (Desai and Sibois, 2016) and IERS2010 (Petit and Luzum, 2010), and the third one being an empirical model, namely Gipson (Gipson and Hesslow, 2015), all mentioned and discussed in Section 2.4. First, all time series were prepared for the tidal amplitude estimation. This was achieved by cleaning the data from outliers (w.r.t. the IERS C04 time series[45]). Later on, amplitudes of ocean tidal variation in polar motion and LoD from the GNSS-based ERP time series were calculated via a least-squares adjustment (LSA). The LSA was performed twice. In the first run, a total of 71 periods were obtained through this adjustment for each time series, including 40 diurnal, 30 semi-diurnal, and 1 terdiurnal (the total number of periods in the IERS model).

In the second run, only the subset of 8 major tidal constituents was acquired through the LSA. In this work, the focus remains on the 8 major tidal waves and thus, those will be shown in the following plots, first them being extracted from the full estimated set of 71 periods (later in the text referred to as "Full Set Adjustment", or short "FSA") and second, the results being derived from the subset estimation (later in the text referred to as "Subset Adjustment", or short "SSA"). In the following figures, four solutions were chosen to be presented, namely all three 3-day arc solutions (GPS+ECOM, GPS/Galileo+ECOM, and GPS/Galileo+ECOM2) and one 1-day arc solution (GPS/Galileo+ECOM2). The selection was based on their performance, i.e. agreement w.r.t. the reference models. The remaining two 1-day arc solutions (GPS+ECOM and GPS/Galileo+ECOM) have revealed considerably larger differences, thus they are not presented in a direct comparison. Amplitude corrections for the 8 main tidal waves from all performed solutions, can be found in Appendix A.2.1 for the FSA-based amplitude corrections and in Appendix A.2.2 for the SSA-based amplitude corrections.

Figure 6.20 shows the pole X-component tidal coefficient corrections for the 8 major tidal waves w.r.t. the (a) Desai-Sibois, (b) IERS2010, and (c) Gipson model. The largest corrections are shown for tidal constituents P1 and K1 in the diurnal band and S2 and K2 in the semi-diurnal band. The P1 and S2 corrections have the largest amplitude when using the 3D GPS/Galileo+ECOM (blue) solution (25-30 $\mu$as for P1 and 17-22 $\mu$as for S2 w.r.t. all reference models), while K1, and especially K2 have resulted in the largest amplitude corrections w.r.t. all reference models when applying the 3D GPS+ECOM (red) solution ($\sim$25 $\mu$as for K1 w.r.t. Desai-Sibois and IERS2010 and 11 $\mu$as w.r.t. Gipson, and 43-45 $\mu$as for K2). In general, the ECOM2 solutions deliver in most cases smaller amplitude corrections w.r.t. chosen reference models, with a few exceptions, for example, tide P1 ((a) Desai-Sibois and (c) Gipson in Figure 6.20) and M2 (all models in Figure 6.20), where the 3D GPS+ECOM solution has shown considerably smaller amplitude corrections overall, meaning having a better agreement with the reference models in these cases. Still, these comparisons are model-dependent and one model might agree better with a solution than the other. Overall, the best agreement among all solutions w.r.t. the reference models was achieved with the 1D GPS/Galileo+ECOM2 (light green) solution, which is closely followed by its 3-day arc

[45] Available at the IERS Datacenter:
https://datacenter.iers.org/versionMetadata.php?filename=latestVersionMeta/224_EOP_C04_14.62-NOW.IAU2000A224.txt/

solution (green) and in some cases surpassed by it (for example the diurnal tide O1 for all reference models, the semi-diurnal N2 in the case of Desai-Sibois and Gipson, and the semi-diurnal S2 in the case of IERS2010 and Gipson). The highest amplitude corrections were recorded in both cases (1-day arc and 3-day arc GPS/Galileo+ECOM2) w.r.t. the Desai-Sibois and IERS2010 reference model for the diurnal K1 tidal wave, where the 1D solution has shown corrections up to ∼10 $\mu$as and the 3D solution corrections up to ∼25 $\mu$as. Except for P1 and K1, which have shown the highest amplitudes for the ECOM2 solutions, differences w.r.t. the reference models for the remaining tides have shown to be below 10 $\mu$as. The inclusion of Galileo satellites, which contribute up to 44% of the overall observation count, has resulted in an improvement in the global solution. This improvement is reflected in a better agreement with the reference models. Furthermore, the utilization of the new ECOM2 model has significantly reduced the amplitude correction for the main tidal waves compared to all reference models.

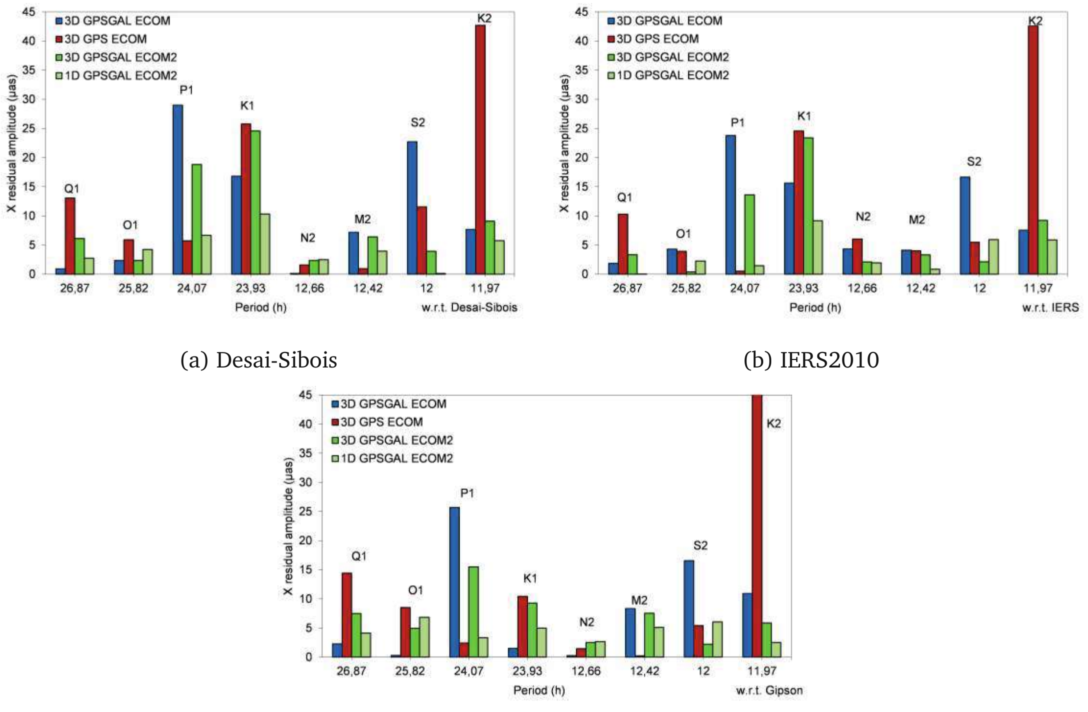


(a) Desai-Sibois

(b) IERS2010

(c) Gipson

Figure 6.20: Pole X-component amplitude corrections showing all 3-day arc (GPS+ECOM, GPS/Galileo+ECOM, GPS/Galileo+ECOM2) and one 1-day arc (GPS/Galileo+ECOM2) GNSS solution w.r.t. different sub-daily models (derived from the full set adjustment).

The pole Y-component tidal coefficient corrections for the 8 major tidal waves w.r.t. the three reference models are introduced in Figure 6.21 below. The major tidal constituents this time are the same two diurnal tides as in the pole X-component, namely P1 (being dominated by the amplitude corrections of the 3D GPS/Galileo+ECOM (blue) solution by 29 $\mu$as w.r.t. Desai-Sibois and ∼25 $\mu$as w.r.t. IERS2010 and Gipson) and K1 (with the maximum corrections derived from the 3D GPS+ECOM solution (red): ∼25 $\mu$as w.r.t. Desai-Sibois and IERS2010 and ∼10 $\mu$as w.r.t. Gipson). Corrections for the semi-diurnal tides did not reveal pronounced amplitudes in the pole Y-component. The major tidal constituent, when observing the two ECOM2 solutions only, is again the diurnal tidal wave K1 (up to 25 $\mu$as when applying the 3-day arc GPS/Galileo+ECOM2 solution (green)), whereby slightly larger amplitude corrections can be found for the diurnal tidal wave P1, being within the range of 14-18 $\mu$as (when applying the 3-day arc GPS/Galileo+ECOM2 solution (green)) w.r.t. Desai-Sibois and IERS2010 reference models. This time, neither did the 1-day arc ECOM2 (light green) reveal any peaks among the amplitude corrections, nor did pronounced amplitude corrections appear when comparing both ECOM2 solutions to the Gipson reference model. If attention is paid to all tidal waves aside from the diurnal P1 and K1, all amplitude corrections for both ECOM2 models show values $< 7$ $\mu$as w.r.t. Desai-Sibois, $< 5$ $\mu$as w.r.t. IERS2010, and $< 13$ $\mu$as w.r.t. Gipson.

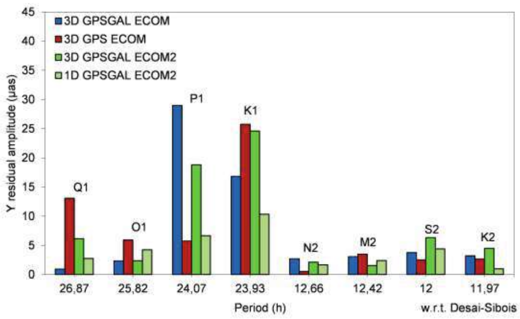


(a) Desai-Sibois

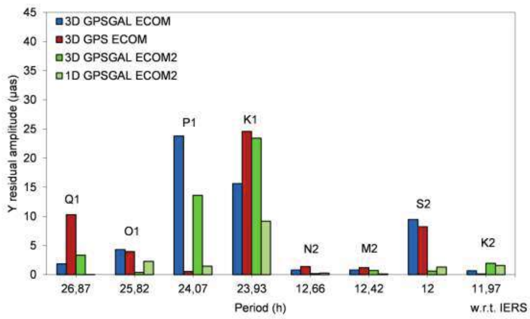


(b) IERS2010

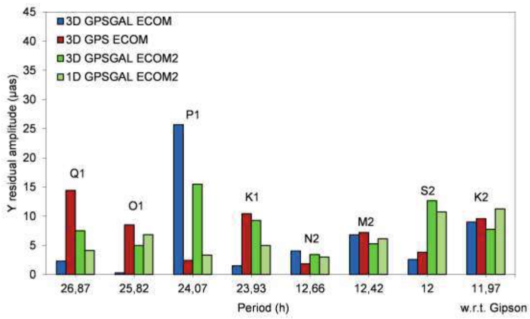


(c) Gipson

Figure 6.21: Pole Y-component amplitude corrections showing all 3-day arc (GPS+ECOM, GPS/Galileo+ECOM, GPS/Galileo+ECOM2) and one 1-day arc (GPS/Galileo+ECOM2) GNSS solution w.r.t. different sub-daily models (derived from the full set adjustment).

Figure 6.22 shows the LoD amplitude corrections for the 8 major tidal waves w.r.t. the three reference models. The major constituents when comparing LoD amplitude corrections are the diurnal tidal waves P1 and K1, and the semi-diurnal M2, S2, and K2. It is clearly visible that w.r.t. all reference models the 3D GPS+ECOM solution experiences the largest amplitude corrections (the highest being P1 w.r.t. Desai-Sibois and Gipson: 20-23 $\mu$s/day and

M2 w.r.t. IERS2010: 23 $\mu$s/day). Aside from one obvious exception, where the amplitude corrections for the semi-diurnal tidal term S2 in the case of Desai-Sibois and Gipson were clearly larger for both ECOM2 solutions compared to the 3D GPS/Galileo+ECOM solution (17 $\mu$s/day, 15 $\mu$s/day, and even <1 $\mu$s/day w.r.t. Desai-Sibois, and 14 $\mu$s/day, 12 $\mu$s/day, and 3$\mu$s/day w.r.t. Gipson for the 3D GPS/Galileo+ECOM2, 1D GPS/Galileo+ECOM2 and 3D GPS+ECOM solution respectively), the majority of tidal term corrections reveal a distinct improvement in agreement with the three reference models. For the two ECOM2 solutions, the largest amplitude differences among the major tidal constituents are observed for S2 w.r.t. Desai-Sibois and Gipson, M2 w.r.t. IERS2010, and K2 only for the 3-day arc solution w.r.t. all reference models. Overall, the ECOM2-based amplitude corrections, except for the already mentioned major constituents, do not exceed 5 $\mu$s/day on average w.r.t. the reference models.

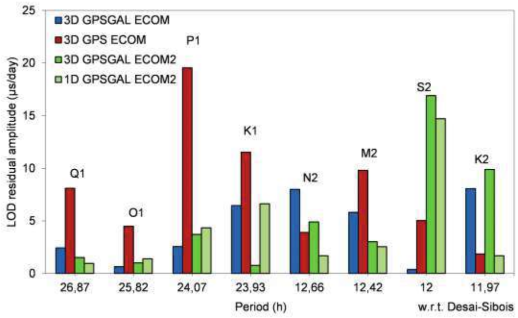


(a) Desai-Sibois

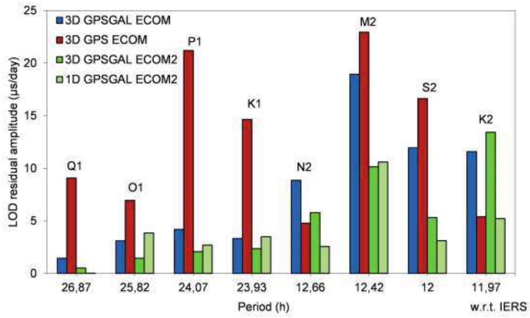


(b) IERS2010

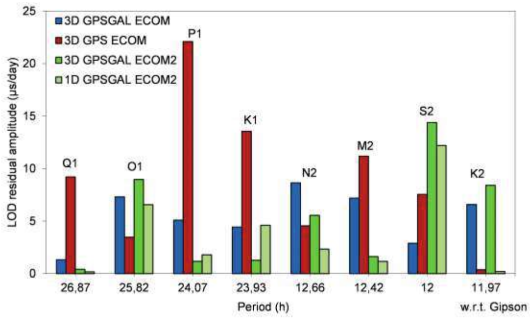


(c) Gipson

Figure 6.22: LoD amplitude corrections showing all 3-day arc (GPS+ECOM, GPS/Galileo+ECOM, GPS/Galileo+ECOM2) and one 1-day arc (GPS/Galileo+ECOM2) GNSS solution w.r.t. different sub-daily models (derived from the full set adjustment).

The application of the ECOM2 model has not only significantly improved the amplitude corrections compared to the reference models but has also been strengthened by the increased percentage of Galileo observations contributing to the final solution. One reliable indicator of this improvement is, for example, the enhanced agreement of the semidiurnal tide K2 with all selected reference models in Figure 6.20 (from ~45 $\mu$as w.r.t. all reference models improvement to ~10 $\mu$as w.r.t. all reference models). As shown in Table 2.2

(Periods of principal tidal constituents), semidiurnal wave K2 has a period of 11.97 hours (Section 2.3.3), which coincides with the GPS revolution period. When the satellite revolution period aligns with the tidal wave cycle, it can introduce systematic errors in GNSS-based measurements. This occurs because the gravitational forces influencing ocean tides can also impact the signals transmitted from satellites to receivers during these periods. The prominent amplitude correction observed in the semi-diurnal tidal constituent K2 (Figure 6.20) can be attributed to orbital signals arising from resonance between the Earth's rotation and the satellite revolution period. In the case of the 3D GPS+ECOM (red) solution, which relies solely on GPS observations, the period of the K2 tide aligns with the orbital period of GPS satellites. The same goes for the constant larger amplitude corrections for tidal wave K1 w.r.t. all reference models, when using the GPS-only solution, observed in both polar motion and LoD (Figures 6.20-6.22), due to the K1 period (23.93h) aligning with the GPS ground repeat period. However, these periodic effects caused by tidal forces have been successfully mitigated by incorporating Galileo observations. It is important to note that the revolution period of Galileo satellites is 14.08 hours (see Table 4.1), which means that Galileo-based observations are not influenced by the gravitational forces responsible for the luni-solar semidiurnal K2 tidal wave.

A direct comparison of all performed solutions (1-day arc and 3-day arcs) can be found in Figures A.7-A.9 in Appendix A.2.1. The corresponding numerical values of amplitude corrections derived from all solutions are given in Table 6.5.

Table 6.5: Tidal corrections of diurnal and semidiurnal variations on pole coordinates (X, Y) and LoD caused by the 8 major ocean tides w.r.t. the Desai-Sibois, IERS2010 and Gipson reference model (derived from the full set adjustment).

| Tide | 3D GPSGAL ECOM | | | 3D GPS ECOM | | | 1D GPSGAL ECOM | | | 1D GPS ECOM | | | 3D GPSGAL ECOM2 | | | 1D GPSGAL ECOM2 | | | Period |
|---|---|---|---|---|---|---|---|---|---|---|---|---|---|---|---|---|---|---|---|
| | X | Y | LOD | X | Y | LOD | X | Y | LOD | X | Y | LOD | X | Y | LOD | X | Y | LOD | (h) |
| **Desai-Sibois** | | | | | | | | | | | | | | | | | | | |
| **Q1** | 0.92 | 0.92 | 2.42 | 13.07 | 13.07 | 8.09 | 2.78 | 2.79 | 2.58 | 15.41 | 15.41 | 0.73 | 6.13 | 6.13 | 1.50 | 2.75 | 2.75 | 0.95 | **26.87** |
| **O1** | 2.34 | 2.33 | 0.65 | 5.90 | 5.91 | 4.49 | 1.42 | 1.41 | 2.99 | 7.32 | 7.33 | 9.90 | 2.35 | 2.36 | 1.01 | 4.22 | 4.23 | 1.39 | **25.82** |
| **P1** | 28.98 | 28.98 | 2.55 | 5.72 | 5.72 | 19.55 | 32.80 | 32.80 | 5.11 | 35.83 | 35.83 | 22.90 | 18.81 | 18.81 | 3.70 | 6.65 | 6.65 | 4.34 | **24.07** |
| **K1** | 16.81 | 16.81 | 6.44 | 25.75 | 25.75 | 11.52 | 41.41 | 41.41 | 17.28 | 54.68 | 54.68 | 0.55 | 24.58 | 24.58 | 0.76 | 10.33 | 10.33 | 6.62 | **23.93** |
| **N2** | 0.10 | 2.70 | 7.98 | 1.59 | 0.52 | 3.89 | 4.53 | 0.65 | 5.00 | 0.06 | 0.19 | 3.81 | 2.35 | 2.10 | 4.89 | 2.50 | 1.66 | 1.67 | **12.66** |
| **M2** | 7.19 | 3.06 | 5.81 | 0.93 | 3.47 | 9.80 | 0.67 | 3.32 | 8.02 | 3.81 | 1.85 | 9.39 | 6.39 | 1.53 | 3.00 | 3.94 | 2.38 | 2.54 | **12.42** |
| **S2** | 22.72 | 3.75 | 0.37 | 11.55 | 2.51 | 5.03 | 35.69 | 4.37 | 3.31 | 40.14 | 10.29 | 4.41 | 3.94 | 6.31 | 16.90 | 0.12 | 4.40 | 14.70 | **12** |
| **K2** | 7.68 | 3.22 | 8.05 | 42.69 | 2.66 | 1.84 | 20.81 | 11.44 | 7.21 | 47.42 | 5.02 | 3.35 | 9.11 | 4.48 | 9.88 | 5.75 | 0.97 | 1.67 | **11.97** |
| **IERS2010** | | | | | | | | | | | | | | | | | | | |
| **Q1** | 1.86 | 1.86 | 1.44 | 10.28 | 10.29 | 9.07 | 0.00 | 0.00 | 1.60 | 12.63 | 12.63 | 1.71 | 3.34 | 3.35 | 0.52 | 0.03 | 0.03 | 0.03 | **26.87** |
| **O1** | 4.30 | 4.29 | 3.10 | 3.94 | 3.95 | 6.94 | 3.38 | 3.37 | 5.44 | 5.36 | 5.37 | 12.35 | 0.39 | 0.40 | 1.44 | 2.26 | 2.27 | 3.84 | **25.82** |
| **P1** | 23.79 | 23.79 | 4.19 | 0.53 | 0.53 | 21.18 | 27.60 | 27.60 | 6.75 | 30.64 | 30.64 | 24.54 | 13.61 | 13.61 | 2.06 | 1.46 | 1.46 | 2.70 | **24.07** |
| **K1** | 15.63 | 15.63 | 3.32 | 24.58 | 24.58 | 14.64 | 40.23 | 40.23 | 20.40 | 53.51 | 53.51 | 2.57 | 23.40 | 23.40 | 2.36 | 9.15 | 9.15 | 3.50 | **23.93** |
| **N2** | 4.34 | 0.78 | 8.86 | 6.03 | 1.40 | 4.78 | 8.97 | 2.58 | 5.88 | 4.38 | 1.73 | 4.70 | 2.09 | 0.18 | 5.78 | 1.94 | 0.26 | 2.56 | **12.66** |
| **M2** | 4.11 | 0.79 | 18.94 | 4.01 | 1.20 | 22.94 | 2.42 | 1.05 | 21.16 | 6.89 | 0.42 | 22.53 | 3.30 | 0.74 | 10.13 | 0.86 | 0.11 | 10.59 | **12.42** |
| **S2** | 16.66 | 9.47 | 11.96 | 5.50 | 8.22 | 16.62 | 29.63 | 10.09 | 8.27 | 34.08 | 16.00 | 7.17 | 2.12 | 0.60 | 5.31 | 5.94 | 1.31 | 3.12 | **12** |
| **K2** | 7.55 | 0.68 | 11.59 | 42.57 | 0.11 | 5.38 | 20.68 | 13.99 | 10.74 | 47.30 | 7.57 | 0.19 | 9.24 | 1.94 | 13.42 | 5.87 | 1.57 | 5.21 | **11.97** |
| **Gipson** | | | | | | | | | | | | | | | | | | | |
| **Q1** | 2.28 | 2.28 | 1.32 | 14.43 | 14.43 | 9.19 | 4.14 | 4.15 | 1.48 | 16.77 | 16.78 | 1.83 | 7.49 | 7.49 | 0.40 | 4.11 | 4.12 | 0.16 | **26.87** |
| **O1** | 0.27 | 0.28 | 7.30 | 8.51 | 8.52 | 3.46 | 1.19 | 1.20 | 4.96 | 9.93 | 9.94 | 1.95 | 4.96 | 4.97 | 8.96 | 6.83 | 6.84 | 6.56 | **25.82** |
| **P1** | 25.67 | 25.67 | 5.09 | 2.41 | 2.41 | 22.09 | 29.49 | 29.49 | 7.65 | 32.52 | 32.52 | 25.44 | 15.50 | 15.50 | 1.16 | 3.34 | 3.34 | 1.79 | **24.07** |
| **K1** | 1.50 | 1.50 | 4.43 | 10.44 | 10.44 | 13.54 | 26.10 | 26.10 | 19.30 | 39.37 | 39.37 | 1.47 | 9.27 | 9.27 | 1.26 | 4.98 | 4.98 | 4.60 | **23.93** |
| **N2** | 0.25 | 4.02 | 8.63 | 1.44 | 1.84 | 4.55 | 4.38 | 0.67 | 5.65 | 0.21 | 1.51 | 4.47 | 2.50 | 3.42 | 5.55 | 2.65 | 2.98 | 2.33 | **12.66** |
| **M2** | 8.33 | 6.80 | 7.19 | 0.22 | 7.22 | 11.18 | 1.81 | 7.06 | 9.40 | 2.66 | 5.59 | 10.77 | 7.53 | 5.27 | 1.62 | 5.09 | 6.12 | 1.16 | **12.42** |
| **S2** | 16.56 | 2.58 | 2.89 | 5.40 | 3.82 | 7.55 | 29.53 | 1.96 | 0.80 | 33.98 | 3.96 | 1.90 | 2.21 | 12.64 | 14.38 | 6.04 | 10.73 | 12.19 | **12** |
| **K2** | 10.92 | 9.00 | 6.57 | 45.94 | 9.56 | 0.37 | 24.05 | 23.66 | 5.73 | 50.67 | 17.24 | 4.82 | 5.87 | 7.74 | 8.41 | 2.50 | 11.25 | 0.20 | **11.97** |

The following plots are referring to the amplitude corrections derived from the subset adjustment of the 8 major tidal waves. Figures 6.23 show the pole X-component tidal coefficient corrections for the 8 major tidal waves w.r.t. the reference models. The most significant amplitude corrections can be noticed for the diurnal tidal waves P1 and K1 and the semi-diurnal tidal waves S2 and K2. Corrections w.r.t all tested reference models have overall shown the largest values derived from the two ECOM versions: 3D GPS/Galileo+ECOM (blue) (13-19 $\mu$as for P1 and 21-28 $\mu$as for S2) and 3D GPS+ECOM (red) (18-19 $\mu$as for K1 w.r.t. Desai-Sibois and IERS2010 and 21-24 $\mu$as for K2). It has to be noted that the amplitude corrections derived from the 3D GPS/Galileo+ECOM2 time series (green) for the tidal wave P1 are smaller w.r.t. the maximum recorded values by only ~1 $\mu$as, whereas the 1D GPS/Galileo+ECOM2 time series (light green) shows the maximum amplitude correction for K1 w.r.t. the Gipson reference model (8 $\mu$as).

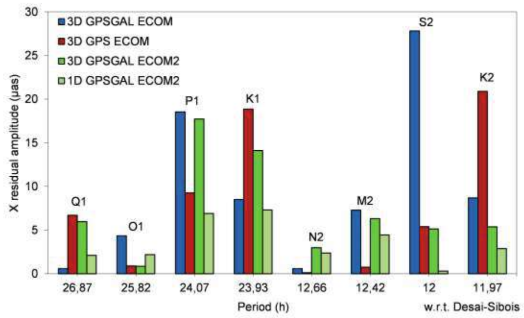


(a) Desai-Sibois

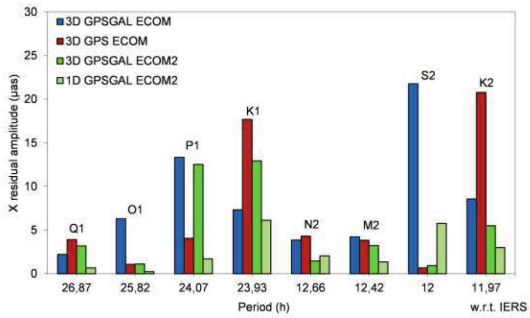


(b) IERS2010

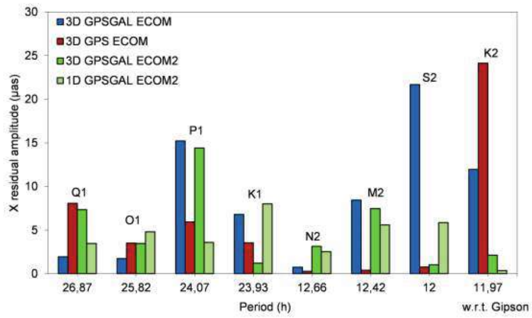


(c) Gipson

Figure 6.23: Pole X-component amplitude corrections showing all 3-day arc (GPS+ECOM, GPS/Galileo+ECOM, GPS/Galileo+ECOM2) and one 1-day arc (GPS/Galileo+ECOM2) GNSS solution w.r.t. different sub-daily models (derived from the subset adjustment - only 8 major tides).

Figure 6.24 shows the pole Y-component tidal coefficient corrections for the 8 major tidal waves w.r.t. the reference models. As in the previous plots dealing with the pole X-coordinate, in the case of the Y-component, the largest amplitude corrections refer to P1 and K1 in the diurnal band and S2 and K2 in the semi-diurnal band. The P1 amplitude corrections reveal again the largest values w.r.t. all reference models when applying the 3D GPS/Galileo+ECOM time series (blue) (13-19 $\mu$as) with the 3D GPS/Galileo+ECOM2-derived values closely following by a difference of only $\sim$1 $\mu$as. The S2 tide shows this time different maxima in each reference model plot. The corresponding amplitude corrections are not as pronounced in the Desai-Sibois plot as in the case of other reference models (Figure 6.24). The maximum value is registered for the 3D GPS/Galileo+ECOM2 time series (green) with $\sim$6 $\mu$as, followed by its 1-day arc version (light green) only by $\sim$1 $\mu$as smaller. The diurnal K1 and the semi-diurnal tide K2 are dominated by the 3D GPS+ECOM-derived (red) amplitude corrections in the Desai-Sibois and IERS2010 plots (18-19 $\mu$as for K1 and 13-15 $\mu$as for K2), while, w.r.t. the Gipson model, the 1D GPS/Galileo+ECOM2 time series (light green) shows the largest corrections (8 $\mu$as for K1 and 14 $\mu$as for K2).

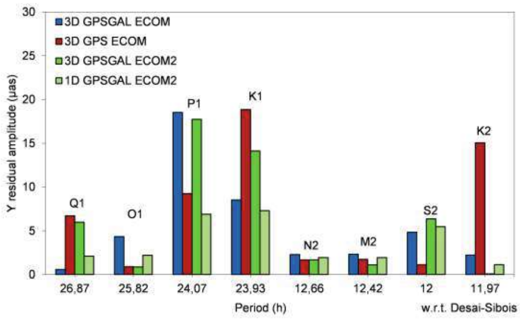


(a) Desai-Sibois

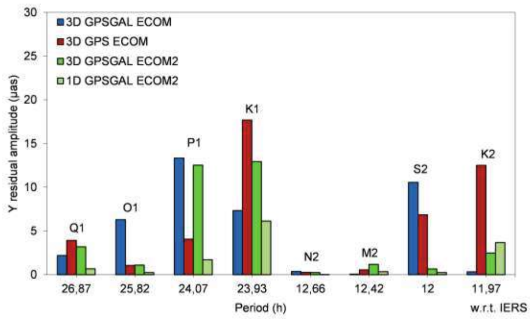


(b) IERS2010

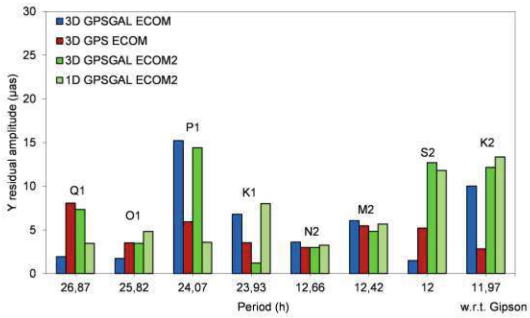


(c) Gipson

Figure 6.24: Pole Y-component amplitude corrections showing all 3-day arc (GPS+ECOM, GPS/Galileo+ECOM, GPS/Galileo+ECOM2) and one 1-day arc (GPS/Galileo+ECOM2) GNSS solution w.r.t. different sub-daily models (derived from the subset adjustment - only 8 major tides).

Figure 6.25 shows the LoD amplitude corrections for the 8 major tidal waves w.r.t. the reference models. Unlike in the previous cases, the biggest amplitude differences appear only in the semi-diurnal band, namely: S2 and K2 w.r.t. all reference models and M2 w.r.t. IERS2010 and Gipson. The 3D GPS+ECOM-derived solution (red) experiences the largest amplitude corrections w.r.t. all reference models in the case of the semi-diurnal M2 tide, with the largest correction being $\sim$ 21 $\mu$as w.r.t. the IERS2010 reference model. For the semi-diurnal K2 tide, on the other hand, the 3D GPS/Galileo+ECOM-derived (blue) amplitude corrections have the largest values w.r.t. all reference models, ranging from 8-12 $\mu$as. The largest amplitude corrections for the semi-diurnal S2 tide show up in different solutions depending on the chosen reference model. In the case of the Desai-Sibois and Gipson reference models, the largest values for S2 are derived from the 3D GPS/Galileo+ECOM2 (green) time series (14-16 $\mu$as), closely followed by its 1-day arc solution (light green), 1D GPS/Galileo+ECOM2 (12-14 $\mu$as). 3D GPS+ECOM-derived (red) amplitude corrections show the largest value w.r.t. the IERS2010 reference model, when observing the semi diurnal S2 tidal wave (19 $\mu$as). In general, larger amplitude corrections are observed for the semi-diurnal S2 tidal wave in the polar motion X-component (Figure 6.23) and LoD (Figure 6.25) for all solutions w.r.t. all reference models. As stated by Zajdel et al. (2022), the source of these signals might originate from errors in the background tidal models, effects of unmodelled tidal and nontidal signal sources, or propagation of errors in the background models. These models (eg. satellite clocks or satellite orbit midnight discontinuities) are computed in 24-hour batch processing. The latter-mentioned factor is most probably the primary source of these signals.

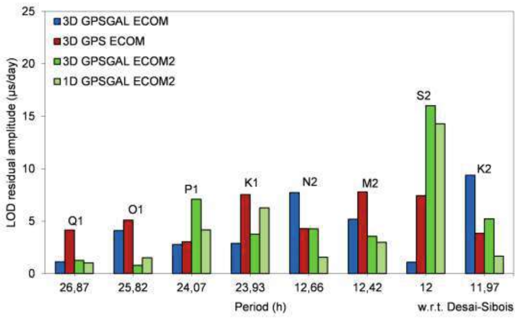


(a) Desai-Sibois

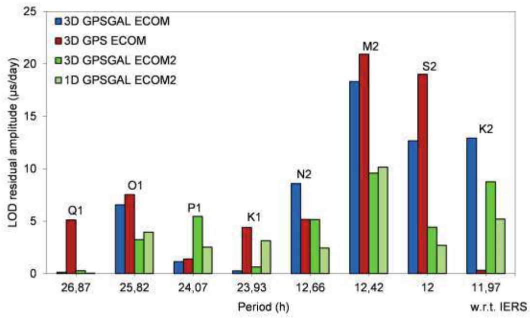


(b) IERS2010

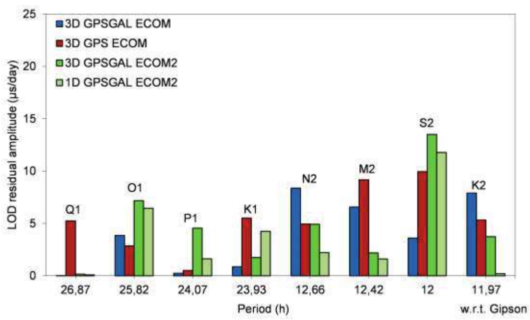


(c) Gipson

Figure 6.25: LoD amplitude corrections showing all 3-day arc (GPS+ECOM, GPS/Galileo+ECOM, GPS/Galileo+ECOM2) and one 1-day arc (GPS/Galileo+ECOM2) GNSS solution w.r.t. different sub-daily models (derived from the subset adjustment - only 8 major tides).

A direct comparison of all performed solutions (1-day arc and 3-day arcs) can be found in Figures A.10-A.12 in Appendix A.2.2. The corresponding numerical values of amplitude corrections derived from all solutions are given in Table 6.6.

Table 6.6: Tidal corrections of diurnal and semidiurnal variations on pole coordinates (X, Y) and LoD caused by the 8 major ocean tides w.r.t. the Desai-Sibois, IERS2010 and Gipson reference model (derived from the subset adjustment: the 8 major tides).

| | 3D GPSGAL ECOM | | | 3D GPS ECOM | | | 1D GPSGAL ECOM | | | 1D GPS ECOM | | | 3D GPSGAL ECOM2 | | | 1D GPSGAL ECOM2 | | | Period |
|---|---|---|---|---|---|---|---|---|---|---|---|---|---|---|---|---|---|---|---|
| **Tide** | **X** | **Y** | **LOD** | **X** | **Y** | **LOD** | **X** | **Y** | **LOD** | **X** | **Y** | **LOD** | **X** | **Y** | **LOD** | **X** | **Y** | **LOD** | **(h)** |
| | | | | | | | | | **Desai-Sibois** | | | | | | | | | | |
| **Q1** | 0.58 | 0.58 | 1.11 | 6.70 | 6.71 | 4.14 | 1.92 | 1.92 | 1.34 | 10.03 | 10.04 | 3.72 | 5.97 | 5.98 | 1.25 | 2.10 | 2.11 | 1.02 | **26.87** |
| **O1** | 4.35 | 4.34 | 4.10 | 0.89 | 0.90 | 5.09 | 1.01 | 1.00 | 6.61 | 1.08 | 1.09 | 9.87 | 0.85 | 0.86 | 0.78 | 2.20 | 2.21 | 1.51 | **25.82** |
| **P1** | 18.53 | 18.53 | 2.77 | 9.25 | 9.25 | 3.04 | 18.28 | 18.28 | 3.57 | 9.03 | 9.03 | 21.52 | 17.72 | 17.72 | 7.08 | 6.89 | 6.89 | 4.16 | **24.07** |
| **K1** | 8.51 | 8.51 | 2.87 | 18.85 | 18.85 | 7.53 | 24.93 | 24.93 | 2.51 | 23.58 | 23.58 | 21.67 | 14.11 | 14.11 | 3.76 | 7.31 | 7.31 | 6.26 | **23.93** |
| **N2** | 0.59 | 2.28 | 7.71 | 0.13 | 1.67 | 4.29 | 3.49 | 1.00 | 5.69 | 2.55 | 0.17 | 4.32 | 2.98 | 1.68 | 4.26 | 2.38 | 1.93 | 1.56 | **12.66** |
| **M2** | 7.30 | 2.33 | 5.17 | 0.75 | 1.73 | 7.79 | 0.42 | 2.69 | 7.57 | 3.74 | 1.78 | 8.59 | 6.32 | 1.10 | 3.56 | 4.44 | 1.93 | 2.98 | **12.42** |
| **S2** | 27.82 | 4.84 | 1.08 | 5.40 | 1.13 | 7.42 | 36.32 | 0.88 | 2.32 | 19.23 | 10.05 | 8.87 | 5.13 | 6.37 | 16.01 | 0.30 | 5.48 | 14.28 | **12** |
| **K2** | 8.69 | 2.21 | 9.37 | 20.89 | 15.05 | 3.85 | 18.58 | 4.50 | 6.61 | 9.05 | 0.54 | 5.67 | 5.38 | 0.07 | 5.21 | 2.88 | 1.13 | 1.66 | **11.97** |
| | | | | | | | | | **IERS2010** | | | | | | | | | | |
| **Q1** | 2.20 | 2.20 | 0.13 | 3.92 | 3.92 | 5.12 | 0.87 | 0.86 | 0.36 | 7.25 | 7.25 | 2.75 | 3.19 | 3.19 | 0.27 | 0.68 | 0.68 | 0.04 | **26.87** |
| **O1** | 6.31 | 6.30 | 6.55 | 1.07 | 1.06 | 7.54 | 2.97 | 2.96 | 9.06 | 0.88 | 0.87 | 12.32 | 1.11 | 1.10 | 3.23 | 0.24 | 0.25 | 3.96 | **25.82** |
| **P1** | 13.34 | 13.34 | 1.14 | 4.05 | 4.05 | 1.40 | 13.09 | 13.09 | 1.93 | 3.84 | 3.84 | 19.88 | 12.53 | 12.53 | 5.45 | 1.70 | 1.70 | 2.52 | **24.07** |
| **K1** | 7.33 | 7.33 | 0.26 | 17.68 | 17.68 | 4.41 | 23.75 | 23.75 | 0.61 | 22.41 | 22.41 | 18.54 | 12.94 | 12.94 | 0.63 | 6.13 | 6.13 | 3.13 | **23.93** |
| **N2** | 3.85 | 0.35 | 8.59 | 4.31 | 0.26 | 5.17 | 7.93 | 0.92 | 6.57 | 1.89 | 2.10 | 5.20 | 1.46 | 0.24 | 5.14 | 2.06 | 0.01 | 2.44 | **12.66** |
| **M2** | 4.21 | 0.05 | 18.31 | 3.83 | 0.54 | 20.92 | 2.67 | 0.42 | 20.71 | 6.83 | 0.50 | 21.73 | 3.23 | 1.17 | 9.58 | 1.36 | 0.34 | 10.15 | **12.42** |
| **S2** | 21.76 | 10.56 | 12.67 | 0.66 | 6.85 | 19.01 | 30.26 | 6.59 | 9.26 | 13.17 | 15.77 | 2.71 | 0.93 | 0.65 | 4.43 | 5.75 | 0.24 | 2.70 | **12** |
| **K2** | 8.57 | 0.33 | 12.91 | 20.76 | 12.51 | 0.31 | 18.45 | 7.04 | 10.15 | 8.92 | 2.00 | 2.13 | 5.50 | 2.47 | 8.75 | 3.01 | 3.67 | 5.20 | **11.97** |
| | | | | | | | | | **Gipson** | | | | | | | | | | |
| **Q1** | 1.94 | 1.95 | 0.01 | 8.07 | 8.07 | 5.24 | 3.28 | 3.28 | 0.24 | 11.40 | 11.40 | 2.62 | 7.34 | 7.34 | 0.15 | 3.47 | 3.47 | 0.08 | **26.87** |
| **O1** | 1.74 | 1.73 | 3.85 | 3.50 | 3.51 | 2.86 | 1.60 | 1.61 | 1.34 | 3.69 | 3.70 | 1.92 | 3.46 | 3.47 | 7.17 | 4.81 | 4.82 | 6.44 | **25.82** |
| **P1** | 15.22 | 15.22 | 0.23 | 5.94 | 5.94 | 0.50 | 14.97 | 14.97 | 1.03 | 5.72 | 5.72 | 18.98 | 14.41 | 14.41 | 4.54 | 3.58 | 3.58 | 1.61 | **24.07** |
| **K1** | 6.80 | 6.80 | 0.85 | 3.54 | 3.54 | 5.51 | 9.62 | 9.62 | 0.49 | 8.27 | 8.27 | 19.65 | 1.20 | 1.20 | 1.74 | 8.00 | 8.00 | 4.24 | **23.93** |
| **N2** | 0.74 | 3.60 | 8.36 | 0.28 | 2.99 | 4.94 | 3.34 | 2.32 | 6.34 | 2.70 | 1.15 | 4.97 | 3.13 | 3.00 | 4.91 | 2.53 | 3.25 | 2.21 | **12.66** |
| **M2** | 8.44 | 6.07 | 6.55 | 0.40 | 5.47 | 9.17 | 1.56 | 6.43 | 8.95 | 2.60 | 5.52 | 9.97 | 7.46 | 4.84 | 2.18 | 5.58 | 5.67 | 1.60 | **12.42** |
| **S2** | 21.67 | 1.49 | 3.60 | 0.76 | 5.20 | 9.94 | 30.16 | 5.45 | 0.19 | 13.08 | 3.72 | 6.36 | 1.02 | 12.70 | 13.50 | 5.85 | 11.81 | 11.77 | **12** |
| **K2** | 11.94 | 10.01 | 7.90 | 24.13 | 2.83 | 5.32 | 21.82 | 16.72 | 5.14 | 12.29 | 11.68 | 7.14 | 2.13 | 12.15 | 3.74 | 0.36 | 13.35 | 0.19 | **11.97** |

The agreement of the two ECOM2-based solutions with the chosen reference models was unambiguously better compared to the ECOM-based solutions when observing the full set adjustment results (FSA) from Figures 6.20, 6.21, and 6.22. In the subset adjustment, by using the 8 major tides only (SSA), the outcome did not appear to be the same for the ECOM-based and the ECOM2-based solutions (Figures 6.23, 6.24, and 6.25). While the former experienced overall an improvement w.r.t. all reference models in terms of amplitude corrections (with a few exceptions, where the corrections worsened), the latter remained on average the same in performance.

Figure 6.26 shows the RMS values of the estimated tidal coefficients in X and Y pole coordinates for the four different solutions (all 3-day arc solutions and one 1-day arc GPS/Galileo + ECOM2 solution).

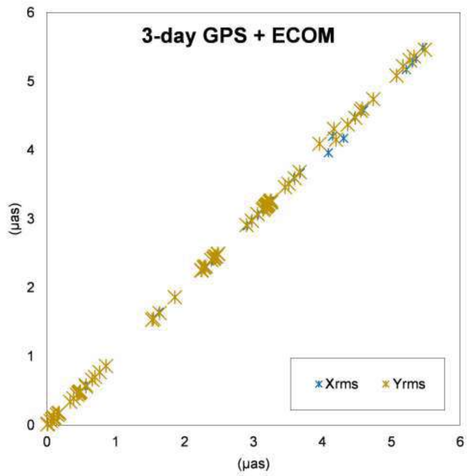


(a) 3-day arc GPS-only solution + ECOM

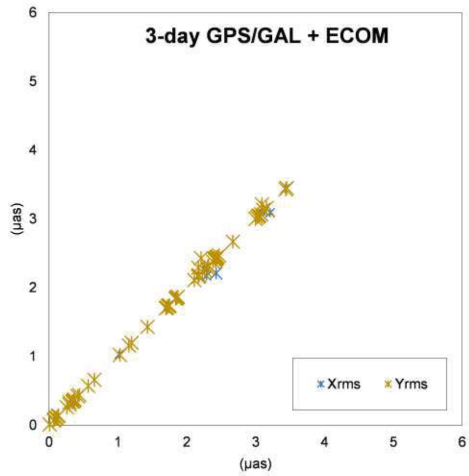


(b) 3-day arc GPS/Galileo solution + ECOM

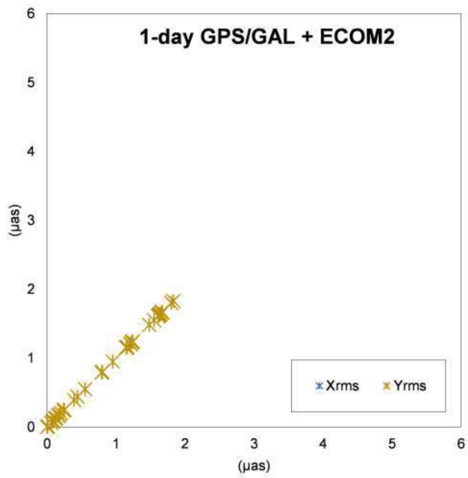


(c) 1-day arc GPS/Galileo solution + ECOM2

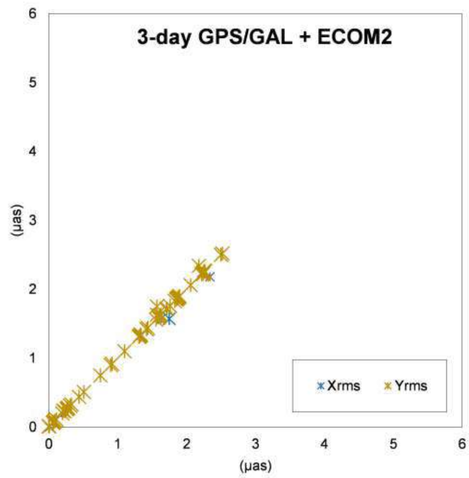


(d) 3-day arc GPS/Galileo solution + ECOM2

Figure 6.26: RMS values for all estimated tidal coefficients in X, Y pole coordinates based on the full set adjustment. Four solution types are presented separately on plots (a) - (d).

The smallest RMS values can be noticed for the 1-day arc GPS/Galileo + ECOM2 solution with the maximum RMS value of 2 $\mu$as, followed closely by its 3-day arc version with a maximum RMS of 2.8 $\mu$as. The largest RMS values are present in the 3-day GPS + ECOM solution (5.5 $\mu$as).

Figure 6.27 shows the RMS values for the estimated tidal coefficients in LoD for the four different solutions. The smallest RMS values can again be noticed for the 1-day arc GPS/Galileo + ECOM2 solution with the maximum RMS value of 3.2 $\mu$s/day, while the largest RMS values are present, again, in the 3-day GPS + ECOM solution (8 $\mu$s/day). The 3-day arc GPS/Galileo + ECOM2 showed again slightly higher values compared to the lowest recorded RMS, 3.9 $\mu$s/day. In general, the GPS-based RMS has shown to be consistently larger compared to the RMS values in the GPS/Galileo solutions.

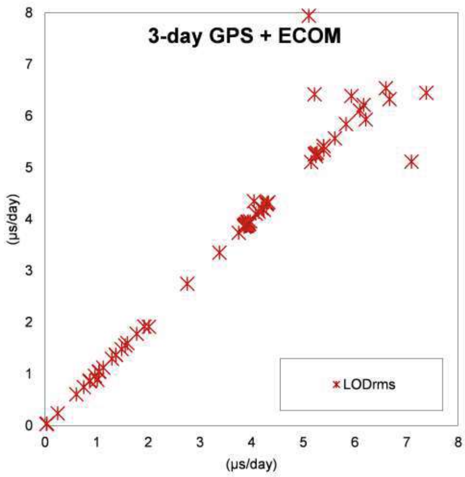


(a) 3-day arc GPS-only solution + ECOM

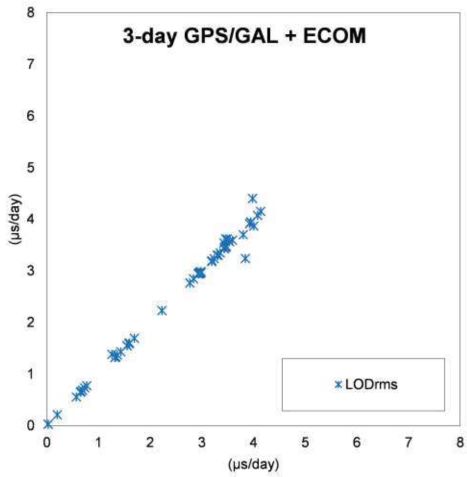


(b) 3-day arc GPS/Galileo solution + ECOM

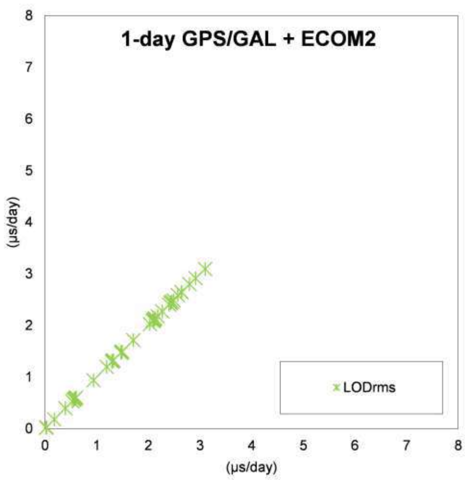


(c) 1-day arc GPS/Galileo solution + ECOM2

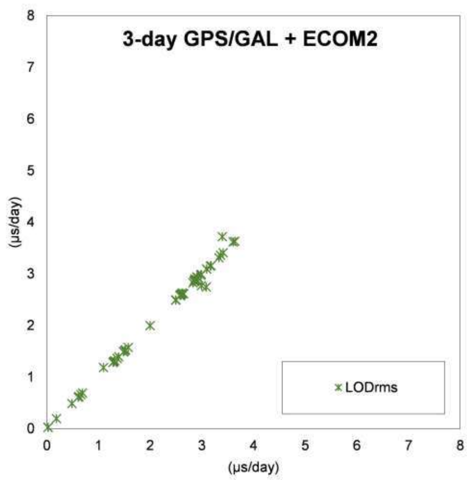


(d) 3-day arc GPS/Galileo solution + ECOM2

Figure 6.27: RMS values for all estimated tidal coefficients in LoD based on the full set adjustment. Four solution types are presented separately on plots (a) - (d).

Irrespective of whether the full-set or subset adjustment approach is utilized, one solution consistently arises as the optimal choice, aligning with the reference models in terms of polar motion, Length of Day (LoD) time series, and tidal coefficients. The incorporation of both GPS and Galileo signals, with Galileo contributing up to 44% of the total satellite count, has brought about significant enhancement, particularly following the application of the ECOM2 model. A minor, albeit statistically insignificant variance between the combined 1-day-arc solution and its 3-day-arc counterpart has been observed. This finding suggests that, with this setup, the performance level remains relatively consistent, thereby offering the possibility of further analysis with the 1-day-arc time series.

Significantly pronounced amplitude corrections observed for the semi-diurnal tidal constituent K2, as well for the diurnal tidal constituent K1, can be addressed to orbital signals resulting from the resonance between Earth's rotation and the satellite's revolution period. Specifically, the K2 tide synchronizes with the orbital period of GPS satellites, while the K1 tide's period of 23.93 hours coincides with the GPS ground repeat period. Consequently, the most substantial impact is observed in the case of GPS-only solutions. Larger amplitude corrections for the semi-diurnal tidal constituent S2 might result from the hourly data sampling at $1/n$ cycles, coinciding at 2 cycles with the tidal period of S2 (12.00 hours).

As mentioned earlier in this chapter, during the study period (2018-2019), approximately 90% of all stations were contributing to the solution, i.e., 100 out of possible 112 stations. The GNSS stations, on average, observed around 31 GPS and 16-24 Galileo satellites daily. Notably, the count of available Galileo satellites increased from 16 to 20-24 following the launch of 4 FOC satellites in mid-2018. Consequently, Galileo's contribution to the overall satellite count rose from 34% to as much as 44%.

The processing time for the GPS-only solution typically falls within the range of 1 to 1.5 hours, while the combined GPS/Galileo solution, regardless of the selected SRP modeling, typically requires 1.5 to 2 hours for completion. This amount of time refers to the calculation of one daily solution. It's important to note that the processing time for both solutions can also be influenced by additional factors, such as computer performance and server response, which are unrelated to the processing scheme itself.

## 6.2. TUWR model validation

The TUWR model was generated and validated in comparison to established and well-known ionosphere models, mentioned and described in Section 3.5.6. It is noteworthy that the TUWR model, utilizing combined GPS and Galileo observation data, serves as a reference model, along with the ionosphere models derived from CODE and IGS. In contrast, the two broadcast ionosphere models, Klobuchar (GPS) and NeQuick G (Galileo), differ from these benchmark models. While the reference models are calculated based on spherical harmonics functions and rely on 15 parameters to accurately describe the ionospheric activity, the broadcast models aim to represent the ionospheric state with significantly fewer parameters, typically ranging from 6 to 8. Consequently, the reference models are expected to provide a more comprehensive depiction of the ionospheric state compared to the broadcast models, Klobuchar and NeQuick G.

The validation was performed from different aspects, which will be described and shown in more detail in the following sections.

### 6.2.1. VTEC maps and analysis

First, the models were compared regarding the VTEC values in the corresponding IONEX files by plotting them directly for the period of 5 days in January (Figure 6.28) and June (Figure 6.29) for specific locations. The choice of the two months for the study was based on the distinct ionospheric behavior observed in winter and summer. The ionospheric activity shows characteristic differences between these two seasons. This is mostly due to variations in solar radiation, atmospheric conditions, and temperature. During winter, the solar radiation is less pronounced leading to lower electron density in the ionosphere, hence the ionosphere having a reduced absorption capability. This, in turn, has a positive impact on radio waves, enabling improved long-distance communication. Overall, the ionosphere has a tendency to be less dynamic in winter. On the other hand, increased solar radiation during summer, as well as higher temperatures cause the ionization level to increase. The electron density rises due to stronger solar activity, which results in increased absorption and dispersion of radio waves leading to signal degradation. Considering the distinct characteristics of ionospheric activity that are season-dependent, the choice of winter and summer months was made to capture and reflect these variations in the tested ionospheric models.

Since the TUWR model is a regional model, mostly covering the European region, the locations were chosen taking this into account. Thus, three locations were chosen: $\varphi = 55°N$, $\lambda = 16°E$, $\varphi = 48°N$, $\lambda = 16°E$ (Austria) and $\varphi = 35°N$, $\lambda = 16°E$ representing high, mid and low latitude regions respectively. When observing the winter and summer days, the biggest difference in performance can be noticed with the Klobuchar and NeQuick G model.

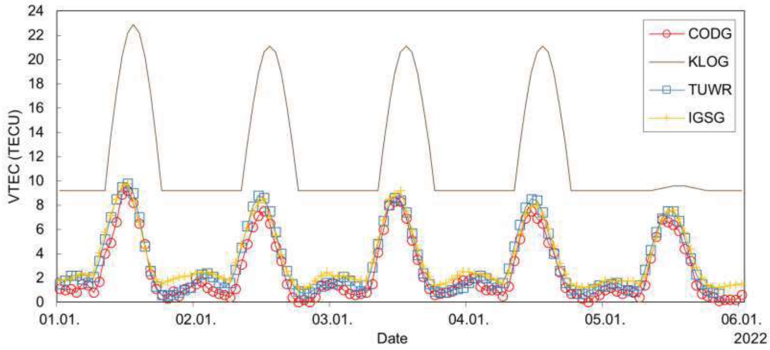


(a) $\varphi = 55°N$, $\lambda = 16°E$

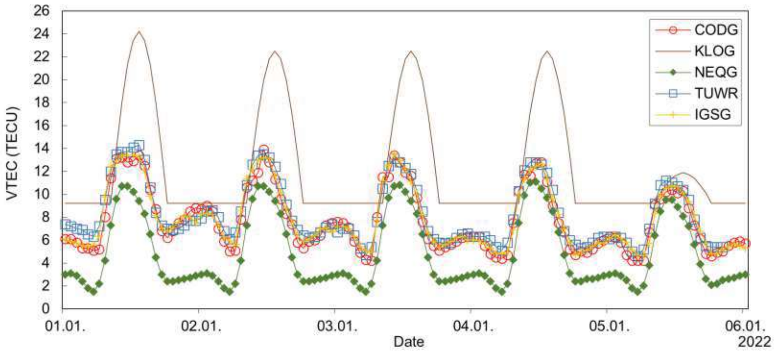


(b) $\varphi = 48°N$, $\lambda = 16°E$ (near Vienna, Austria)

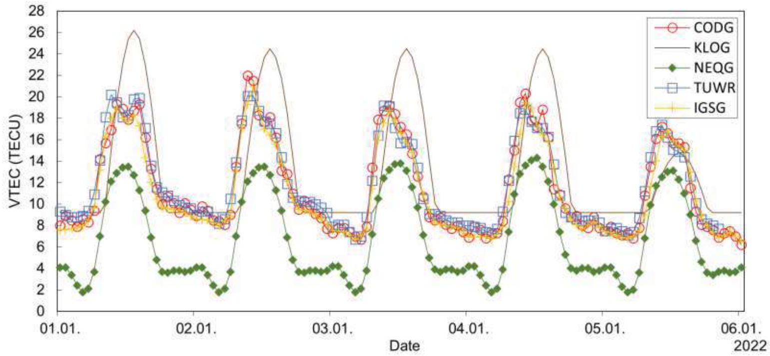


(c) $\varphi = 35°N$, $\lambda = 16°E$

Figure 6.28: VTEC comparison between different models for 3 latitude regions in January 2022 (CODG: Code Global; KLOG: Klobuchar Global; NEQG: NeQuick G; TUWR: TU Vienna Regional; IGSG: IGS Global).

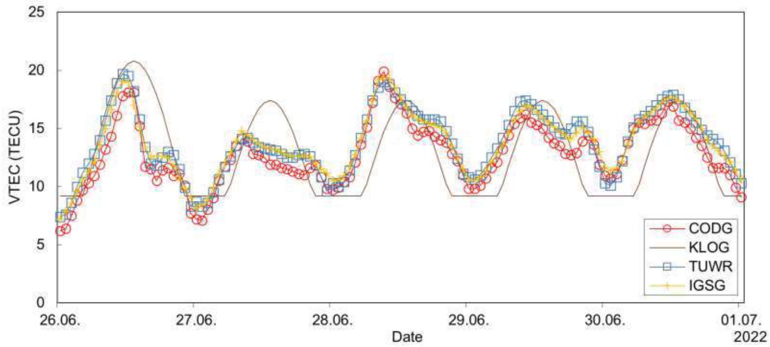


(a) $\varphi = 55°N$, $\lambda = 16°E$

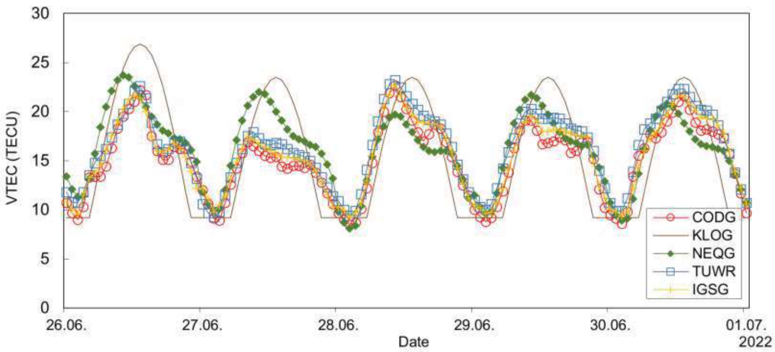


(b) $\varphi = 48°N$, $\lambda = 16°E$ (near Vienna, Austria)

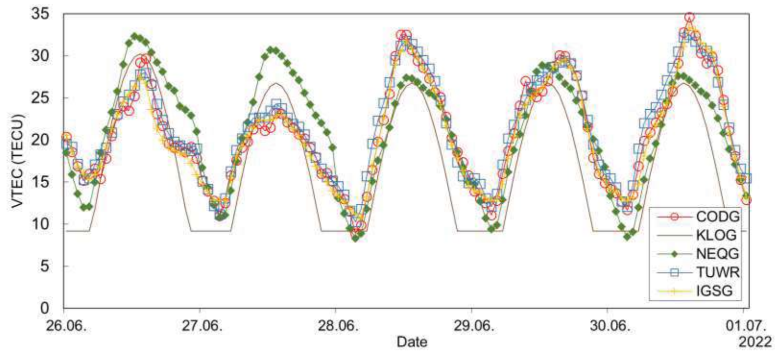


(c) $\varphi = 35°N$, $\lambda = 16°E$

Figure 6.29: VTEC comparison between different models for 3 latitude regions in June 2022 (CODG: Code Global; KLOG: Klobuchar Global; NEQG: NeQuick G; TUWR: TU Vienna Regional; IGSG: IGS Global).

Klobuchar is overestimating the VTEC up to 10 TECU in (a) and (b) in Figure 6.28 compared to CODE, IGS, and TUWR. In (c), at lower latitudes, Klobuchar seems to reach closer to the other models but remains with a difference of up to 5 TECU. It is visible from the figures, that Klobuchar delivers a constant value for the night-time, which happens to agree for some days and models at certain hours. Still, these night-time values might be too optimistic and thus, not reliable. NeQuick G, on the other hand, appears to underestimate the VTEC values in (b) and (c) in Figure 6.28 by approximately 5 TECU compared to the CODE, IGS, and TUWR model, while overestimating the VTEC values in the summer plot (Figure

6.29). The three remaining models show a good agreement and mostly overlap over these 5 days in winter. The summer plot (Figure 6.29) shows a more or less good agreement among all tested models at all latitude regions. When paying attention to the VTEC pattern of the TUWR model, compared to CODE and IGS, a relatively good consistency among those three models is evident in both, winter and summer time. To be more precise, the TUWR-derived VTEC values at high latitudes during winter (plot (a), Figure 6.28) appear to have a somewhat better agreement with the IGS-derived VTEC at day-time, having slightly higher values than the CODE-derived VTECs by approximately 1 TECU (except for 03.01.2022, where all three models reveal almost identical VTEC peaks during day-time). In the same plot, during night-time, TUWR matches more with CODE, while IGS has higher values up to 2 TECU. At mid- and low latitudes in winter (plots (b) and (c), Figure 6.28), TUWR shows a very good agreement with CODE and IGS at day- and night-times with a discrepancy of up to 1.5 TECU compared to CODE and IGS. The high latitudes in summer (plot (a) Figure 6.29) reveal an almost complete agreement between the TUWR-derived VTEC and the IGS-derived VTEC, while CODE-derived values are usually slightly lower (around 1 TECU). The mid-latitudes in summer (plot (b) Figure 6.29) are dominated with a more-less good consistency among those three models, with CODE delivering somewhat smaller values during day-time VTEC peaks. The difference here does not exceed 2 TECU. The VTEC values derived from TUWR have a very good consistency with both, CODE and IGS values, at low latitudes in summer (plot (c) Figure 6.29). Overall, in winter and summer at all three latitude regions, TUWR mostly agrees with the reference models CODE and IGS, showing a maximum discrepancy of up to 2 TECU, compared to the reference values. Klobuchar and NeQuick G show a higher disagreement compared to CODE and IGS, where Klobuchar usually overestimates the VTEC values in winter and has both, over- and underestimated VTEC values during summer (observed at high and mid-latitudes, where overestimation appears during day-time and underestimation during night-time). On the other hand, a constant underestimation of NeQuick G-derived VTEC values with respect to CODE and IGS is visible during winter (plots (b) and (c) Figure 6.28). In summer, NeQuick G VTEC values at night-time are more-less consistent with the night-time values from CODE and IGS, with slight disagreements of up to 3 TECU for some days. At daytime, similar to Klobuchar, there appears an over- and underestimation of NeQuick G-derived VTEC values compared to CODE and IGS, with differences of up to approximately 5 TECU.

Next, ionosphere maps as well as difference maps were generated by using the associate IONEX files for the different 5 ionosphere models. The maps cover, again, the European region. Both, model-specific and difference maps are plotted as daily maps containing 12 plots for every two hours. Figures 6.30 - 6.33 show ionospheric maps for 5 ionosphere models and their corresponding VTEC difference maps of (a) TUWR w.r.t. (b) CODE, IGS, Klobuchar and NeQuick G respectively for January 01$^{st}$, 2022.

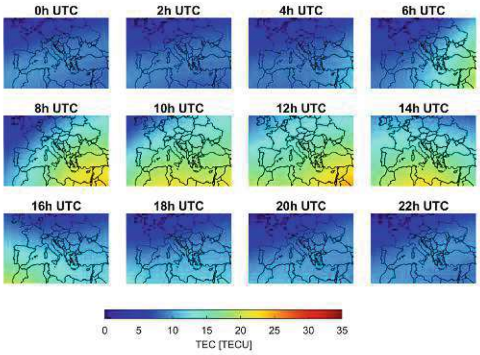


(a) TUWR

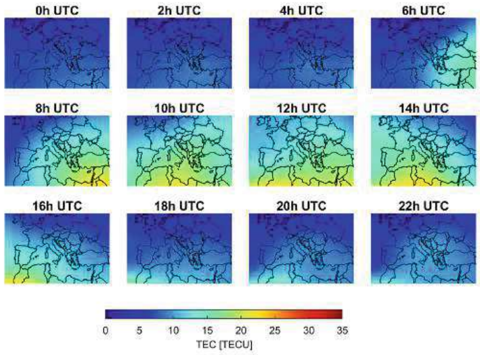


(b) CODE

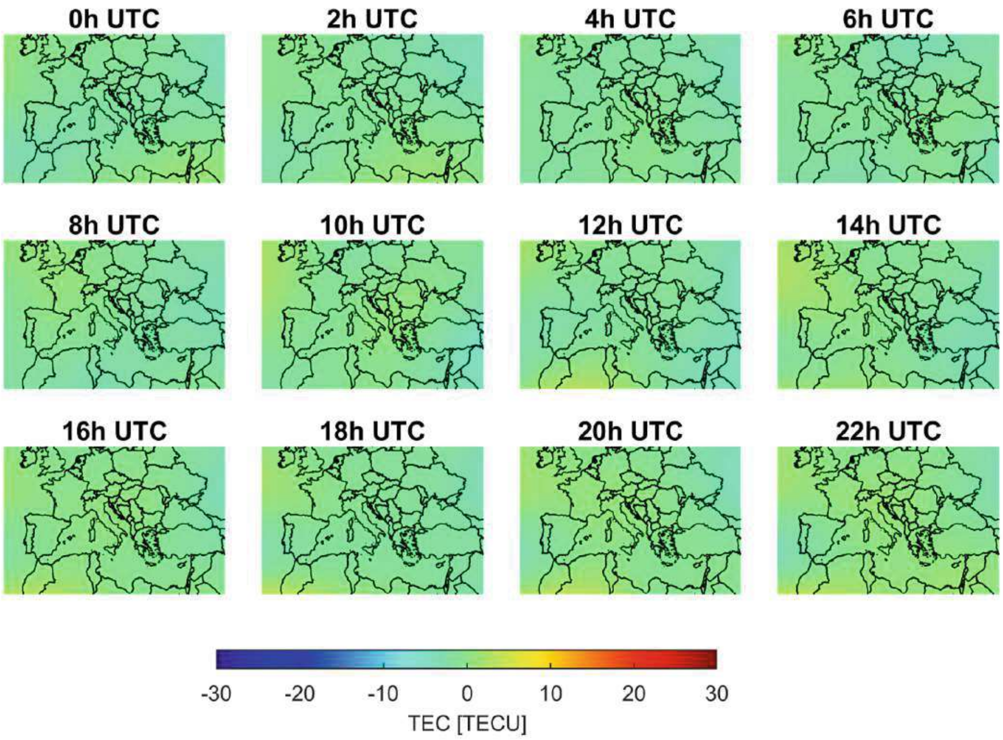


(c) Difference plot (CODE - TUWR)

Figure 6.30: Regional VTEC maps of (a) TUWR and (b) CODE. Plot (c) shows the difference map between model (a) and (b) for January 01 2022 (doy 001 2022).

The TUWR model demonstrates a good agreement with the CODE model (Figure 6.30). The differences between these two models range from -3 TECU up to +4 TECU. These difference maxima were mostly found at map boundaries (predominantly in the west, southwest, and northeast) due to the poor coverage with stations used for the calculation of the TUWR model and thus having less reliable VTEC values in these areas. A similar scenario can be seen in the TUWR - IGS comparison (Figure 6.31) with discrepancies between -3 TECU and +2 TECU, again, mostly found at map boundaries. Overall, the two models show a very good consistency.

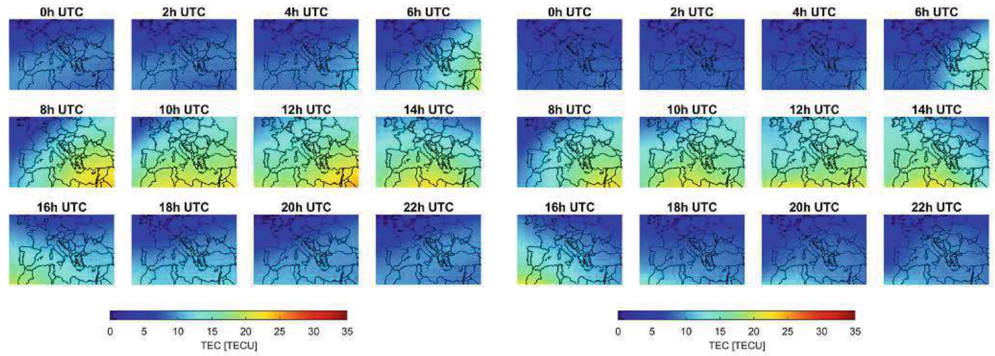


(a) TUWR (b) IGS

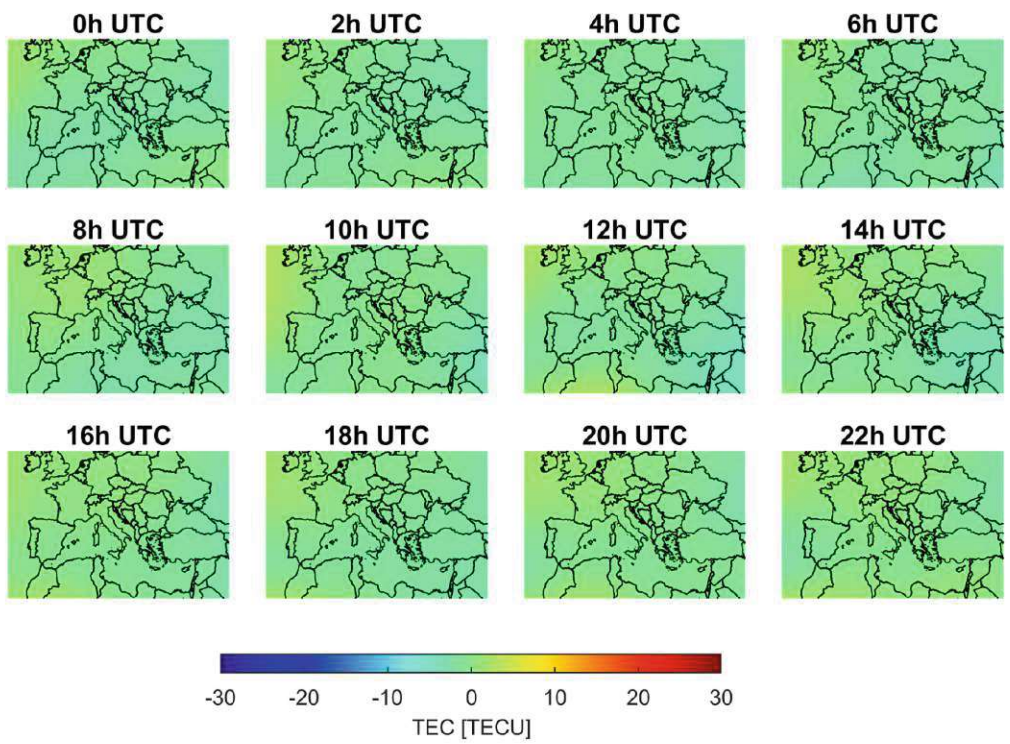


(c) Difference plot (IGS - TUWR)

Figure 6.31: Regional VTEC maps of (a) TUWR and (b) IGS. Plot (c) shows the difference map between model (a) and (b) for January 01 2022 (doy 001 2022).

As already seen in the winter plot (Figure 6.28), the Klobuchar model has overestimated the VTEC, which is further reflected in the corresponding VTEC map and VTEC difference map for January 1st (Figure 6.32). The difference between the TUWR and the Klobuchar model reaches an amplitude between -5 TECU (mostly visible between 6h-10h) and +13 TECU (mostly visible between 14h-18h). The negative maximum can be noticed in the south and southeast parts, while the positive maximum is highly prominent in the northwest part of the maps.

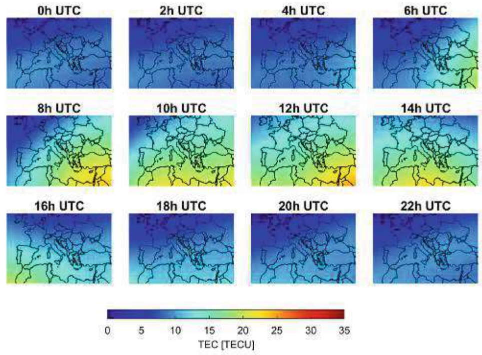


(a) TUWR

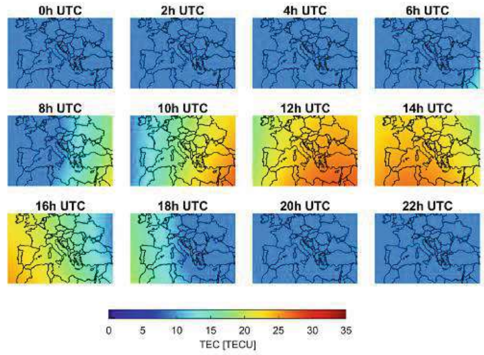


(b) Klobuchar

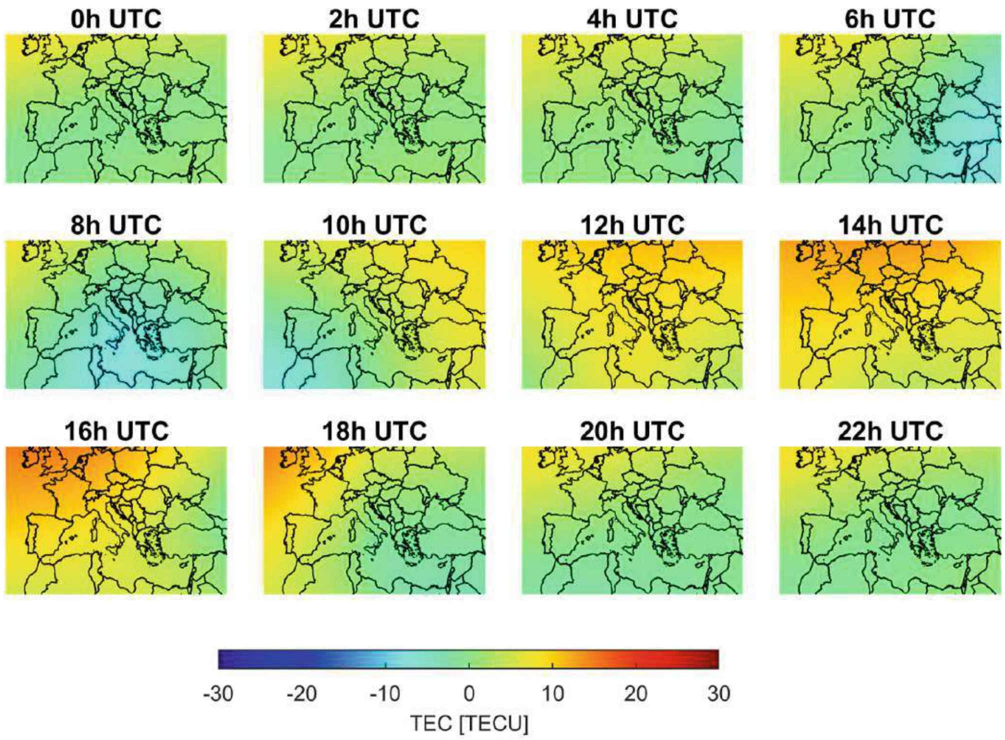


(c) Difference plot (Klobuchar - TUWR)

Figure 6.32: Regional VTEC maps of (a) TUWR and (b) Klobuchar. Plot (c) shows the difference map between model (a) and (b) for January 01 2022 (doy 001 2022).

The previously mentioned winter plots were dominated by underestimated NeQuick G-derived VTEC values compared to the VTEC from other models. Accordingly, the appropriate VTEC and VTEC difference map (Figure 6.33) show the same behavior. Differences between the TUWR model and the NeQuick G model reach from -8 TECU (at 12h UTC) up to +2 TECU. The pronounced negative maximum is mainly visible in the southeast part of the map.

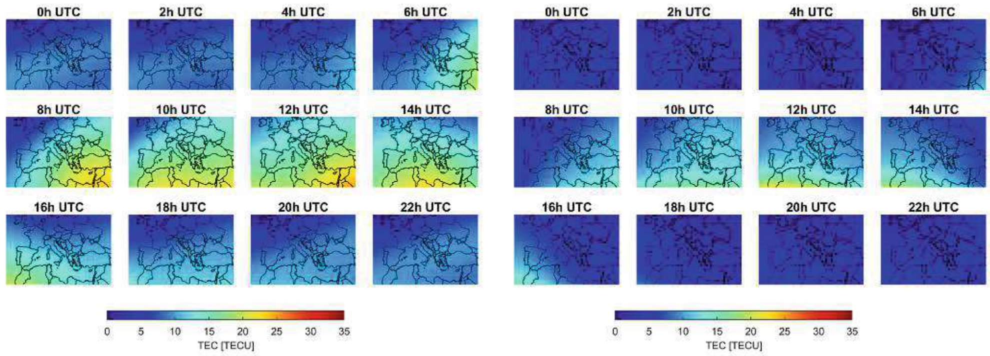


(a) TUWR (b) NeQuick G

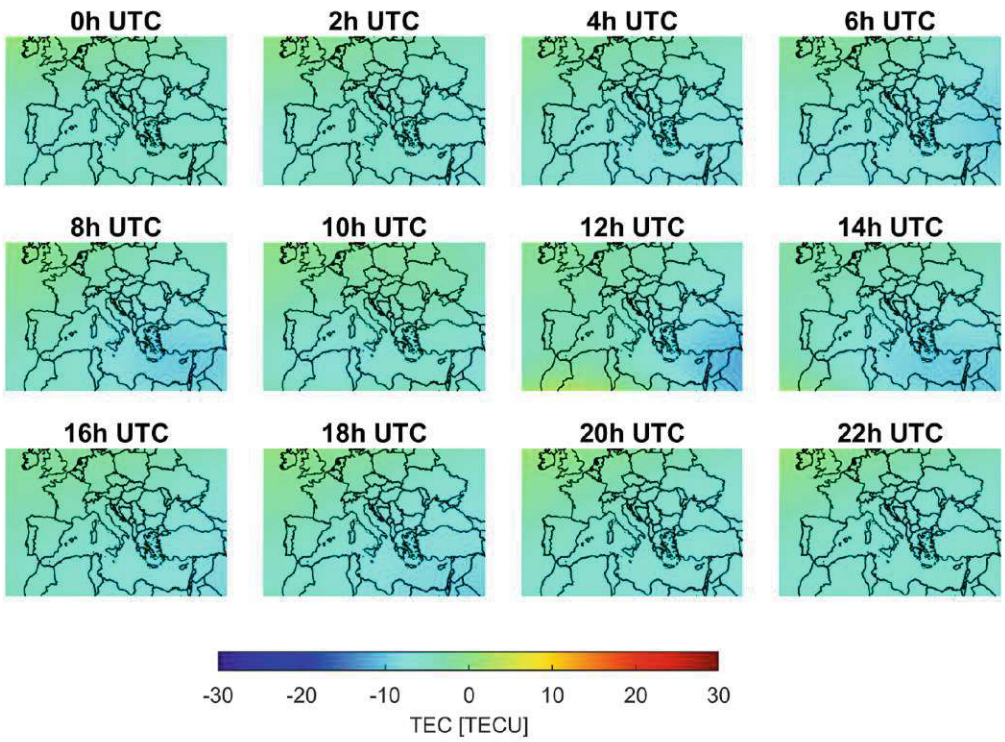


(c) Difference plot (NeQuick G - TUWR)

Figure 6.33: Regional VTEC maps of (a) TUWR and (b) NeQuick G. Plot (c) shows the difference map between model (a) and (b) for January 01 2022 (doy 001 2022).

Figures 6.34 - 6.37 show again ionospheric maps for 5 ionosphere models and the difference plots between the TUWR model and the remaining models, this time, for June 30$^{th}$, 2022. The ionospheric maps for TUWR and CODE, as well as their difference map, are visible in Figure 6.34. The VTEC differences range mostly between -3 TECU and +4 TECU, with outliers of -8 TECU spotted in the southeast of the difference map at 12h UTC and +7 TECU in the southwest between 14h-18h UTC, which appeared most likely, as mentioned before, due to the lack of stations used for the model generation at this boundary area.

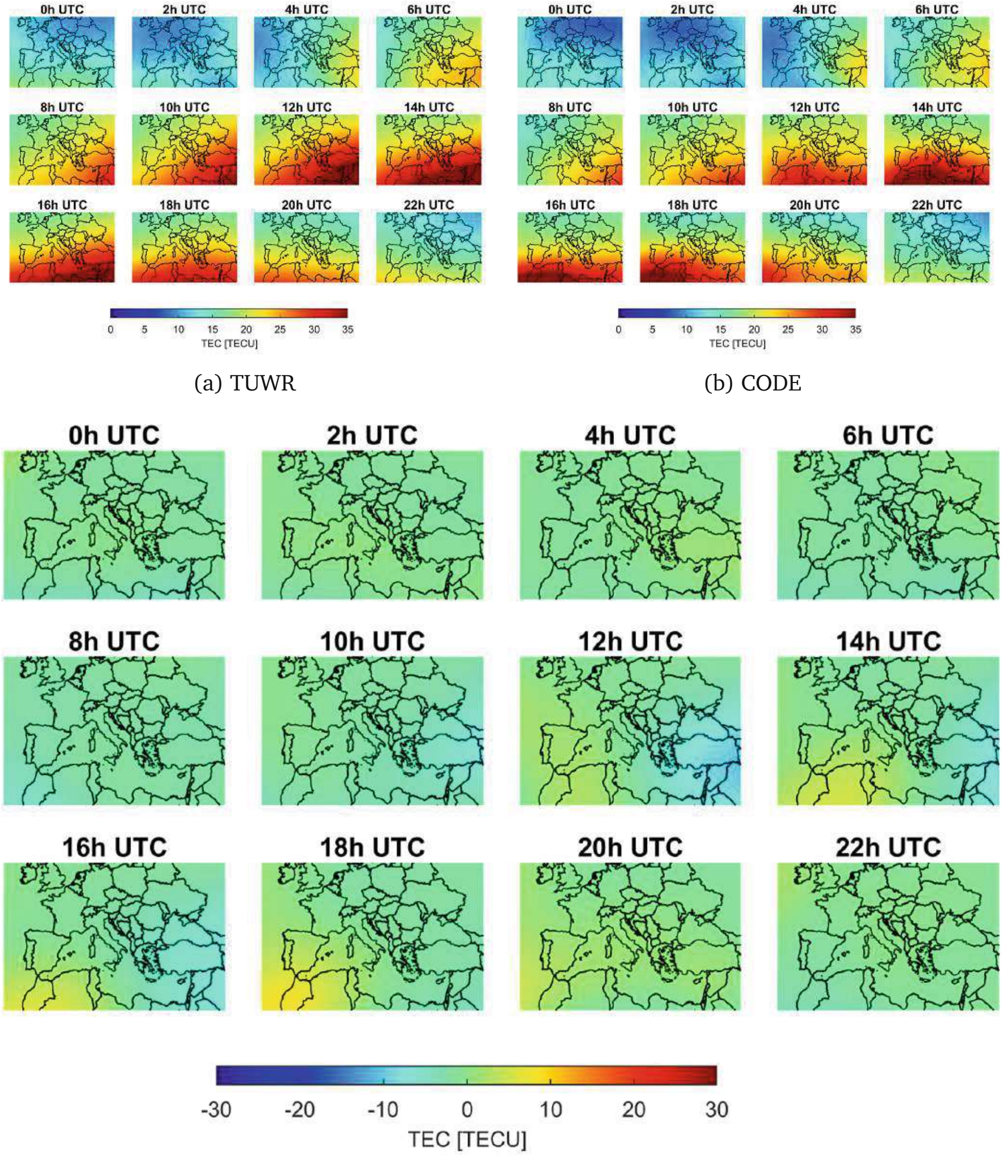


(a) TUWR

(b) CODE

(c) Difference plot (CODE - TUWR)

Figure 6.34: Regional VTEC maps of (a) TUWR and (b) CODE. Plot (c) shows the difference map between model (a) and (b) for June 30, 2022 (doy 181 2022).

The comparison between TUWR and IGS (Figure 6.34) reveals an identical difference pattern, having two maxima (positive and negative) at the same locations and hours of the day, being slightly smaller than the CODE-TUWR differences. On average, discrepancies usually range between -2 TECU and +2 TECU, with outliers of -6 TECU in the southeast of the map at 12h UTC and +7 TECU in the southwest between 16h-18h UTC.

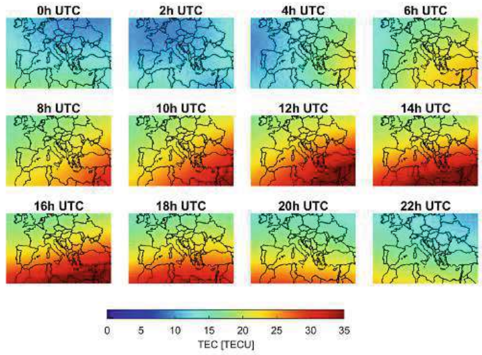


(a) TUWR

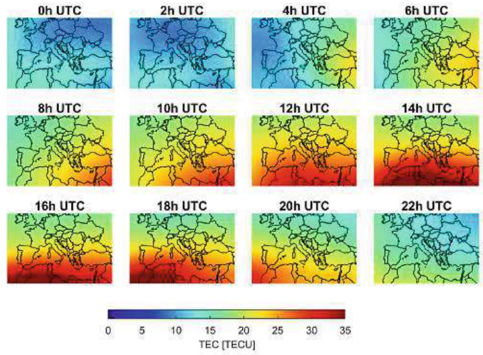


(b) IGS

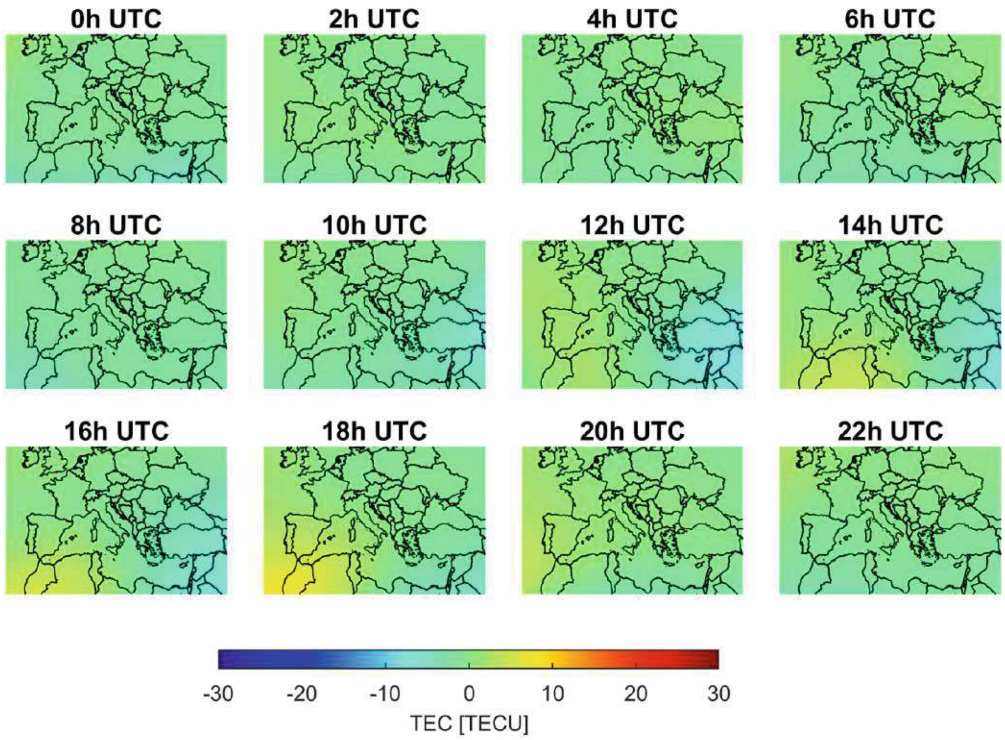


(c) Difference plot (IGS - TUWR)

Figure 6.35: Regional VTEC maps of (a) TUWR and (b) IGS. Plot (c) shows the difference map between model (a) and (b) for June 30, 2022 (doy 181 2022).

By having a look at plots (a) and (b) of Figure 6.36 it becomes clearly visible that for the whole day, Klobuchar underestimated the VTEC values compared to TUWR, especially during night-time, when this model, as already stated before, delivers constant values. As a result, the corresponding VTEC difference plot mainly contains negative values, especially in the south and southeast part of the regional map. The differences range between -20 TECU at 18h UTC in the southeast and 0 TECU in the north part of the map.

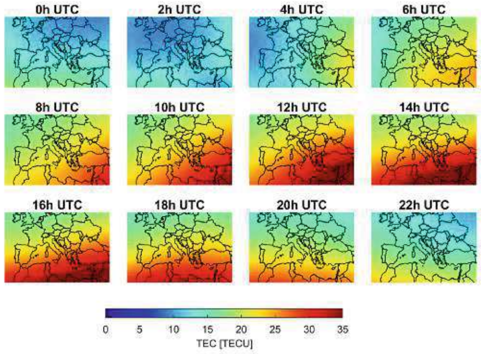


(a) TUWR

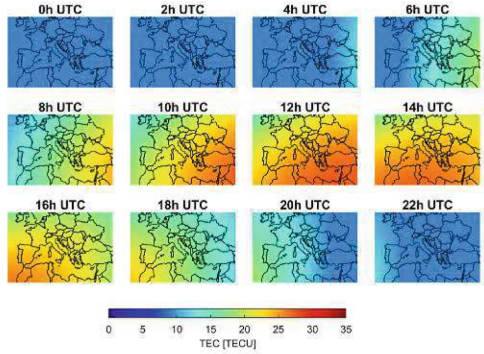


(b) Klobuchar

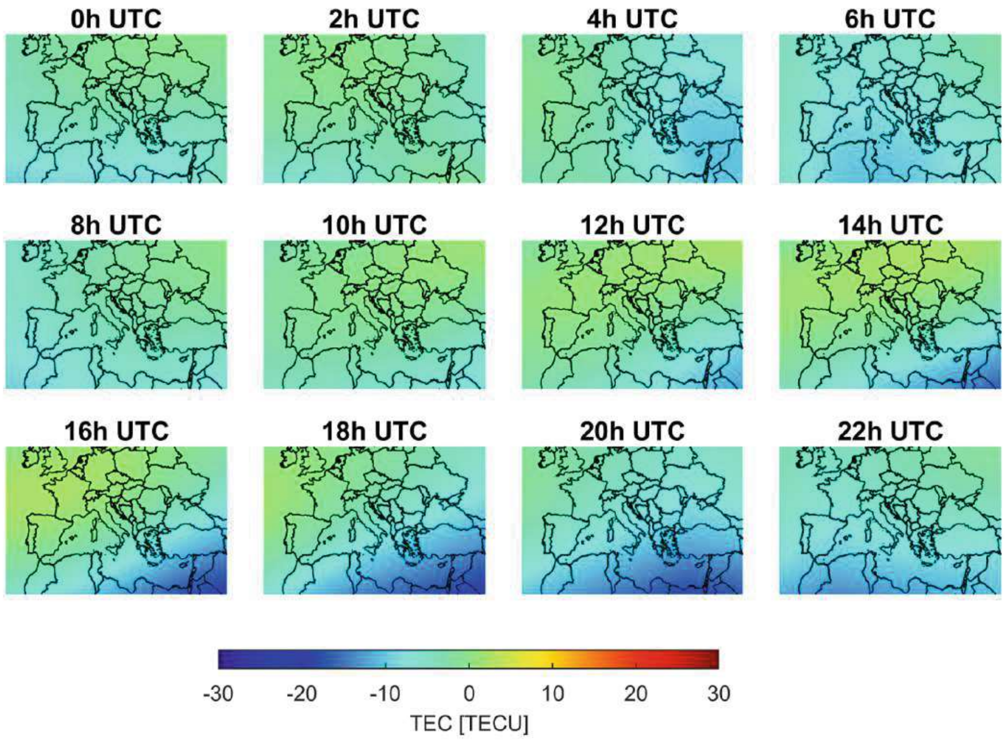


(c) Difference plot (Klobuchar - TUWR)

Figure 6.36: Regional VTEC maps of (a) TUWR and (b) Klobuchar. Plot (c) shows the difference map between model (a) and (b) for June 30, 2022 (doy 181 2022).

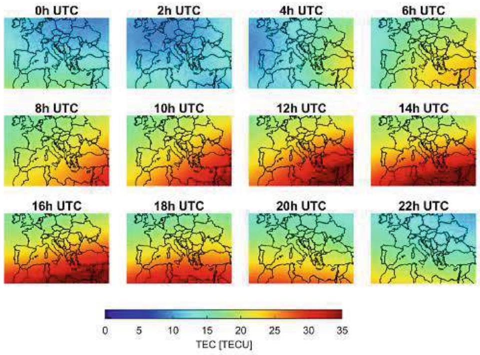


(a) TUWR

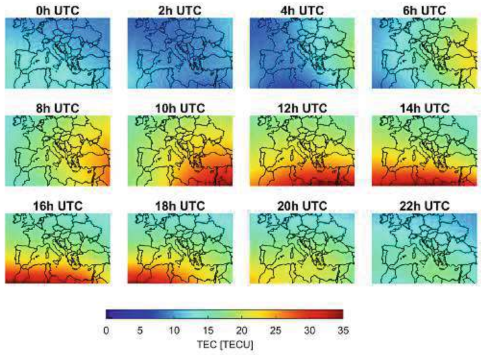


(b) NeQuick G

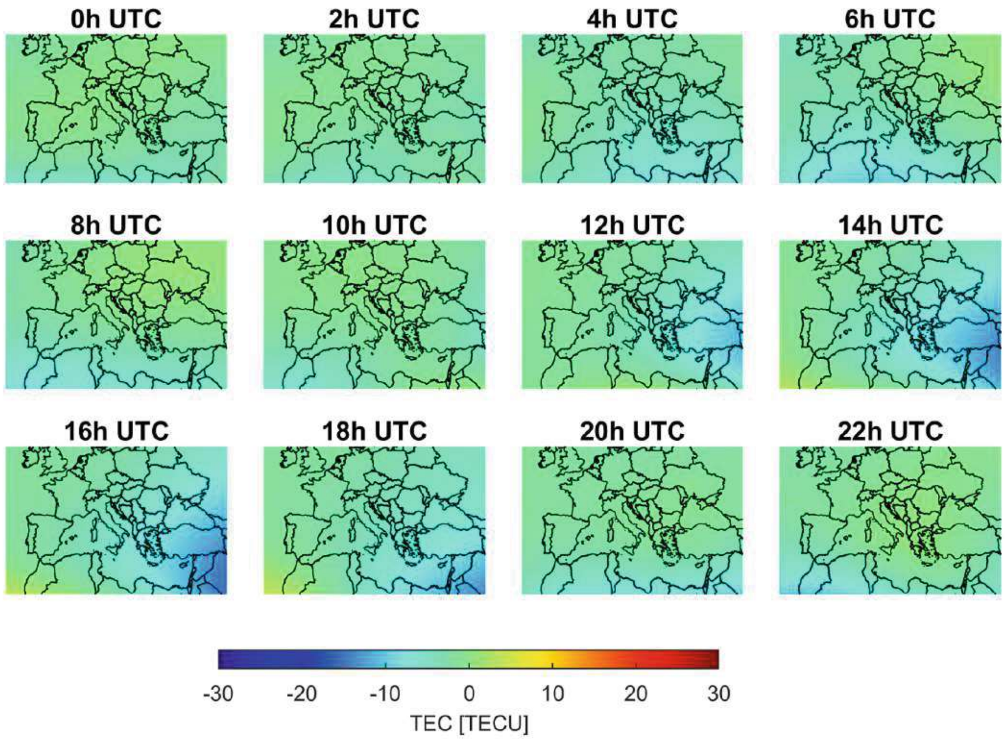


(c) Difference plot (NeQuick G - TUWR)

Figure 6.37: Regional VTEC maps of (a) TUWR and (b) NeQuick G. Plot (c) shows the difference map between model (a) and (b) for June 30, 2022 (doy 181 2022).

In Figure 6.37 TUWR is plotted against the NeQuick G model. Similar to Klobuchar, but less pronounced, NeQuick G underestimated the VTEC values throughout the whole day compared to TUWR. Therefore, the VTEC differences for this day ranged between -15 TECU at 16h UTC in the southeast and +3 TECU between 16h-18h UTC in the southwest.

### 6.2.2. Station-specific pseudorange corrections and STEC comparison

The second part of the TUWR model validation deals with the model-specific STEC values and consists of two parts. In the first part, pseudorange corrections for each model were calculated and compared. Five IGS validation stations were chosen for this purpose. The table containing information about the validation sites and the corresponding site location map can be found in Appendix B.1. In this section, graphics for two stations will be presented. The plots for the remaining validation stations can be found in Appendix B.1.

The calculation is performed station-wise. VTEC values for each IONEX file of five ionosphere models were extracted and converted to their corresponding STEC values via a mapping function (Eq. 5.34, se Chapter 5.2). These values were further used to derive their respective range corrections. At each station, range corrections from every model were applied to their phase-smoothed L1 pseudoranges, getting the value that needs to be evaluated. This value is further compared to the ionosphere-free linear combination (calculated from phase-smoothed code observations) from the current station. This value fulfills the function of the 'reference value'. Figures 6.38 and 6.39 show the daily difference between the model-specific corrected L1 pseudoranges and the ionosphere-free linear combination for all five models at two different IGS stations for June 30$^{th}$, 2022. The colored markers on the plots indicate the residuals of the previously described calculation, which were plotted every 30 minutes to every visible satellite. The green color on the markers denotes residuals are smaller than ± 0.5 m, yellow markers show residuals within the range ± 1.0 m, whereas red markers indicate all remaining residuals.

The range residual plots for station DYNG (Greece) in Figure 6.38 show that the best agreement with the ionosphere-free linear combination was achieved when correcting pseudorange observations with CODE-model-based range corrections. Almost all range residuals in this plot fall between -2.0 m and +1.5 m. Slightly higher range residuals can be noticed for the IGS and TUWR ionosphere models, which appear to perform quite similarly. This only underlines the already observed agreement from the VTEC difference map between IGS and TUWR from Figure 6.35. The majority of the IGS and TUWR range residuals are to be found within the span of -2.5 m and +1.5 m, with a few outliers reaching up to ± 4.0 m. NeQuick G reveals visibly worse range residuals, especially between 12h-20h, when also the highest disagreement between the NeQuick G model and the TUWR model could be seen in the corresponding VTEC difference plot (Figure 6.37). Finally, Klobuchar has visibly shown the worst performance at this station regarding ionospheric range correction of pseudorange observations. When applying Klobuchar corrections, residuals up to ± 4.0 m remain.

At station WSRT (the Netherlands) in Figure 6.39, it is visible that the performance of the TUWR model is pretty similar to the CODE and IGS model performance. All three models show range residuals mostly up to ± 2.0 m, except for a few outliers. A slightly worse performance can, at least visually, be noticed in the case of the NeQuick G model.

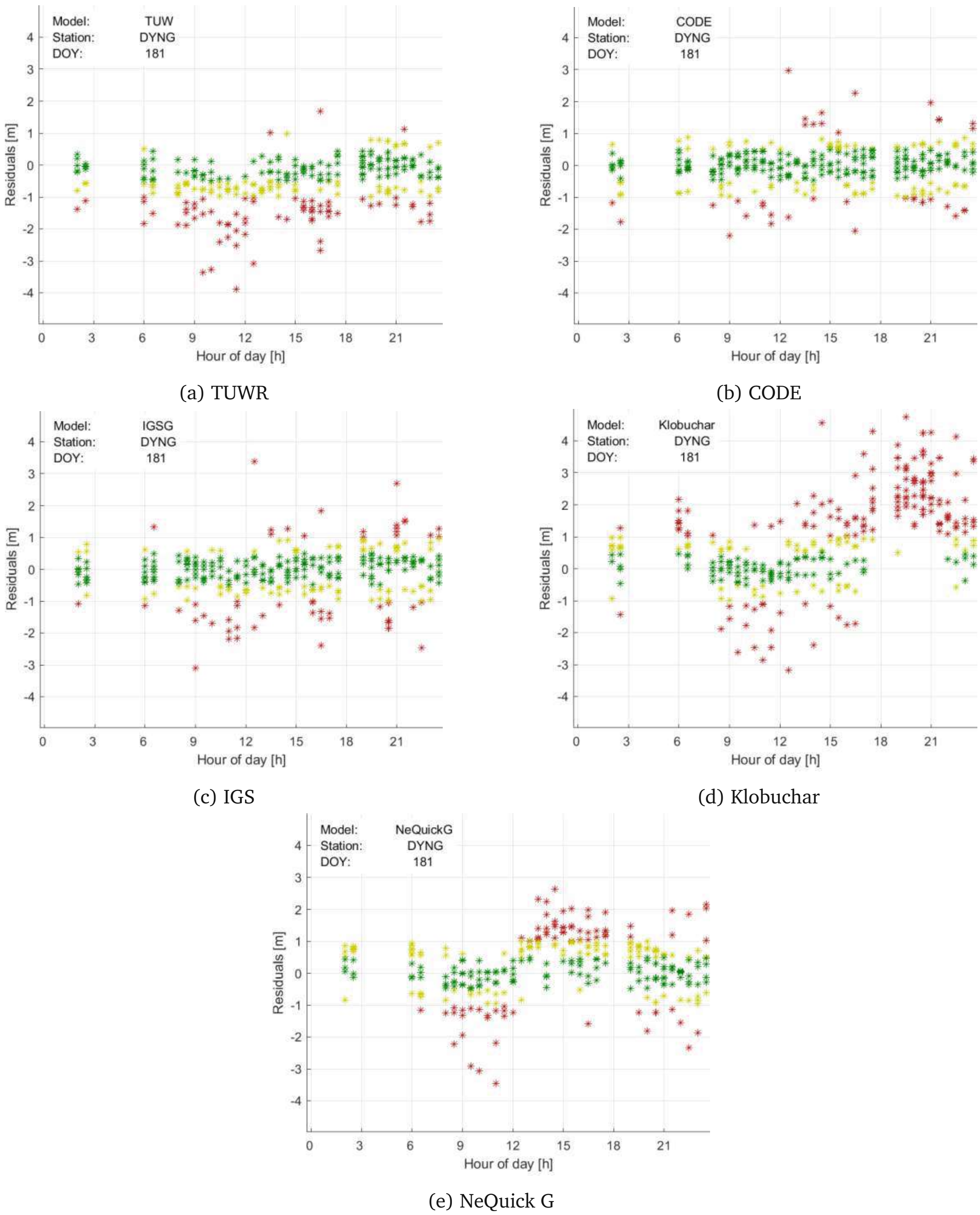


Figure 6.38: Difference between corrected L1 pseudoranges by ionosphere models (a) - (e) and the ionosphere-free linear combination on IGS station DYNG (Dionysos, Greece; $\varphi = 38.08°N$, $\lambda = 23.93°E$) for June 30, 2022 (doy 181 2022).

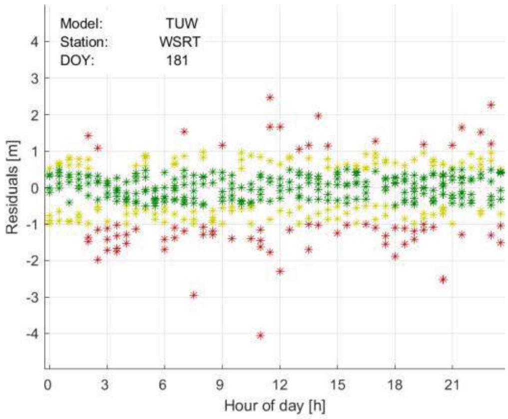


(a) TUWR

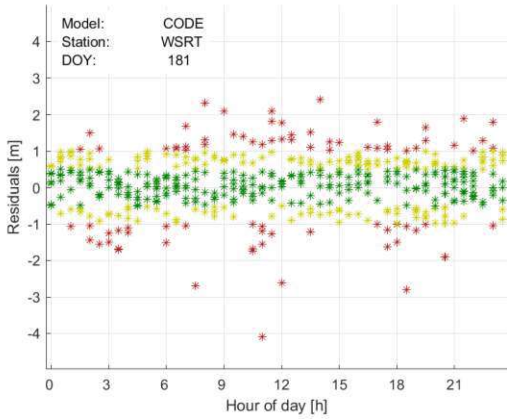


(b) CODE

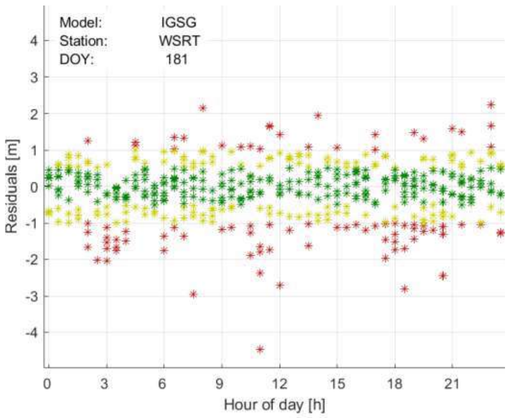


(c) IGS

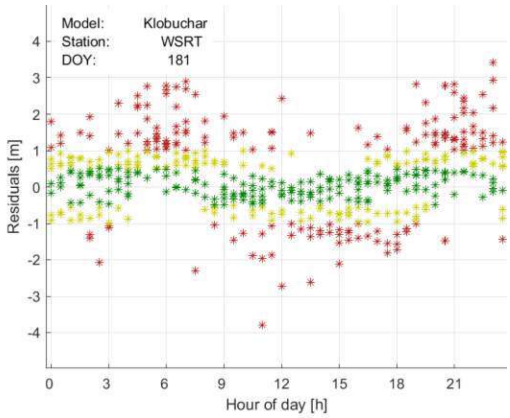


(d) Klobuchar

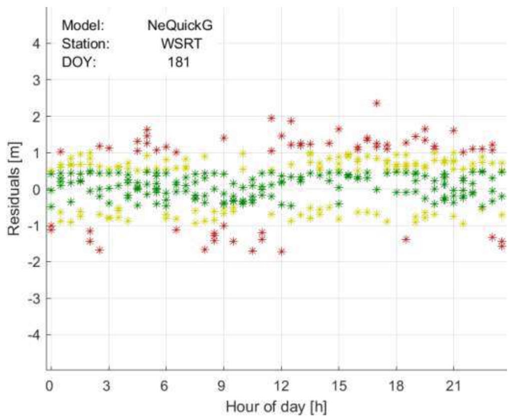


(e) NeQuick G

Figure 6.39: Difference between corrected L1 pseudoranges by ionosphere models (a) - (e) and the ionosphere-free linear combination on IGS station WSRT (Westerbork, the Netherlands; $\varphi = 52.91°N$, $\lambda = 6.60°E$) for June 30, 2022 (doy 181 2022).

In general, the residuals from the corresponding plot (e) remain mostly within the range ± 2.0 m, as in the case of the previous three models. However, between 12h-18h, all residuals move from the center of the plot for around 0.5 m up, indicating that within this period of the day, the ionospheric range corrections did not agree with the reference value. This matches the previously discussed VTEC difference plot for the same day in Figure 6.35, where NeQuick G in general has slightly underestimated the VTEC value on this day w.r.t. the TUWR model, especially between 16h-18h UTC. The worst performance can be seen in plot (d) for the Klobuchar model. In this case, range residuals show up to approximately ± 3.0 m, with residuals moved upward between 03h-09h and 18h-24h. The previously discussed VTEC difference map for Klobuchar (Figure 6.36) has, similar to NeQuick G, revealed a constant underestimation in VTEC values for this day compared to the TUWR model, showing a peak at 18h UTC. This performance is later reflected in the range residuals.

Table 6.7 summarizes the performances of all tested ionosphere models over all five validation stations for the displayed day. In this table, the percentages of all range residuals < ± 0.5 m (in green), < ± 1.0 m (in yellow), and < ± 1.5 m (in red) are shown for each model for the tested day (June 30$^{\text{th}}$, 2022). As previously mentioned, the plots for the remaining validation stations can be found in Appendix B.1. Numbers shown in bold indicate the best percentage values among the models for each group of differences. For this day, in all three difference categories the CODE model has proven to perform the best pseudorange correction over the five chosen stations (CODE: 50.67 % of range residuals < ± 0.5 m). Still, IGS and TUWR are not far away from these results. IGS is worse than CODE by only 1% (IGS: 49.79 % of range residuals < ± 0.5 m), while the difference between CODE and TUWR for this day is not larger than 3% (TUWR: 47.61 % of range residuals < ± 0.5 m). The NeQuick G model, even though being worse below the ± 0.5 m and ± 1.0 m limit, still proves to get range residuals < ± 1.5 m at almost the same level as TUWR and IGS (TUWR: 89.62 %, IGS: 91.12 % and NeQuick G: 88.68 % of range residuals < ± 1.5 m). The Klobuchar model performs the worst for this day (Klobuchar: 75.53 % of range residuals < ± 1.5 m). To have a better insight, into how well these models perform over a longer time, Figure 6.40 illustrates percentages as time series for the period April 1$^{\text{st}}$, 2022 - June 30$^{\text{th}}$, 2022.

Table 6.7: Percentage of differences between corrected L1 pseudoranges by ionosphere models and the ionosphere-free linear combination which are smaller than the specified differences on the left. Percentages are given for all tested models on all five testing stations for June 30, 2022 (doy 181, 2022).

| Difference | TUWR | CODE | IGS | Klobuchar | NeQuick G |
|---|---|---|---|---|---|
| < ± 0.5 m | 47.61 % | **50.67 %** | 49.79 % | 32.14 % | 41.54 % |
| < ± 1.0 m | 76.08 % | **81.14 %** | 78.32 % | 57.65 % | 73.06 % |
| < ± 1.5 m | 89.62 % | **93.01 %** | 91.12 % | 75.53 % | 88.68 % |

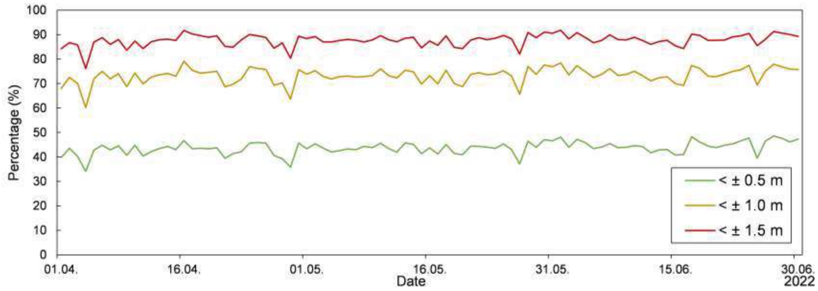


(a) TUWR

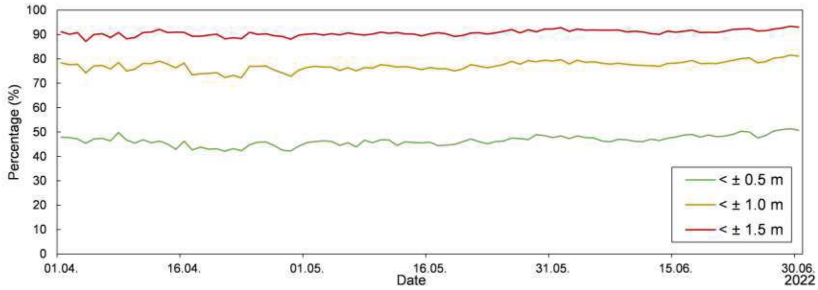


(b) CODE

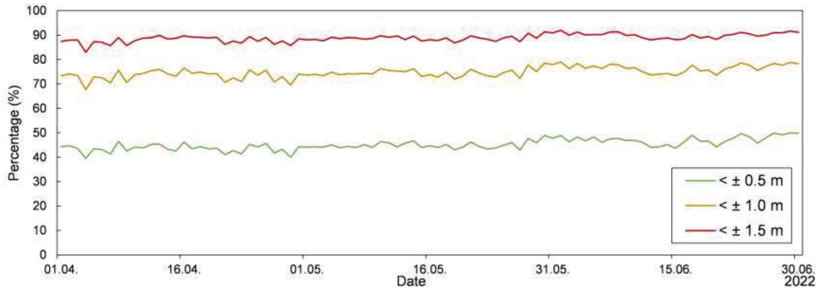


(c) IGS

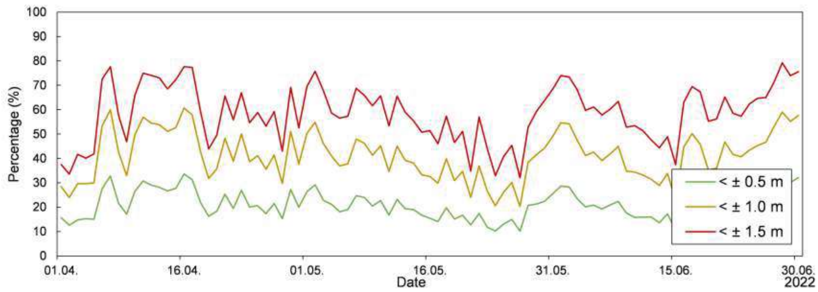


(d) Klobuchar

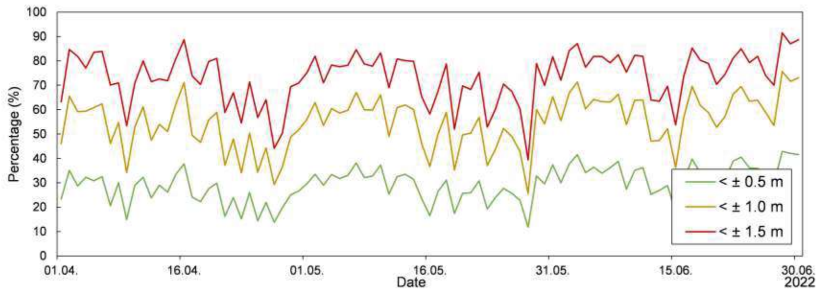


(e) NeQuick G

Figure 6.40: Time series of daily percentages between L1 pseudoranges corrected with models (a) - (e) and the L3 linear combination, which are smaller than 0.5 m, 1.0 m, and 1.5 m, for the period April 1 - June 30, 2022 (doy 091 - 181, 2022).

The corresponding statistics for each model are extracted in Tables 6.8 - 6.12.

Table 6.8: Statistics extracted from Fig. 6.40a for the TUWR model.

| TUWR | $< \pm$ 0.5 m | $< \pm$ 1.0 m | $< \pm$ 1.5 m |
|---|---|---|---|
| mean | 43.65 % | 73.27 % | 87.72 % |
| median | 43.81 % | 73.60 % | 87.93 % |
| max | 48.54 % | 79.17 % | 91.77 % |
| min | 34.06 % | 60.21 % | 76.15 % |

Table 6.9: Statistics extracted from Fig. 6.40b for the CODE model.

| CODE | $< \pm$ 0.5 m | $< \pm$ 1.0 m | $< \pm$ 1.5 m |
|---|---|---|---|
| mean | 46.48 % | 77.21 % | 90.67 % |
| median | 46.35 % | 77.33 % | 90.76 % |
| max | 51.37 % | 81.54 % | 93.36 % |
| min | 42.11 % | 72.33 % | 87.18 % |

Table 6.10: Statistics extracted from Fig. 6.40c for the CODE model.

| IGS | $< \pm$ 0.5 m | $< \pm$ 1.0 m | $< \pm$ 1.5 m |
|---|---|---|---|
| mean | 45.18 % | 74.77 % | 88.83 % |
| median | 44.86 % | 74.62 % | 88.85 % |
| max | 49.94 % | 78.99 % | 91.95 % |
| min | 39.56 % | 67.69 % | 82.98 % |

Table 6.11: Statistics extracted from Fig. 6.40d for the Klobuchar model.

| Klobuchar | $< \pm$ 0.5 m | $< \pm$ 1.0 m | $< \pm$ 1.5 m |
|---|---|---|---|
| mean | 21.04 % | 41.09 % | 58.42 % |
| median | 20.84 % | 41.14 % | 58.78 % |
| max | 33.67 % | 60.67 % | 79.18 % |
| min | 10.15 % | 20.28 % | 32.01 % |

Table 6.12: Statistics extracted from Fig. 6.40e for the NeQuick G model.

| NeQuick G | $< \pm$ 0.5 m | $< \pm$ 1.0 m | $< \pm$ 1.5 m |
|---|---|---|---|
| mean | 29.35 % | 54.84 % | 73.27 % |
| median | 30.00 % | 56.85 % | 75.18 % |
| max | 42.90 % | 75.67 % | 91.51 % |
| min | 11.83 % | 25.57 % | 39.37 % |

As expected, the CODE model offers in general the values closest to the true reference values (ionosphere-free linear combination), achieving a mean of 46.48 % of observations being corrected with < ± 0.5 m range residuals. IGS and TUWR are not far from the CODE performance, with IGS being the closest with a three-monthly mean of 45.18 % of observations having range residuals < ± 0.5 m, followed by the TUWR model with 43.65 % of all observations showing range residuals < ± 0.5 m.

Both Klobuchar and NeQuick G, as evidenced by their plots and corresponding tables, demonstrate performance levels that fall short when compared to those of CODE, IGS, and even the TUWR model. However, upon closer examination of Table 6.12, it becomes apparent that NeQuick G achieved a maximum percentage of 91.51% of all observations to have range residuals < ± 1.5 m over three months. This suggests a potential for NeQuick G to deliver improved performance in pseudorange corrections

Another way of comparing the TUWR model to other ionosphere models is presented in Figures 6.41 and 6.42. On these plots, monthly STEC differences are shown station-wise for each model. Again, plots for two validation stations are shown, while the remaining plots can be found in Appendix B.2. First, STEC values for each model for each station, are collected for a month and stored. The reference values were again calculated based on the phase-smoothed code observations, by extracting the STEC via the geometry-free linear combination. The reference values are also collected for a month and stored for each station. Next, the model-specific STEC values were compared to the observation-based STEC values and plotted over a month (in this case for June 2022). The monthly TUWR STEC differences range between -6 TECU and -1 TECU at station DYNG (Greece), while in the case of station WSRT (the Netherlands) the STEC differences range between -3 TECU and 1 TECU. DYNG and WSRT demonstrate similar patterns in STEC residuals, particularly noticeable in the case of Klobuchar and NeQuick G applied models, where the variations in STEC differences are more pronounced. One consistent finding across all tested models is that the southern station, DYNG, displays larger STEC differences between the modeled and observed values compared to the northern station, WSRT. Considering that the ionospheric activity is more pronounced near the equator and low latitudes (up to 30° north and south from the equator), compared to higher latitude regions, where the ionosphere exhibits less fluctuations, it was anticipated to observe this pattern for the two validation sites. The STEC differences, when using the ionospheric models (a) - (c) at station WSRT, show a relatively consistent behavior. CODE shows in both figures, as expected again, the best agreement between model-based STEC and observation-based STEC with discrepancies between -3 TECU and 0 TECU for DYNG (Greece) and between -1 TECU and 1 TECU for WSRT (the Netherlands). IGS follows closely with differences ranging between -3 TECU and 1 TECU for DYNG (Greece) and between -2 TECU and 1 TECU for WSRT (the Netherlands), indicating slightly more variations in the first plot (Figure 6.41) in STEC differences compared to CODE. NeQuick G reveals STEC differences between -7 TECU and 7 TECU for DYNG (Greece) and between -5 TECU and 5 TECU for WSRT (the Netherlands). Again, Klobuchar shows the worst results with an STEC discrepancy range between -4 TECU and 17 TECU for DYNG (Greece) and between -8 TECU and 9 TECU for WSRT (the Netherlands).

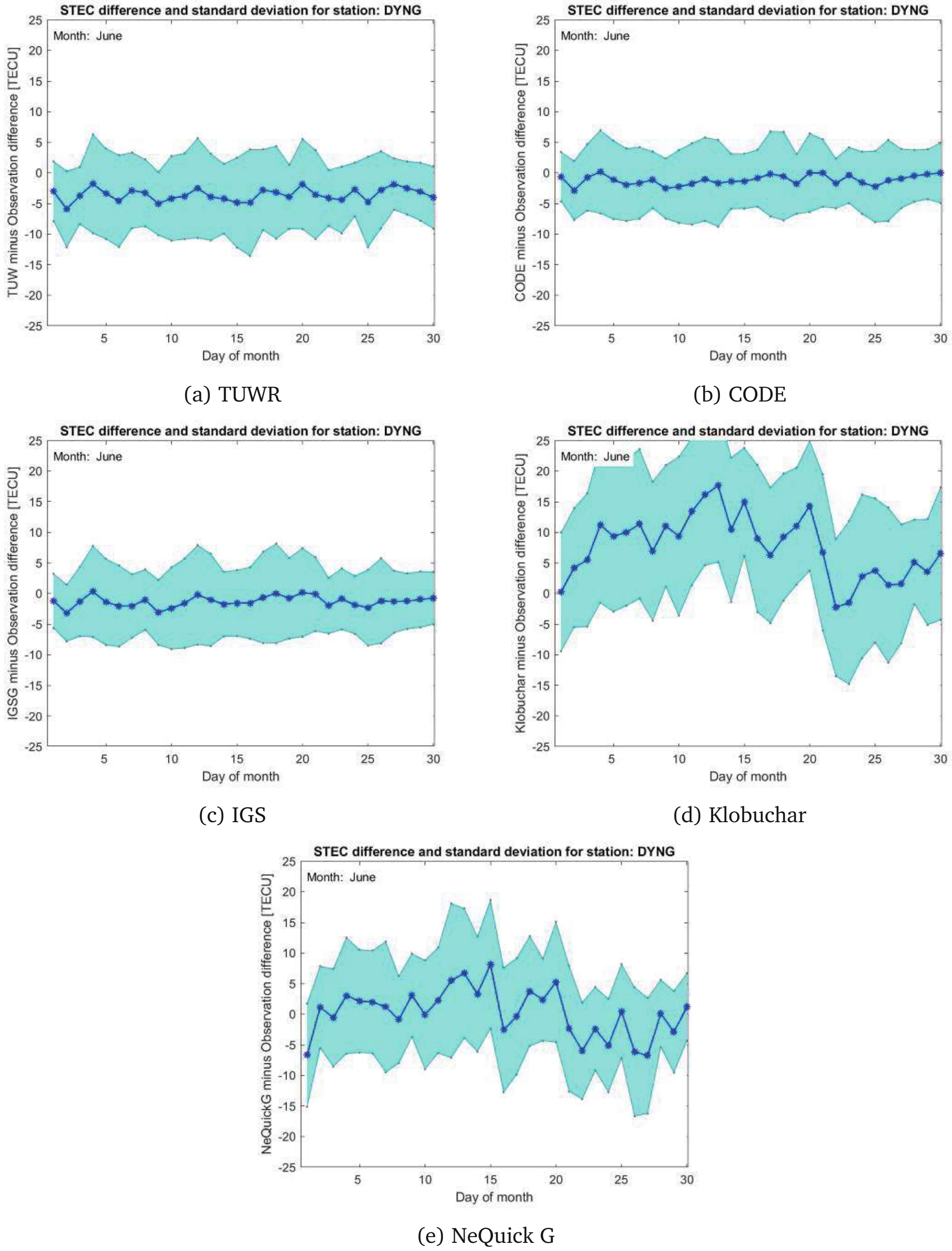


(a) TUWR

(b) CODE

(c) IGS

(d) Klobuchar

(e) NeQuick G

Figure 6.41: Monthly STEC differences and standard deviations between the STEC value derived from the tested models (a) - (e) and the observation-based STEC on IGS station DYNG (Dionysos, Greece; $\varphi = 38.08°N$, $\lambda = 23.93°E$) for June 2022 (doy 181 2022).

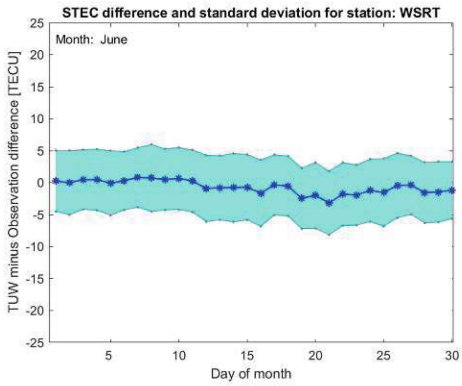


(a) TUWR

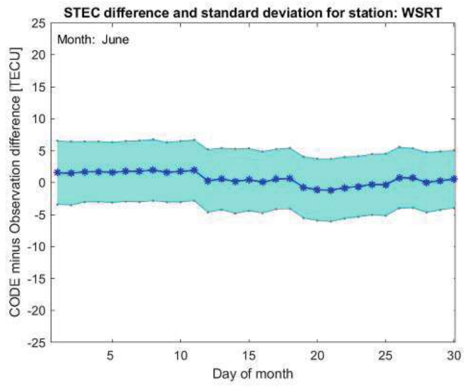


(b) CODE

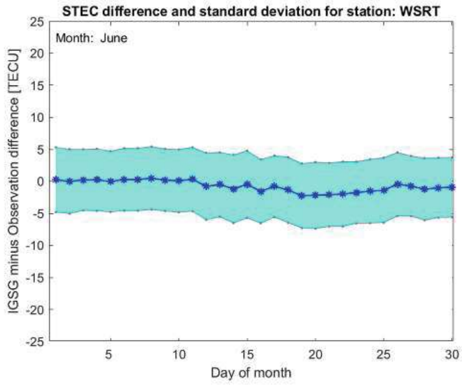


(c) IGS

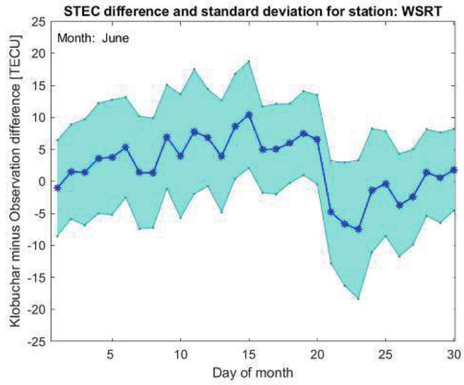


(d) Klobuchar

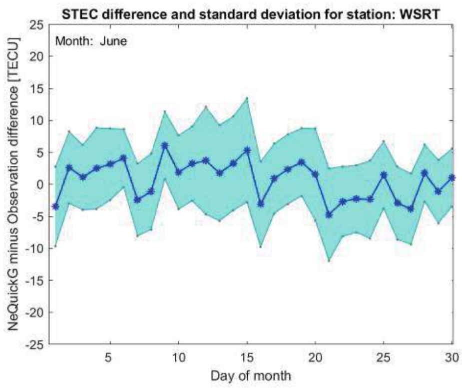


(e) NeQuick G

Figure 6.42: Monthly STEC differences and standard deviations between the STEC value derived from the tested models (a) - (e) and the observation-based STEC on IGS station WSRT (Westerbork, the Netherlands; $\varphi = 52.91°N$, $\lambda = 6.60°E$) for June 2022 (doy 181 2022).

The processing time required for the TUWR ionosphere model to generate a single 1-hour resolution daily file can take as long as 25 minutes. Each day, a maximum of 35 stations contribute to the solution, with 19 of them capable of receiving Galileo signals alongside GPS (multi-GNSS). This results in Galileo contributing up to 24% of the total satellite count in the regional ionosphere modeling processing.

# 7. Summary and Outlook

In pursuit of constant improvement and development, and in order to keep pace with the ever-changing conditions of the Earth's movement and structure, the geodetic community has to review, refine and, if needed, redefine methods for the determination of fundamental global geodetic parameters. Nowadays, the term GNSS can no longer be associated with only GPS. Despite GPS having the longest history and for many years a stable constellation as well, which, aside from GLONASS, had yet to be reached by Galileo and BeiDou, today it can be said that four GNSS constellations can be reliably used in GNSS practice and research.

This thesis examines the use of the Galileo system and investigates its impact on the determination of global geodetic parameters, such as pole coordinates and LoD when combining GPS with Galileo. Moreover, this combination is explored on a regional scale, by estimating VTEC values over European mid-latitudes.

The research hypothesis that was set to be verified throughout the thesis was that the use of the Galileo system enhances the quality of determination of these parameters and as a result, improves the estimation of GNSS-based products relying on these parameters. It has to be noted that any outcome described in this work as "improvement", or similarly, refers to a noticed improvement w.r.t. the used reference models, and therefore the outcome might differ depending on which model was used. However, after using multiple models as references in both, the global (three models) and the regional (four models) analysis, the findings from this work can be considered as a reliable statement.

Based on the findings presented in the preceding chapter of this dissertation (see Chapter 6), the key conclusions derived can be categorized into two main groups:

- The multi GNSS-based ERP solution (pole coordinates and LoD), based on the combination of GPS and Galileo observations shows an indisputable improvement compared to the individual GPS solution.

The improvement can be noticed in several aspects. By observing the corresponding parameter time series as 1-day and 3-day arc solutions, the noise floor is the highest in the GPS-only case, which is further reflected in the respective amplitude spectra of the polar motion time series. The add-on of GPS observations by using Galileo has proven to bring the estimated parameters closer to the reference model. Moreover, the additional run with the extended ECOM2 model has shown that Galileo-based processing needs definitely to be performed by choosing the ECOM2 over the ECOM model (the difference between these two models was discussed earlier in Section 5.1.1) to achieve the largest improvement. The advantage of the subsequently derived 3-day arc solutions should not be disregarded, which can also be seen in the results. The statistics for pole coordinates from Tables 6.1 and 6.2 show smaller mean differences and standard deviations of the combined GPS/Galileo+ECOM2 solution w.r.t. the reference model compared to the GPS only+ECOM solution by ~25% and ~30% respectively, when observing 1-day and 3-day arc solutions separately. The GPS/Galileo+ECOM solutions have, in most cases, shown slightly better results compared to the GPS only+ECOM solutions, by 1-2 mas in pole coordinates (when comparing 1-day and 3-day arc solutions individually). The statistics of the LoD time series (Table 6.3) reveal comparable results for all solution types, while still the multi-GNSS solutions are at a slight advantage w.r.t. the reference model by up to ~3 ms/day. However, the benefit of applying the ECOM2 instead of the ECOM model is not as pronounced in this case as it was with the pole coordinates time series.

The tidal coefficient corrections for the 8 major tides, derived from the different GNSS solutions, were compared to three chosen reference models. Besides small discrepancies among the reference models themselves, a few consistencies can be observed. First, the 1-day arc GPS-only+ECOM solution shows by far the largest amplitude corrections in all cases, reaching up to ~50 $\mu$as in pole coordinates (for the diurnal K1 and semi-diurnal K2 tide) and up to ~25 $\mu$s/day in LoD (for the diurnal P1 tide). The combined 1-day arc GPS/Galileo+ECOM solution follows closely in terms of amplitude corrections. Due to their large amplitudes, those two solutions were kept out of the main analysis, but are shown in Appendix A.2, as stated previously in Chapter 6. The remaining solutions exhibit likewise consistently larger amplitude corrections for the diurnal components P1 and K1 and the semi-diurnal components S2 and K2 in pole coordinates, as well as for the semi-diurnal component M2 in LoD. In most cases, as shown in the previous Chapter (Section 6.1.3), the amplitude corrections derived from the 3-day arc GPS-only+ECOM and GPS/Galileo+ECOM solutions show the maximum values for these major tidal constituents. The largest discrepancies, among those four tested solutions, can be noticed in the case of the 3-day arc GPS-only+ECOM solution (~9.5 $\mu$as and ~10 $\mu$s/day w.r.t. all reference models in pole coordinates and LoD, respectively), after which follows the 3-day arc GPS/Galileo+ECOM (~8 $\mu$as and ~6 $\mu$s/day w.r.t. all reference models in pole coordinates and LoD, respectively). The 3-day GPS/Galileo+ECOM2 solution shows average amplitude corrections of ~7.5 $\mu$as and ~5 $\mu$s/day w.r.t. all reference models in pole coordinates and LoD, respectively, whereby the 1-day arc GPS/Galileo+ECOM2-derived solution delivers on average the smallest amplitude corrections, namely ~4 $\mu$as and ~4 $\mu$s/day w.r.t. all reference models in pole coordinates and LoD, respectively. This only proves the significance of combining more GNSS and adapting models relevant to different satellite systems used.

- A regional ionosphere model, based on multi-GNSS observation data, can provide comparable results to well-known established models, having on average less than 1 TECU difference w.r.t. to those models.

This statement has been confirmed in different ways, as seen in Section 6.2, from a latitude-dependent VTEC comparison of the estimated TUWR model with other chosen reference models (see Figures 6.28 and 6.29), over a comparison of their respective ionosphere maps (Figures 6.30-6.37), up to a station-specific analysis of the model performance (Figures 6.38-6.39, 6.41-6.42). The two most relevant reference models are the ones offered by CODE and IGS, therefore, the validation mostly leaned towards comparing them to the TUWR model.

The multi-GNSS-based ionosphere model presented in this work offers reliable information on the ionospheric state, comparable in performance to established models provided by CODE and IGS. Furthermore, this model can be applied when observation data from single-frequency receivers has to be processed in order to mitigate the error source, which originates from ionospheric effects on the satellite signal as it travels from satellite to receiver.

Based on the comprehensive research and analysis presented in this thesis, it is evident that the integration of the Galileo system alongside GPS has brought about significant enhancements in the determination of global geodetic parameters. The multi-GNSS approach, combining GPS and Galileo observations, has demonstrated indisputable improvements compared to relying solely on GPS. These enhancements are particularly noticeable in reduced noise levels, improved parameter estimation, and reduced discrepancies when compared to reference models.

These findings reveal that a regional ionosphere model based on multi-GNSS observations offers highly comparable results to well-established models, with minimal differences. This implies that the multi-GNSS approach can be a valuable asset in providing reliable information about the ionospheric state, particularly useful when processing data from single-frequency receivers to mitigate ionospheric signal effects.

In conclusion, this research not only reaffirms the importance of continuously evolving geodetic methodologies but also underscores the significance of multi-GNSS systems, specifically the Galileo system, in advancing the accuracy and quality of geodetic parameters and ionosphere modeling. These advancements hold promising implications for a wide range of applications, from satellite navigation to Earth monitoring and beyond. The pursuit of constant improvement and innovation within the geodetic community remains essential in adapting to the dynamic conditions of our planet's movement and structure.

# A. Appendix

## A.1. ERP timeseries

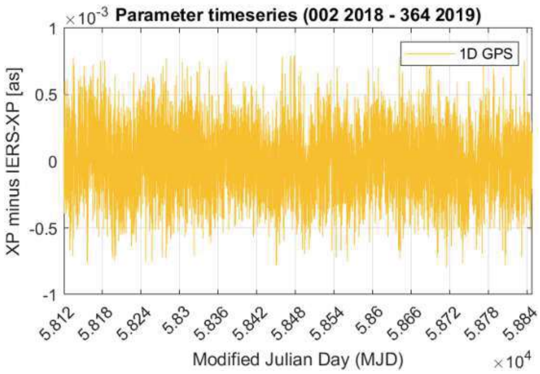


(a) 1-day arc GPS-only solution + ECOM

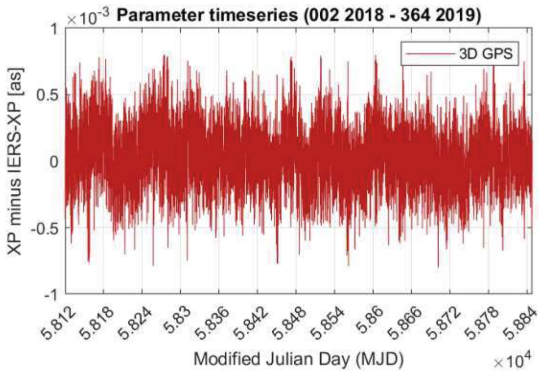


(b) 3-day arc GPS-only solution + ECOM

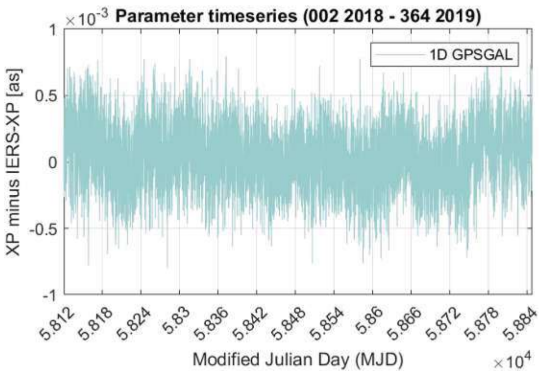


(c) 1-day arc GPS/Galileo solution + ECOM

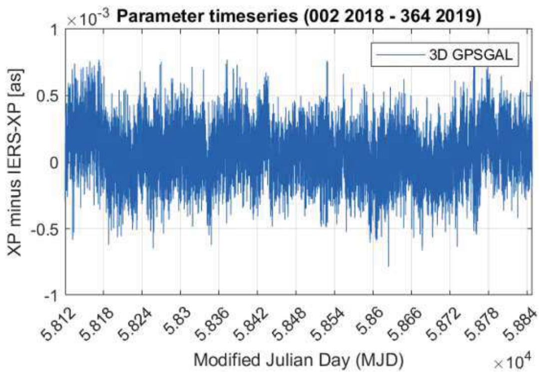


(d) 3-day arc GPS/Galileo solution + ECOM

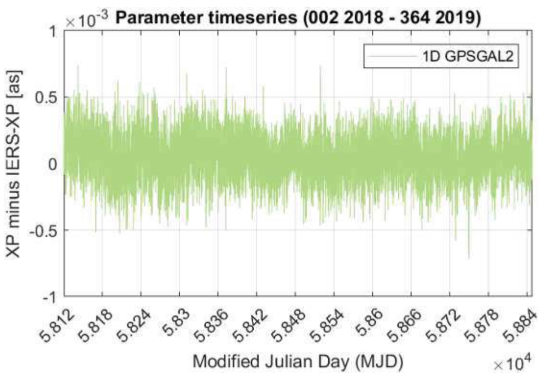


(e) 1-day arc GPS/Galileo solution + ECOM2

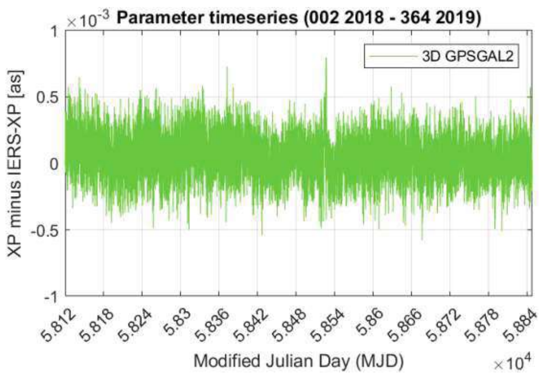


(f) 3-day arc GPS/Galileo solution + ECOM2

Figure A.1: Polar motion time series (X coordinate) w.r.t. the IERS C04 14 reference model (Jan 2018 - Dec 2019). All solution types are presented separately on plots (a) - (f).

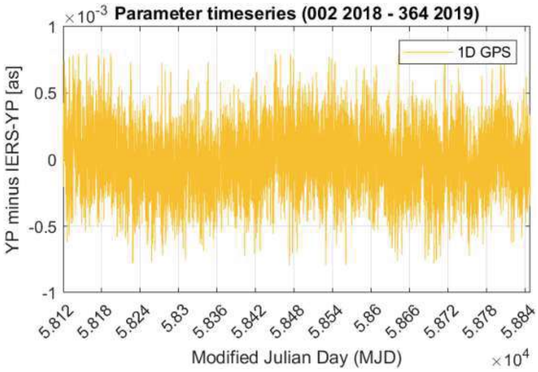


(a) 1-day arc GPS-only solution + ECOM

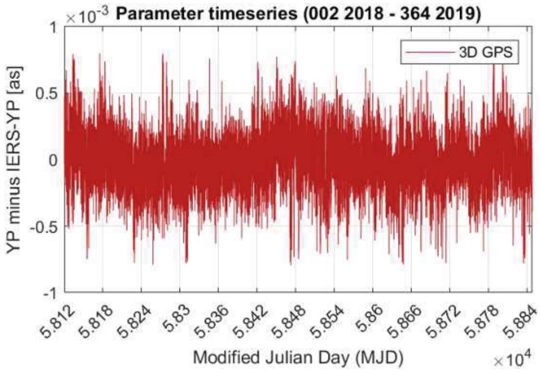


(b) 3-day arc GPS-only solution + ECOM

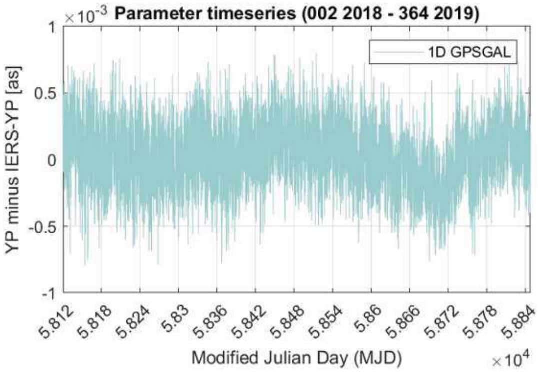


(c) 1-day arc GPS/Galileo solution + ECOM

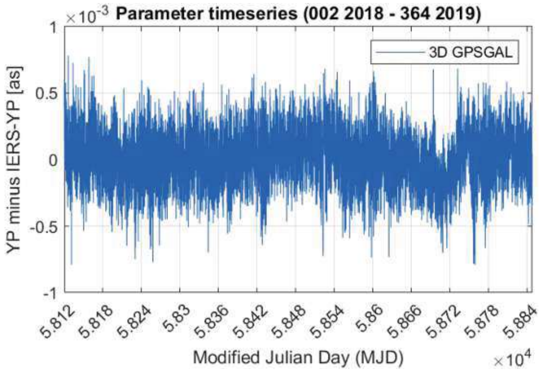


(d) 3-day arc GPS/Galileo solution + ECOM

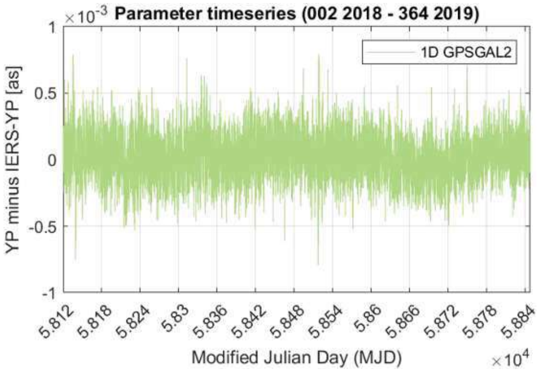


(e) 1-day arc GPS/Galileo solution + ECOM2

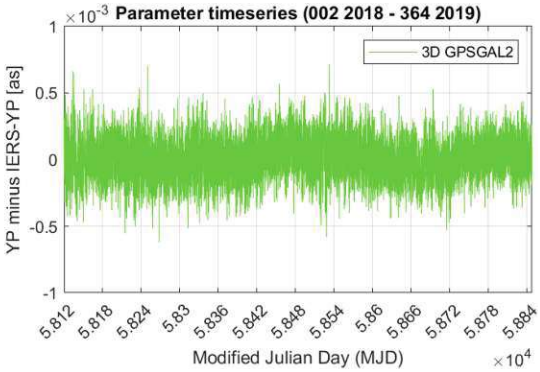


(f) 3-day arc GPS/Galileo solution + ECOM2

Figure A.2: Polar motion time series (Y coordinate) w.r.t. the IERS C04 14 reference model (Jan 2018 - Dec 2019). All solution types are presented separately on plots (a) - (f).

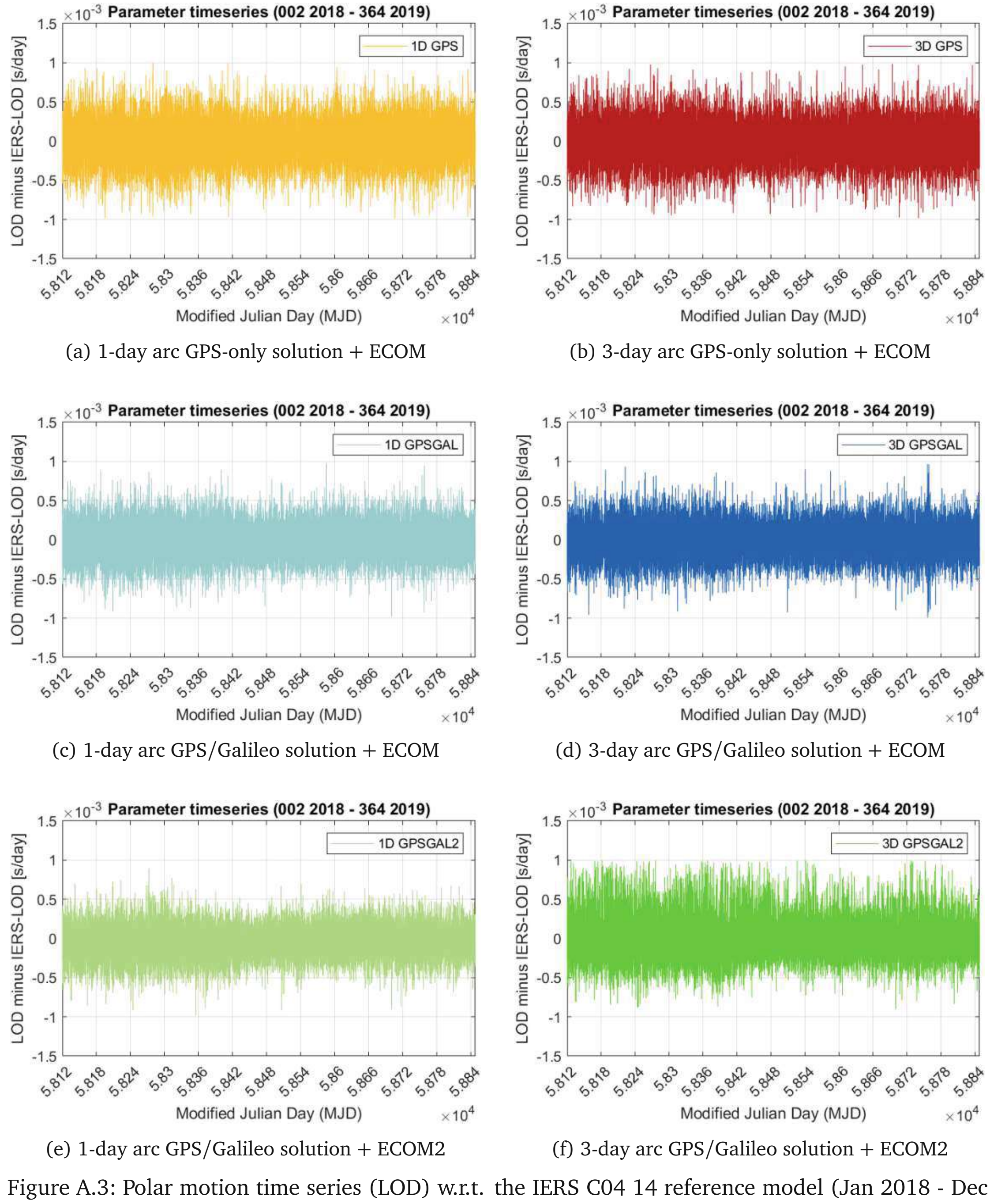


(a) 1-day arc GPS-only solution + ECOM

(b) 3-day arc GPS-only solution + ECOM

(c) 1-day arc GPS/Galileo solution + ECOM

(d) 3-day arc GPS/Galileo solution + ECOM

(e) 1-day arc GPS/Galileo solution + ECOM2

(f) 3-day arc GPS/Galileo solution + ECOM2

Figure A.3: Polar motion time series (LOD) w.r.t. the IERS C04 14 reference model (Jan 2018 - Dec 2019). All solution types are presented separately on plots (a) - (f).

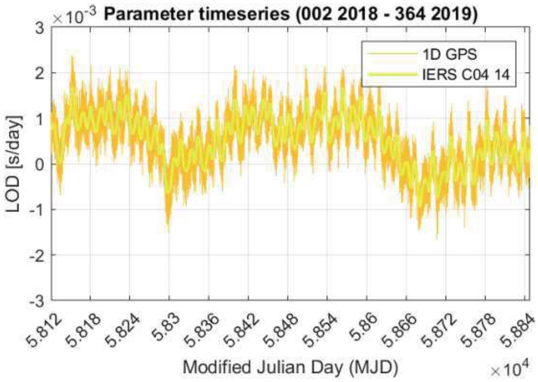


(a) 1-day arc GPS-only solution + ECOM

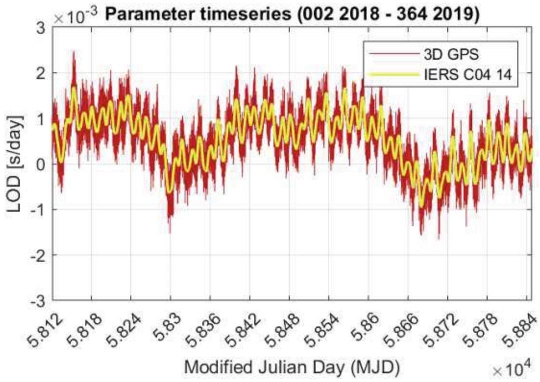


(b) 3-day arc GPS-only solution + ECOM

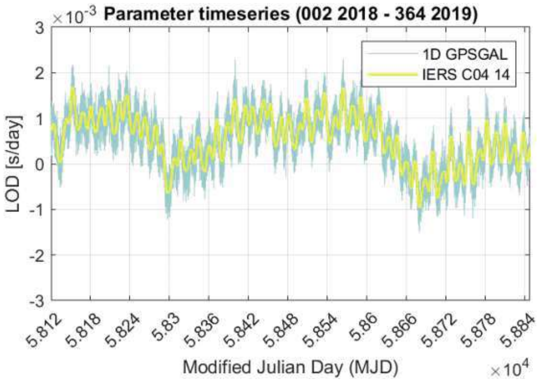


(c) 1-day arc GPS/Galileo solution + ECOM

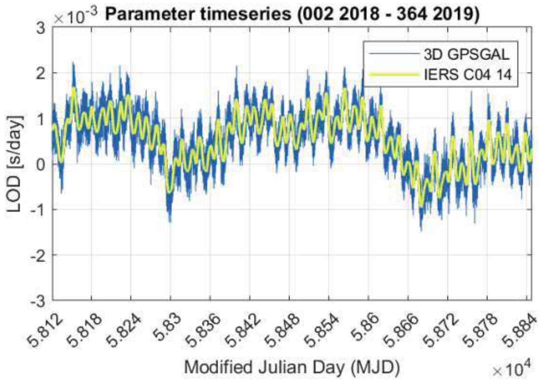


(d) 3-day arc GPS/Galileo solution + ECOM

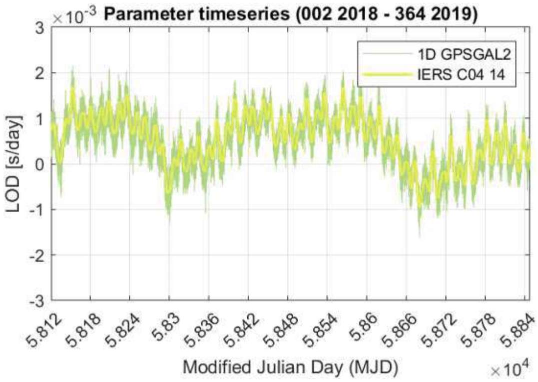


(e) 1-day arc GPS/Galileo solution + ECOM2

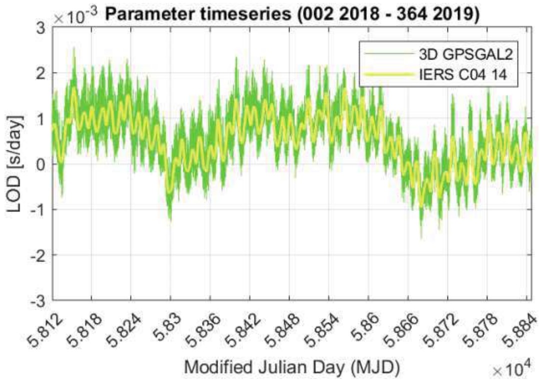


(f) 3-day arc GPS/Galileo solution + ECOM2

Figure A.4: Polar motion time series (raw LOD) w.r.t. the IERS C04 14 reference model (Jan 2018 - Dec 2019). All solution types are presented separately on plots (a) - (f).

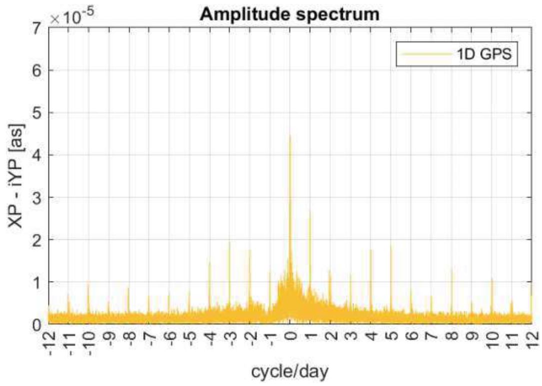


(a) 1-day arc GPS-only solution + ECOM

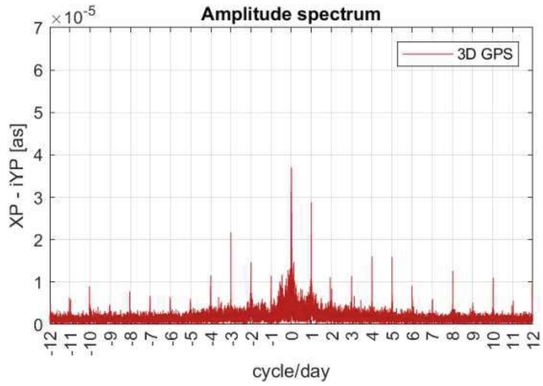


(b) 3-day arc GPS-only solution + ECOM

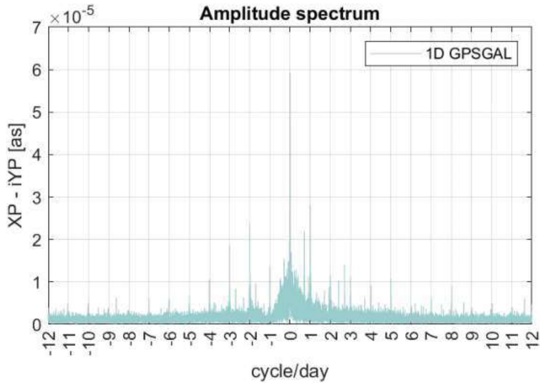


(c) 1-day arc GPS/Galileo solution + ECOM

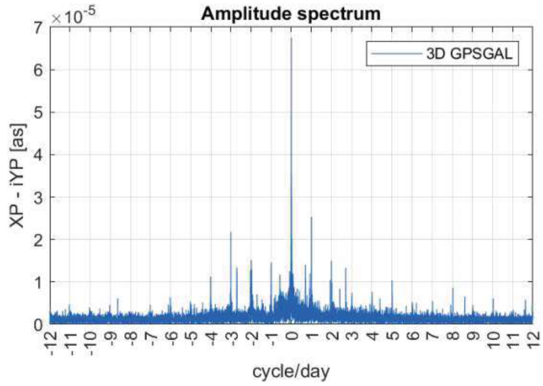


(d) 3-day arc GPS/Galileo solution + ECOM

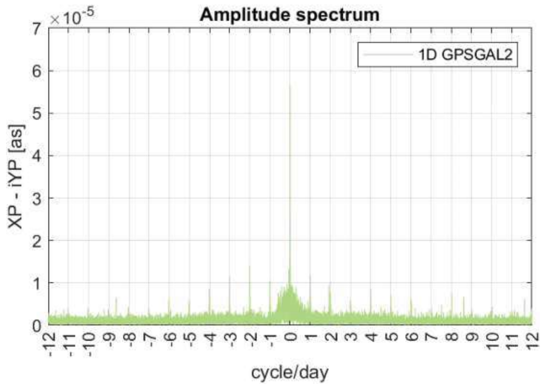


(e) 1-day arc GPS/Galileo solution + ECOM2

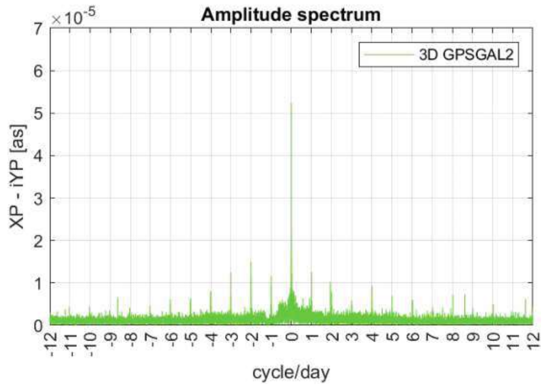


(f) 3-day arc GPS/Galileo solution + ECOM2

Figure A.5: XY pole Amplitude spectrum of polar motion time series w.r.t. the subdiurnal IERS C04 14 reference model (Jan 2018 - Dec 2019). All solution types are presented separately on plots (a) - (f).

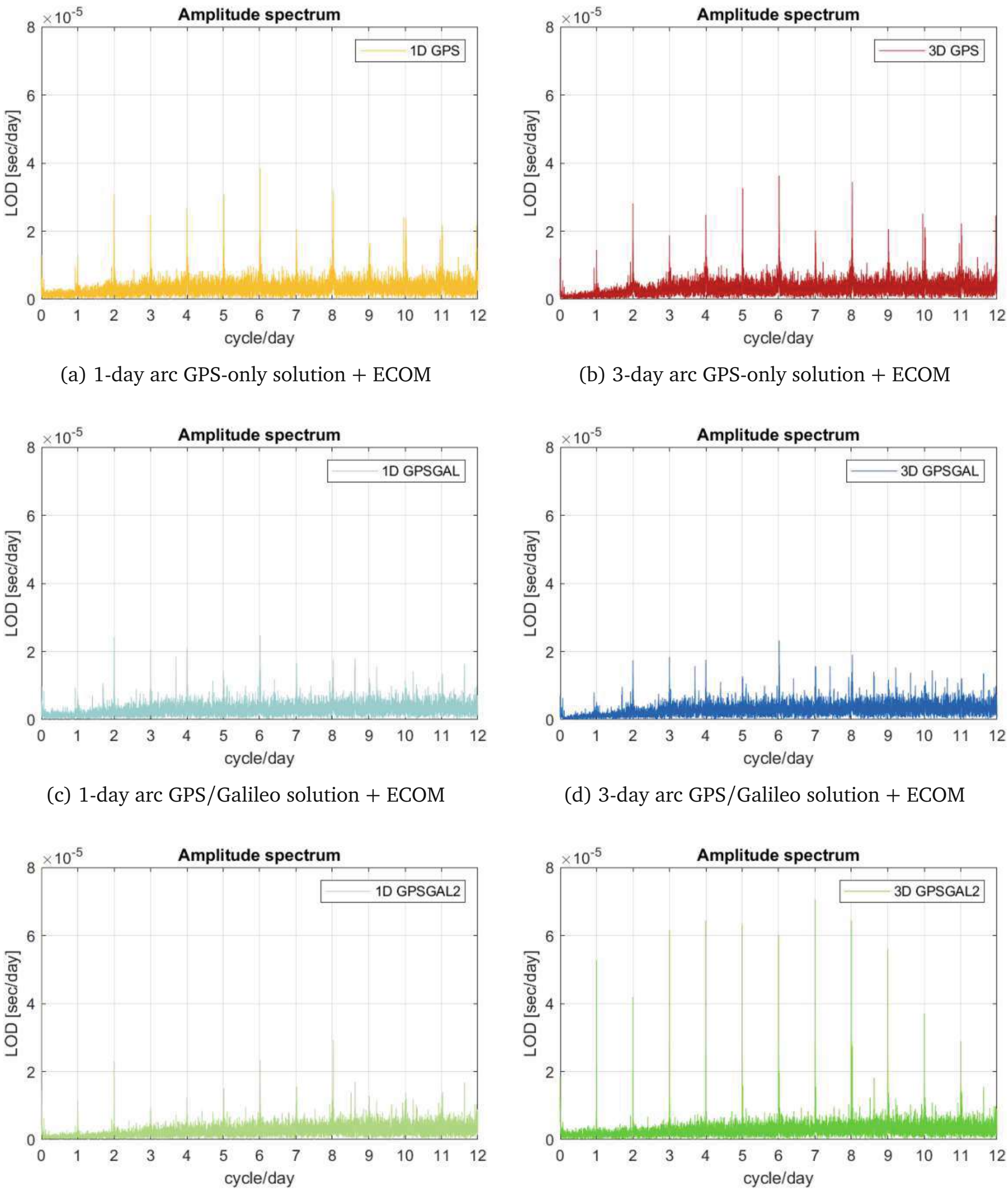


(a) 1-day arc GPS-only solution + ECOM

(b) 3-day arc GPS-only solution + ECOM

(c) 1-day arc GPS/Galileo solution + ECOM

(d) 3-day arc GPS/Galileo solution + ECOM

(e) 1-day arc GPS/Galileo solution + ECOM2

(f) 3-day arc GPS/Galileo solution + ECOM2

Figure A.6: LOD Amplitude spectrum of polar motion time series w.r.t. the subdiurnal IERS C04 14 reference model (Jan 2018 - Dec 2019). All solution types are presented separately on plots (a) - (f).

## A.2. Diurnal and subdiurnal tidal variation in polar motion

### A.2.1. Amplitude corrections w.r.t. reference sub-daily models for the 8 major ocean tides - derived from the full set adjustment

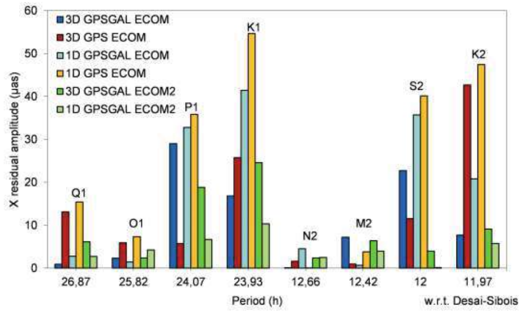


(a) Desai-Sibois

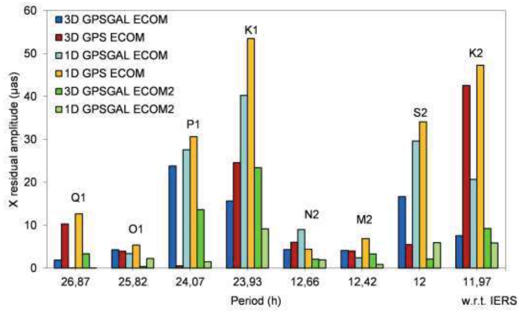


(b) IERS2010

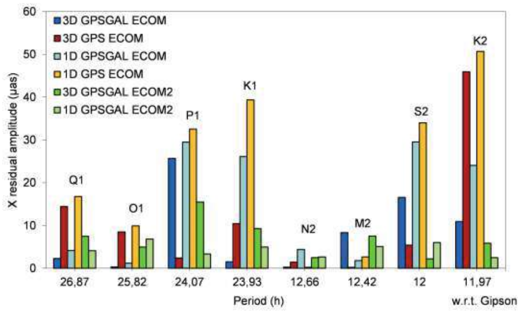


(c) Gipson

Figure A.7: Pole x-component amplitude corrections showing all performed GNSS solutions w.r.t. different sub-daily models (Full set adjustment).

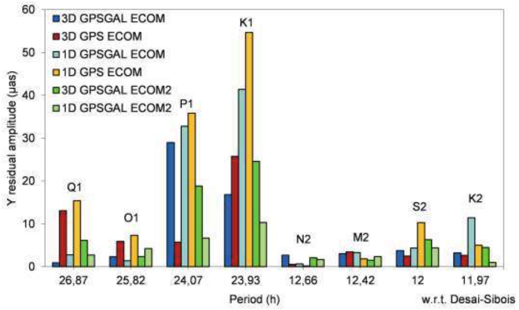


(a) Desai-Sibois

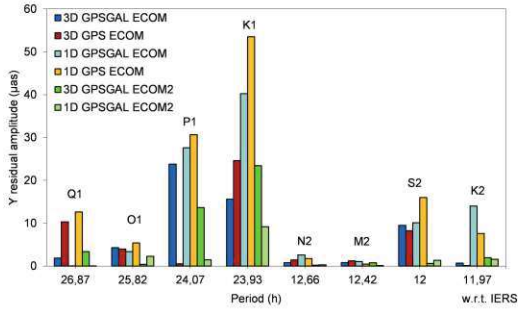


(b) IERS2010

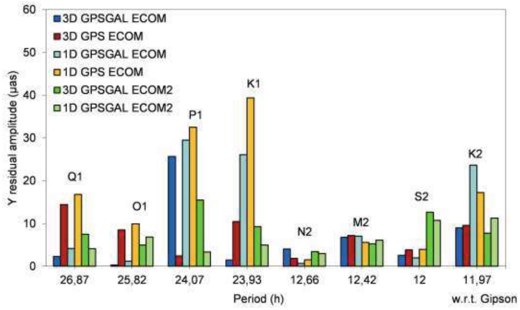


(c) Gipson

Figure A.8: Pole y-component amplitude corrections showing all performed GNSS solutions w.r.t. different sub-daily models (Full set adjustment).

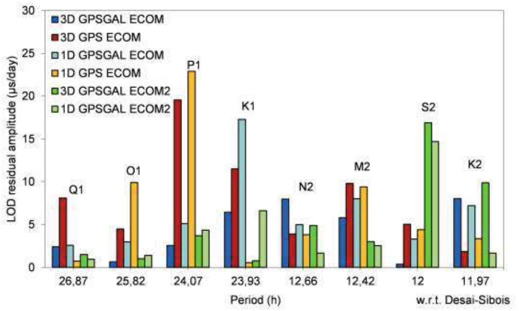


(a) Desai-Sibois

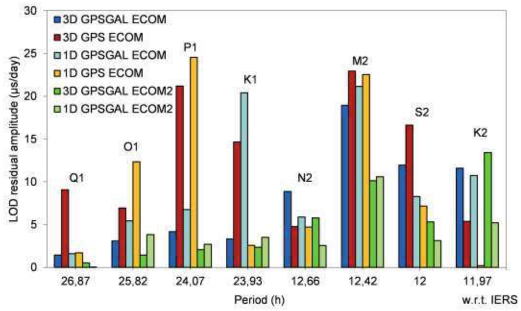


(b) IERS2010

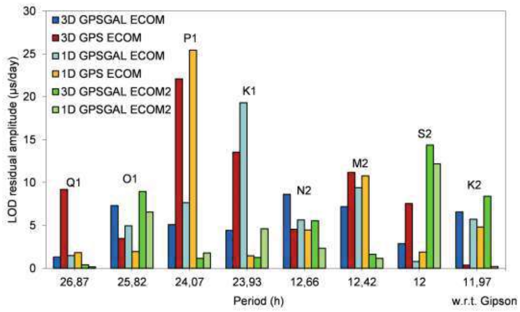


(c) Gipson

Figure A.9: LOD amplitude corrections showing all performed GNSS solutions w.r.t. different sub-daily models (Full set adjustment).

### A.2.2. Amplitude corrections w.r.t. reference sub-daily models for the 8 major ocean tides - derived from the subset adjustment (8 major ocean tides)

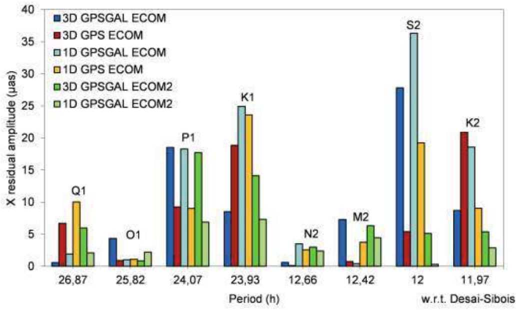


(a) Desai-Sibois

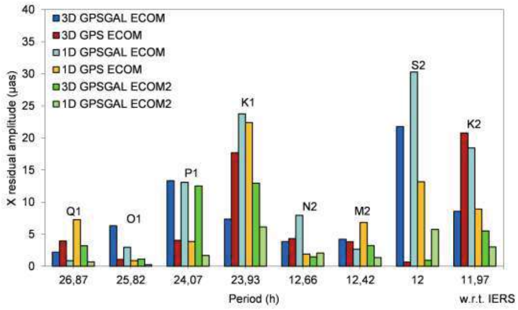


(b) IERS2010

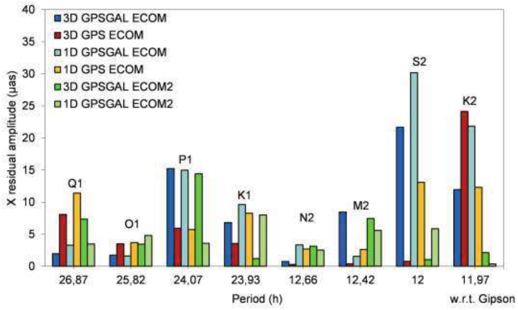


(c) Gipson

Figure A.10: Pole x-component amplitude corrections showing all performed GNSS solutions w.r.t. different sub-daily models (Subset adjustment).

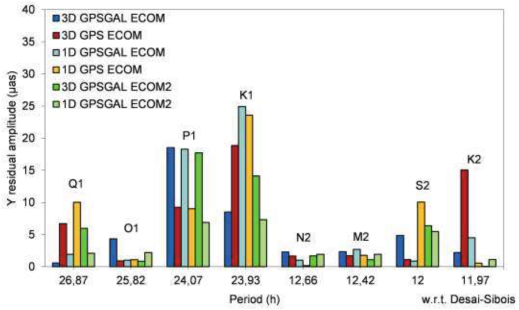


(a) Desai-Sibois

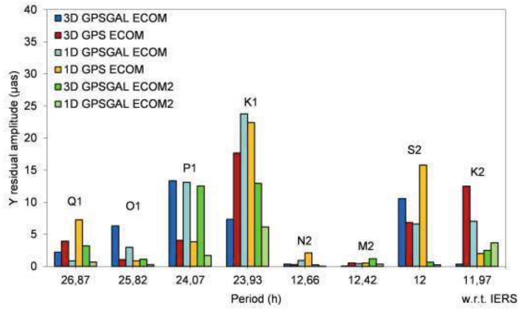


(b) IERS2010

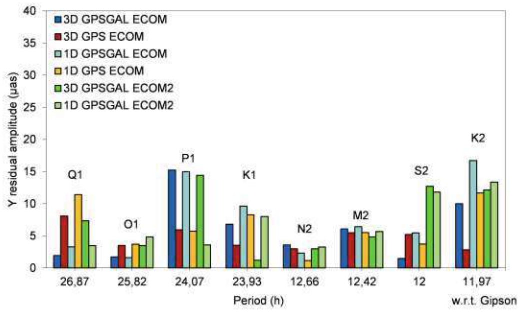


(c) Gipson

Figure A.11: Pole y-component amplitude corrections showing all performed GNSS solutions w.r.t. different sub-daily models (Subset adjustment).

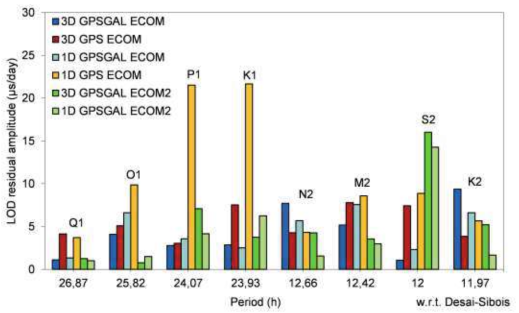


(a) Desai-Sibois

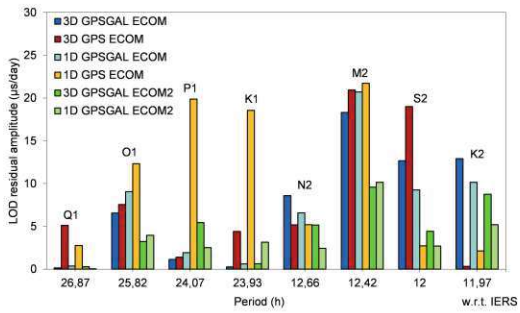


(b) IERS2010

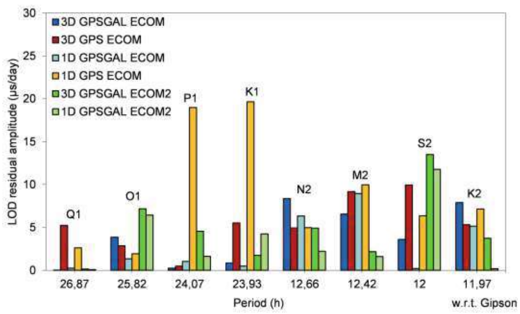


(c) Gipson

Figure A.12: LOD amplitude corrections showing all performed GNSS solutions w.r.t. different sub-daily models (Subset adjustment).

### A.2.3. Tables of ocean tide constituents (reference models)

Table A.1: Coefficients of sin(argument) and cos(argument) of sub diurnal variations in pole coordinates $x_p$ and $y_p$ and LOD caused by the 8 major ocean tides. The units are $\mu$as for pole coordinates and $\mu$s for LOD; $\gamma$ denotes GMST + $\pi$ (**Desai - Sibois**).

| | | argument | | | | | $x_p$ | | $y_p$ | | LOD | | Period |
|---|---|---|---|---|---|---|---|---|---|---|---|---|---|
| **Tide** | $\gamma$ | $l$ | $l'$ | $F$ | $D$ | $\Omega$ | **sin** | **cos** | **sin** | **cos** | **sin** | **cos** | **(h)** |
| **Q1** | 1 | -1 | 0 | -2 | 0 | -2 | 7.08 | 28.95 | -28.95 | 7.08 | -14.48 | -27.39 | **26.87** |
| **O1** | 1 | 0 | 0 | -2 | 0 | -2 | 68.16 | 126.32 | -126.32 | 68.16 | -73.30 | -94.50 | **25.82** |
| **P1** | 1 | 0 | 0 | -2 | 2 | -2 | 30.11 | 42.73 | -42.73 | 30.11 | -19.30 | -32.71 | **24.07** |
| **K1** | 1 | 0 | 0 | 0 | 0 | 0 | -102.68 | -134.45 | 134.45 | -102.68 | 62.69 | 102.63 | **23.93** |
| **N2** | 2 | -1 | 0 | -2 | 0 | -2 | -53.18 | -8.81 | 12.56 | 30.30 | -19.54 | 45.75 | **12.66** |
| **M2** | 2 | 0 | 0 | -2 | 0 | -2 | -326.96 | -28.72 | 46.64 | 191.61 | -98.46 | 205.67 | **12.42** |
| **S2** | 2 | 0 | 0 | -2 | 2 | -2 | -134.55 | 69.53 | 70.34 | 85.37 | -8.92 | 106.06 | **12** |
| **K2** | 2 | 0 | 0 | 0 | 0 | 0 | -40.28 | 14.62 | 17.05 | 26.66 | -3.40 | 29.86 | **11.97** |

Table A.2: Coefficients of sin(argument) and cos(argument) of sub diurnal variations in pole coordinates $x_p$ and $y_p$ and LOD caused by the 8 major ocean tides. The units are $\mu$as for pole coordinates and $\mu$s for LOD; $\gamma$ denotes GMST + $\pi$ (**IERS2010**).

| | | argument | | | | | $x_p$ | | $y_p$ | | LOD | | Period |
|---|---|---|---|---|---|---|---|---|---|---|---|---|---|
| **Tide** | $\gamma$ | $l$ | $l'$ | $F$ | $D$ | $\Omega$ | **sin** | **cos** | **sin** | **cos** | **sin** | **cos** | **(h)** |
| **Q1** | 1 | -1 | 0 | -2 | 0 | -2 | 6.20 | 26.30 | -26.30 | 6.20 | -14.02 | -28.72 | **26.87** |
| **O1** | 1 | 0 | 0 | -2 | 0 | -2 | 48.80 | 132.90 | -132.90 | 48.80 | -70.47 | -93.58 | **25.82** |
| **P1** | 1 | 0 | 0 | -2 | 2 | -2 | 26.10 | 51.20 | -51.20 | 26.10 | -19.40 | -34.54 | **24.07** |
| **K1** | 1 | 0 | 0 | 0 | 0 | 0 | -77.50 | -151.70 | 151.70 | -77.50 | 53.86 | 111.01 | **23.93** |
| **N2** | 2 | -1 | 0 | -2 | 0 | -2 | -56.90 | -12.90 | 11.10 | 32.90 | -18.57 | 45.20 | **12.66** |
| **M2** | 2 | 0 | 0 | -2 | 0 | -2 | -330.20 | -27.00 | 37.60 | 195.90 | -86.79 | 196.58 | **12.42** |
| **S2** | 2 | 0 | 0 | -2 | 2 | -2 | -144.10 | 63.60 | 59.20 | 86.60 | -2.00 | 94.83 | **12** |
| **K2** | 2 | 0 | 0 | 0 | 0 | 0 | -38.50 | 19.10 | 17.70 | 23.10 | 0.52 | 26.51 | **11.97** |

Table A.3: Coefficients of sin(argument) and cos(argument) of sub diurnal variations in pole coordinates $x_p$ and $y_p$ and LOD caused by the 8 major ocean tides. The units are $\mu$as for pole coordinates and $\mu$s for LOD; $\gamma$ denotes GMST + $\pi$ (**Gipson**).

| | | argument | | | | | $x_p$ | | $y_p$ | | LOD | | Period |
|---|---|---|---|---|---|---|---|---|---|---|---|---|---|
| **Tide** | $\gamma$ | $l$ | $l'$ | $F$ | $D$ | $\Omega$ | **sin** | **cos** | **sin** | **cos** | **sin** | **cos** | **(h)** |
| **Q1** | 1 | -1 | 0 | -2 | 0 | -2 | 7.74 | 30.19 | -30.19 | 7.74 | -15.04 | -28.34 | **26.87** |
| **O1** | 1 | 0 | 0 | -2 | 0 | -2 | 57.57 | 134.33 | -134.33 | 57.57 | -76.92 | -101.74 | **25.82** |
| **P1** | 1 | 0 | 0 | -2 | 2 | -2 | 29.03 | 47.40 | -47.40 | 29.03 | -21.62 | -34.27 | **24.07** |
| **K1** | 1 | 0 | 0 | 0 | 0 | 0 | -101.38 | -154.13 | 154.13 | -101.38 | 57.14 | 108.11 | **23.93** |
| **N2** | 2 | -1 | 0 | -2 | 0 | -2 | -53.17 | -7.90 | 12.08 | 29.07 | -20.37 | 44.67 | **12.66** |
| **M2** | 2 | 0 | 0 | -2 | 0 | -2 | -326.70 | -15.62 | 49.66 | 186.98 | -103.44 | 201.66 | **12.42** |
| **S2** | 2 | 0 | 0 | -2 | 2 | -2 | -138.99 | 74.31 | 73.81 | 90.71 | 0.00 | 103.92 | **12** |
| **K2** | 2 | 0 | 0 | 0 | 0 | 0 | -37.46 | 12.86 | 13.10 | 14.34 | 1.26 | 31.50 | **11.97** |

### A.2.4. Tables of ocean tide constituents (FSA results)

Table A.4: Coefficients of sin(argument) and cos(argument) of sub diurnal variations in pole coordinates $x_p$ and $y_p$ and LOD caused by the 8 major ocean tides. The units are $\mu$as for pole coordinates and $\mu$s for LOD; $\gamma$ denotes GMST + $\pi$ (**3D GPS/Galileo + ECOM2**).

| | argument | | | | | | $x_p$ | | $y_p$ | | LOD | | Period |
|---|---|---|---|---|---|---|---|---|---|---|---|---|---|
| **Tide** | $\gamma$ | $l$ | $l'$ | $F$ | $D$ | $\Omega$ | **sin** | **cos** | **sin** | **cos** | **sin** | **cos** | **(h)** |
| **Q1** | 1 | -1 | 0 | -2 | 0 | -2 | 8.39 | 22.14 | -22.14 | 8.38 | -17.24 | -27.53 | **26.87** |
| **O1** | 1 | 0 | 0 | -2 | 0 | -2 | 60.24 | 127.69 | -127.68 | 60.24 | -71.92 | -94.30 | **25.82** |
| **P1** | 1 | 0 | 0 | -2 | 2 | -2 | 30.24 | 64.33 | -64.33 | 30.24 | -22.54 | -35.06 | **24.07** |
| **K1** | 1 | 0 | 0 | 0 | 0 | 0 | -107.01 | -161.52 | 161.52 | -107.01 | 56.19 | 107.19 | **23.93** |
| **N2** | 2 | -1 | 0 | -2 | 0 | -2 | -55.06 | -11.52 | 15.00 | 31.51 | -11.99 | 53.31 | **12.66** |
| **M2** | 2 | 0 | 0 | -2 | 0 | -2 | -332.49 | -37.57 | 44.58 | 193.67 | -69.87 | 213.90 | **12.42** |
| **S2** | 2 | 0 | 0 | -2 | 2 | -2 | -145.56 | 54.40 | 47.48 | 92.87 | 6.64 | 89.29 | **12** |
| **K2** | 2 | 0 | 0 | 0 | 0 | 0 | -32.49 | 9.09 | 13.62 | 23.50 | -2.10 | 39.88 | **11.97** |

Table A.5: Coefficients of sin(argument) and cos(argument) of sub diurnal variations in pole coordinates $x_p$ and $y_p$ and LOD caused by the 8 major ocean tides. The units are $\mu$as for pole coordinates and $\mu$s for LOD; $\gamma$ denotes GMST + $\pi$ (**3D GPS/Galileo + ECOM**).

| | argument | | | | | | $x_p$ | | $y_p$ | | LOD | | Period |
|---|---|---|---|---|---|---|---|---|---|---|---|---|---|
| **Tide** | $\gamma$ | $l$ | $l'$ | $F$ | $D$ | $\Omega$ | **sin** | **cos** | **sin** | **cos** | **sin** | **cos** | **(h)** |
| **Q1** | 1 | -1 | 0 | -2 | 0 | -2 | 8.05 | 27.74 | -27.74 | 8.04 | -15.38 | -29.65 | **26.87** |
| **O1** | 1 | 0 | 0 | -2 | 0 | -2 | 67.26 | 129.44 | -129.43 | 67.26 | -73.85 | -94.90 | **25.82** |
| **P1** | 1 | 0 | 0 | -2 | 2 | -2 | 20.65 | 78.59 | -78.59 | 20.65 | -16.99 | -31.09 | **24.07** |
| **K1** | 1 | 0 | 0 | 0 | 0 | 0 | -93.71 | -160.65 | 160.65 | -93.71 | 63.18 | 109.83 | **23.93** |
| **N2** | 2 | -1 | 0 | -2 | 0 | -2 | -52.37 | -13.20 | 15.69 | 31.85 | -19.09 | 54.48 | **12.66** |
| **M2** | 2 | 0 | 0 | -2 | 0 | -2 | -333.84 | -32.39 | 52.61 | 193.23 | -72.71 | 222.24 | **12.42** |
| **S2** | 2 | 0 | 0 | -2 | 2 | -2 | -164.49 | 57.26 | 42.77 | 106.07 | 1.77 | 106.79 | **12** |
| **K2** | 2 | 0 | 0 | 0 | 0 | 0 | -49.84 | 8.30 | -0.84 | 28.41 | 3.35 | 37.95 | **11.97** |

Table A.6: Coefficients of sin(argument) and cos(argument) of sub diurnal variations in pole coordinates $x_p$ and $y_p$ and LOD caused by the 8 major ocean tides. The units are $\mu$as for pole coordinates and $\mu$s for LOD; $\gamma$ denotes GMST + $\pi$ (**3D GPS + ECOM**).

| | argument | | | | | | $x_p$ | | $y_p$ | | LOD | | Period |
|---|---|---|---|---|---|---|---|---|---|---|---|---|---|
| **Tide** | $\gamma$ | $l$ | $l'$ | $F$ | $D$ | $\Omega$ | **sin** | **cos** | **sin** | **cos** | **sin** | **cos** | **(h)** |
| **Q1** | 1 | -1 | 0 | -2 | 0 | -2 | 3.03 | 16.46 | -16.46 | 3.02 | -13.38 | -18.57 | **26.87** |
| **O1** | 1 | 0 | 0 | -2 | 0 | -2 | 62.46 | 122.65 | -122.64 | 62.46 | -72.37 | -100.79 | **25.82** |
| **P1** | 1 | 0 | 0 | -2 | 2 | -2 | 23.91 | 52.84 | -52.84 | 23.91 | -9.14 | -16.01 | **24.07** |
| **K1** | 1 | 0 | 0 | 0 | 0 | 0 | -100.25 | -167.17 | 167.17 | -100.25 | 65.54 | 86.77 | **23.93** |
| **N2** | 2 | -1 | 0 | -2 | 0 | -2 | -50.73 | -12.77 | 15.29 | 29.61 | -16.83 | 50.93 | **12.66** |
| **M2** | 2 | 0 | 0 | -2 | 0 | -2 | -325.75 | -31.72 | 42.11 | 196.21 | -73.71 | 226.11 | **12.42** |
| **S2** | 2 | 0 | 0 | -2 | 2 | -2 | -156.84 | 44.41 | 42.81 | 104.71 | 51.71 | 98.75 | **12** |
| **K2** | 2 | 0 | 0 | 0 | 0 | 0 | -83.92 | 16.59 | 11.86 | 26.45 | 9.86 | 30.34 | **11.97** |

Table A.7: Coefficients of sin(argument) and cos(argument) of sub diurnal variations in pole coordinates $x_p$ and $y_p$ and LOD caused by the 8 major ocean tides. The units are $\mu$as for pole coordinates and $\mu$s for LOD; $\gamma$ denotes GMST + $\pi$ (**1D GPS/Galileo + ECOM2**).

| | argument | | | | | | $x_p$ | | $y_p$ | | LOD | | Period |
|---|---|---|---|---|---|---|---|---|---|---|---|---|---|
| **Tide** | $\gamma$ | $l$ | $l'$ | $F$ | $D$ | $\Omega$ | **sin** | **cos** | **sin** | **cos** | **sin** | **cos** | **(h)** |
| **Q1** | 1 | -1 | 0 | -2 | 0 | -2 | 9.06 | 25.49 | -25.49 | 9.05 | -14.33 | -28.53 | **26.87** |
| **O1** | 1 | 0 | 0 | -2 | 0 | -2 | 58.69 | 126.35 | -126.34 | 58.69 | -75.19 | -94.79 | **25.82** |
| **P1** | 1 | 0 | 0 | -2 | 2 | -2 | 36.17 | 46.52 | -46.52 | 36.17 | -21.74 | -36.30 | **24.07** |
| **K1** | 1 | 0 | 0 | 0 | 0 | 0 | -101.49 | -148.06 | 148.06 | -101.49 | 56.77 | 113.48 | **23.93** |
| **N2** | 2 | -1 | 0 | -2 | 0 | -2 | -54.86 | -13.11 | 13.57 | 31.68 | -14.71 | 49.27 | **12.66** |
| **M2** | 2 | 0 | 0 | -2 | 0 | -2 | -329.71 | -40.30 | 46.56 | 194.08 | -69.56 | 214.48 | **12.42** |
| **S2** | 2 | 0 | 0 | -2 | 2 | -2 | -138.82 | 60.85 | 54.34 | 91.26 | 9.01 | 91.29 | **12** |
| **K2** | 2 | 0 | 0 | 0 | 0 | 0 | -35.79 | 9.79 | 13.19 | 27.69 | -3.09 | 31.58 | **11.97** |

Table A.8: Coefficients of sin(argument) and cos(argument) of sub diurnal variations in pole coordinates $x_p$ and $y_p$ and LOD caused by the 8 major ocean tides. The units are $\mu$as for pole coordinates and $\mu$s for LOD; $\gamma$ denotes GMST + $\pi$ (**1D GPS/Galileo + ECOM**).

| | argument | | | | | | $x_p$ | | $y_p$ | | LOD | | Period |
|---|---|---|---|---|---|---|---|---|---|---|---|---|---|
| **Tide** | $\gamma$ | $l$ | $l'$ | $F$ | $D$ | $\Omega$ | **sin** | **cos** | **sin** | **cos** | **sin** | **cos** | **(h)** |
| **Q1** | 1 | -1 | 0 | -2 | 0 | -2 | 11.84 | 24.29 | -24.29 | 11.83 | -15.77 | -29.63 | **26.87** |
| **O1** | 1 | 0 | 0 | -2 | 0 | -2 | 63.37 | 130.37 | -130.36 | 63.37 | -76.41 | -95.86 | **25.82** |
| **P1** | 1 | 0 | 0 | -2 | 2 | -2 | 13.07 | 84.06 | -84.06 | 13.07 | -28.09 | -17.07 | **24.07** |
| **K1** | 1 | 0 | 0 | 0 | 0 | 0 | -113.06 | -177.66 | 177.66 | -113.06 | 44.82 | 92.72 | **23.93** |
| **N2** | 2 | -1 | 0 | -2 | 0 | -2 | -48.23 | -10.58 | 17.02 | 27.27 | -20.05 | 50.94 | **12.66** |
| **M2** | 2 | 0 | 0 | -2 | 0 | -2 | -327.77 | -27.08 | 52.98 | 193.40 | -75.40 | 223.68 | **12.42** |
| **S2** | 2 | 0 | 0 | -2 | 2 | -2 | -182.56 | 41.16 | 29.54 | 111.13 | 29.64 | 98.77 | **12** |
| **K2** | 2 | 0 | 0 | 0 | 0 | 0 | -63.60 | 2.68 | -15.94 | 40.03 | 16.28 | 33.51 | **11.97** |

Table A.9: Coefficients of sin(argument) and cos(argument) of sub diurnal variations in pole coordinates $x_p$ and $y_p$ and LOD caused by the 8 major ocean tides. The units are $\mu$as for pole coordinates and $\mu$s for LOD; $\gamma$ denotes GMST + $\pi$ (**1D GPS + ECOM**).

| | argument | | | | | | $x_p$ | | $y_p$ | | LOD | | Period |
|---|---|---|---|---|---|---|---|---|---|---|---|---|---|
| **Tide** | $\gamma$ | $l$ | $l'$ | $F$ | $D$ | $\Omega$ | **sin** | **cos** | **sin** | **cos** | **sin** | **cos** | **(h)** |
| **Q1** | 1 | -1 | 0 | -2 | 0 | -2 | 4.09 | 13.80 | -13.80 | 4.08 | -20.75 | -22.02 | **26.87** |
| **O1** | 1 | 0 | 0 | -2 | 0 | -2 | 66.07 | 119.12 | -119.11 | 66.07 | -66.09 | -111.36 | **25.82** |
| **P1** | 1 | 0 | 0 | -2 | 2 | -2 | 33.10 | 81.65 | -81.65 | 33.10 | 9.65 | -11.59 | **24.07** |
| **K1** | 1 | 0 | 0 | 0 | 0 | 0 | -146.64 | -169.14 | 169.14 | -146.64 | 104.65 | 60.37 | **23.93** |
| **N2** | 2 | -1 | 0 | -2 | 0 | -2 | -52.17 | -13.81 | 17.62 | 27.89 | -13.30 | 51.89 | **12.66** |
| **M2** | 2 | 0 | 0 | -2 | 0 | -2 | -322.58 | -34.43 | 43.03 | 194.35 | -76.43 | 224.77 | **12.42** |
| **S2** | 2 | 0 | 0 | -2 | 2 | -2 | -187.78 | 38.03 | 39.29 | 114.34 | 80.10 | 63.19 | **12** |
| **K2** | 2 | 0 | 0 | 0 | 0 | 0 | -88.72 | -16.67 | 12.61 | 34.43 | 22.57 | 14.28 | **11.97** |

### A.2.5. Tables of ocean tide constituents (SSA results)

Table A.10: Coefficients of sin(argument) and cos(argument) of sub diurnal variations in pole coordinates $x_p$ and $y_p$ and LOD caused by the 8 major ocean tides. The units are $\mu$as for pole coordinates and $\mu$s for LOD; $\gamma$ denotes GMST + $\pi$ (**3D GPS/Galileo + ECOM2**).

| | argument | | | | | | $x_p$ | | $y_p$ | | LOD | | Period |
|---|---|---|---|---|---|---|---|---|---|---|---|---|---|
| **Tide** | $\gamma$ | $l$ | $l'$ | $F$ | $D$ | $\Omega$ | **sin** | **cos** | **sin** | **cos** | **sin** | **cos** | **(h)** |
| **Q1** | 1 | -1 | 0 | -2 | 0 | -2 | 8.51 | 22.26 | -22.26 | 8.50 | -14.90 | -28.58 | **26.87** |
| **O1** | 1 | 0 | 0 | -2 | 0 | -2 | 60.41 | 129.27 | -129.26 | 60.41 | -73.20 | -95.57 | **25.82** |
| **P1** | 1 | 0 | 0 | -2 | 2 | -2 | 32.60 | 61.94 | -61.94 | 32.60 | -27.52 | -35.68 | **24.07** |
| **K1** | 1 | 0 | 0 | 0 | 0 | 0 | -103.42 | -151.32 | 151.32 | -103.42 | 57.30 | 109.99 | **23.93** |
| **N2** | 2 | -1 | 0 | -2 | 0 | -2 | -55.78 | -11.16 | 14.76 | 31.16 | -11.44 | 52.78 | **12.66** |
| **M2** | 2 | 0 | 0 | -2 | 0 | -2 | -332.45 | -37.30 | 44.52 | 193.24 | -69.21 | 213.53 | **12.42** |
| **S2** | 2 | 0 | 0 | -2 | 2 | -2 | -146.89 | 54.24 | 48.67 | 92.19 | 5.21 | 90.27 | **12** |
| **K2** | 2 | 0 | 0 | 0 | 0 | 0 | -37.16 | 4.85 | 18.51 | 25.58 | -0.56 | 35.26 | **11.97** |

Table A.11: Coefficients of sin(argument) and cos(argument) of sub diurnal variations in pole coordinates $x_p$ and $y_p$ and LOD caused by the 8 major ocean tides. The units are $\mu$as for pole coordinates and $\mu$s for LOD; $\gamma$ denotes GMST + $\pi$ (**3D GPS/Galileo + ECOM**).

| | argument | | | | | | $x_p$ | | $y_p$ | | LOD | | Period |
|---|---|---|---|---|---|---|---|---|---|---|---|---|---|
| **Tide** | $\gamma$ | $l$ | $l'$ | $F$ | $D$ | $\Omega$ | **sin** | **cos** | **sin** | **cos** | **sin** | **cos** | **(h)** |
| **Q1** | 1 | -1 | 0 | -2 | 0 | -2 | 9.46 | 27.65 | -27.65 | 9.45 | -15.11 | -28.31 | **26.87** |
| **O1** | 1 | 0 | 0 | -2 | 0 | -2 | 69.32 | 130.63 | -130.62 | 69.32 | -74.55 | -98.70 | **25.82** |
| **P1** | 1 | 0 | 0 | -2 | 2 | -2 | 26.47 | 65.67 | -65.67 | 26.47 | -25.73 | -31.61 | **24.07** |
| **K1** | 1 | 0 | 0 | 0 | 0 | 0 | -97.00 | -148.87 | 148.87 | -97.00 | 58.24 | 108.49 | **23.93** |
| **N2** | 2 | -1 | 0 | -2 | 0 | -2 | -52.76 | -13.65 | 15.87 | 31.28 | -18.04 | 54.55 | **12.66** |
| **M2** | 2 | 0 | 0 | -2 | 0 | -2 | -333.87 | -33.18 | 52.90 | 192.39 | -71.57 | 221.94 | **12.42** |
| **S2** | 2 | 0 | 0 | -2 | 2 | -2 | -170.77 | 54.56 | 46.14 | 105.84 | 2.09 | 107.50 | **12** |
| **K2** | 2 | 0 | 0 | 0 | 0 | 0 | -50.79 | 8.79 | 11.27 | 27.19 | 9.14 | 38.35 | **11.97** |

Table A.12: Coefficients of sin(argument) and cos(argument) of sub diurnal variations in pole coordinates $x_p$ and $y_p$ and LOD caused by the 8 major ocean tides. The units are $\mu$as for pole coordinates and $\mu$s for LOD; $\gamma$ denotes GMST + $\pi$ (**3D GPS + ECOM**).

| | argument | | | | | | $x_p$ | | $y_p$ | | LOD | | Period |
|---|---|---|---|---|---|---|---|---|---|---|---|---|---|
| **Tide** | $\gamma$ | $l$ | $l'$ | $F$ | $D$ | $\Omega$ | **sin** | **cos** | **sin** | **cos** | **sin** | **cos** | **(h)** |
| **Q1** | 1 | -1 | 0 | -2 | 0 | -2 | 8.27 | 21.57 | -21.57 | 8.26 | -10.47 | -24.72 | **26.87** |
| **O1** | 1 | 0 | 0 | -2 | 0 | -2 | 64.12 | 127.42 | -127.41 | 64.12 | -73.22 | -100.93 | **25.82** |
| **P1** | 1 | 0 | 0 | -2 | 2 | -2 | 35.29 | 50.39 | -50.39 | 35.29 | -26.83 | -31.03 | **24.07** |
| **K1** | 1 | 0 | 0 | 0 | 0 | 0 | -97.72 | -160.64 | 160.64 | -97.72 | 61.58 | 111.98 | **23.93** |
| **N2** | 2 | -1 | 0 | -2 | 0 | -2 | -52.44 | -13.02 | 13.69 | 31.63 | -15.86 | 51.66 | **12.66** |
| **M2** | 2 | 0 | 0 | -2 | 0 | -2 | -325.90 | -32.05 | 41.05 | 194.65 | -72.37 | 224.43 | **12.42** |
| **S2** | 2 | 0 | 0 | -2 | 2 | -2 | -149.78 | 46.56 | 44.65 | 102.44 | 38.46 | 107.17 | **12** |
| **K2** | 2 | 0 | 0 | 0 | 0 | 0 | -61.30 | 17.46 | -1.59 | 16.52 | 3.46 | 25.97 | **11.97** |

Table A.13: Coefficients of sin(argument) and cos(argument) of sub diurnal variations in pole coordinates $x_p$ and $y_p$ and LOD caused by the 8 major ocean tides. The units are $\mu$as for pole coordinates and $\mu$s for LOD; $\gamma$ denotes GMST + $\pi$ (**1D GPS/Galileo + ECOM2**).

| | argument | | | | | | $x_p$ | | $y_p$ | | LOD | | Period |
|---|---|---|---|---|---|---|---|---|---|---|---|---|---|
| **Tide** | $\gamma$ | $l$ | $l'$ | $F$ | $D$ | $\Omega$ | **sin** | **cos** | **sin** | **cos** | **sin** | **cos** | **(h)** |
| **Q1** | 1 | -1 | 0 | -2 | 0 | -2 | 9.02 | 26.19 | -26.19 | 9.01 | -14.34 | -28.61 | **26.87** |
| **O1** | 1 | 0 | 0 | -2 | 0 | -2 | 58.79 | 128.53 | -128.52 | 58.79 | -74.36 | -95.58 | **25.82** |
| **P1** | 1 | 0 | 0 | -2 | 2 | -2 | 36.30 | 46.72 | -46.72 | 36.30 | -21.86 | -36.02 | **24.07** |
| **K1** | 1 | 0 | 0 | 0 | 0 | 0 | -100.18 | -145.29 | 145.29 | -100.18 | 56.89 | 113.01 | **23.93** |
| **N2** | 2 | -1 | 0 | -2 | 0 | -2 | -54.79 | -12.89 | 13.92 | 31.82 | -14.61 | 49.18 | **12.66** |
| **M2** | 2 | 0 | 0 | -2 | 0 | -2 | -330.19 | -40.44 | 46.29 | 193.68 | -68.72 | 214.29 | **12.42** |
| **S2** | 2 | 0 | 0 | -2 | 2 | -2 | -138.86 | 61.22 | 53.23 | 90.67 | 8.67 | 91.74 | **12** |
| **K2** | 2 | 0 | 0 | 0 | 0 | 0 | -38.48 | 10.80 | 15.59 | 28.83 | -1.03 | 31.70 | **11.97** |

Table A.14: Coefficients of sin(argument) and cos(argument) of sub diurnal variations in pole coordinates $x_p$ and $y_p$ and LOD caused by the 8 major ocean tides. The units are $\mu$as for pole coordinates and $\mu$s for LOD; $\gamma$ denotes GMST + $\pi$ (**1D GPS/Galileo + ECOM**).

| | argument | | | | | | $x_p$ | | $y_p$ | | LOD | | Period |
|---|---|---|---|---|---|---|---|---|---|---|---|---|---|
| **Tide** | $\gamma$ | $l$ | $l'$ | $F$ | $D$ | $\Omega$ | **sin** | **cos** | **sin** | **cos** | **sin** | **cos** | **(h)** |
| **Q1** | 1 | -1 | 0 | -2 | 0 | -2 | 9.19 | 26.33 | -26.33 | 9.18 | -13.49 | -29.37 | **26.87** |
| **O1** | 1 | 0 | 0 | -2 | 0 | -2 | 64.64 | 129.29 | -129.28 | 64.64 | -75.90 | -100.83 | **25.82** |
| **P1** | 1 | 0 | 0 | -2 | 2 | -2 | 27.16 | 65.12 | -65.12 | 27.16 | -25.92 | -32.47 | **24.07** |
| **K1** | 1 | 0 | 0 | 0 | 0 | 0 | -103.06 | -164.48 | 164.48 | -103.06 | 51.57 | 111.42 | **23.93** |
| **N2** | 2 | -1 | 0 | -2 | 0 | -2 | -49.17 | -11.14 | 18.39 | 28.36 | -18.68 | 52.19 | **12.66** |
| **M2** | 2 | 0 | 0 | -2 | 0 | -2 | -327.44 | -28.01 | 52.79 | 192.80 | -74.12 | 223.63 | **12.42** |
| **S2** | 2 | 0 | 0 | -2 | 2 | -2 | -184.23 | 36.30 | 32.74 | 106.58 | 26.06 | 100.80 | **12** |
| **K2** | 2 | 0 | 0 | 0 | 0 | 0 | -59.93 | -13.48 | 16.49 | 32.16 | 16.10 | 32.94 | **11.97** |

Table A.15: Coefficients of sin(argument) and cos(argument) of sub diurnal variations in pole coordinates $x_p$ and $y_p$ and LOD caused by the 8 major ocean tides. The units are $\mu$as for pole coordinates and $\mu$s for LOD; $\gamma$ denotes GMST + $\pi$ (**1D GPS + ECOM**).

| | argument | | | | | | $x_p$ | | $y_p$ | | LOD | | Period |
|---|---|---|---|---|---|---|---|---|---|---|---|---|---|
| **Tide** | $\gamma$ | $l$ | $l'$ | $F$ | $D$ | $\Omega$ | **sin** | **cos** | **sin** | **cos** | **sin** | **cos** | **(h)** |
| **Q1** | 1 | -1 | 0 | -2 | 0 | -2 | 7.77 | 18.18 | -18.18 | 7.76 | -14.40 | -31.58 | **26.87** |
| **O1** | 1 | 0 | 0 | -2 | 0 | -2 | 66.52 | 125.97 | -125.96 | 66.52 | -76.81 | -104.22 | **25.82** |
| **P1** | 1 | 0 | 0 | -2 | 2 | -2 | 40.14 | 46.34 | -46.34 | 40.14 | -32.43 | -49.88 | **24.07** |
| **K1** | 1 | 0 | 0 | 0 | 0 | 0 | -104.10 | -162.23 | 162.23 | -104.10 | 67.47 | 124.87 | **23.93** |
| **N2** | 2 | -1 | 0 | -2 | 0 | -2 | -54.87 | -13.27 | 15.72 | 28.59 | -13.41 | 52.38 | **12.66** |
| **M2** | 2 | 0 | 0 | -2 | 0 | -2 | -322.58 | -35.02 | 43.13 | 194.25 | -75.13 | 224.37 | **12.42** |
| **S2** | 2 | 0 | 0 | -2 | 2 | -2 | -167.12 | 34.70 | 44.26 | 112.26 | 55.57 | 80.19 | **12** |
| **K2** | 2 | 0 | 0 | 0 | 0 | 0 | -50.50 | 11.96 | 5.79 | 30.56 | 4.85 | 23.90 | **11.97** |

# B. Appendix

## B.1. Pseudorange corrections

Table B.1: IGS stations used for the validation process (pseudorange corrections, STEC and VTEC comparison).

| Station | Abbrev. | Lat (°) | Lon (°) | Height (m) | Network |
|---|---|---|---|---|---|
| Dionysos, Greece | DYNG | 38.08 | 23.93 | 510.6 | IGS Multi-GNSS |
| Roquetes, Spain | EBRE | 40.82 | 0.49 | 107.3 | IGS Multi-GNSS |
| Ondrejov, Czechia | GOP6 | 49.91 | 14.79 | 592.6 | IGS Multi-GNSS |
| Caussols, France | GRAS | 43.76 | 6.92 | 1319.3 | IGS Multi-GNSS |
| Westerbork, the Netherlands | WSRT | 52.91 | 6.60 | 86.0 | IGS Multi-GNSS |

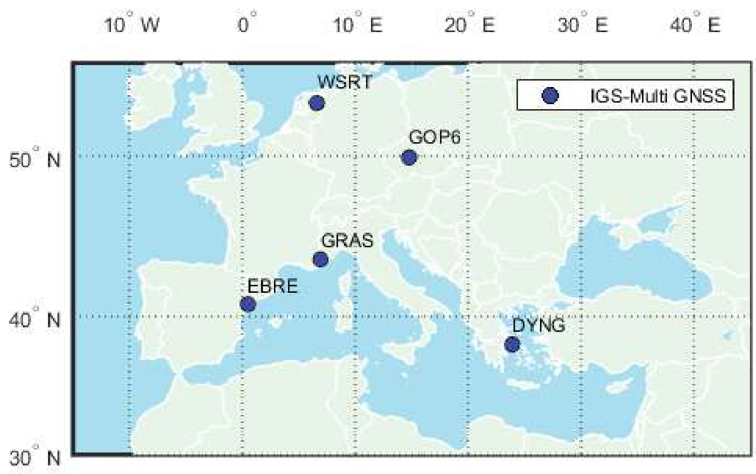


Figure B.1: Site location map for stations from Table B.1.

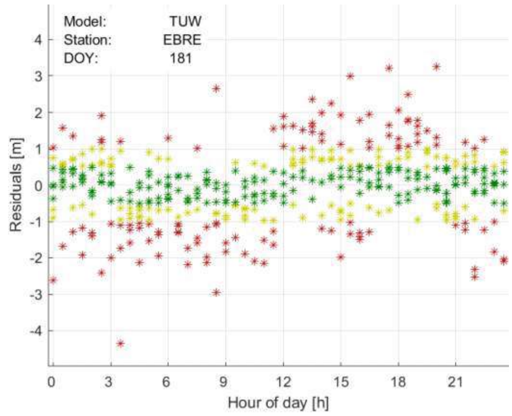


(a) TUWR

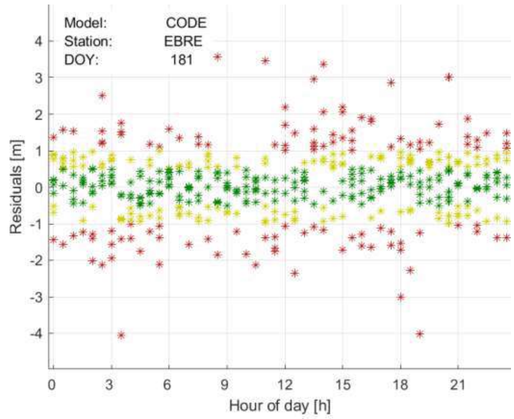


(b) CODE

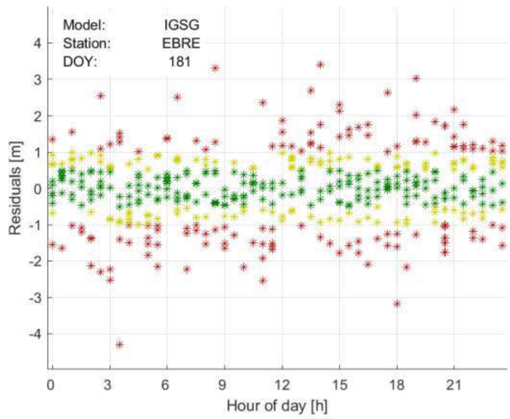


(c) IGS

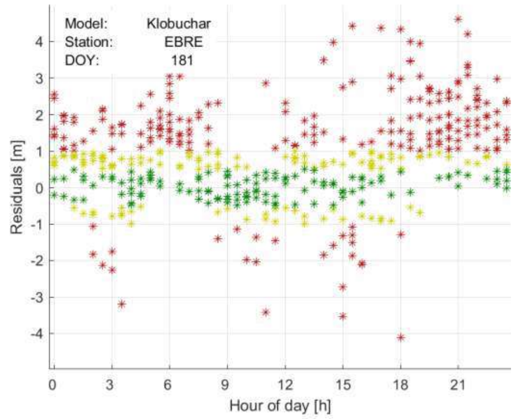


(d) Klobuchar

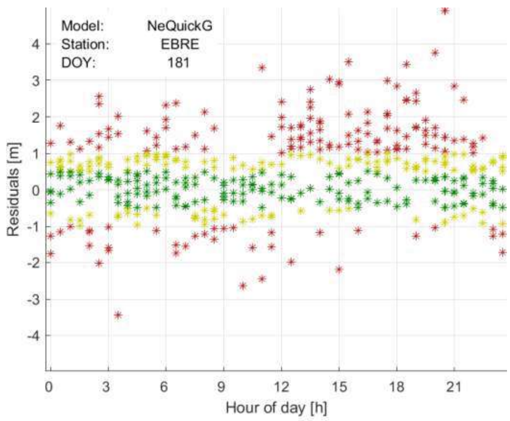


(e) NeQuick G

Figure B.2: Difference between corrected L1 pseudoranges by ionosphere models (a) - (e) and the ionosphere-free linear combination on IGS station EBRE (Roquetes, Spain) for June 30, 2022 (doy 181 2022).

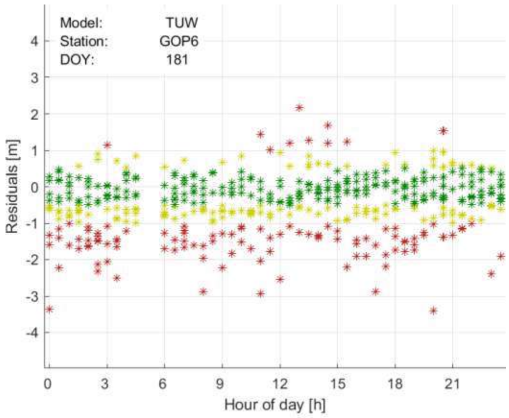


(a) TUWR

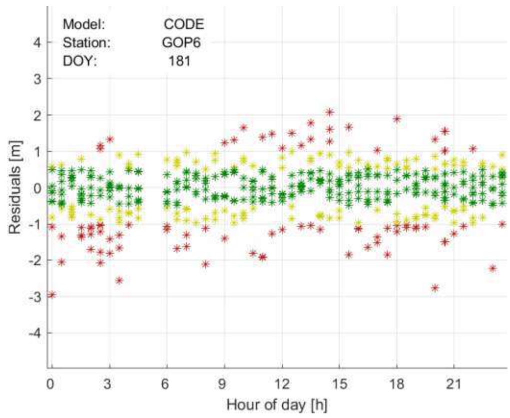


(b) CODE

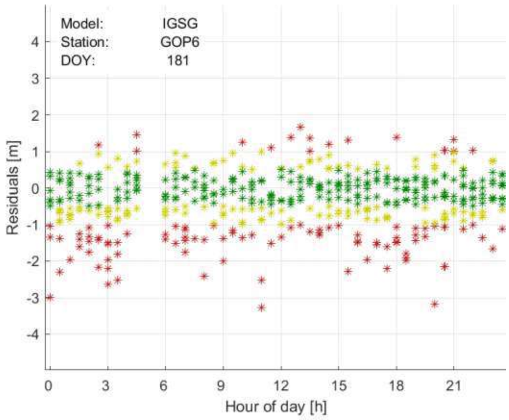


(c) IGS

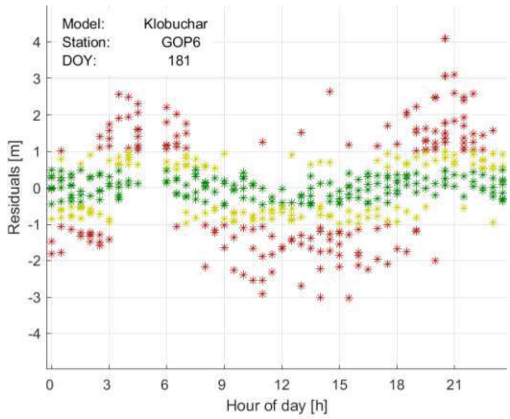


(d) Klobuchar

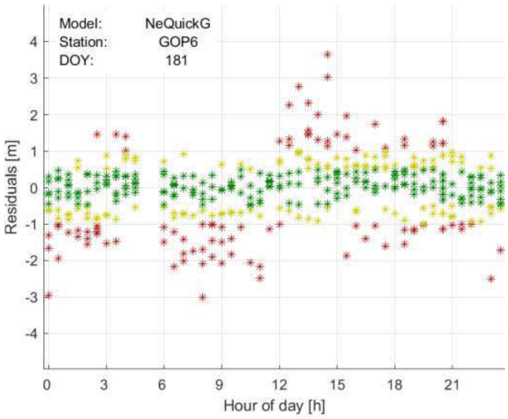


(e) NeQuick G

Figure B.3: Difference between corrected L1 pseudoranges by ionosphere models (a) - (e) and the ionosphere-free linear combination on IGS station GOP6 (Ondrejov, Czechia) for June 30, 2022 (doy 181 2022).

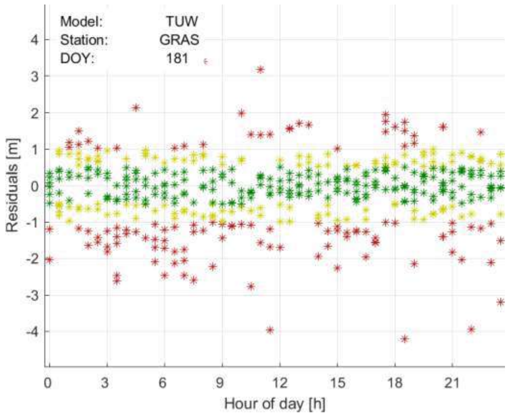


(a) TUWR

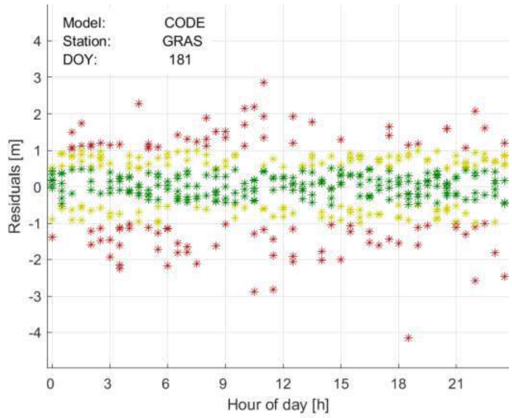


(b) CODE

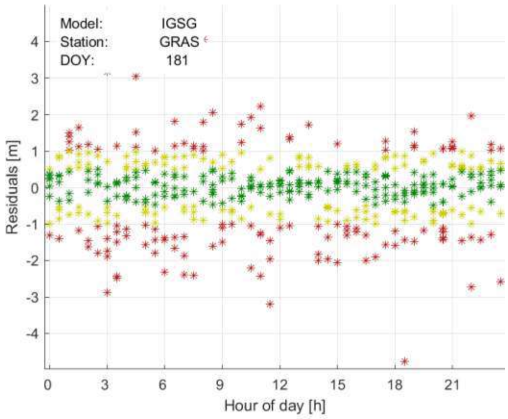


(c) IGS

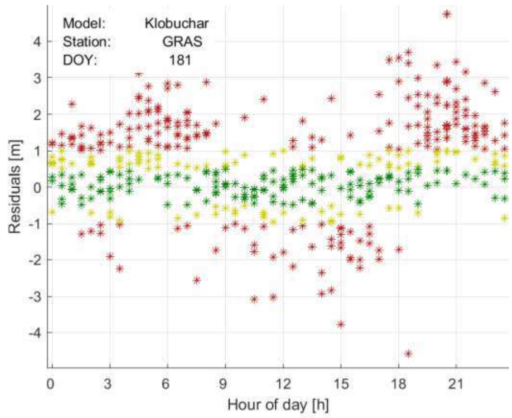


(d) Klobuchar

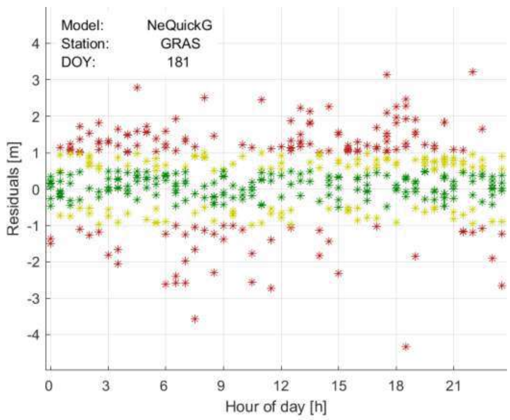


(e) NeQuick G

Figure B.4: Difference between corrected L1 pseudoranges by ionosphere models (a) - (e) and the ionosphere-free linear combination on IGS station GRAS (Caussols, France) for June 30, 2022 (doy 181 2022).

## B.2. Monthly STEC differences

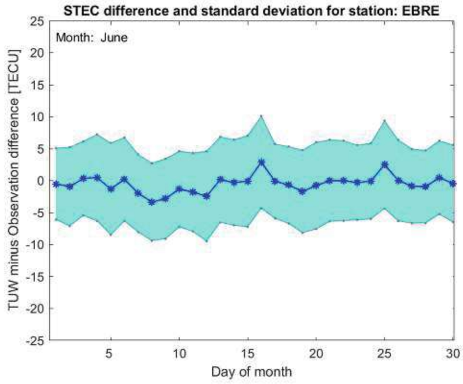


(a) TUWR

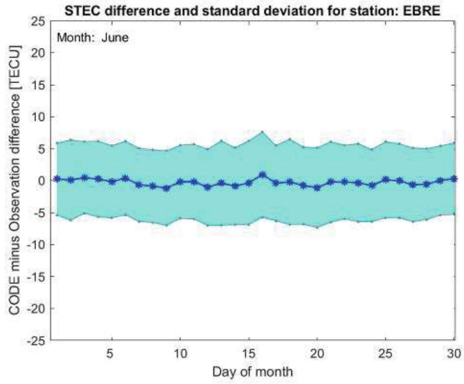


(b) CODE

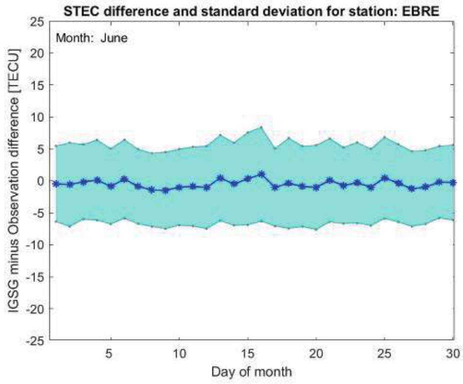


(c) IGS

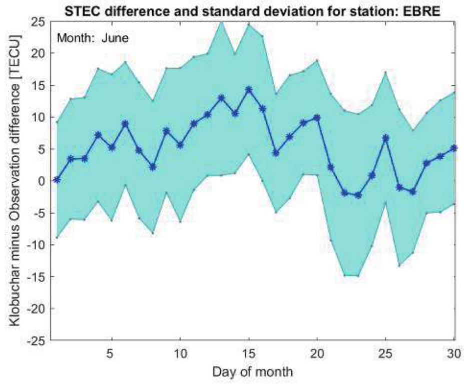


(d) Klobuchar

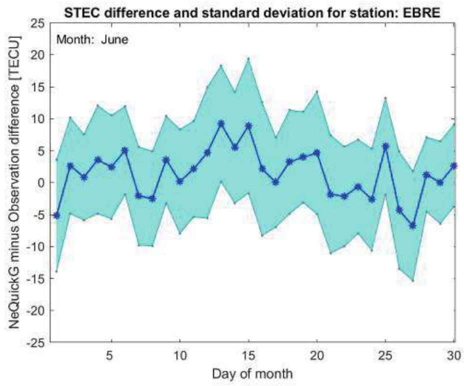


(e) NeQuick G

Figure B.5: Monthly STEC differences and standard deviations between the derived STEC value from the tested models (a) - (e) and the observation based STEC on IGS station EBRE (Roquetes, Spain) for June, 2022 (doy 181 2022).

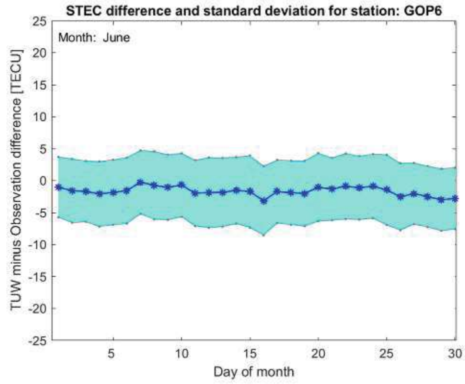


(a) TUWR

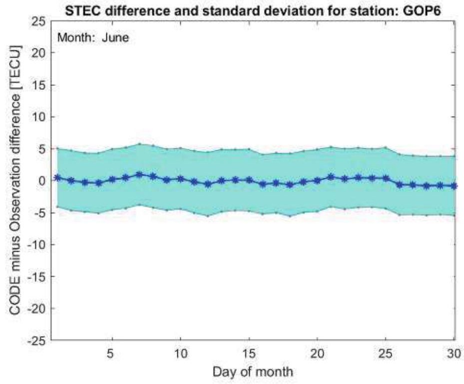


(b) CODE

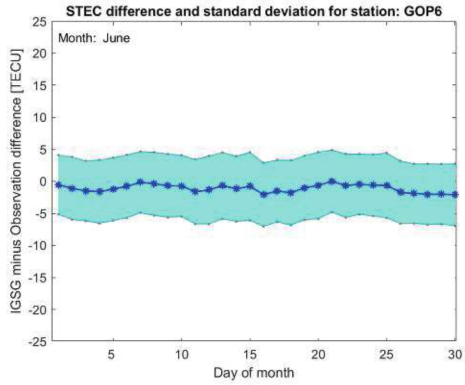


(c) IGS

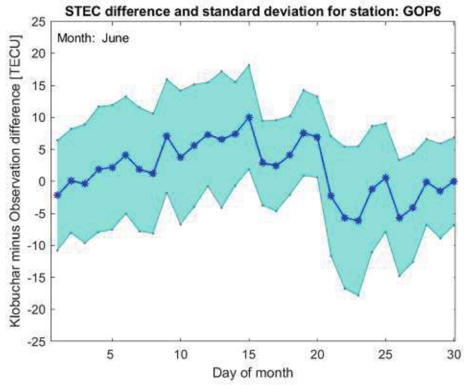


(d) Klobuchar

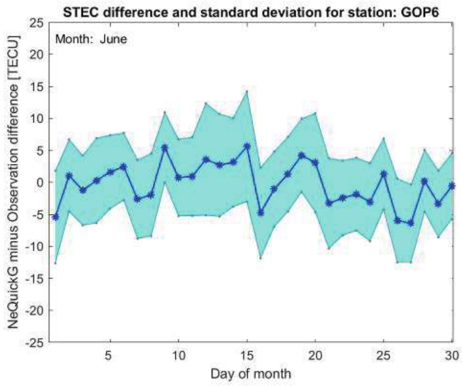


(e) NeQuick G

Figure B.6: Monthly STEC differences and standard deviations between the derived STEC value from the tested models (a) - (e) and the observation based STEC on IGS station GOP6 (Ondrejov, Czechia) for June, 2022 (doy 181 2022).

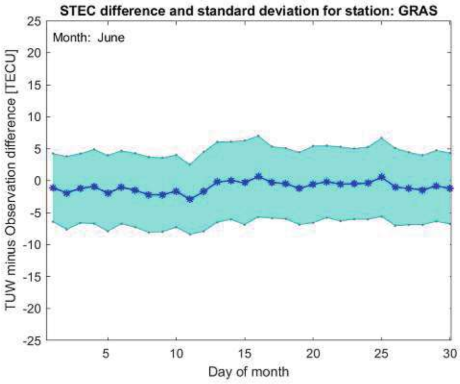


(a) TUWR

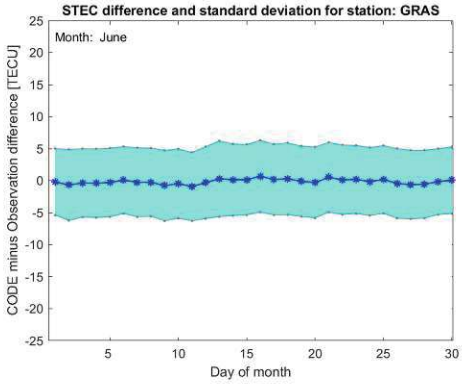


(b) CODE

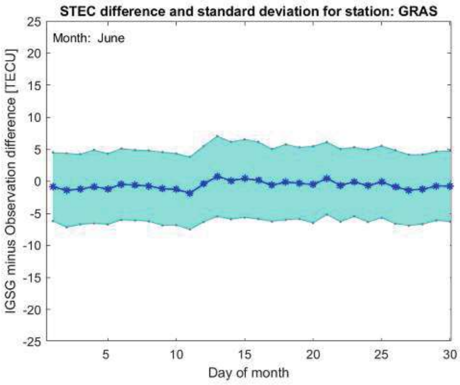


(c) IGS

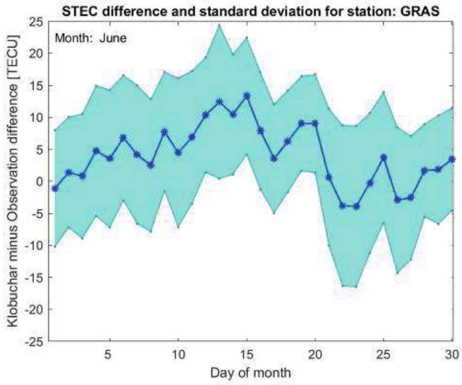


(d) Klobuchar

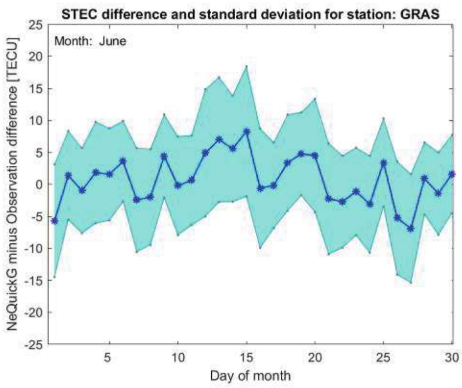


(e) NeQuick G

Figure B.7: Monthly STEC differences and standard deviations between the derived STEC value from the tested models (a) - (e) and the observation based STEC on IGS station GRAS (Caussols, France) for June, 2022 (doy 181 2022).

# Weblinks

AIUB. (2022). *Index of /BSWUSER52/STA/*. Retrieved July 28, 2022, from http://ftp.aiub.unibe.ch/BSWUSER52/STA/

AIUB FTP Server. (2022). Retrieved July 28, 2022, from http://ftp.aiub.unibe.ch/

Barradas Pereira, R., & GMV. (2011). *GNSS Applications*. Retrieved December 13, 2021, from https://gssc.esa.int/navipedia/index.php/GNSS_Applications

CDDIS. (2022a). Retrieved July 28, 2022, from https://cddis.nasa.gov/archive/gnss/data/daily/

CDDIS. (2022b). *Daily 30-second data*. Retrieved July 28, 2022, from https://cddis.nasa.gov/Data_an_Derived_Products/GNSS/daily_30second_data.html/

CODE. (2022). Retrieved July 28, 2022, from http://ftp.aiub.unibe.ch/CODE/

Data Analysis Center for Geomagnetic and Space Magnetism Faculty of Science. (2023). *World Data Center for Geomagnetism, Kyoto*. Retrieved March 24, 2023, from https://wdc.kugi.kyoto-u.ac.jp/

Desai and Sibois Model. (2018). Retrieved March 21, 2023, from https://ivscc.gsfc.nasa.gov/hfeop_wg/models/desai_model_jgrb51665-sup-0002-ds01.txt

EOP-PC. (2016). *The Mean Pole Readme*. Retrieved March 21, 2023, from https://hpiers.obspm.fr/eoppc/eop/eopc01/mean-pole.readme

EOP-PC. (2023a). *Earth orientation parameters series eopc01*. Retrieved March 21, 2023, from https://hpiers.obspm.fr/eoppc/eop/eopc01/eopc01.1900-now.dat

EOP-PC. (2023b). *Earth orientation parameters series eopc01: mean pole*. Retrieved March 21, 2023, from https://hpiers.obspm.fr/eoppc/eop/eopc01/mean-pole.tab

EOP-PC. (2023c). *The EOP (IERS) C01 Guide*. Retrieved March 21, 2023, from https://hpiers.obspm.fr/eoppc/eop/eopc01/EOPC01.GUIDE

EOP-PC. (2023d). *The EOP (IERS) C01 Readme*. Retrieved March 21, 2023, from https://hpiers.obspm.fr/eoppc/eop/README.EOP

ESOC/ESA. (2022). *GNSS products*. Retrieved July 28, 2022, from http://navigation-office.esa.int/products/gnss-products/

Euspa. (2021a). *Galileo Public Regulated Service (PRS)*. Retrieved June 6, 2023, from https://www.euspa.europa.eu/european-space/galileo/services/prs

Euspa. (2021b). *NOTICE ADVISORY TO GALILEO USERS (NAGU) 2021008*. Retrieved April 19, 2023, from https://www.gsc-europa.eu/notice-advisory-to-galileo-users-nagu-2021008

Euspa. (2021c). *What is GNSS?* Retrieved December 3, 2021, from https://www.euspa.europa.eu/european-space/eu-space-programme/what-gnss

Euspa. (2022). *Galileo Services*. Retrieved October 25, 2022, from https://www.euspa.europa.eu/galileo/services

Euspa. (2023). *Galileo High Accuracy Service (HAS)*. Retrieved June 6, 2023, from https://www.euspa.europa.eu/european-space/galileo/services/galileo-high-accuracy-service-has

GFZ Helmholtz Centre. (2023). *Geomagnetic Kp index*. Retrieved March 23, 2023, from https://kp.gfz-potsdam.de/

GGOS. (2023). *Earth Orientation Parameters*. Retrieved June 2, 2023, from https://ggos.org/item/earth-orientation-parameter/#toggle-id-3

Gipson tidal model (libration included). (2018). Retrieved March 21, 2023, from https://ivscc.gsfc.nasa.gov/hfeop_wg/models/2017a_astro_lib_xyu.txt

Gipson tidal model (libration not included). (2018). Retrieved March 21, 2023, from https://ivscc.gsfc.nasa.gov/hfeop_wg/models/2017a_astro_xyu.txt

IAU Commission C.A3 Fundamental Standards. (2018). *The IAU 2000-2012 Resolutions on Reference Systems*. Retrieved March 21, 2023, from https://www.iaufs.org/res.html

IERS Datacenter. (2022). *EOP 14 C04 series for 1962-2023 (IAU2000)*. Retrieved July 28, 2022, from https://datacenter.iers.org/versionMetadata.php?filename=latestVersionMeta/224_EOP_C04_14.62-NOW.IAU2000A224.txt

IERS Earth Orientation Parameters Product Center (EOP-PC). (2023). *Earth orientation parameters series eopc01*. Retrieved March 21, 2023, from https://hpiers.obspm.fr/eoppc/eop/eopc01/eopc01.iau2000.1900-now.dat

IERS2010 Model. (2018). Retrieved March 21, 2023, from https://ivscc.gsfc.nasa.gov/hfeop_wg/models/iers2010_xyu.txt

International Reference Ionosphere - IRI (2016). (2022). Retrieved July 24, 2022, from https://ccmc.gsfc.nasa.gov/modelweb/models/iri2016_vitmo.php/

IRI model. (2022). *International Reference Ionosphere Description*. Retrieved July 24, 2022, from http://irimodel.org/

NOAA. (2023). *About Harmonic Constituents*. Retrieved April 3, 2023, from https://tidesandcurrents.noaa.gov/about_harmonic_constituents.html

Royal Observatory of Belgium. (2023). *Solar Influences Data Analysis Center*. Retrieved March 23, 2023, from https://www.sidc.be/

Sanz Subirana, J., Juan Zornoza, J. M., & Hernández-Pajares, M. (2011). *Combining pairs of signals and clock definition*. Retrieved September 23, 2018, from https://gssc.esa.int/navipedia/index.php/Combining_pairs_of_signals_and_clock_definition

Space Weather Live. (2023). *Numbers of days with a geomagnetic storm per year*. Retrieved March 23, 2023, from https://www.spaceweatherlive.com/en/solar-activity/solar-cycle.html

U.S. Air Force GPS Directorate. (2021). *NAVSTAR GPS Space Segment/Navigation User Interfaces IS-GPS-200*. Retrieved April 14, 2023, from https://www.gps.gov/technical/icwg/IS-GPS-200M.pdf

VMF1. (2022). Retrieved July 28, 2022, from https://vmf.geo.tuwien.ac.at/trop_products/GRID/2.5x2/VMF1/VMF1_OP/

# Bibliography


Alizadeh, M. (2013). *Multi-Dimensional modelling of the ionospheric parameters, using space geodetic techniques* (Doctoral dissertation). Technische Universität Wien, Institut für Geodäsie und Geophysik. Wien.

Altamimi, Z., Collilieux, X., & Métivier, L. (2011). ITRF2008: an improved solution of the international terrestrial reference frame. *Journal of Geodesy*, *85*(8), 457–473.

Altamimi, Z., Rebischung, P., Collilieux, X., Métivier, L., & Chanard, K. (2023). Itrf2020: An augmented reference frame refining the modeling of nonlinear station motions. *Journal of Geodesy*, *97*(5), 47.

Altamimi, Z., Rebischung, P., Métivier, L., & Collilieux, X. (2016). ITRF2014: A new release of the International Terrestrial Reference Frame modeling nonlinear station motions. *Journal of Geophysical Research: Solid Earth*, *121*(8), 6109–6131.

Arias, E. F., Charlot, P., Feissel, M., & Lestrade, J.-F. (1995). The extragalactic reference system of the International Earth Rotation Service, ICRS. *Astronomy & Astrophysics*, *303*, 604–608.

Arnold, D., Meindl, M., Beutler, G., Dach, R., Schaer, S., Lutz, S., Prange, L., Sośnica, K., Mervart, L., & Jäggi, A. (2015). CODE's new solar radiation pressure model for GNSS orbit determination. *Journal of Geodesy*, *89*(8), 775–791.

Arora, K. (2020). Geodesy, Figure of the Earth. In H. K. Gupta (Ed.), *Encyclopedia of Solid Earth Geophysics* (pp. 1–4). Springer International Publishing.

Artz, T., Bernhard, L., Nothnagel, A., Steigenberger, P., & Tesmer, S. (2012). Methodology for the combination of sub-daily Earth rotation from GPS and VLBI observations. *Journal of Geodesy*, *86*(3), 221–239.

Artz, T., Tesmer née Böckmann, S., & Nothnagel, A. (2011). Assessment of periodic subdiurnal Earth rotation variations at tidal frequencies through transformation of VLBI normal equation systems. *Journal of Geodesy*, *85*(9), 565–584.

Bilitza, D. (2018). IRI the International Standard for the Ionosphere. *Advances in Radio Science*, *16*, 1–11.

Bilitza, D., Altadill, D., Truhlik, V., Shubin, V., Galkin, I., Reinisch, B., & Huang, X. (2017). International Reference Ionosphere 2016: From ionospheric climate to real-time weather predictions. *Space Weather*, *15*(2), 418–429.

Bizouard, C., Lambert, S., Gattano, C., Becker, O., & Richard, J.-Y. (2019). The IERS EOP 14C04 solution for Earth orientation parameters consistent with ITRF 2014. *Journal of Geodesy*, *93*(5), 621–633.

Böhm, J., Werl, B., & Schuh, H. (2006). Troposphere mapping functions for GPS and VLBI from ECMWF operational analysis data. *Journal of Geophysical Research: Solid Earth*, *111*(B2), B02406.

Böhm, S. (2012). *Tidal excitation of Earth rotation observed by VLBI and GNSS* (Doctoral dissertation). Technische Universität Wien, Institut für Geodäsie und Geoinformation. Vienna.

Brosche, P., & Schuh, H. (1998). Tides and Earth rotation. *Surveys in geophysics*, *19*(5), 417–430.

Budden, K. G. (1988). *The propagation of radio waves: the theory of radio waves of low power in the ionosphere and magnetosphere*. Cambridge University Press.

Cartwright, D., & Edden, A. C. (1973). Corrected tables of tidal harmonics. *Geophysical journal international*, *33*(3), 253–264.

Cartwright, D., & Tayler, R. (1971). New computations of the tide-generating potential. *Geophysical Journal International*, *23*(1), 45–73.

Cerveira, P. J. M. (2009). Die Rotation der Erde. *Österreichische Zeitschrift für Vermessung & Geoinformation*, *4*, 415–421.

Charlot, P., Jacobs, C. S., Gordon, D., Lambert, S., De Witt, A., Böhm, J., Fey, A., Heinkelmann, R., Skurikhina, E., Titov, O., Arias, E. F., Bolotin, S., Bourda, G., Ma, C., Z, M., Nothnagel, A., D, M., MacMIlan, D. S., Nilsson, T., & Gaume, R. (2020). The third realization of the International Celestial Reference Frame by very long baseline interferometry. *Astronomy & Astrophysics*, *644*, A159.

Chen, G., & Herring, T. (1997). Effects of atmospheric azimuthal asymmetry on the analysis of space geodetic data. *Journal of Geophysical Research: Solid Earth*, *102*(B9), 20489–20502.

Chen, J., Ren, X., Zhang, X., Zhang, J., & Huang, L. (2020). Assessment and Validation of Three Ionospheric Models (IRI-2016, NeQuick2, and IGS-GIM) From 2002 to 2018. *Space Weather*, *18*(6), e2019SW002422.

Dach, R., Lutz, S., Walser, P., & Fridez, P. (2015). Bernese GNSS Software Version 5.2.

Dach, R., Schaer, S., Arnold, D., Orliac, E., Prange, L., Susnik, A., Villiger, A., & Jäggi, A. (2016). Code final product series for the igs.

Davies, K. (1965). *Ionospheric radio propagation* (Vol. 80). US Department of Commerce, National Bureau of Standards.

Davies, K. (1990). Ionospheric radio. *IEEE Electromagnetic Waves Series*, *31*.

Desai, S. D., & Sibois, A. E. (2016). Evaluating predicted diurnal and semidiurnal tidal variations in polar motion with GPS-based observations. *Journal of Geophysical Research: Solid Earth*, *121*(7), 5237–5256.

DiMarco, S. F., & Reid, R. O. (1998). Characterization of the principal tidal current constituents on the Texas-Louisiana shelf. *Journal of Geophysical Research: Oceans*, *103*(C2), 3093–3109.

Doodson, A. T. (1921). The harmonic development of the tide-generating potential. *Proceedings of the Royal Society of London. Series A, Containing Papers of a Mathematical and Physical Character*, *100*(704), 305–329.

Egbert, G. D., Bennett, A. F., & Foreman, M. G. (1994). TOPEX/POSEIDON tides estimated using a global inverse model. *Journal of Geophysical Research: Oceans*, *99*(C12), 24821–24852.

European Commission. (2016). European GNSS (Galileo) Open Service – Ionospheric Correction Algorithm for Galileo Single Frequency Users.

Falcone, M., Hahn, J., & Burger, T. (2017). Galileo. In P. J. Teunissen & O. Montenbruck (Eds.), *Springer Handbook of Global Navigation Satellite Systems* (pp. 247–272). Springer.

Feynman, R. P., Leighton, R. B., & Sands, M. (1963). *The Feynman Lectures in Physics, Volume 1*. Addison-Wesley, Reading.

Forbes, J., Palo, S., & Zhang, X. (2000). Variability of the ionosphere. *Journal of Atmospheric and Solar-terrestrial Physics - J ATMOS SOL-TERR PHYS*, *62*, 685–693.

Fowler, C. M. R. (2005). *The Solid Earth: An introduction to Global Geophysics*. Cambridge University Press.

Gauss, C. F. (1828). *Bestimmung des Breitenunterschiedes zwischen den Sternwarten von Göttingen und Altona: durch Beobachtungen am Ramsdenschen Zenithsector*. Bei Vandenhoeck und Ruprecht.

Gipson, J. *IERS Working Group on HF-EOP*. 2018 FALL AGU, Washington, DC. 2018. https://ivscc.gsfc.nasa.gov/hfeop_wg/presentations/2018AGU_HFEOP_Gipson.pdf

Gipson, J., & Hesslow, L. *A new model of HF-EOP variation derived from 35 years of VLBI* [Geophysical Research Abstracts, 17. EGU2015-14756]. EGU General Assembly 2015, Vienna. Geophysical Research Abstracts, 17. EGU2015-14756. 2015.

Girdiuk, A., Schindelegger, M., Krasna, H., & Böhm, J. (2017). Assessing recent high-frequency Earth rotation models with Very Long Baseline Interferometry. *Journees 2017 Abstract Book*, 1.

Glaner, M. F. (2017). *Eigenschaften und Einsatzmöglichkeiten von GPS und Galileo Signal - Linearkombinationen* (Master Thesis, Master's thesis). Technische Universität Wien, Institut für Geodäsie und Geoinformation. Vienna.

Glaner, M. F. (2022). *Towards instantaneous PPP convergence using multiple GNSS signals* (Doctoral dissertation). Wien.

Gross, R. S. (2000). The excitation of the Chandler wobble. *Geophysical Research Letters*, *27*(15), 2329–2332.

Halilović, D., Mulić, M., & Weber, R. (2023). Earth rotation and its parameters. *International Symposium on Innovative and Interdisciplinary Applications of Advanced Technologies*, 492–506.

Hargreaves, J. K. (1992). *The Solar-Terrestrial Environment: An Introduction to Geospace - the Science of the Terrestrial Upper Atmosphere, Ionosphere, and Magnetosphere*. Cambridge University Press.

Hartmann, T., & Wenzel, H.-G. (1995). The HW95 tidal potential catalogue. *Geophysical research letters*, *22*(24), 3553–3556.

Hathaway, D. H. (2015). The Solar Cycle. *Living Reviews in Solar Physics*, *12*(4), 1614–4961.

Hauschild, A. (2017a). Basic observation equations. In P. J. Teunissen & O. Montenbruck (Eds.), *Springer Handbook of Global Navigation Satellite Systems* (pp. 561–582). Springer.

Hauschild, A. (2017b). Combinations of observations. In P. J. Teunissen & O. Montenbruck (Eds.), *Springer Handbook of Global Navigation Satellite Systems* (pp. 583–604). Springer.

Hefty, J., Rothacher, M., Springer, T., Weber, R., & Beutler, G. (2000). Analysis of the first year of Earth rotation parameters with a sub-daily resolution gained at the CODE processing center of the IGS. *Journal of Geodesy*, *74*(6), 479–487.

Hegarty, C. J. (2017). The global positioning system (GPS). In P. J. Teunissen & O. Montenbruck (Eds.), *Springer Handbook of Global Navigation Satellite Systems* (pp. 197–218). Springer.

Hernández-Pajares, M., Juan, J. M., & Sanz, J. (2006). Medium-scale traveling ionospheric disturbances affecting GPS measurements: Spatial and temporal analysis. *Journal of Geophysical Research: Space Physics*, *111*(A7).

Hernández-Pajares, M., Roma-Dollase, D., Krankowski, A., García-Rigo, A., & Orús-Pérez, R. (2017). Methodology and consistency of slant and vertical assessments for ionospheric electron content models. *Journal of Geodesy*, *91*(12), 1405–1414.

Hobiger, T., & Jakowski, N. (2017). Atmospheric Signal Propagation. In P. J. Teunissen & M. O (Eds.), *Springer Handbook of Global Navigation Satellite Systems* (pp. 165–193). Springer International Publishing.

Hofmann-Wellenhof, B., Lichtenegger, H., & Collins, J. (1993). Surveying with GPS. In *Global Positioning System: Theory and Practice* (pp. 115–158). Springer Vienna.

Hofmann-Wellenhof, B., Lichtenegger, H., & Wasle, E. (2007). *GNSS–global navigation satellite systems: GPS, GLONASS, Galileo, and more*. Springer Science & Business Media.

Hofmann-Wellenhof, B., & Moritz, H. (2005). *Physical Geodesy*. Springer.

Horozović, D. (2014). *Investigation of Ionosphere and Space Weather and their application in positioning and navigation* (Master thesis, Master's thesis). University of Sarajevo, Faculty of Civil Engineering, Department of Geodesy. Sarajevo.

Horozović, D., Krdžalić, D., & Mulić, M. (2015). Monitoring of Ionosphere and space weather in Bosnia and Herzegovina. *Geodetski glasnik*, *46*, 111–131. http://www.suggsbih.ba/GEODETSKI%20GLASNIK/GEODETSKI_GLASNIK_46/gg_46_8_e.htm

Jee, G., Lee, H.-B., Kim, Y. H., Chung, J.-K., & Cho, J. (2010). Assessment of GPS global ionosphere maps (GIM) by comparison between CODE GIM and TOPEX/Jason TEC data: Ionospheric perspective. *Journal of Geophysical Research: Space Physics*, *115*(A10).

Karbon, M., Balidakis, K., Belda, S., Nilsson, T., Hagedoorn, J., & Schuh, H. (2018). Long-Term Evaluation of Ocean Tidal Variation Models of Polar Motion and UT1, 1611–1629.

Langley, R. B. (2000). Gps, the ionosphere, and the solar maximum. *GPS world*, *11*(7), 44–49.

Langley, R. B., Teunissen, P. J., & Montenbruck, O. (2017). Introduction to GNSS. In P. J. Teunissen & O. Montenbruck (Eds.), *Springer Handbook of Global Navigation Satellite Systems* (pp. 3–23). Springer.

Liu, G. C. (2001). *Ionosphere weighted global positioning system carrier phase ambiguity resolution* (Master's thesis). University of Calgary, Department of geomatics Engineering. Graduate Studies.

Liu, L., Wan, W., Chen, Y., & Le, H. (2011). Solar activity effects of the ionosphere: A brief review. *Chinese Science Bulletin*, *56*(12), 1202–1211.

Lyard, F., Lefevre, F., Letellier, T., & Francis, O. (2006). Modelling the global ocean tides: modern insights from FES2004. *Ocean dynamics*, *56*(5), 394–415.

Madzak, M., Schindelegger, M., Böhm, J., Bosch, W., & Hagedoorn, J. (2016). High-frequency Earth rotation variations deduced from altimetry-based ocean tides. *Journal of Geodesy*, *90*(11), 1237–1253.

Magnet, N. (2019). *Giomo: a robust modeling approach of ionospheric delays for GNSS real-time positioning applications* (Doctoral dissertation). Technische Universität Wien, Institut für Geodäsie und Geoinformation. Wien. https://repositum.tuwien.at/handle/20.500.12708/8537

Mathews, P. M., & Bretagnon, P. (2003). Polar motions equivalent to high frequency nutations for a nonrigid Earth with anelastic mantle. *Astronomy & Astrophysics*, *400*(3), 1113–1128.

McCarthy, D. D. (1996). IERS Conventions (1996). *IERS Technical Note*, *21*, 1–95.

Meindl, M. (2011). *Combined analysis of observations from different global navigation satellite systems* (Doctoral dissertation). University of Bern. Bern.

Mervart, L. (1995). *Ambiguity resolution techniques in geodetic and geodynamic applications of the Global Positioning System* (Vol. 53). Schweizerische Geodätische Kommission.

Mervart, L., Beutler, G., Rothacher, M., & Wild, U. (1994). Ambiguity resolution strategies using the results of the International GPS Geodynamics Service (IGS). *Bulletin géodésique*, *68*(1), 29–38.

Modiri, S., Belda, S., Hoseini, M., Heinkelmann, R., Ferrándiz, J. M., & Schuh, H. (2020). A new hybrid method to improve the ultra-short-term prediction of lod. *Journal of Geodesy*, *94*(2), 1–14.

Mulić, M. (2018). *Geodetski referentni sistemi*. Građevinski fakultet Univerziteta u Sarajevu.

Ng, C.-K. (2015). How tidal forces cause ocean tides in the equilibrium theory. *Physics Education*, *50*(2), 159.

Ngayap, U., Paparini, C., Poretta, M., Buist, P., Jacobsen, K. S., Dähnn, M., Hanna, N., Halilović, D., Świątek, A., & Gajdowska, P. (2023). Comparison of NeQuick G and Klobuchar model performances at single frequency user level.

Nilsson, T. (2018). Evaluation of different high frequency EOP models using VLBI [Memos written by members of the working group]. https://ivscc.gsfc.nasa.gov/hfeop_wg/memos/hf_eop_mods_eval_nilsson.pdf

Nothnagel, A., Artz, T., Behrend, D., & Malkin, Z. (2017). International VLBI service for geodesy and astrometry. *Journal of Geodesy*, *91*(7), 711–721.

Parker, B. B. (2007). Tidal analysis and prediction.

Parkinson, B. W., Morton, Y. J., van Diggelen, F., & Spilker Jr, J. J. (2020). Introduction, Early History, and Assuring PNT (PTA). *Position, Navigation, and Timing Technologies in the 21st Century: Integrated Satellite Navigation, Sensor Systems, and Civil Applications*, *1*, 1–42.

Pavlis, N. K., Holmes, S. A., Kenyon, S. C., & Factor, J. K. (2012). The development and evaluation of the Earth Gravitational Model 2008 (EGM2008). *Journal of Geophysical Research: Solid Earth*, *117*(B4).

Petit, G., & Luzum, B. (2010). *IERS Conventions (2010), IERS Technical Note 36*. Verlag des Bundesamts für Kartographie und Geodäsie, Frankfurt am Main.

Rahman, M. M., Paul, G. C., & Hoque, A. (2017). A study on tidal potential and tide generating force. *GANIT: Journal of Bangladesh Mathematical Society*, *37*, 29–37.

Ray, R. D., Steinberg, D. J., Chao, B. F., & Cartwright, D. E. (1994). Diurnal and semidiurnal variations in the Earth's rotation rate induced by oceanic tides. *Science*, *264*(5160), 830–832.

Rebischung, P., & Schmid, R. (2016). IGS14/igs14. atx: a new framework for the IGS products. *AGU fall meeting 2016*.

Rishbeth, H., & Garriott, O. K. (1969). *Introduction to ionospheric physics*. Academic Press New York.

Rodríguez, J. Á. Á., Hahn, J., Bautista, M. M., & Chatre, E. (2020). Galileo. In Y. T. J. Morton, F. Diggelen, J. J. Spilker, B. W. Parkinson, S. Lo, & G. Gao (Eds.), *Position, Navigation, and Timing Technologies in the 21st Century* (pp. 105–142). John Wiley & Sons, Ltd.

Roma-Dollase, D., Hernández-Pajares, M., Krankowski, A., Kotulak, K., Ghoddousi-Fard, R., Yuan, Y., Li, Z. [Zishen], Zhang, H., Shi, C., Wang, C., et al. (2018). Consistency of seven different GNSS global ionospheric mapping techniques during one solar cycle. *Journal of Geodesy*, *92*(6), 691–706.

Rothacher, M., Beutler, G., Herring, T. A., & Weber, R. (1999). Estimation of nutation using the Global Positioning System. *Journal of Geophysical Research: Solid Earth*, *104*(B3), 4835–4859.

Rothacher, M., Beutler, G., Weber, R., & Hefty, J. (2001). High-frequency variations in Earth rotation from Global Positioning System data. *Journal of Geophysical Research: Solid Earth*, *106*(B7), 13711–13738.

Schaer, S. (1999). *Mapping and predicting the Earth's ionosphere using the Global Positioning System* (Doctoral dissertation). Bern University, Switzerland. Bern.

Schaer, S., Beutler, G., Mervart, L., Rothacher, M., & Wild, U. (1996). Global and regional ionosphere models using the GPS double difference phase observable. *Proceedings of the IGS Workshop*.

Schindelegger, M. (2014). *Atmosphere-induced short period variations of Earth rotation* (Doctoral dissertation). Technische Universität Wien, Institut für Geodäsie und Geoinformation. Vienna.

Schuh, H., & Böhm, S. (2020). Earth Rotation. In H. K. Gupta (Ed.), *Encyclopedia of Solid Earth Geophysics* (pp. 1–8). Springer International Publishing.

Seeber, G. (2003). *Satellite Geodesy, 2nd Edition*. Walter de Gruyter.

Seitz, F., & Schuh, H. (2010). Earth Rotation. In G. Xu (Ed.), *Sciences of Geodesy - I: Advances and Future Directions* (pp. 185–227). Springer Berlin Heidelberg.

Shi, C., & Wei, N. (2020). Satellite navigation for digital Earth. In H. Guo, M. F. Goodchild, & A. Annoni (Eds.), *Manual of Digital Earth* (pp. 125–160). Springer, Singapore.

Sidorenkov, N. S. (2009). *The interaction between Earth's rotation and geophysical processes*. John Wiley & Sons.

Sośnica, K., Prange, L., Kaźmierski, K., Bury, G., Drożdżewski, M., Zajdel, R., & Hadas, T. (2018). Validation of Galileo orbits using SLR with a focus on satellites launched into incorrect orbital planes. *Journal of Geodesy*, *92*(2), 131–148.

Sośnica, K., Thaller, D., Dach, R., Steigenberger, P., Beutler, G., Arnold, D., & Jäggi, A. (2015). Satellite laser ranging to GPS and GLONASS. *Journal of Geodesy*, *89*(7), 725–743.

Springer, T. A., Beutler, G., & Rothacher, M. (1999). Improving the orbit estimates of GPS satellites. *Journal of Geodesy*, *73*(3), 147–157.

Standish Jr, E. M. (1990). The observational basis for JPL's DE 200, the planetary ephemerides of the Astronomical Almanac. *Astronomy & Astrophysics*, *233*, 252–271.

Tapping, K. F. (2013). The 10.7 cm solar radio flux (F10.7). *Space Weather*, *11*(7), 394–406.

Teunissen, P. J. G., & Montenbruck, O. (2017). *Springer Handbook of Global Navigation Satellite Systems* (Vol. 10). Springer International Publishing.

Todorova, S. (2008). *Combination of space geodetic techniques for global mapping of the ionosphere* (Doctoral dissertation). Technische Universität Wien, Institut für Geodäsie und Geophysik. Vienna.

Torge, W. (2001). *Geodesy*. Walter de Gruyter, Berlin, Germany.

Tseng, T.-P., & Moore, M. (2018). Impact of solar radiation pressure mis-modeling on GNSS satellite orbit determination. IGS Workshop 2018, Wuhan, China.

Wild, U. (1994). Ionosphere and geodetic satellite systems: permanent GPS tracking data for modelling and monitoring. *Geod.-Geophys. Arb. Schweiz*, *48*.

Wunsch, C., Haidvogel, D. B., Iskandarani, M., & Hughes, R. (1997). Dynamics of the long-period tides. *Progress in Oceanography*, *40*(1-4), 81–108.

Zajdel, R. (2021). *Determination of Global Geodetic Parameters Using the GPS, GLONASS, and Galileo Satellite Systems* (Doctoral dissertation). Wrocław University of Environmental, Life Sciences, Institute of Geodesy, and Geoinformatics. Wrocław.

Zajdel, R., Kazmierski, K., & Sośnica, K. (2022). Orbital artifacts in multi-gnss precise point positioning time series. *Journal of Geophysical Research: Solid Earth*, *127*(2), e2021JB022994.

Zajdel, R., Sośnica, K., Bury, G., Dach, R., Prange, L., & Kazmierski, K. (2021). Sub-daily polar motion from gps, glonass, and galileo. *Journal of geodesy*, *95*(1), 1–27.

Zhang, V., & Li, Z. [Zhiqi]. (2015). Measured Ionospheric Delay Corrections for Code-based GPS Time Transfer. *NCSLI Measure*, *10*, 66–71.

Zolesi, B., & Cander, L. (2014). *Ionospheric Prediction and Forecasting*.